Title
Quantifying conflict and its associations with infectious diseases in Yemen, Ukraine, and Syria

ISBN
9798186331636

Author
Tarnas, Maia C.

Publication Date
2026-08-08

UNIVERSITY OF CALIFORNIA,
IRVINE

Quantifying conflict and its associations with infectious diseases in Yemen, Ukraine, and Syria

DISSERTATION

submitted in partial satisfaction of the requirements
for the degree of

DOCTOR OF PHILOSOPHY

in Public Health

by

Maia C. Tarnas

Dissertation Committee:
Associate Professor Daniel M. Parker, Chair
Professor Volodymyr M. Minin
Assistant Professor Tetyana I. Vasylyeva

2026

DEDICATION

To

My grandmother, Patricia Stewart, for your bravery, resilience, and dedication to helping others.
احبك

"If innocence has any meaning, the epidemiology reveals that the victims are those with the most striking moral claims. If the scale of suffering has any meaning, epidemiology demands that indirect effects not be ignored. If the failure to act when capability exists has any meaning, the science of indirect effects testifies to a damning global complacency."

- Paul H. Wise (1)

TABLE OF CONTENTS

LIST OF FIGURES

LIST OF TABLES

ACKNOWLEDGMENTS

Daniel, you believed in me when I was on the other end of a cold email and in every other moment, especially those when I didn't believe in myself. You understand exactly how my brain works, and you've spent the last five years encouraging my growth and exploration. How did I get so lucky? Thank you for your patience, for leading by example, and for your unwavering support. I'm a better person and a better scholar having learned from you.

Volodymyr and Tanya, thank you for your support, guidance, and trust to work on a topic near and dear to you both. I'm grateful not only for how much you've taught me, but also how you've welcomed me into your labs with open arms and showed me the strength (and fun) of working in teams.

Aula, it is not an exaggeration to say that I wouldn't be here without you. Your mentorship and friendship have steered my work and passion from the very beginning. Thank you for always advocating for me, trusting me, and believing in me. You make the world a better place, and I'm so grateful to get to be in yours.

To my colleagues who have been on this path with me, and especially Muhammad Zaman, Naser Almhawish, Mohammad Darwish, Mohamed Hamze, and Ruwan Ratnayake. Thank you for giving me opportunities to grow and the space to learn. My wonderful labmates: Natasha, Gaëlle, José, Marcela, Chel, and Adriana. There's no other group I would want to go through this with. I'm so grateful to have gotten to learn from you and laugh with you.

To all the wonderful staff that helped walk me through this process, especially Gabriella Pham, Yuting Wu, Ephie Bakou, Chenda Seng, Brianna Porter, Lauren Nguyen, Eric Portillo, and Madison Spiva. Thank you for answering my many (*many*) questions, guiding me through the entire F31 process, and keeping me on track.

Educators throughout my life have encouraged me to think with nuance, work across disciplines, and fall in love with learning. Their support and guidance taught me how to form and defend my opinions, challenge authorities, and advocate for myself and others in and out of the classroom. I was also fortunate to have my love of science and math recognized and supported at an early age, which many young girls do not. Thanks especially to Ms. Kassis, Ms. Doherty, Naj, Dr. Hamilton, Dr. Kosinski, Dr. Tendulkar, Dr. Cuevas, Rana Abdul-Aziz, Dr. Gideonse, Dr. Timberlake, Dr. Vieira, and Dr. Jiang.

To my amazing family—there are no words strong enough. Dad, thank you for teaching me how to tell stories and to always fight for what is right. Mom, you showed me what it looks like to love our communities and selflessly advocate for them. Jesse, you've always given me a safe place to land and seen me as the best version of myself. I couldn't have asked for a better person to brave the world with. Tasia, thank you for the joy, competition, and deep understanding. To the Tarnas and Stewart families: I am so lucky to come from such kind, strong, and generous people. You show me how to nurture, forgive, and love unconditionally.

I am also so lucky to have been raised by a strong extended and chosen family. Susan, Marius, Georgine, Robert, Clem, JP, Aunty Kristin, Uncle Bon, Uncle Earl—from making sure I was properly swaddled to instilling my love of music and camping to helping send me off to college, you're the very definition of love. Ben and Shannon, you gave me a family 2,500 miles from home and wrapped me into your arms without question. Thank you for seeing me through so many ups and downs, laughing (or at least, groaning) at my jokes, and understanding me so completely. The Shapiro family, thank you for embracing me.

My friends, who have seen every version of me and loved me through it. Sean, Gvantsa, Gabie, Leah, Mary, Noa, Sarah, Jenny, and Ryan, I've been able to become who I am, and who I am still yet to be, because you've shown that you'll be by my side no matter what. Thank you for loving me across continents, oceans, and many, many years. Sean, you help me realize life while I live it. Raquel and Mariam, you made Irvine a home. To my wonderful soccer team, who were my first friends in Irvine and who have been an incredible source of support, laughter, and adventure. And, to Luka, for reminding me that existing is reason enough to be loved.

And finally, to Sam. Thank you for helping me find my wings and my voice. You are, and always will be, the best thing.

The text of Chapter 2 of this dissertation is a reprint of the material as it appears in Tarnas MC, Al-Dheeb N, Zaman MH, Parker DM (2023). Association between air raids and reported incidence of cholera in Yemen, 2016–2019: an ecological modelling study. *The Lancet Global Health, 11*(12), E1955-E1963, used with permission from Elsevier Ltd (CC BY 4.0). The coauthors listed in this publication are Najwa Al-Dheeb, Muhammad H. Zaman, and Daniel M. Parker.

The text of Chapter 3 of this dissertation is a reprint of the material as it appears in Tarnas MC, Abbara A, Desai AN, Parker DM (2024). Ecological study measuring the association between conflict, environmental factors, and annual global cutaneous and mucocutaneous leishmaniasis incidence (2005–2022). *PLoS Neglected Tropical Diseases, 18*(9), e0012549, used with permission from PLoS (CC BY 4.0). The coauthors listed in this publication are Aula Abbara, Angel N. Desai, and Daniel M. Parker.

The text of Chapter 4 of this dissertation is a reprint of the material as it appears in Tarnas MC, Vasylyeva TI, Minin VM, Parker DM (2026). Nighttime lights as a proxy for conflict intensity and infrastructure recovery in Yemen and Ukraine. *Conflict and Health,* used with permission from Springer Nature (CC BY 4.0). The coauthors listed on this publication are Tetyana I. Vasylyeva, Volodymyr M. Minin, and Daniel M. Parker.

This dissertation was supported by the U.S. National Institute of Allergy and Infectious Diseases (F31AI183632).

VITA

Maia C. Tarnas

EDUCATION

2026	PhD in Public Health (Global Health concentration), University of California, Irvine
2019	BA in Community Health, Tufts University
2019	BA in Middle Eastern Studies (Arabic minor), Tufts University

APPOINTMENTS

2026–	Research Fellow, NASA Lifelines
2025	Consultant, World Health Organization
2024–25	Consultant, Syrian American Medical Society
2024–25	Instructor of Record, University of California, Irvine

FELLOWSHIP

F31AI183632: U.S. National Institute of Allergy and Infectious Diseases, National Research Service Award Predoctoral Individual Fellowship ($93,656)

FIELD OF STUDY

Conflict and Health; Global Health; Epidemiology

SELECTED PUBLICATIONS

Tarnas MC, Vasylyeva TI, Minin VM, Parker DM (2026). Nighttime lights as a viable tool for measuring armed conflict in Yemen and Ukraine. *Conflict and Health.* doi:10.1186/s13031-026-00801-5

Polinori C, **Tarnas MC**, Wagner K, Darwish M, Lazieh SM, Alnasser A, Ghandour A, Alkhatib I, Bellizzi S, Zuhaili B, Burnham G (2026). Post-operative care in conflict-affected northwest Syria: A mixed-methods study assessing the perspectives of patients, health workers, and NGOs. *Conflict and Health*. doi:10.1186/s13031-026-00802-4

Abu-Khalil AS, Sayeeda RJ, Shaikh B, Salih A, Omulo S, Amulen E, Bukenya JN, Byonanebye DM, Gross N, Joly MJA, Kirumira E, Lubogo D, Munna AK, Nakisita OE, Ntale E, Wagaba MT, Ching C, **Tarnas MC**, Orach C, Zaman MH (2026). Advancing health research practices among

forcibly displaced populations: A multidisciplinary stakeholder workshop. *Health Research Policy and Systems.* doi:10.1186/s12961-026-01446-9

Ching C, Sayeeda RJ, **Tarnas MC**, Gross N, Abu-Khalil A, Shaikh B, Zaman MH (2025). Mapping utility and applicability of research and ethics frameworks for displaced populations. *Global Public Health*. doi:10.1080/17441692.2025.2557322

Tarnas MC, Almhawish N, Ratnayake N, Elferruh Y, Aladhan I, Alhaffar MBA, Abbara A (2025). Climate change, conflict, forced displacement, and epidemic-prone diseases: an exploratory study in northern Syria. *BMC Public Health*. doi:10.1186/s12889-025-23918-3

Gross N*, **Tarnas MC***, Sayeeda R, Ching C, Zaman MH (2025). Current infectious disease research practices with forcibly displaced people in the top ten low- and middle-income host countries: A systematic review. *Journal of Migration and Health.* doi:10.1016/j.jmh.2025.100341

Tarnas MC, Al-Jobury S, Al-Dheeb N, Quradi A, Metry N, Hadjiabduli S, Awad I, Ching C, Parker DM, Zaman MH (2025). Reimagining refugee camps: Toward ethical, sustainable, and integrated health systems. *International Migration.* doi:10.1111/imig.70060

Abu El Kheir-Mataria W, **Tarnas MC**, Simonek T, Al-Jadba G, Boatemaa Setrana M, Ellis K, Heck G, Ayoub M, İçduygu A, Zaman MH, Parker DM (2025). Rethinking health in refugee camps: Addressing socioeconomic and geopolitical constraints. *International Migration.* doi:10.1111/imig.70048

Lazieh SM, **Tarnas MC**, Wagner K, Alkhatib I, Polinori C, Netfagi M, Ghandour A, Qaddour S, Zuhaili B, Burnham G. (2025). Healthcare workers' perceptions of postoperative care and implementation challenges in conflict-affected Northwest Syria: a mixed-methods analysis. *BMJ Public Health*. doi:10.1136/bmjph-2024-001236

Alhaffar MBA, Abbara A, Almhawish N, **Tarnas MC**, AlFaruh Y, Erikson A. (2025). The early warning and response systems in Syria: A functionality and alert threshold assessment. *IJID Regions.* doi:10.1016/j.ijregi.2024.100563

Tarnas MC, Hamze M, Tajaldin B, Sullivan R, Parker DM, Abbara A. (2024). Exploring relationships between conflict intensity, forced displacement, and healthcare attacks: a retrospective analysis from Syria, 2016–2022. *Conflict and Health*. doi:10.1186/s13031-024-00630-4

Tarnas MC, Abbara A, Desai AN, Parker DM. (2024). Ecological study measuring the association between conflict, environmental factors, and annual global cutaneous and mucocutaneous leishmaniasis incidence (2005–2022). *PLOS Neglected Tropical Diseases*. doi:10.1371/journal.pntd.0012549

Kampalath V, **Tarnas MC,** Patel V, Hamze M, Loutfi R, Tajaldin B, Albik A, Kassas A, Khashata A, Abbara A. (2024). An analysis of paediatric clinical presentations in northwest Syria and the effect of forced displacement, 2018–2022. *Global Epidemiology*. doi:10.1016/j.gloepi.2024.100146

Tarnas MC, Al Dheeb N, Zaman MH, Parker DM. (2023). Association between air raids and reported incidence of cholera in Yemen, 2016 – 19: An ecological modelling study. *The Lancet Global Health.* doi:10.1016/S2214-109X(23)00272-3

Hmaideh A*, **Tarnas MC***, Zakaria W, Rifai AO, Ibrahem M, Hashoom Y, Ghazal N, Abbara A (2023). Geographical origin, WASH access, and clinical descriptions for patients admitted to a cholera treatment center in northwest Syria between October and December 2022. *Avicenna Journal of Medicine*. doi:10.1055/s-0043-1776045

Tarnas MC, Almhawish N, Karah N, Abbara A (2023). Communicable diseases in northwest Syria in the context of protracted armed conflict and earthquakes. *The Lancet Infectious Diseases.* doi:10.1016/S1473-3099(23)00201-3

Tarnas MC, Karah N, Almhawish N, Aladhan I, Alobaid R, Abbara A (2023). Politicization of water, humanitarian response, and health in Syria as a contributor to the ongoing cholera outbreak. *International Journal of Infectious Diseases.* doi:10.1016/j.ijid.2023.03.042

Tabor R, Almhawish N, Aladhan I, **Tarnas M**, Sullivan R, Karah N, Zeitoun M, Ratnayake R, Abbara A. (2023). Disruption to water supply and waterborne communicable diseases in northeast Syria: a spatiotemporal analysis. *Conflict and Health*. doi:10.1186/s13031-023-00502-3

Tarnas MC, Ching C, Lamb JB, Parker DM, Zaman MH. Analyzing health of forcibly displaced communities through an integrated ecological lens. (2023). *American Journal of Tropical Medicine and Hygiene*. doi:10.4269/ajtmh.22-0624

Tarnas MC, Desai AN, Parker DM, Almhawish N, Zakieh O, Rayes D, Whalen-Browne M, Abbara A. (2022) Syndromic surveillance of respiratory infections during protracted conflict: experiences from northern Syria 2016-2021. *International Journal of Infectious Diseases*. doi:10.1016/j.ijid.2023.03.042

ABSTRACT OF THE DISSERTATION

Quantifying conflict and its associations with infectious diseases in Yemen, Ukraine, and Syria

By

Maia C. Tarnas
Doctor of Philosophy in Public Health
University of California, Irvine, 2026
Associate Professor Daniel M. Parker, Chair

This dissertation seeks to untangle how armed conflict exacerbates infectious disease risk through physical, environmental, social, and geographic factors. Across multiple conflict settings, I analyze how conflict intensity impacts cholera and cutaneous leishmaniasis risk in conjunction with relevant environmental factors, as well as suggest an additional tool for measuring conflict's effects on the built environment. I do this by 1) assessing the association between violent conflict events and cholera in Yemen, 2) exploring Earth observation tools for measuring conflict intensity and infrastructure recovery in Yemen and Ukraine, 3) analyzing how environmental and conflict-related factors modify leishmaniasis risk at an ecological scale, and 4) quantifying cutaneous leishmaniasis surveillance gaps in northern Syria. Together, this work provides insights on how armed conflict actively shapes infectious disease dynamics. It also presents a viable tool for measuring conflict intensity and infrastructure damage that is unbound by many of the limitations of traditional tools. In doing so, this dissertation highlights that increases in infectious disease during armed conflict are not naturally occurring or unfortunate collateral damage, but rather the result of intentional human action. These findings have important implications for preparedness, response, and advocacy on behalf of civilians who bear the brunt of conflict.

CHAPTER ONE: Introduction

Armed conflicts create environments in which infectious diseases thrive. As conflicts have become increasingly violent and protracted, the scale and breadth of infectious disease outbreaks have followed in parallel. The nature of conflict is also shifting; violations of international humanitarian law (IHL) are increasingly normalized with little accountability, and health itself is frequently weaponized. Moreover, an estimated 123.2 million people globally were forcibly displaced at the end of 2024, reflecting a near-doubling of displacement over the past decade (2). In 2024, there were 130 recorded armed conflicts, more than 20 of which had been ongoing for over two decades (3). UNICEF estimated at this time that one in six children globally live in areas affected by conflict. In the past year, however, the conflict landscape has measurably grown (4). Over the span of three months in early 2026, the United States ousted the president of Venezuela and began a war with Iran following joint airstrikes with Israel that killed the country's leader. In late 2025, Sudan's paramilitary Rapid Support Forces conducted a widescale massacre in El Fasher following at 18-month siege, actions which showed the "hallmarks of genocide" (5). Hundreds of Palestinians in Gaza have been killed by Israeli strikes despite a ceasefire in October 2025 (6). Throughout these and other ongoing conflicts, the damage and destruction of critical civilian infrastructure have become hallmarks.

IHL prohibits the targeting of civilian infrastructure during conflict (including indiscriminate attacks that cannot distinguish between civilian and military infrastructure), with special protections afforded to healthcare infrastructure (7–9). Despite numerous accountability efforts, including by the World Health Organization's Surveillance System for Attacks on Health and Physicians for Human Rights, there has been widespread impunity for perpetrators of healthcare attacks (10). Not only do these attacks contribute to the broader destruction of healthcare systems, but they also inform larger conflict dynamics. In Syria, where attacks on healthcare have taken many forms including air strikes, kidnapping and murdering of healthcare workers, and armed assaults, attacks on healthcare have preceded escalations in general conflict in the same area and population displacement for many months following the attacks (11). Such actions are examples of the weaponization of healthcare, defined by Fouad et al. as “a strategy of using people's need for health care as a weapon against them by violently depriving them of it” (12). Similar tactics have been used against water, sanitation, and hygiene (WASH)-related infrastructure (13,14). In Gaza, nearly half of all WASH facilities were damaged within the first five months after the escalation of military activities in October 2023 (15). In Yemen, where more than half the population lack access to sufficient water, Houthis have blocked water from flowing into government-controlled areas from well basins, water trucking, and humanitarian organizations; Houthi-laid landmines around water infrastructure and facilities have also been reported (16). Response from the government has likewise included airstrikes on water infrastructure. Such conflict actions have tangible effects on infectious diseases: 70% of cases of epidemic-prone diseases occur in fragile and conflict-affect countries, as do 60% of preventable maternal deaths, 45% of infant deaths, and 53% of deaths in children under 5 years old (17).

The armed conflicts in Yemen, Syria, and Ukraine are three examples of where widespread violent attacks (including on civilian infrastructure), largescale displacement, and notable infectious disease outbreaks converge. This dissertation uses these unique conflict contexts to answer the following questions: 1) Can we quantify the impact of conflict events on disease risk during an outbreak? 2) Are there alternative ways that we can measure conflict and related infrastructural changes that do not rely on ground reporting? 3) Does conflict still affect vector-borne diseases, which have their own unique environmental risk factors? And 4) Can we use this collective information to fill surveillance gaps in conflict-affected settings?

Chapter Two presents an ecological modeling study that assesses the association between air raids and cholera incidence in Yemen between 2016–2019 (18). During this time, Yemen experienced recorded history’s largest cholera outbreak, with over 2.5 million cases and over 4,000 related deaths. I integrated monthly governorate-level (administrative unit 1) epidemiological, environmental, conflict-related, and economic data in a negative binomial generalized additive model (GAM) to assess the contribution of conflict factors to cholera risk while accounting for other epidemiologically relevant factors. This work uses rolling 3-month cumulative counts of air raids from a conflict event database to define conflict severity. Though an important resource in conflict-related work, there are limitations to such event-based tools including short time series, under-reporting, and varying methods.

Chapter Three explores the use of satellite-based nighttime lights (NTL) as a tool for measuring conflict intensity and infrastructure recovery in Yemen and Ukraine (19). NTL is not subject to many of the limitations of event-based tools and has additional benefits given its long time series, global coverage, and lack of reliance on affected populations. It also gives a functional tool for assessing infrastructure damage and recovery during conflict, which has important implications for disease dynamics. I integrate an NTL-based conflict intensity specification and infrastructure recovery metric into the GAM from Chapter Two to assess the utility of NTL in epidemiological applications.

While Chapters Two and Three focus primarily on cholera, there are other considerations when examining vector-borne diseases in conflict settings. Vectors are sensitive to environmental phenomena that influence factors such as their lifecycles, hospitable environments, and parasite development. Chapter Four uses data on cutaneous and mucocutaneous leishmaniasis, spread via sandflies, from 52 countries over 18 years to understand how conflict, displacement, and environmental factors affect leishmaniasis risk at an ecological scale (20). This Chapter seeks to understand whether conflict still meaningfully affects disease risk even when considering vectors' unique dynamics, especially as they vary over time and space.

Lastly, Chapter Five applies the ecological findings from the previous chapter at a much finer granularity by using spatiotemporal statistical modeling to quantify cutaneous leishmaniasis surveillance gaps in northern Syria. At these smaller spatial scales (and especially in settings experiencing intense violent conflict, such as northern Syria), there are practical considerations of data missingness due to interruptions in health care access and related disease reporting.

Understanding the spatiotemporal heterogeneity of disease risk and potential underreporting has practical applications for preparedness and response efforts, especially given changes in conflict dynamics and environmental factors.

Together, this dissertation positions conflict as a primary driver in elevating disease risk across multiple pathogens and contexts. It is guided by a practical desire to contribute to preparedness and accountability efforts related to disease outbreaks and IHL violations, as well as to push for new ways of measuring conflict that are sustainable and approachable. Conflict affects every aspect of health, and generations of individuals continue to feel the reverberating effects of violence long after attacks end. Ultimately, this dissertation seeks to shine light on the sheer preventability of morbidity and mortality from infectious diseases in these settings.

CHAPTER TWO: Association between air raids and reported incidence of cholera in Yemen, 2016–19: an ecological modelling study

Introduction

Since the onset of the ongoing conflict in Yemen in late 2014 and early 2015, more than 24 million individuals have required humanitarian aid and protection (21). The conflict has been marked by infrastructural destruction, displacement, devastating environmental events, economic collapse, and widespread disease and malnutrition. The combination of these factors has created what is frequently referred to as one of the world's worst humanitarian crises (22).

Yemen has long been among the poorest nations (according to gross domestic product per capita) in the WHO Eastern Mediterranean region and has experienced economic, health-care, food-security, and water, sanitation, and hygiene (WASH) difficulties since long before the conflict (22,23). Yemen's exclusive reliance on ground and rain water, combined with ineffective policies set by the Yemen Government regarding agriculture and development, as well as water-intensive crop growth, poor enforcement of regulations related to water use throughout the country, and climate vulnerability, has created a severe water crisis (24). The conflict has massively exacerbated this and other vulnerabilities. Because of conflict-related damage and destruction of health infrastructure, only 50% of Yemen's health facilities were fully functional as of April, 2021 (25). The demand for health care, however, has increased because of the conflict: cases of infectious diseases and malnutrition are rising, maternal and child health are declining, and immunization campaigns have been interrupted, all of which have created a dire health situation (23,26,27).

Before the conflict's onset, 50% of Yemen's population was impoverished (28). Unprecedented depreciation of the Yemeni Rial (YER) since the conflict began has severely limited purchasing power, especially given simultaneous increases in food and fuel prices. Food insecurity and malnutrition now affect 17.4 million people (29). Malnutrition has many effects on health, and can directly cause mortality. People with malnutrition also have increased susceptibility to infectious diseases (30). With nearly 80% of the Yemen population now living in poverty and external humanitarian funding substantially decreasing, prospects for economic revitalization are slim (22,25). Humanitarian aid has also been weaponized by conflict parties: for example, Houthi authorities, representing one of the primary conflict parties, blocked over 250 WHO containers of humanitarian supplies in Al Hudaydah port in May, 2020, and used them as bargaining tools in negotiations (31). This obstruction of aid hinders humanitarian response measures that could otherwise help to alleviate widespread suffering.

Against this background, the largest cholera outbreak in terms of cases in recent recorded history has flourished. Cholera, caused by infection with *Vibrio cholerae*, is a waterborne disease that causes watery diarrhea and can lead to death in 50% of cases if not properly treated (death occurs in <1% of cases if appropriately managed) (32). Since 2016, around 2.5 million cases of cholera and more than 4000 cholera-related deaths have been reported in Yemen (33). A planned cholera vaccination campaign in 2017 was cancelled by the UN, WHO, and the Yemen Government, citing reasons such as the large scale of the outbreak, the need to restore WASH access to the population, and the benefits not outweighing the risks, despite evidence for its necessity and feasibility (34). Almost 18 million people lack access to safe WASH infrastructure in Yemen, and the existing water network reaches less than 30% of the population (33). Because cholera is waterborne, severe rain and flooding also contribute to its spread, as do forced displacement and overcrowding, all of which are occurring in Yemen (35–37).

However, the cholera crisis in Yemen has received little attention in the medical and global health literature. In some studies the outbreak and the response to it have been discussed, but to our knowledge no one has previously attempted to quantify the association between the Yemen conflict and the cholera outbreak while taking into account the environmental, economic, and demographic factors that affect cholera's epidemiology (38–40). Camacho and colleagues, for example, suggested that rainfall was the primary driver of the outbreak, but this hypothesis has been questioned because they excluded conflict-related measures (41,42). In this study, we aimed to quantitatively assess the association between conflict, as measured via air raids, and cholera incidence in 2016–19 while controlling for other potential contributory factors.

Methods

Study setting and data sources

We did an ecological study to assess the association between air raids and cholera incidence in Yemen between 2016 and 2019. Most of Yemen's population resides in the west of the country, which is organized into 22 governorates (the country's largest administrative unit). During our study period, Sana'a City (mean population density 7807 people per km^2 [SD 179]), Aden (1283 per km^2 [29]), and Ibb (542 per km^2 [13]) were the most densely populated governorates. Al Hudaydah and Aden are important port cities given their high number of imports and exports, and have been sites of conflict over port control (43,44).

We collected data from a range of sources (**Appendix 1**). Cholera case counts and population estimates between Sept 12, 2016 (when the first wave was estimated to have started), and Dec 29, 2019, came from a dataset that was created previously by Simpson and colleagues (45), who compiled data up until this timepoint. Briefly, the case data were extracted directly from the WHO Eastern Mediterranean Regional Office's epidemiological bulletins, which reported data gathered by the Yemen Ministry of Health and WHO's joint electronic Disease Early Warning System (eDEWS). eDEWS has been operational since 2013 and reports data from over 1900 health facilities throughout Yemen. Its resiliency and completeness have been affirmed in the literature (46). The bulletins are reported at differing temporal and geographical scales over time. Weekly case numbers were therefore standardized at the governorate level by Simpson and colleagues (45). Data were missing for 9 weeks, and Hadramawt and Socotra governorate were excluded because of missing data.

Weekly governorate-level population estimates were calculated by Simpson and colleagues on the basis of data from the WHO Eastern Mediterranean Regional Office, the Yemeni Central Statistical Organization's 2004 population projection for 2005–06, and the International Organization for Migration Displacement Tracking Matrix 2017 population estimate (45). These estimates were corrected using fatality counts from the Armed Conflict Location and Event Data Project by iteratively subtracting fatalities from the previous week's population estimate and multiplying that difference by the prorated annual growth rate (45). We used these population estimates and governorate area to create weekly population density estimates, which we log-transformed to account for skewness (47). We chose to account for population density rather than population size because governorate sizes vary considerably and because we hypothesize that density is more important for transmission of cholera than is the crude population size. We also extracted the latitude and longitude of each governorate's geometric centroid (by using QGIS [version 2.33.1]) to account for any baseline spatial predictors of cholera that were not captured by other variables in the model.

We used air raid counts, as gathered by the Yemen Data Project (YDP) as a measure of conflict (48). Air raids by the Saudi-led coalition have been an integral component of the Yemen conflict. Although this measure does not capture other types of conflict events, it is useful as an intensity measure of aerial warfare and as a proxy measurement for other ground conflict (49,50). YDP data have previously been used to measure conflict severity in Yemen, validate other conflict data sources, identify attacks by target, measure insecurity levels (i.e., by weighting the number of annual fatalities by the number of reported conflict events), and estimate child fatalities and injuries (50–52). The open-sourced data undergo cross-referencing and verification through several streams of information, such as local and international news agencies and media reports; social media accounts and WhatsApp; reports from international and national non-governmental organizations; official records from local authorities; and reports by international human rights groups. The YDP reports both a minimum air raid number, which includes one or more verified air strikes, and a maximum number that includes all reported air strikes, some of which might be unverified. In our analysis, we used the minimum air raid counts to provide conservative severity estimates and to ensure that all air raids included were verified. We aggregated the air raid counts into rolling 3-month measures (other aggregations and lags were tested; **Tables S1.3–1.7**) and categorized these into quintiles to create severity levels: low (no air raids), intermediate (between one and four), medium (five to 18), high (19–75), and severe (≥76). We used an ordinal categorization scheme to account for the erratic nature of air raid reporting while keeping the quantitative nature of the variable intact.

We attempted to account for environmental conditions and events that affect cholera by incorporating data for several environmental factors. Monthly governorate-level measures of total recorded precipitation and mean recorded temperature were extracted from the World Bank's Climate Change Knowledge Portal (CCKP) (53). We calculated weekly precipitation data by equally dividing the cumulative precipitation across the weeks in each month, and weekly temperature data by assigning the monthly mean to each respective week in that month. We conducted a sensitivity analysis using daily modelled precipitation data from the Climate Hazards Group Infrared Precipitation with Stations (CHIRPS) dataset and found no difference between models (**Table S1.1**) (54,55). Although the two data sources align in their general temporal trends, the CHIRPS data report short-term (i.e., daily) fluctuations that are not apparent in the CCKP data. Use of the CHIRPS data assumes that these observed fluctuations occur homogeneously throughout the administrative units to which they are assigned, which we do not believe to be realistic. We therefore opted to use the CCKP data as we believe that the smoothed data are more realistic with regard to the general trends in precipitation that occur at weekly scales across governorates.

We also extracted the governorate-level normalized difference vegetation index (NDVI) and surface water index by using the National Aeronautics and Space Administration's Terra Moderate Resolution Imaging Spectroradiometer satellite with 500 m spatial resolution (56). NDVI measures surface vegetation levels and ranges from –1 (low surface vegetation) to 1 (high surface vegetation), and data were available every 16 days. We calculated weekly NDVIs by assigning the data to weeks that fell within the 16-day period or by calculating a weighted mean using the NDVIs of surrounding weeks for periods that straddled two 16-day periods (weighted by number of days that fell within each 16-day period). Similar to the NDVI, the surface water index is a temporally varying measure of surface water that ranges from –1 (extremely dry) to 1 (extremely high level of surface water). We calculated the index using red and shortwave infrared 2 bands via the following formula: (red band – shortwave infrared 2 band)/(red band + shortwave infrared 2 band). Surface water data were available every 8 days, which we converted to a weekly value as per the NDVI data. We also included a temporal variable (week of study period) in the model to account for seasonal variations not already captured by the other variables.

Finally, we extracted monthly mean petrol prices, food basket prices, and YER parallel market exchange rates from the World Food Program's monthly market watch bulletins (57). However, data for the July 2017 exchange rate were missing for all governorates, and no market watch bulletins were released from September to December, 2019. First, we converted these monthly data to weekly data by assigning the mean value to each week in a given month. Then we used a principal component analysis to combine these three variables into one variable. We used the first principal component (of three) because it explained 83.32% of the variance.

Model building

We used a generalized additive model (GAM) with a negative binomial probability distribution for our model, and used a combination of scientific hypotheses and model fit statistics to select the final covariates (**Appendix 1**). GAMs use smooth spline functions to model covariates non-parametrically; these functions can be used in combination with parametric model components. The model accounted for geography, population density, time, environmental factors, the economy, and conflict severity (as measured by air raid frequency; **Table 1**). In the model specification process, we tried different aggregations and lags for the air raid variable, finally settling on a 3-month aggregation with no lag based on model fit statistics (**Tables S1.3–1.7**). We also stratified the model over three time periods to assess the fixed effects' variation across time (**Table S1.8**).

Table 1: Description of variables included in the final model

	Variable description	**Sources**	**Date range**	**Reporting frequency**
Outcome	Suspected and confirmed cases of infection	Simpson et al. (45)	Sept 12, 2016–Dec 29, 2019	Weekly
Demography	Log-transformation of estimated number of people per km^2 (density)	Simpson et al. (45) (population); Berghof Foundation and Political Development Forum Yemen (47) (area)	Sept 12, 2016–Dec 29, 2019	Weekly
Temporal	Week of study (week 1 was the first week of the study and week 172 the last)	NA	Sept 12, 2016–Dec 29, 2019	Weekly
Air raid severity				
Low	No air raids in previous 3 months	Yemen Data Project	June 20, 2016–Dec 29, 2019*	3 months
Interm.	1–4 air raids in previous 3 months	Yemen Data Project	June 20, 2016–Dec 29, 2019*	3 months
Medium	5–18 air raids in previous 3 months	Yemen Data Project	June 20, 2016–Dec 29, 2019*	3 months
High	19–75 air raids in previous 3 months	Yemen Data Project	June 20, 2016–Dec 29, 2019*	3 months
Severe	≥76 air raids in previous 3 months	Yemen Data Project	June 20, 2016–Dec 29, 2019*	3 months
Environmental factors				
Precipitation†	Total recorded rainfall per governorate (mm)	Climate Change Knowledge Portal	Sept 1, 2016–Dec 31, 2019	Monthly‡
Surface water†	Surface water index per governorate	NASA MODIS (56)	Sept 5, 2016–Jan 4, 2020	8 days§
Temperature†	Mean temperature per governorate (°C)	Climate Change Knowledge Portal	Sept 1, 2016–Dec 31, 2019	Monthly‡
Normalized difference vegetation index†	Standardized vegetation level per governorate	NASA MODIS (56)	Aug 28, 2016–Jan 12, 2020	16 days§

Longitude	Longitude of governorate's centroid	QGIS	Sept 12, 2016–Dec 29, 2019	Constant
Latitude	Latitude of governorate's centroid	QGIS	Sept 12, 2016–Dec 29, 2019	Constant
Economic	First principal component of petrol price, food basket price, and the parallel market Yemeni Rial exchange rate	World Food Program (57)	Sept 1, 2016–Aug 31, 2019	Monthly

NA=not applicable. NASA MODIS=National Aeronautics and Space Administration Moderate Resolution Imaging Spectroradiometer. *June 20, 2016, was the date of the first recorded attack within our study period; Dec 29, 2019 was the date of the last recorded attack within our study period. †Mean centered and standardized. ‡Converted to weekly by evenly distributing the total distribution across the weeks in the month. §Converted to weekly via weighted averages.

We tested the robustness of the observed association by sequentially adding groups of related variables to a base model (model A). Model A accounted for governorate-level population density, week, geographical location, and air raid severity. Model B incorporated environmental variables in addition to all those included in model A, and model C (the final model) included the economic principal component in addition to everything included in models A and B. The equations for each model are in **Appendix 1**. Model coefficients are reported as incidence rate ratios. p values of less than 0.05 were considered significant, as were 95% CIs that did not contain the null of one. All statistical analyses were done in R (version 4.0.4). Maps were created in QGIS (version 2.33.1).

Results

Between Sept 12, 2016, and Dec 29, 2019, 2 107 912 cholera cases were reported. Mean weekly incidence was highest in Amran (97.9 cases [SD 94.9] per 100 000 people), Mahwit (92.3 [90.7] per 100 000), Sana'a (83.6 [64.7] per 100 000), and Al-Bayda (75.2 [79.0] per 100 000). Cholera incidence peaked at week 43 (July 3–9, 2017). **Figure 1** shows maps of week 43 to illustrate the geographical variability of the environmental variables at the peak of cholera cases, as well as time series of cholera cases, economic principal component, and air raids over the study period.

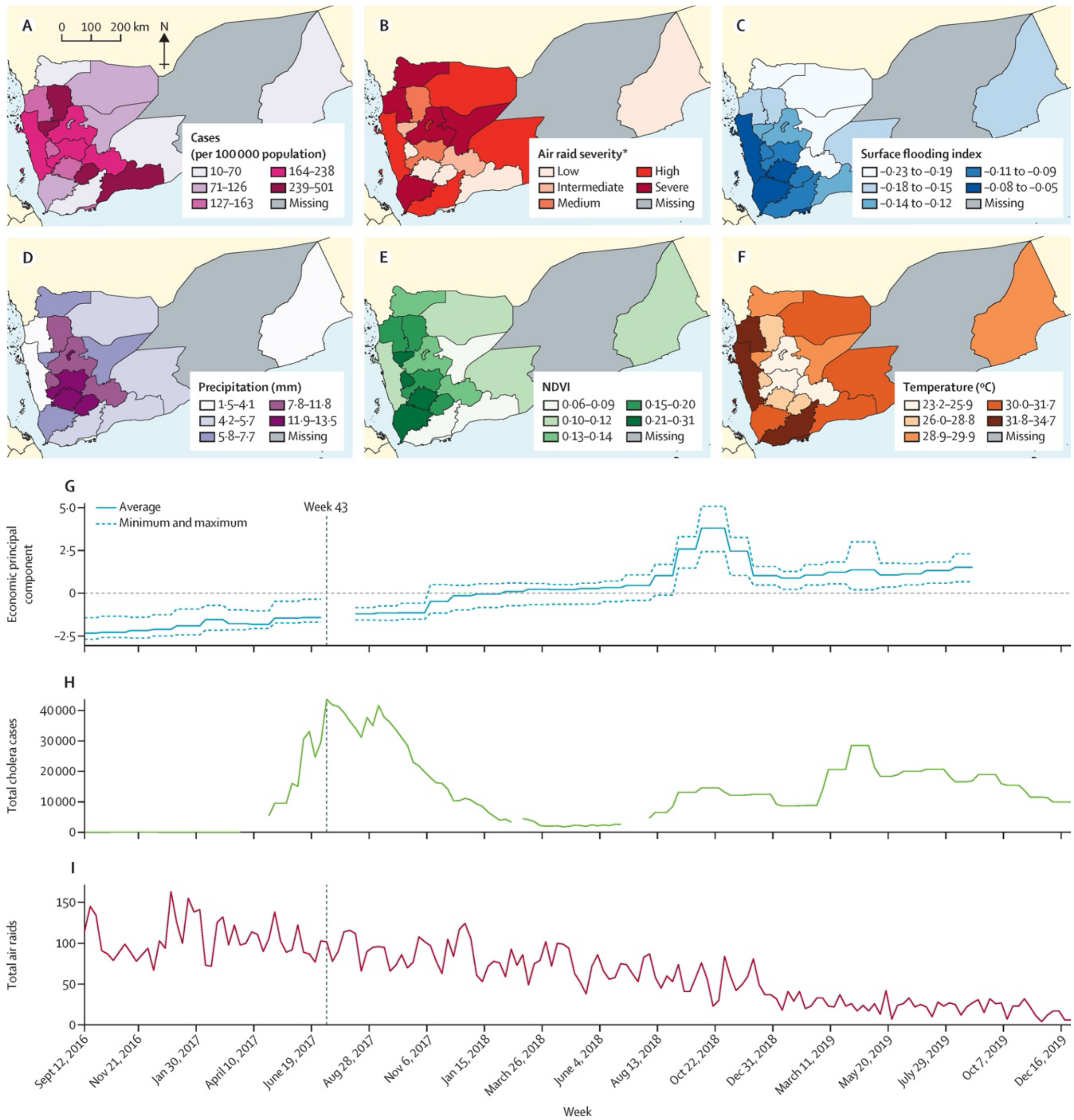

Figure 1: Environmental variables in Yemen at week 43 and time series over the study period Cholera incidence (A), air raid severity (B), surface water (C), precipitation (D), NDVI (E), and temperature (F) in Yemen at study week 43 (July 3–9, 2017). A map of Yemen with the different governorates labelled is provided in **Figure S1.6**. The three time series at the bottom of the figure show the economic principal component (G; the values below zero on the y axis indicate a better-than-average economy and values above 0 indicate a worse-than-average economy), total cholera cases (H), and total air raids (I) over the study period. NDVI=normalized difference vegetation index. *Severity is defined according to the number of air raids in the previous 3 months as low (none), intermediate (1–4), medium (5–18), high (19–75), or severe (≥76). *Used with permission of the publisher.*

YDP recorded a minimum of 11 366 air raids during the study period and a maximum of 35,830. Of the 11,366 air raids, 3294 (29%) occurred in Sa'ada, 1,632 (14%) in Hajja, 1,414 (12%) in Taizz, 1,357 (12%) in Al-Hudaydah, and 1,167 (10%) in Sana'a (**Figure 2**). 5,233 (46%) of the minimum number of recorded air raids occurred in 2017, which aligned with the peak of cholera incidence.

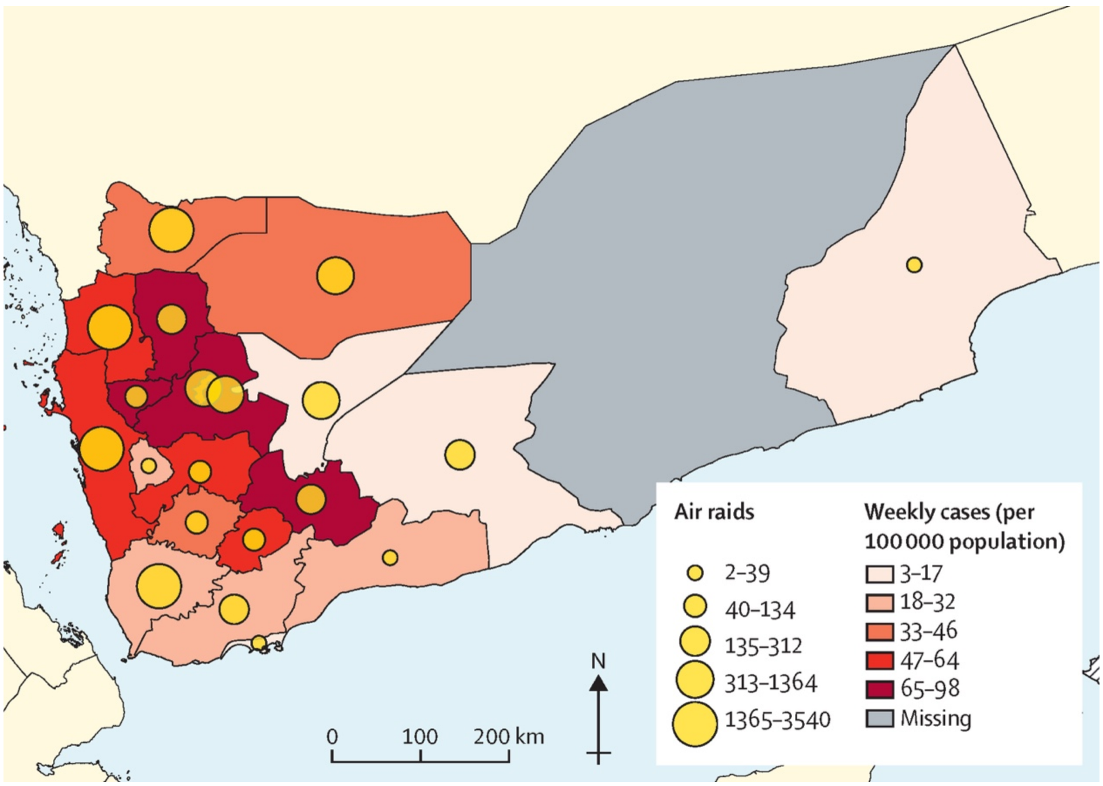

Figure 2: Cumulative air raids and mean weekly cholera incidence (per 100,000 population) in Yemen 2016–19
A map of Yemen with the different governorates labelled is provided in **Figure S1.6**. *Used with permission of the publisher*.

Compared with low air raid severity, all other severity levels of air raids were significantly associated with cholera incidence after adjustment for geographical, demographic, environmental, and economic variables (**Table 2**). In governorates with the most air raids, the risk of cholera was double that of governorates with no air raids (incidence rate ratio 2.06 [95% CI 1.59–2.69]; p<0.0001; **Table 2**). The NDVI had an inverse association with the incidence of cholera, and governorates with more vegetation (i.e., high NDVI) had a lower cholera risk than those with more arid landscapes (**Table 2**).

Table 2: Incidence rate ratios for each linear variable through each model iteration

	Model A*		Model B†		Model C‡	
	IRR (95% CI)	p value	IRR (95% CI)	p value	IRR (95% CI)	p value
Air raid severity§						
Low	1 (ref)		1 (ref)		1 (ref)	
Intermediate	1.59 (1.39–1.81)	<0.0001	1.52 (1.33–1.74)	<0.0001	1.76 (1.51–2.05)	<0.0001
Medium	1.43 (1.22–1.68)	<0.0001	1.30 (1.11–1.52)	0.0015	1.57 (1.31–1.89)	<0.0001
High	1.53 (1.28–1.83)	<0.0001	1.43 (1.19–1.70)	0.0001	1.87 (1.53–2.29)	<0.0001
Severe	1.61 (1.28–2.02)	<0.0001	1.54 (1.22–1.93)	0.0002	2.06 (1.59–2.69)	<0.0001
Environmental factors						
Surface water			0.83 (0.73–0.93)	0.0012	0.89 (0.78–1.03)	0.11
Precipitation			0.99 (0.92–1.06)	0.76	0.98 (0.91–1.06)	0.69
NDVI			0.70 (0.63–0.77)	<0.0001	0.72 (0.64–0.80)	<0.0001
Temp (mean)			1.16 (0.97–1.39)	0.10	1.11 (0.91–1.36)	0.29
AIC¶	36,826.77		36,787.85		30,240.97	

A forest plot of these data can be found in **Figure S1.1**. AIC=Akaike information criterion. NDVI=normalized difference vegetation index. *Adjusted for population density, air raid severity, week, latitude, and longitude. †Adjusted for population density, air raid severity, week, latitude, longitude, surface water, temperature, precipitation, and NDVI. ‡ Adjusted for population density, air raid severity, week, latitude, longitude, surface water, temperature, precipitation, and NDVI, plus economic principal component (as spline). § Severity is defined according to the number of air raids in the previous 3 months as low (none), intermediate (1–4), medium (5–18), high (19–75), or severe (≥76). ¶ A test of model fit; lower numbers indicate better model fit.

When we used different temporal aggregations and lags for air raid severity, results were broadly similar (**Tables S1.3–1.7**). However, the effect size for high and severe air raids began to decrease at 6-month and 12-month aggregations (**Tables S1.3–1.4**).

The smoothed variables in our model were significantly associated with cholera incidence (**Figure 3**). Lower population densities were associated with lower cholera incidence (**Figure 3B**). By contrast, population densities higher than around 60.34 people per km^2 (corresponding to around 4.1 when log-transformed), were associated with increased cholera incidence (**Figure 3B**). The economic covariate spline suggested that economic downturn was associated with increased risk of cholera (**Figure 3C**).

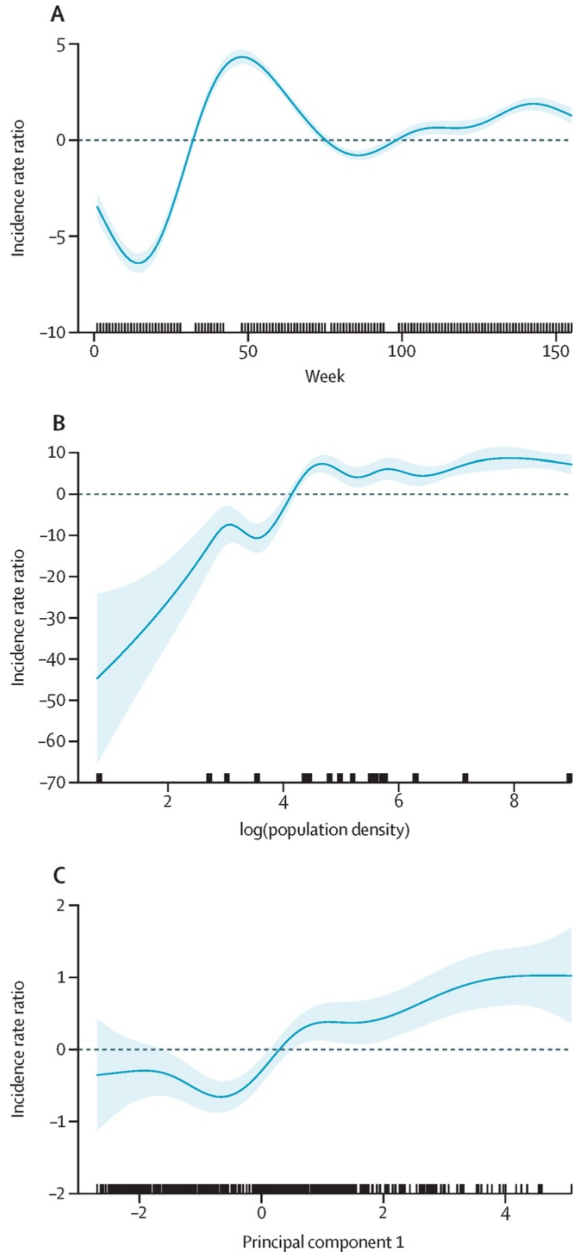

Figure 3: Incidence rate ratios for study week (A), population density (B), and the economic principal component (C)

Shaded areas represent 95% CIs. The output is significant for values whereby the solid trend line and shaded areas are entirely above or below the horizontal dashed line. *Used with permission of the publisher*.

Discussion

Our ecological model showed significant associations between conflict (as measured by air raid severity) and the incidence of cholera in Yemen in 2016–19, even after adjustment for other factors related to cholera transmission. We used a conservative measure of air raids, and thus our measure of conflict is probably an underestimate, yet still the association between conflict and cholera is clear. Although the true magnitude of the Yemen conflict's association with cholera incidence is difficult to measure because of data constraints and the various causal pathways implicated, our findings offer an important baseline understanding of the relationship.

Our study accords with previous work (37,39) suggesting that the Yemen cholera outbreak is largely a result of human action, and provides an important counterpoint to work (41) that attributes the severity of the outbreak to environmental events. By quantifying the association between conflict and cholera while accounting for environmental and economic variables, we are able to position conflict as an important consideration in outbreak response. Other studies in which attempts were made to model Yemen's cholera outbreak could have possibly benefited from including similar covariates for environmental, economic, and conflict-related factors in view of the significant associations between these measures and disease incidence in our model (58,59). Our findings show that Yemen's cholera burden is complex, multifaceted, and has important associations with conflict and the economy.

The links between air raids and cholera incidence are complex, and the association is important to consider from a mechanistic standpoint. We are not suggesting that the air raids themselves are solely responsible for Yemen's cholera burden, but rather that air raids damage and destroy infrastructure, which leads to contamination of available water, limits transportation capabilities, and hinders the ability to treat cholera cases in a timely manner. Air raids also contribute to widespread displacement, which is associated with poor WASH access (49). When testing air raid aggregations for our model, the effect size for high and severe conflict levels decreased at 6-month and 12-month aggregations. These decreases could reflect large-scale displacement and destruction of health-care infrastructure that are likely to occur following long periods of high or severe conflict, and that would therefore reduce case incidence or reporting. The damage done by air raids is likely to be long lasting. Yemen's economic collapse and the dire funding situation make it unlikely that damaged infrastructure will be repaired or that demands for new infrastructure will be met quickly, if at all (49,60). In 2021, less than a third of required funds were pledged by world leaders, and existing funding is not supporting infrastructure repair or building (61). Although some infrastructure repair is ongoing, it is not at the scale necessary to counteract the lasting effect of destruction caused by air raids. Research to better understand the causal mechanisms behind this association will be an important continuation of this work.

The economy is also an important contributor to Yemen's cholera burden for reasons beyond the funding of infrastructure repairs. The conflict has destroyed the country's economy, which had already been precarious. Increasing food and fuel costs with concurrent depreciation of the YER have created an untenable position, especially given that 80% of the country is impoverished. Increased fuel prices have led to fuel crises with cross-sector effects: health facilities are unable to use key equipment, humanitarian aid cannot be delivered, food and transportation prices have increased, and clean water and electricity supplies are threatened (62,63). The fuel crisis has worsened since the study period because fuel continues to be weaponized by conflict parties: Yemen's internationally recognized government and the Saudi-led coalition have tightened restrictions on fuel shipments into Yemen's ports and increased holding delays. In early 2022, fuel vessels spent a mean of 112 days in the coalition's holding area, an increase of 543% from 2019's mean of 17 days (62).

Food and water prices are intrinsically linked to fuel prices given Yemen's reliance on food imports, humanitarian aid distribution, and water trucking. As of late July, 2022, the cost of a food basket had increased by 48% compared with its price in late 2021 (63). The need for humanitarian food assistance far exceeds the abilities of aid organizations to provide such assistance: 8 million aid recipients now receive only 25% of daily calorie requirements, and a further 5 million receive only 50% of daily calorie requirements (63). The rising prices of food and fuel in combination with the reduction in humanitarian aid have driven widespread malnutrition, which in turn increases the likelihood of cholera infection (30). High fuel prices similarly increase the cost of clean water via water trucking, because fuel prices hinder drivers' ability to widely and consistently deliver water. Fuel is also essential to produce clean water, thereby leading to increasing costs of water due to lower supply.

In this study we used data from various sources, many of which had limitations. Cases of cholera have probably been under-reported due to conflict and difficulties accessing health care and testing, and data quality was affected by inconsistent reporting at spatial and temporal scales. However, we are confident in using these data as eDEWS' robustness has been previously validated and the data encompass reports from nearly 2000 health centers across the country (46). Other data sources, such as the Emergency Operations Center (EOC) dashboard, reported case counts during portions of the outbreak (64,65). However, such data sources face similar limitations, and our collaborators on the ground trust the eDEWS data. We provide analyses using the EOC data, which yield similar results to our model, in the appendix for comparison (**Table S1.2**).

Because there are little demographic data available, we relied on extrapolated population data. Across each of the covariates we used, we were also limited by the spatial and temporal granularity. Because most data were available at the governorate level only over periods of several days, we could not account for within-governorate differences. This assumption of intra-governorate homogeneity could mask changes in weather patterns that occur at a smaller scale and affect cholera locally. Future research should assess similar associations between conflict and cholera at smaller spatial and temporal scales.

Importantly, we were unable to account for any conflict measures other than air raids due to a lack of available data. We recognize that the Yemen conflict is multifactorial and that air raids represent only a portion of the violence experienced throughout the country. However, comprehensive reporting of ground conflict is scarce. Because YDP reports verified air raids, we chose this measure as a baseline level of conflict, but acknowledge that the true impacts of conflict are probably much greater. We also could not account for other important, indirect pathways through which conflict affects cholera incidence, such as through exacerbation of malnutrition (30). Finally, we anticipate that conflict has similar effects on the incidence of other infectious diseases too, but data availability meant that we had to focus on cholera only.

The toll of Yemen's conflict is vast. Air raids have an immediate impact on the country's infrastructure, with broader effects on displacement, the interruption of public health campaigns, and the availability of health care. All these factors contribute to the cholera burden in Yemen. Environmental drivers of cholera alone are unlikely to have produced an outbreak of this scale. Direct attacks on health care, WASH, and food infrastructure show a stark weaponization of health, whereby warring parties have created an environment primed to nurture cholera (37).

Cholera in Yemen cannot be untangled from the conflict itself. Further destruction of healthcare and WASH infrastructure, widespread malnutrition, and declining economic power will probably extend an epidemic that has already caused unfathomable suffering. As climate change increases the frequency and intensity of flooding and precipitation in the region, these underlying environmental factors could also contribute to an increased baseline of cholera, which conflict-related drivers of disease might further exacerbate. Our work has implications for future research on the weaponization of health in Yemen, further consequences of infrastructure destruction (i.e., what are the other direct and indirect effects of having infrastructure destroyed during conflict), and on advocacy efforts to increase aid and push for a solution to the conflict. Restoring infrastructure and bolstering Yemen's economy, alongside promoting ceasefire and peacebuilding efforts, are important considerations in addressing the country's cholera burden. Understanding the association between conflict and cholera could also be useful for preparedness efforts. As with all conflicts, the actions of the warring parties are felt most heavily by civilians who have endured nearly a decade of compounding crises.

CHAPTER THREE: Nighttime lights as a proxy for conflict intensity and infrastructure recovery in Yemen and Ukraine

Introduction

Armed conflict has profound impacts on people and their environments. Critical civil infrastructure (e.g., roads and hospitals) is frequently damaged or destroyed, contributing to and compounding other adverse conflict effects. Such conditions are primed for infectious disease spread and large-scale population displacement (11,18). Although these pervasive impacts are well recognized, effects of armed conflict on civilian populations are difficult to measure systematically and quantitatively. Several tools have been developed to monitor armed conflicts using various methodologies. The Armed Conflict Location and Event Database (ACLED) (66) and the Uppsala Conflict Data Program (UCDP) (67), for example, monitor conflict globally and report on individual conflict events. More targeted tools, such as the Yemen Data Project (YDP) (48), monitor specific conflicts, while others, like the WHO's Surveillance System for Attacks on Health Care, focus on particular types of conflict-related violence. Each of these tools is valuable and has important implications for advocacy and accountability.

Despite their importance, existing tools face limitations. Many rely on secondary reports (e.g., national media outlets), which introduces challenges, particularly in heavily affected areas where communication infrastructure is degraded or where other security or political concerns can prevent accurate documentation of conflict events. As a result, conflict events may be underreported, particularly in regions experiencing the most severe impacts. Delays in documentation, especially in early stages, can also limit the available data. Differences in reporting standards across contexts further complicate comparisons. Importantly, existing tools only capture violent events and actions that cause damage, offering limited insight into broader impacts of armed conflict, such as disruptions to infrastructure and economic activity, as well as recovery. As armed conflicts are often protracted, research arguably should also consider how and where recovery occurs, especially given the role of infrastructure in moderating some health outcomes (68). For example, infrastructure damage can lead to poor sanitation, which can in turn increase the prevalence of diseases associated with poor sanitation; conversely, recovery of this infrastructure can limit the conditions in which these diseases thrive.

Given these gaps, complementary data sources are valuable for reducing potential biases, providing extended time series, and offering recovery insights. Earth observation, particularly nighttime lights (NTL), offers useful tools. Visible and near-infrared light are captured through the Suomi National Polar-Orbiting Partnerships Visible Infrared Imaging Radiometer Suite's (SNPP VIIRS) Day-Night Band (DNB) sensor at a 15 arc-second spatial resolution (roughly 450m at the equator). NTL has been applied in several research areas, including light pollution (69–71), human settlement and development (72–74), economics (75), and migration (76). In conflict settings, changes in NTL have been studied descriptively (77) and in the context of power supply disruptions (78,79), declines in economic activity (80), and population movement and behavior, among other topics (80–82). NTL has also been used by humanitarian and media organizations to track ongoing conflict (83). However, none to our knowledge have quantified the relationship between NTL and conflict events or showed NTL's utility in infectious disease epidemiology.

We aim to assess NTL as a tool for quantifying armed conflict and recovery during conflict, as well as their impact on health outcomes, in Yemen (**Figure S2.1**) and Ukraine (**Figure S2.2**). Yemen has faced protracted armed conflict since late 2014, fought largely between Houthis and the internationally recognized government backed by a Saudi-led coalition (84). The ongoing fighting has left 4.5 million people internally displaced (many of whom have been displaced multiple times) and 66% of the population in need of humanitarian aid and protection (85,86). The conflict has contributed to widespread infrastructural damage and destruction, economic collapse, and increased disease incidence (18). Recent armed conflict in Ukraine began around a similar time in 2014 with Russia's annexation of Crimea and its occupation of parts of the Donbas region in the country's east (87). Following ongoing tension, Russia launched a full-scale invasion of

Ukraine on February 24, 2022. As of February 2025, 6.9 million people have fled Ukraine, with an additional 3.7 million displaced internally; close to 35% of Ukraine's population are in need of humanitarian assistance (88). Russian attacks have caused extensive infrastructural damage, including to water, sanitation, and hygiene (WASH), healthcare, education, and energy sectors.

Using these contexts, we assess the relationship between NTL and reported aerial attacks, in addition to the use of NTL in an existing disease model. We hypothesize that NTL declines largely reflect conflict-related infrastructural damage and destruction; this infrastructure damage has been examined in other remote sensing-based work (77,89). To be clear, we are not advocating for the use of NTL as a universal conflict detection tool; rather, we aim to demonstrate its use as a complementary and accessible proxy that responds to some of the limitations of event-based reporting and which can offer additional insights with a relatively low barrier to entry. NTL provides another practical tool in our toolbox for understanding conflict dynamics and their association with health outcomes, which is increasingly necessary as conflicts reach heightened levels of violence and protraction globally.

Methods

In this retrospective analysis, we use monthly Black Marble NTL data (VNP46A3) during January 2012–March 2022 in Yemen and January 2019–June 2024 in Ukraine, extracted using *blackmarbleR* (90). The creation and processing of these products have been described in detail elsewhere (91). Briefly, Black Marble uses the SNPP VIIRS DNB sensor and corrects for atmospheric, thermal, stray light, terrain, and lunar bidirectional reflectance distribution (BRDF) function effects to reduce background noise (92). The monthly products, available beginning January 2012, are composites of daily corrected images with outliers removed; monthly mean values are calculated using remaining observations with contaminated pixels gap-filled and background noise removed (92). In both countries, we utilized the all-angles snow-free observations (see **Figure S2.3** for view-angle comparison and **Figure S2.4** for quality and completeness). We also applied a mask at 300 nW·cm^{-2}·sr^{-1} in Yemen to remove gas flares from the country's oil production (77).

Following this processing, we first calculated monthly mean NTL levels for all administrative units and months in the study period. In Ukraine, mean values for months of missing or contaminated data were interpolated by seasonally decomposing the time series, linearly interpolating the adjusted data, and reinserting the seasonal component using the *forecast* package (93). Results from a sensitivity analysis for this interpolation can be found in **Table S2.1** and **Figure S2.5**. This missingness (occurring in summer months) was expected because of Ukraine's latitude and Black Marble's stray light correction methodology. We then calculated month-specific baseline NTL levels by taking the mean light level for each respective month (January–December) across three years of data leading up to the onset of large-scale military operations (our 'event') across both countries for a total of 38 months in Yemen and 37 in Ukraine. These baselines were used to calculate the ratio of pre- to post-event NTL levels for each month, referred to as the NTL ratio. Lastly, light recovery was calculated by identifying the post-event two-month rolling NTL minimum (nadir) for each administrative unit and calculating the ratio of light levels for subsequent months. A two-month minimum was chosen to capture nadirs before recovery while limiting the potential seasonal bias seen with shorter periods. Across all analyses, Socotra (Yemen) was not included given its distance from mainland Yemen, and we refer to all of Ukraine's 27 regions in the first administrative level as 'oblast' for simplicity.

To account for the number of reported aerial attacks in each country, we used YDP (48) and ACLED (66). YDP reports on Saudi-led air raids in Yemen between their onset in March 2015 through March 2022. Each reported air raid contains a minimum value of one or more verified air strikes and a maximum value of air strikes, some of which may not be verified. We used the minimum verified number in our study as a conservative measurement of conflict. ACLED likewise provides disaggregated information on conflict events gathered from media sources, reports, and local partners that are cross-referenced and verified. We used reported attacks in the following categories to account for aerial attacks in Ukraine beginning February 2022: shelling/artillery/missile attack, air/drone strike, grenade, remote explosive, and suicide bomb. For both countries, aerial attacks were aggregated monthly for each administrative unit.

We also extracted population size estimates from WorldPop and data on the built environment for each administrative unit. WorldPop provides annual unconstrained UN-adjusted population estimates at 100m through 2020 (94). Years after 2020 were linearly extrapolated. We ran secondary models with population size as the response variable (**Figure S2.6** and **Table S2.2**) and sensitivity analyses for all models using Gridded Population of the World data (**Tables S2.3–S2.5** and **Figures S2.7–2.8**). To account for the amount of built environment in each administrative unit, we used Sentinel-2's Dynamic World Land Use/Land Cover (LULC) annual data, available at a 10m scale, and calculated the percentage of pixels classified as built from the total number of pixels in each unit (95). In Ukraine, we only used LULC data from summer months to avoid snow cover. Population size and built percentage for both countries were log-transformed to account for skewness. Lastly, we obtained data from the World Food Program on the monthly price of diesel in Yemen, as its electrical grid operates on diesel (96).

Assessing the alignment of breakpoints and aerial attack onset

We used the Breaks for Additive Season and Trend (BFAST) change detection approach to identify negative breakpoints in the mean NTL time series for each administrative unit while accounting for seasonality (97); this was used to assess whether the onset of attacks was evident in units' NTL signals, especially given that onset timing varied with countries. BFAST decomposes time series into seasonal, trend, and noise components while estimating the number, timing, magnitude, and direction of abrupt changes within them. If the onset of aerial attacks in the administrative unit fell within the 95% confidence window for a negative breakpoint, we considered the NTL signal as having captured the onset of attacks.

To validate the use of BFAST in this context and better understand the nuances in the time series' signals, we simulated NTL time series with breakpoints using parameters informed by Yemen and Ukraine's real data (**Figures S2.9–S2.13**). To set the simulation model parameters, we decomposed each administrative unit's time series into seasonal, trend, and noise components. For each administrative unit, mean trend values were calculated for three periods: pre-break (month 0 to the month prior to the breakpoint), peri-break (12 months following the breakpoint), and post-break (remaining months). In these calculations, breakpoint timing was standardized as month 38 (February 2022) in all oblasts and month 39 (March 2015) in all governorates to align with the onset of armed conflict in both countries. Standard deviation of the noise was also found for each period, adjusted for any short-term pulse in noise around the break. The mean monthly seasonal values were also calculated from the decomposed data for each administrative unit. Using these parameters, median and quartile values across all administrative units in each country were calculated and used to inform a range of parameters for the simulations (**Table S2.6**). The simulated NTL time series were generated by reconstructing time series from individually simulated trend, noise, and seasonal components.

First, trend values for the pre-, peri-, and post-break periods were sampled from a range of parameters and temporally aligned around the simulated breakpoint. Secondly, noise was simulated using a normal distribution $N(\mu = 0, \sigma = x)$, where x was informed by parameters estimated from the real data. Pulses of varying strength (i.e., median, mean, and quartile values) were added to the noise surrounding the breakpoint (4 months prior to the break, month of the break, and 3 months following), though median pulse values were used in presented outputs as there was minimal change in results across the varying strengths. Thirdly, seasonality was set using the median of all administrative units' mean seasonal values in each country. Lastly, each simulation was given a breakpoint between months 9 and 57 in the Ukraine-informed simulations and 18 and 105 in the Yemen-informed simulations, which account for BFAST's default minimum segment size of 15% of the time series length. Ten simulations were generated for each set of parameters across every breakpoint (**Figures S2.10–2.13**).

Model building

In both nations we used a generalized additive model (GAM) with a Gaussian response distribution to measure the relationship between NTL (run with both monthly mean NTL and NTL ratio specifications as the response) and reported aerial attacks, while accounting for other potentially important covariates. Both specifications were log-transformed to handle skewness and based on model residuals (**Figures S2.14–2.15**). To do so, a small constant was added to all values. In Yemen, we assumed that log-NTL was a linear function of aerial attacks and diesel price, whereas population size and built environment were modeled as splines. To preserve the nonlinear nature of aerial attacks in Ukraine while increasing interpretability, we specified aerial attacks categorically by quintiles using levels of none, low (1–2 attacks), medium (3–6), high (7–117), and severe (118+). Population size and built environment had high concurvity in Ukraine, and built environment was included based on our hypothesis of infrastructural damage. All models included a spline-based function with the study month number as its argument and an interaction term between each administrative unit centroid’s latitude and longitude to account for any baseline temporal and spatial factors that were not captured elsewhere in the model. All GAMs were run with the *mgcv* package in R (98), and equations are in **Appendix 2**.

Epidemiological application: Cholera outbreak in Yemen, 2016–2019

Mean NTL and light recovery were applied to an existing model on the association between armed conflict and cholera in Yemen during the 2016–2019 outbreak. Raymah was not included in this application as its light recovery ratio could not be calculated given its nadir of zero (**Table S2.7**). The details of the original study, which included data from 20 governorates, can be found elsewhere (18). Briefly, we used case counts from the WHO Eastern Mediterranean

Regional Office's epidemiological bulletins, which report data from the Yemen Ministry of Health and WHO's joint electronic Disease Early Warning System (45). The model also accounts for population density, displacement (specified within the population variable), vegetation levels, surface water, precipitation, ambient temperature, and economic factors (as a principal component for petrol prices, food basket prices, and the Yemeni rial parallel market exchange rate) using a GAM with a negative binomial distribution.

In the original model, conflict was measured using air raid counts from YDP. The number of verified weekly air raids in each governorate was used to create rolling 3-month aggregate measures which were categorized into severity levels of low (zero air raids in prior 3 months), intermediate (1–4), medium (5–18), high (19–75), and severe (≥76). In this application, we used mean NTL to create conflict categories that aligned with the original categories. These were low (0.087–5.904 $nW \cdot cm^{-2} \cdot sr^{-1}$), intermediate (0.031–0.086), medium (0.016–0.030), high (0.007–0.015), and severe (0–0.006). The light recovery ratio was also included in the model as an interaction term with the number of months since the light nadir; this was done to attempt to capture related infrastructural restoration while accounting for differences in the speed of recovery. Models were also run using the NTL ratios to define conflict categories, and these can be found in **Table S2.8** and **Figures S2.16–2.17.**

Results

Aerial attacks and NTL varied spatiotemporally in each country, reflecting the duration of conflict and geopolitical priorities. YDP recorded 25,054 attacks in Yemen between March 2015 and March 2022, primarily in Sa'ada (n=5,576; 22.3% of total air raids), Marib (n=3,384; 13.5%), Taizz (n=2,722; 10.9%), Hajjah (n=2,587; 10.5%), and Sana'a (n=2,623; 10.5%) (**Figure S2.1**). Sana'a City, Aden, and Sa'ada experienced the most air raids per square kilometer at 4.0, 0.50, and 0.49, respectively. Sana'a City's attack density likely reflects its small size ($385km^2$), high population density (mean of 7,806.7 per km^2), and military importance. Between February 2022 and June 2024, Ukraine experienced 80,608 recorded aerial attacks. Most occurred in Donetsk (n=30,122; 37.4%), Kharkiv (n=13,633; 16.9%), Zaporizhzhya (n=10,258; 12.7%), Kherson (n=8,308; 10.3%), and Sumy (n=6,473; 8.0%) (**Figure S2.2**). These oblasts also had the highest attack density at 1.13, 0.43, 0.38, 0.33, and 0.27 respectively. Note that throughout our analyses, we assessed aerial attacks over the entire oblast, which includes areas under varying political control; this likely influences the timing and distribution of attacks.

For the whole of Yemen, NTL generally declined ($\bar{x}$=-53.3%) following the onset of large-scale military operations, though some areas experienced growth (range: -91.0% to 98.1%). The whole of Ukraine experienced similar effects ($\bar{x}$=-21.0%, range: -68.2% to 81.1%) (**Figures 4 and S2.17**). In Yemen, NTL in 18 governorates (85.7%) declined; this was greatest in Al-Mahwit (-91.0%), Ibb (-87.9%), Sana'a City (-87.5%), and Sana'a (-86.8%), all in the west. In Ukraine, 17 oblasts (63.0%) had decreased NTL, notably in Dnipropetrovsk (-68.2%) and Kharkiv (-60.1%) in the east, Mykolaiv (-58.8%) in the south, and Kyiv City (-52.3%) in the north. Areas primarily under Russian control experienced some of the greatest NTL increases post-event; this included Crimea (66.6%), Luhansk (41.8%), and Sevastopol (33.5%).

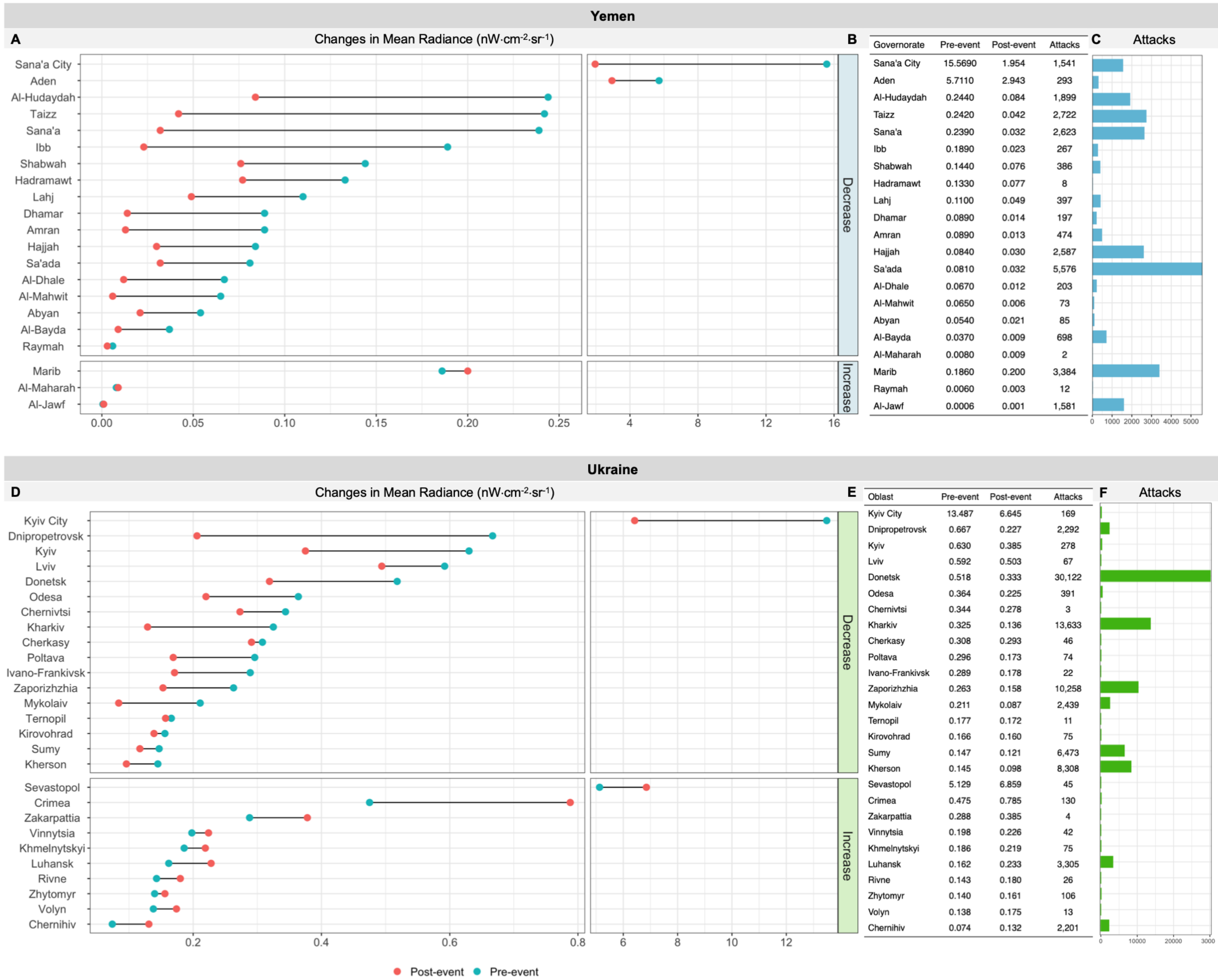

Figure 4: Changes in mean NTL before and after the onset of large-scale military operations These are defined as March 2015 in Yemen and February 2022 in Ukraine (the ‘event’). Panel A shows radiance changes for Yemen. For example, Sana’a City experienced a decrease in mean radiance from approximately 15.6 nW·cm^{-2}·sr^{-1} (blue point) in the pre-event period to 2 nW·cm^{-2}·sr^{-1} (red point) in the post-event period. Estimate values for pre- and post-event in Yemen are indicated in the table in B, along with the total number reported aerial attacks (which are also plotted in C). Ukraine’s are presented in panels D, E, and F, respectively. Note the different x-axes for each country.

In analyzing light recovery, NTL in 10 governorates (47.6%) reached their NTL nadir between December 2015 and January 2016 (n=4) or January and February 2016 (n=6), 9 to 11 months after the onset of air raids. On average, governorates’ mean NTL increased by 1,473.6% from their nadirs; however, NTL levels in the last 6 months of the study period were only 30.9%

of pre-event levels. In Ukraine, 11 oblasts (40.7%) reached NTL nadirs beginning 2 months after event onset (March–April 2022), and 7 oblasts (25.9%) had nadirs beginning 7 months after onset (September–October 2022); oblasts subsequently recovered by a mean of 730.4%. Across all oblasts, mean NTL levels in the last 6 months of the study period had recovered to 81.1% of pre-event levels. In both countries, recovery varied heterogeneously across administrative units.

Alignment of breakpoints and aerial attack onset

The 95% confidence intervals of BFAST-identified negative breakpoints aligned with attack onset in 85.7% (n=18) of governorates and 51.9% (n=14) of oblasts (**Figure 5** and **Tables S2.9–2.10).** The three governorates where these did not align were those with the fewest attacks. In Kherson, Mykolayiv, Odesa, and Vinnytsya oblasts, NTL levels had already been steadily declining over the study period, and the onset of attacks did not meaningfully alter this trajectory. Conversely, Crimea, Luhansk, Sevastopol, Rivne, and Volyn experienced increasing trends that were not notably affected by the full-scale invasion. Kirovograd had no noted change in mean NTL across the entire study period.

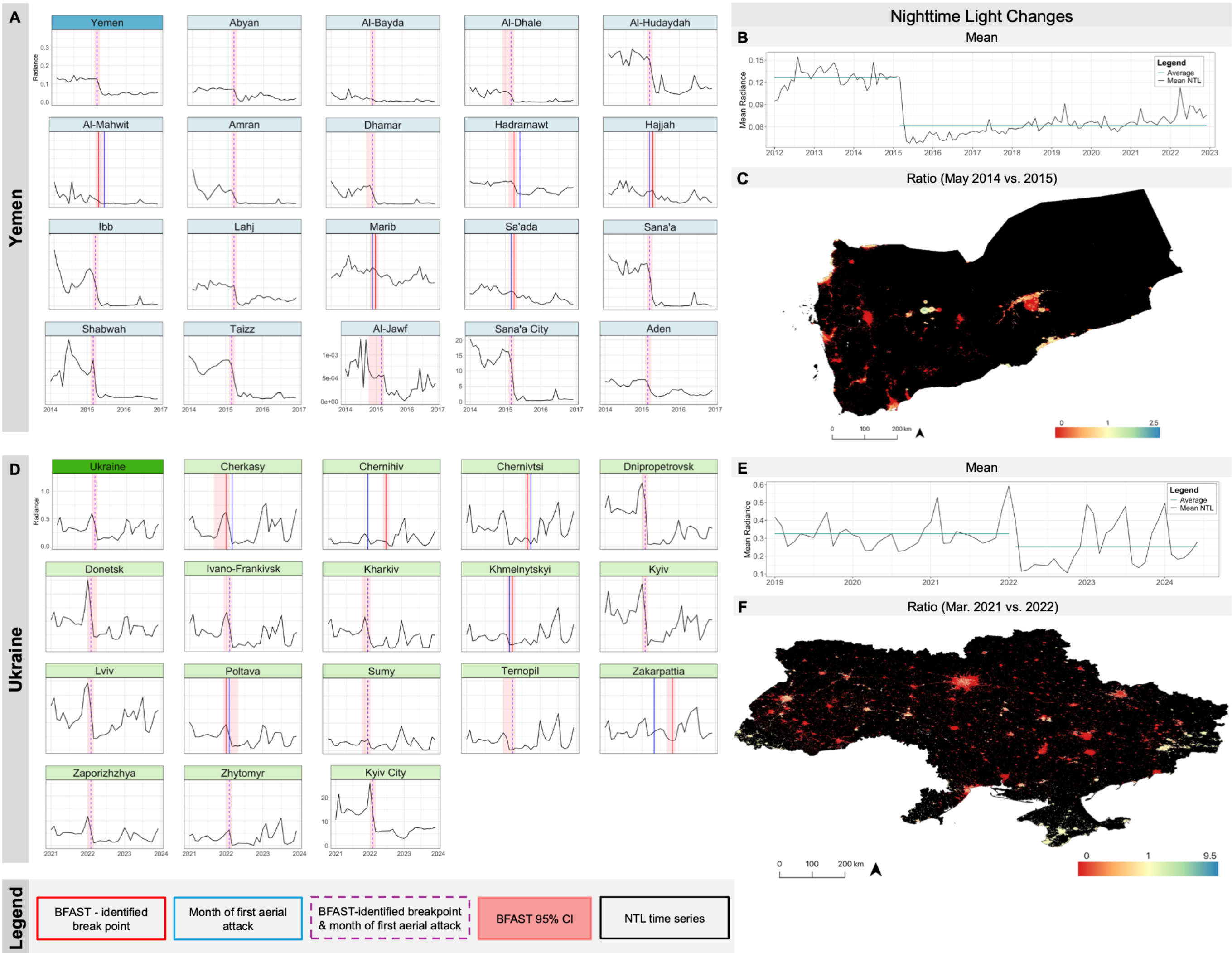

Figure 5: BFAST-identified breakpoints in NTL time series and onset of aerial attacks
The time series (A and D) for each administrative unit is truncated for interpretability. Administrative units for which the NTL signal did not have a detectible negative breakpoint are not shown (Al-Maharah and Raymah in Yemen; Crimea, Kherson, Kirovograd, Luhansk, Mykolayiv, Odesa, Rivne, Sevastopol, Vinnytsya, and Volyn in Ukraine). The full time series for each country is shown in B and E. The maps (C and F) display the overall ratio of mean NTL between the pre- and post-event periods.

In the validation simulations, BFAST successfully identified the true breakpoint in 92% of simulations informed by Yemen’s parameters and 56% of those informed by Ukraine’s. In Yemen-based simulations, accurate identification was primarily driven by a sharp drop in trend values following the breakpoint; seasonality and noise played minimal roles, consistent with their low levels in the real data. In contrast, the Ukraine-informed simulations were noisier and more variable. In these simulations, BFAST was more likely to identify a breakpoint when the trend dropped significantly from the pre- to peri-break period and when a short-term pulse in the noise occurred near the breakpoint—enhancing the detectability of change amid generally noisy conditions. These findings both validate the use of BFAST on the real data and highlight important contextual differences. The mean NTL time series in Yemen had clear signals and limited recovery, which made identifying the signal changes occurring concurrently with attack onset more straightforward. In Ukraine, however, the peri-break period had to be isolated to overcome the masking effects from infrastructure resilience that limited breakpoint identification. Overall, these results suggest that the ability to see the onset of aerial attacks in NTL time series through BFAST or other change detection methods is likely sensitive to underlying country-specific infrastructure resilience and patterns in trend, noise, and recovery.

Associations between nighttime light and aerial attacks

In Yemen, 14 attacks (the mean number of attacks per month) were associated with a -8.97% (95% CI: -13.40%, -4.31%) change in mean NTL and a -12.38% (-17.94%, -6.45%) change in the NTL ratio (**Table 3**). All attack quintiles were associated with mean NTL decreases in Ukraine, with the highest indicating a -69.19% (-77.65%, -57.53%) change. Changes in the NTL ratio followed a similar pattern, with a maximum decrease of -59.72% (-69.49%, -46.82%) (**Table 3**). Spline variable outputs are in **Figure S2.19**.

Table 3: Outputs of GAMs showing the association between attacks and NTL

	Mean NTL		NTL Ratio	
	β (95% CI)	% change in outcome (95% CI)	β (95% CI)	% change in outcome (95% CI)
Yemen				
Air raids				
Individual	0.997 (0.995, 0.998)	-0.35% (-0.53%, -0.16%)	0.995 (0.993, 0.998)	-0.49% (-0.73%, -0.25%)
Scaled	0.910 (0.866, 0.957)	-8.97% (-13.40%, -4.31%)	0.876 (0.821, 0.936)	-12.38% (-17.94%, -6.45%)
Diesel (10% change)	0.976 (0.964, 0.988)	-2.40% (-2.41%, -2.38%)	0.975 (0.959, 0.992)	-2.46% (-2.48%, -2.44%)
Ukraine				
Aerial attacks				
None	Comparison		Comparison	
1 – 2	0.759 (0.649, 0.889)	-24.05% (-35.10%, -11.13%)	0.808 (0.705, 0.927)	-19.18% (-29.54%, -7.30%)
3 – 6	0.761 (0.631, 0.918)	-23.88% (-36.88%, -8.19%)	0.813 (0.690, 0.958)	-18.69% (-31.00%, -4.18%)
7–117	0.562 (0.438, 0.721)	-43.76% (-56.16%, -27.86%)	0.655 (0.528, 0.814)	-34.47% (-47.23%, -18.62%)
118 +	0.308 (0.224, 0.425)	-69.19% (-77.65%, -57.53%)	0.403 (0.305, 0.532)	-59.72% (-69.49%, -46.82%)

For attacks, percentage change of the dependent variable was calculated as $100 \cdot (\beta - 1)$, and each β was calculated by exponentiating the model coefficient. Note that diesel was log-transformed in the model, and thus the β value for a 10% change in diesel price was calculated by raising the base (1.10) to the power of the coefficient. In Yemen, separate GAMs were run with air raids specified individually and scaled ($\bar{x}$: 14 air raids, SD: 27 air raids).

Epidemiological application

The expanded cholera model, which included an interaction term for light recovery, produced similar results across the original conflict specification (air raids) and the NTL-based specification (**Table 4** and **Figure S2.20**).

Table 4: Outputs of the original cholera model and model using NTL-based conflict categorization

		With Recovery	
	Original Model *No. gov. = 20*	**Original Model** *No. gov. = 19*	**Mean NTL Model** *No. gov. = 19*
	IRR (95% CI)	IRR (95% CI)	IRR (95% CI)
Conflict severity			
Low	Comparison	Comparison	Comparison
Intermediate	1.76 (1.51, 2.05)	1.78 (1.52, 2.09)	1.34 (1.06, 1.69)
Medium	1.57 (1.31, 1.89)	1.63 (1.34, 1.98)	1.89 (1.42, 2.52)
High	1.87 (1.53, 2.29)	1.74 (1.41, 2.14)	1.94 (1.38, 2.73)
Severe	2.06 (1.59, 2.69)	2.38 (1.83, 3.09)	1.71 (1.10, 2.64)
Surface water	0.89 (0.78, 1.03)	0.89 (0.78, 1.01)	0.90 (0.79, 1.02)
Precipitation	0.98 (0.91, 1.06)	1.10 (1.02, 1.19)	1.10 (1.02, 1.19)
Vegetation index	0.72 (0.64, 0.80)	0.74 (0.65, 0.83)	0.74 (0.66, 0.84)
Temperature	1.11 (0.91, 1.36)	1.08 (0.90,1 .29)	1.10 (0.92, 1.32)
AIC	30,240.97	28,268.20	28,307.06

Akaike Information Criteria (AIC) is a model fit statistic where lower values indicate a better fit. Note that the models with recovery do not include Raymah governorate, and the models' AIC values should therefore not be compared to the AIC of the original model.

Across all levels of conflict severity, the outcome remained significantly associated with cholera incidence at comparable levels, regardless of which data source was used to specify the conflict categories. The inclusion of the light recovery interaction—which we were unable to do when using just event-based conflict tools—improved model fit (via AIC and deviance explained) across both specifications. Areas that took over 20 months to recover faced increased cholera risk, with the highest risk in areas that had the slowest (>40 to 45 months) recoveries (**Figure 6**). Conversely, areas that recovered quickly (<10 months) had the lowest risk.

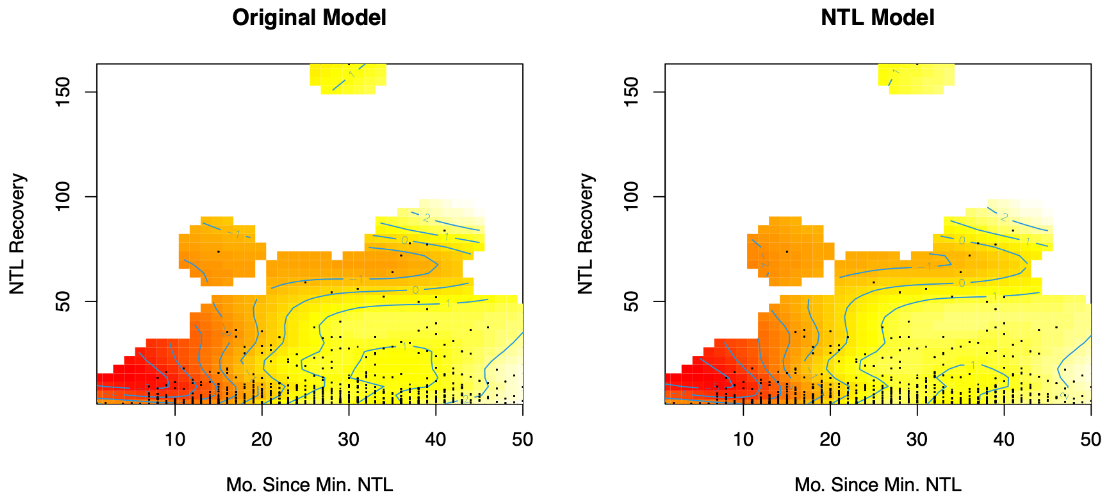

Figure 6: Outputs for the interaction term between light recovery and the number of months since the NTL nadir
Reds indicate lower cholera risk and yellows indicate higher cholera risk after controlling for other variables in the model.

Discussion

NTL is a viable tool for measuring armed conflict in some conflict-affected settings and is particularly adept at filling in gaps left by event-based conflict measurement tools. This includes providing additional insights on conflict dynamics, such as recovery processes, that are otherwise not normally captured in conflict databases. This work has several practical implications. NTL is not subject to many limitations of event-based tools, including reliability, consistency, lack of standardization, and the impact of conflict on reporting itself. It may also provide a longer time series of available and consistent data, given that the data are temporally constrained only by the satellite's activation. Use of NTL has a low barrier to entry, especially when compared to advanced tools such as synthetic aperture radar; this makes it more accessible to humanitarian actors during armed conflict. Importantly, NTL does not rely on the affected population to report on or document conflict events (though we advocate for its use to fill gaps in data rather than to replace on-the-ground reports).

In both Yemen and Ukraine, aerial attacks were significantly associated with decreases in NTL at the first administrative unit level. In the majority of instances, the onset of aerial attacks was identifiable in the mean NTL time series through negative breakpoints. This was true in fewer oblasts than governorates, as many oblasts had upward or downward trends that began prior to the full-scale invasion and continued largely unchanged. The course of NTL over the study period in Ukraine also reflected the conflict's geopolitical context, with areas primarily under Russian control experiencing a growth in NTL following the full-scale invasion. Similar increases were found in other work (80). This may reflect the aggregation of Russian troops in occupied areas and Russian-backed infrastructure development.

The ability of NTL to elucidate regional recovery is a key strength. We hypothesize that much of this light recovery is capturing infrastructure restoration, as infrastructure is a critical component in countries' physical recovery (99,100). Ukraine's recovery resulted in light levels closer to those before the full-scale invasion, whereas levels in Yemen remained low. Yemen's weak infrastructure pre-conflict and economic devastation have limited its infrastructure restoration, while international aid remains insufficient (49,60,61). Pre-conflict infrastructure in Ukraine, however, was largely more robust and resilient (101), and international support for recovery has generally been strong (102). This infrastructure resilience also made it more difficult for BFAST to identify significant breakpoints in the model. Our simulations suggest that the 'noisy' conditions of Ukraine, which we hypothesize reflect its infrastructure's ability to adjust to dynamic and often tumultuous conditions rather than remain stagnant (as was the case in Yemen), made it difficult to detect breakpoints unless certain conditions were met. Understanding the baseline resilience and how this translates across time series components is important for using NTL in similar environments, especially for assessing the areas in which its use may or may not be appropriate.

Monitoring recovery also has meaningful epidemiological applications. When used in the cholera model, governorates' cholera risk was modified by their recovery: governorates with fast and strong recovery had the lowest risk, whereas those that had slow and weak recovery had the highest risk. Such findings highlight the importance of infrastructure in disease transmission mechanisms (and the importance of investing in infrastructure recovery during armed conflicts), and NTL gives us a tool to integrate it into epidemiological models.

Using NTL data is not without limitations and caveats, and there are environments in which it may be less useful for our present purposes. In Yemen and Ukraine, population centers are predominately in areas where satellites can capture NTL levels clearly—something that would be difficult in environments where the built environment is covered by forest, for example. Ukraine's NTL data are impacted by missingness due to its latitude. Black Marble drops pixels heavily contaminated by stray light, meaning that data in northern regions are frequently missing between June and August. We could interpolate data in these months given our time series length, but this does affect the ability to use NTL in northern latitudes. The missingness (and related interpolation) may also lead to an underestimation of conflict events or infrastructure damage that occurs during that period, though this was unlikely in the present study (**Table S2.1** and **Figure S2.5**). Additionally, NTL changes do not inherently indicate armed conflict (and vice versa – a lack of change or detectable NTL does not necessarily indicate lack of conflict (103)), and NTL should not be used as a universal conflict detection mechanism. Rather, users should establish the presence of armed conflict (or other event which could disrupt NTL, such as a natural hazard or disaster) before using NTL to measure it. Likewise, an area without detectable NTL should not be automatically considered unpopulated (103). NTL data may also be too coarse to detect precise changes, as the pixel size is roughly 450 by 450 meters. This is also true temporally: we used monthly composites given our long study period, and daily images are likely more appropriate in certain instances. However, these may have inconsistent quality and coverage based on cloud cover and other effects. There may be other artifacts (e.g., sensor saturation) that affect NTL quality, though we expect minimal effects on our data given Black Marble's preprocessing. This study also relies on attack data from YDP and ACLED, which may face reporting biases in areas under frequent attack or that are occupied.

Even in conflict-affected areas, not all changes in NTL may be related to physical changes and could reflect individual behavior or policy. Of particular note in Ukraine is the influence of rolling blackouts following the full-scale invasion that heavily targeted power infrastructure. It is possible that some of the NTL changes we observe in this study reflect these rolling blackouts in the oblasts where they were implemented. While we hypothesize that the overarching NTL changes are due to infrastructural damage or destruction (which also contribute to the decision to implement blackouts), it is difficult to parse out the true cause of NTL changes at this spatial scale, and more research on these mechanisms is needed. However, we ran a sensitivity analysis that compared the number of days between January 2023 and June 2024 with planned outages (all of which affected most or all regions) by NPC Ukrenergo, Ukraine's national electrical grid operator, and the country-level mean NTL (104). Outages did not appear to have a meaningful impact on country-level mean NTL (**Figure S2.21**). Importantly, these blackouts are run to stabilize the electrical system following attacks on infrastructure; in other words, these stabilization blackouts are inherently linked to the destruction of infrastructure (105). There is little evidence to suggest that residents are choosing to go without electricity to avert detection (i.e., security-related blackouts). We also expect that our data's monthly temporal scale likely smooths over most of the NTL instability from rolling blackouts, and we observe similar NTL trends in oblasts where blackouts have been used and where they have not.

Issues of spatial and temporal scale are central to the interpretation of NTL. The modifiable areal unit problem, closely related to the ecological fallacy, is a geographic analytic problem whereby changing the size or configuration of spatial units can alter statistical results (106). A key question, therefore, is the scale at which NTL is both appropriate and analytically informative. We analyzed data at the first administrative level because this scale provides a tractable overview of conflict-related change across large areas and time periods and aligns with the spatial resolution of available epidemiological data. We also sought to provide an ecological foundation on which future work can build. As conflict events and disease transmission occur at finer spatial scales, analyses at smaller administrative units or using a grid system would be a welcomed next phase of work. However, analyses at smaller scales must account for spatial dependence (e.g., spatial autocorrelation) and the relationship between NTL resolution and the geographic extent of the phenomena under study. We encourage future work to use spatial extents that are operationally meaningful; cholera data in our study were available at the first administrative unit, which contributed to our analytical scale. A grid system, while perhaps more methodologically appealing, may not be usable for individuals translating findings on the ground. In addition, areas with no detected light also require contextual interpretation, distinguishing between expected low-light regions and conflict-related disruption. Temporal context is equally important, as NTL observed at a single point in time is difficult to interpret without reference to prior trends or neighboring areas.

When choosing whether and how to use NTL, it is important to identify its use case. In this paper, we are interested in understanding if, at an ecological scale, NTL could serve as a proxy for aerial attacks and capture broad recovery trends. At this scale, NTL can be used by humanitarians to identify affected areas, track large-scale recovery processes (which is also useful for epidemiologists, as illustrated), and visualize conflict impacts, among other purposes. To work at small spatial scales, it is likely that NTL would need to be paired with more granular Earth observation tools in some humanitarian use cases. For example, NTL can direct humanitarian actors where to look, and other tools can provide local granularities and detail. This could include synthetic aperture radar (89,107) and repeated high-resolution imagery (108). That NTL may not be directly transferable to all spatial scales, however, is not necessarily to its detriment; we advocate that NTL be used complementarily with other Earth observation tools to understand conflict dynamics, and this remains consistent across scales.

Conclusion

NTL offers a viable tool for measuring armed conflict in some settings and can provide insights on dynamics that are difficult to capture systematically. Its ability to assess recovery has especially strong potential in epidemiological investigations, where the relationship between disease dynamics and infrastructure is crucial in understanding transmission mechanisms. Event-based conflict measurement tools have vast utility in research, advocacy, and accountability, and we show that NTL can complement these tools with specific strengths and means of application. NTL can also be paired with other Earth observation tools, such as synthetic aperture radar, to increase the accuracy and durability of conflict measurements. Continuing to show the effects of armed conflict through a variety of techniques is critical for accountability and to seek relief for civilians.

CHAPTER FOUR: Ecological study measuring the association between conflict, environmental factors, and annual global cutaneous and mucocutaneous leishmaniasis incidence (2005–2022)

Introduction

Leishmaniasis thrives in environments that conflict creates: those with poor living conditions, high malnutrition, and widespread poverty and displacement (109). This vector-borne protozoal infection is spread by infected sandflies (namely of the *Phlebotomus and Lutzomyia* genera) and comes in three primary forms, of which cutaneous leishmaniasis (CL) is the most common (110). CL causes lesions on the skin that easily scar and can lead to disability and stigma (111). The World Health Organization (WHO) estimates that between 600,000 to 1 million new CL cases occur annually despite underreporting (only around 20–33% of cases are estimated to be reported), and are found primarily in the Eastern Mediterranean, Central Asia, and the Americas (111,112). The second main form of leishmaniasis is mucocutaneous (ML), which can partially or completely destroy nose, mouth, and throat mucous membranes (111). The majority of ML cases occur in Bolivia, Brazil, Ethiopia, and Peru (111). Lastly, visceral leishmaniasis (VL) is the most severe form, with fever, severe splenomegaly and hepatomegaly, and anemia that can cause death in 95% of cases if left untreated. There is also significant underreporting of VL, with only 25–45% of the estimated 50,000–90,000 annual cases reported to WHO (111). VL is thought to cause more deaths globally than any other neglected tropical disease (113). Most cases occur in east Africa, India, and Brazil (111).

While the disease has existed throughout history, leishmaniasis cases have been rising globally in recent decades (114). Conflict and environmental changes related to climate change are thought to be the primary contributors to this increase (109,111,115). Higher global temperatures can widen the geographic range of the sandfly vector, leading to a larger distribution of leishmaniasis cases (114). Temperature changes are also thought to increase parasite development in sandfly guts (116). Deforestation and similar changes in land cover cause increased human interaction with vector habitats; the establishment of dwellings in or near areas of high vegetation has been associated with increased incidence of leishmaniasis (115,117). This is because excess vegetation is conducive to sandfly breeding, as are precipitation and humidity (though too much precipitation can decrease vector populations) (117). These environmental factors are all closely linked and often interact nonlinearly. Environmental phenomena also indirectly lead to increased leishmaniasis exposure via human population displacement because of droughts, floods, and famine; this disaster-related displacement can cause an influx of people into areas with high leishmaniasis transmission risk (111).

Vector-borne diseases generally do increase during conflict; following the onset of the Syrian conflict, reports of vector-borne diseases in Syria and neighboring nations rose by 458.5% (118). Prior work by Berry and Berrang-Ford shows a significant dose-response relationship between leishmaniasis and levels of political terror and conflict (109). This increase in leishmaniasis incidence, similar to increases in communicable disease incidence generally during conflict, results from a breakdown in water, sanitation, and hygiene (WASH), widespread infrastructure destruction (including that related to healthcare, WASH, and homes), displacement, poor living conditions, increased poverty, and interrupted vector control measures (109,119,120).

In this ecological study, we aim to explore the effects of conflict and environmental factors on CL and ML cases in nations reporting leishmaniasis cases to the WHO between 2005 and 2022. We focus on CL because of its global prevalence and presence in areas affected by conflict, though cases of ML are also included due to norms in case reporting. While prior studies have measured the associations between either environmental factors or conflict on leishmaniasis, none to our knowledge have analyzed both in tandem (109,121,122). This study aids in understanding these joint effects on leishmaniasis, especially given that these factors will likely intertwine further in the future.

Methods

This is a retrospective ecological study that uses routinely collected and reported public leishmaniasis data. We used a generalized additive model (GAM) with a negative binomial probability distribution and random nation-level intercept to model the relationship between conflict, environmental factors, and leishmaniasis cases at the nation level and across the globe while controlling for other relevant factors (also measured at the nation level). We included all nations that reported CL and ML cases to the WHO for at least half the years between 2005 and 2022 and for which conflict intensity scores were provided.

Data sources

Nation-level CL and ML case counts between 2005–2022 (the outcome variable) were pulled from the WHO's Global Health Observatory, which routinely collects annual counts of total reported cases from nations' surveillance systems and Ministry of Health reports (123). CL and ML case numbers are combined in WHO reporting and cannot be differentiated. Between 2005–2012, the WHO reported combined cases of imported and autochthonous leishmaniasis but separated imported cases beginning in 2013. To maintain consistency, we combined the imported and autochthonous cases for each nation from 2013 onwards; however, we did conduct a sensitivity analysis with just autochthonous cases between 2013–2022. The WHO reports cases from 90 total nations for CL and ML, but nations that had less than half of the reported years of cases or that were missing conflict intensity data were excluded from the analysis as their inclusion would have required us to drastically reduce the time series. Nation-years that were missing data were coded as missing and could be differentiated between years that had zero reported cases. Over the 18-year period, there were 107 nation-years (11%) with missing data. Case counts for Pakistan in 2017 were incomplete and we interpolated counts for that year by averaging cases from the preceding and succeeding years. We controlled for nations' population size by using annual nation-level estimates from the World Bank, which were included in the model as an offset term (124).

In addition to the population offset, we included several covariates in this model (summarized in **Table S3.1**). The Bertelsmann Transformation Index (BTI) reports a measure of nation-level conflict intensity every two years beginning in 2006 using insight from nearly 300 national and regional experts (125). The conflict intensity score measures social, ethnic, and religious conflict severity within a nation on a scale of one to ten, where one indicates no violent social, ethnic, or religious-based incidents and ten indicates widespread violent conflict or civil war within the prior two years. BTI uses the following as indicators of conflict intensity: 1) “the confrontational nature of politics,” 2) “the polarization and split of society along one or several cleavages,” 3) “the mobilization of large groups of the population,” and 4) “the use and spread of violence” (126). To have annual measurements, we averaged the conflict intensity scores for the years between reports; other tested interpolation techniques can be found in **Table S3.2**. Conflict intensity was lagged one year based on scientific hypotheses and model fit (**Table S3.3**) (109). Briefly, this means that conflict in one year was used to potentially predict cases in the subsequent year.

To account for differences in nations’ wealth, we included each nation’s annual GDP, in US dollars, from the World Bank (127). These were mean centered and standardized. We also included an estimate of the proportion of the total population internally displaced from conflict, violence, and natural disasters at the nation level from the Internal Displacement Monitoring Center (128). We used the total number of internally displaced people at the end of each year to capture long-term displacement related to conflict and summed it with counts of post-disaster displacement to estimate total annual displacement. These data, which begin in 2008, are conservative estimates and likely underestimate the true amount of displacement seen within each nation. To account for scale differences related to varying population sizes between nations, we calculated the proportion of population displaced by dividing the total number of people displaced by total population for each year. These estimates were log-transformed to account for skewness.

Lastly, we utilized environmental data from several sources. Nation-level total observed precipitation and ambient temperature (mean, minimum, and maximum) were extracted from the World Bank's Climate Change Knowledge Portal (53). Minimum and maximum ambient temperature data were used to calculate a nation-level temperature range. We used NASA's Global Land Data Assimilation System Land Surface Model to extract nation-level mean, minimum, and maximum measures of monthly specific humidity (originally collected at a 1°x1° spatial scale) in QGIS v.3.22.10 (129). These monthly measures were transformed into annual mean humidity and humidity range. Lastly, we extracted normalized difference vegetation index (NDVI) data from NASA's Terra MODIS satellite using Google Earth Engine (130). The data were originally collected monthly at a 1km spatial scale, which we transformed into an annual nation-level measure. NDVI provides a measurement of vegetation levels on a scale of -1 to 1, where -1 indicates low surface vegetation and 1 indicates high surface vegetation. All measures were mean centered and standardized.

Model building

To account for non-linear associations between variables and cases as well as the large number of zeros in our case data, we utilized a negative binomial GAM with CL and ML cases as the outcome, population (logged) as the offset term, and the remaining variables as model covariates. Since the analysis contains repeated observations within nations, we included a nation-level random intercept to account for likely differences in variance within and between nations. Initially, all variables were included as spline functions so as to not assume linearity. Variables that had a linear output were then put into the model as linear predictors to increase the model's interpretability. The final model accounts for temporal, demographic, environmental, economic, and conflict-related measures. We also tested two interaction terms: one between conflict and displacement, and another between conflict and year. These interactions were not statistically significant and did not markedly improve model fit so were ultimately excluded (though each variable is included as a predictor). They can be found in **Figure S3.3–S3.4**. The model coefficients can be interpreted as incidence rate ratios (IRR). For continuous variables the coefficient indicates the IRR for a one-unit increase in the value for that variable. Analyses were done using R v.4.0.4.

Results

Descriptive epidemiology

Over the study period, the WHO reported 3,777,149 cases of CL and ML in the 52 nations included in the study (**Figure 7**). Only 21,963 cases (0.6%) were imported. The majority of the included nations were in Africa (n = 11) and the Middle East (n = 10), though the remainder of nations had a wide geographic spread between South America (n = 8), Central America (n = 7), Europe (n = 6), Central Asia (n = 5), South Asia (n = 4), and East Asia (n = 1). As of 2022, 51 of the 52 analyzed nations (98.1%, all but Ukraine) were classified as CL-endemic by the WHO (131).

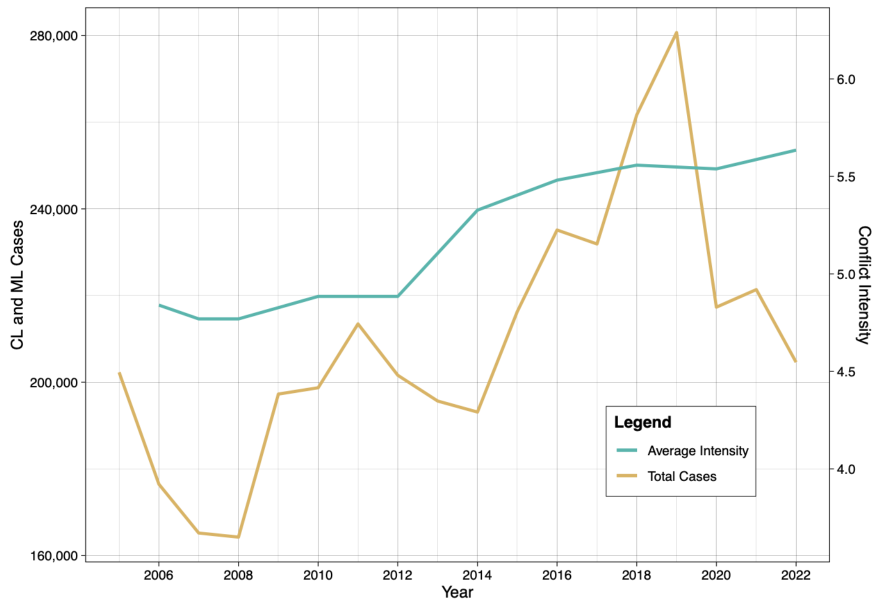

Figure 7: Leishmaniasis cases with average conflict intensity
Time series plot showing total number of cutaneous and mucocutaneous leishmaniasis cases over the study period with the average conflict intensity (not lagged) for each year.

Most cases were in Syria (n = 929,111; 24.6%), Afghanistan (n = 592,153; 15.7%), Brazil (n = 344,549; 9.1%), and Iran (n = 328,980; 8.7%). Syria also had the highest mean incidence (249.7 cases per 100,000), followed by Afghanistan (102.0 per 100,000), Nicaragua (52.4 per 100,000), and Tunisia (47.1 per 100,000) (**Figure 8**). Cases between 2020 and 2022 were relatively low, which may be due to the COVID-19 pandemic. Across all years, the mean conflict intensity score was 5.2 out of 10, though this increased over the study period (**Figure 7**). Mean conflict intensity was highest in Sudan (9.5), Afghanistan (9.2), Iraq (9.1), and Nigeria (8.4) and lowest in Oman (1.6) and Costa Rica (1.0) (**Figure 8**). Seven nations (Afghanistan, Côte d'Ivoire, Iraq, Libya, Sudan, Syria, and Yemen) reached the highest conflict intensity of 10 in at least one year.

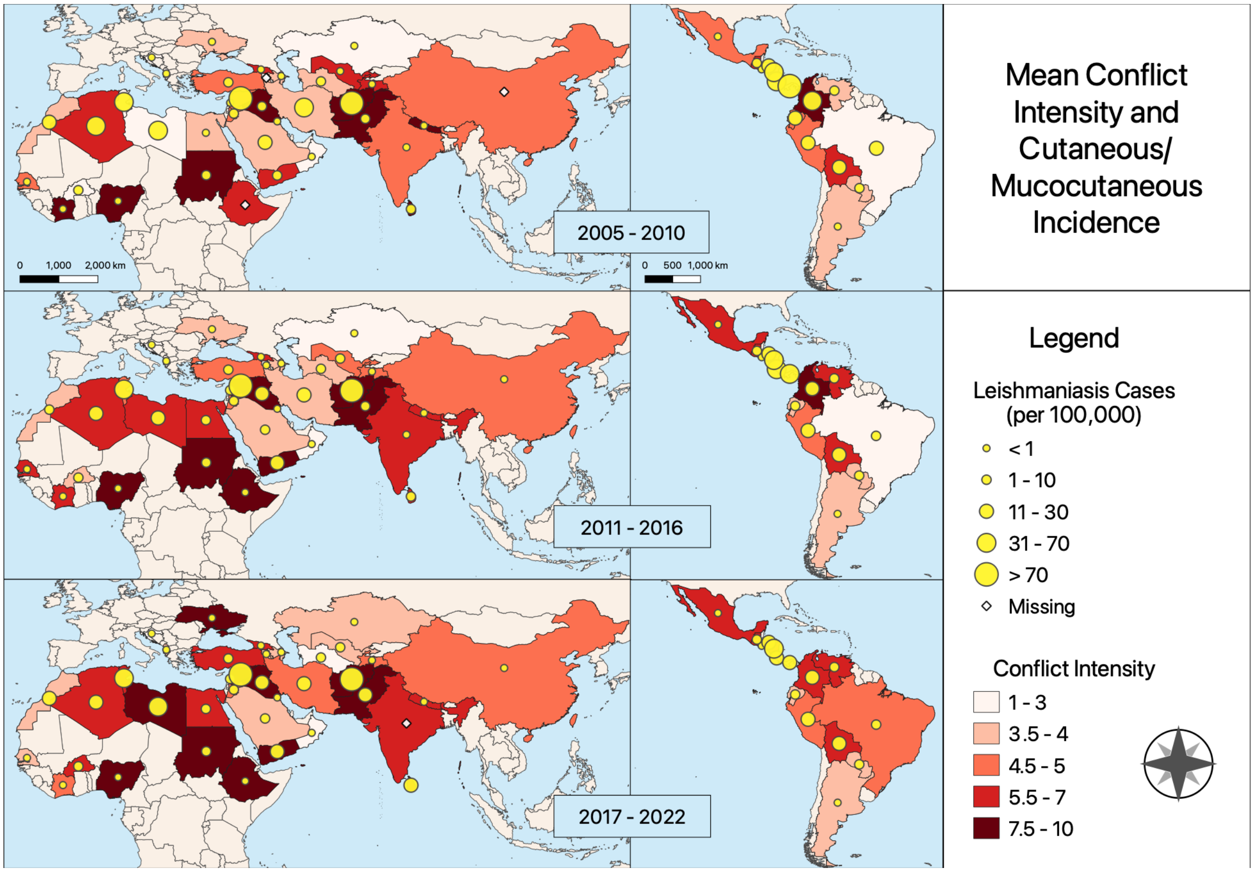

Figure 8: Map of mean conflict intensity and CL/ML incidence
Maps show incidence per 100,000 in 2005–2010, 2011–2016, and 2017–2022 for nations in the analysis. Maps were created using QGIS version 3.22.10. All layers were created by the authors.

Model results

We sequentially added groups of variables to a base model, Model A, which contained year, conflict intensity, GDP, population (as an offset), and the random nation-level intercept (**Table 5**). This allowed us to assess model improvements and potential mediating effects between different groups of variables. In Model B, we added to Model A the proportion of population displaced, and in Model C subsequently added all the environmental variables (including 3 as splines). The model equations can be found in **Appendix 3**.

Adding displacement to the model markedly improved overall model fit, as indicated by the lower Akaike's Information Criterion (AIC) value in Model B versus Model A (**Table 5**). Results also remained consistent across each model. Conflict intensity was associated with increased

CL/ML incidence in the following year. The conflict intensity levels are ranked from 1–10, and a one-unit increase in ranking was associated with a 9% increase in incidence (IRR: 1.09, 95% CI: 1.01–1.16, p = 0.03) (**Figure 9**). Nations with the most severe conflict levels (an intensity score of ten) had 2.09 ($e^{(0.0821*9)}$) times greater risk of CL/ML than nations with a conflict intensity of one (very low conflict). When excluding data from 2020–2022 (the reporting of which was likely affected by COVID-19 (132)), this overall association increased slightly to 1.11 (95% CI: 1.02–1.20, p = 0.01, **Table S3.4** and **Figure S3.1**), or a 2.54 ($e^{(0.1035*9)}$) increase in risk between conflict intensities of one and ten. Similarly, this relationship held when only considering autochthonous cases between 2013–2022 (**Table S3.5** and **Figure S3.2**). The interaction term between conflict and year—while not included in the final model—showed that the relationship between conflict and CL/ML cases has changed over time; in the beginning of the study period, conflict levels had to be higher to have a significant effect on cases, but in more recent years lower levels of conflict have had significant effects (**Figure S3.3**).

Table 5: Results, including the IRR and 95% confidence intervals, for each linear variable throughout each model iteration

	Model A		Model B		Model C	
Covariate	Year, conflict severity, GDP, population offset, and random nation-level intercept		Model A + displacement proportion		Model B + precipitation, temperature, humidity + NDVI	
	IRR (95% CI)	p value	IRR (95% CI)	p value	IRR (95% CI)	p value
Conflict intensity	1.06 (1.001–1.12)	0.0453	1.09 (1.02–1.17)	0.0119	1.09 (1.01–1.16)	0.0200
GDP	0.85 (0.68–1.05)	0.1249	0.85 (0.69–1.05)	0.1335	0.86 (0.70–1.06)	0.1643
Year	1.00 (0.98–1.01)	0.6050	1.01 (0.99–1.02)	0.5345	1.00 (0.98–1.01)	0.6859
Displacement prop.			0.97 (0.93–1.01)	0.0976	0.96 (0.93–1.00)	0.0724
Precipitation					1.12 (0.78–1.62)	0.5318
Humidity (mean)					1.39 (0.67–2.90)	0.3771
Humidity (range)					0.74 (0.63–0.86)	0.0001
AIC	10,090.43		7,724.05		7,748.41	

AIC = Akaike Information Criterion, a model fit statistic where a lower number indicates better model fit.

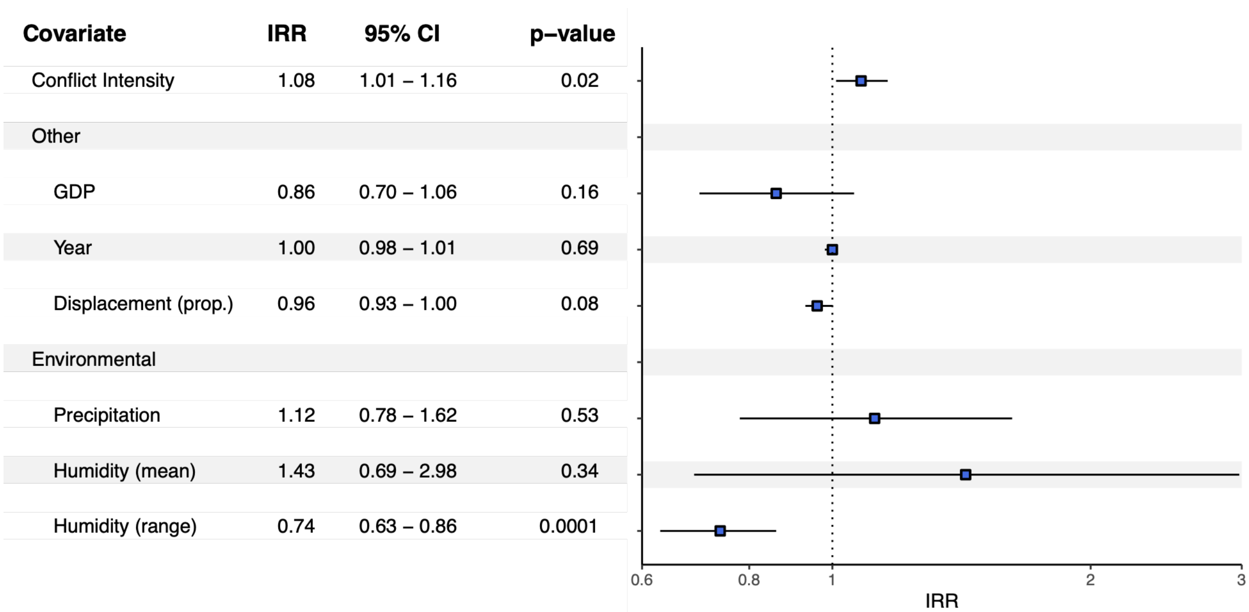

Figure 9: Forest plot of model output for cutaneous and mucocutaneous leishmaniasis
Plot shows the IRR and associated confidence intervals. Results are considered significant when the confidence interval does not go through the null of one. GDP = Gross Domestic Product. IRR = Incidence Rate Ratio.

In the spline outputs (**Figure 10**), lower mean temperature was largely protective against CL/ML cases. However, between approximately 17.02°C–23.58°C (-0.50 to 0.50 standard deviations from the mean), mean annual temperature was associated with increased risk of

CL/ML cases. NDVI was negatively associated with CL/ML cases between levels of 0.34–0.57 (-0.25 to 0.75 standard deviations), or moderate vegetation levels.

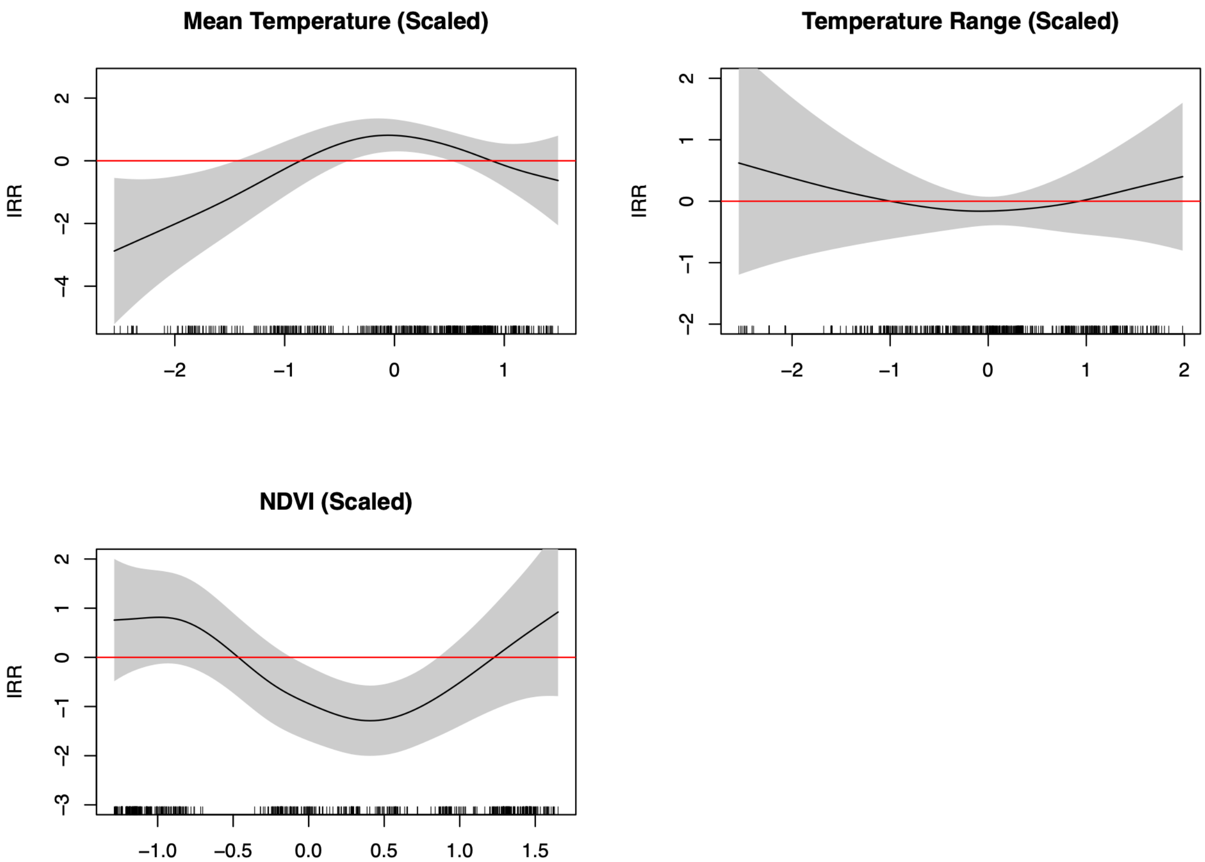

Figure 10: Spline outputs for the model
The variable is significant when both the black line and 95% confidence intervals (gray shaded area) are entirely above or below the red line.

Discussion

Our results suggest that conflict is significantly associated with increased risk of CL/ML in the following year, even when accounting for relevant environmental factors, which is consistent with other literature (109). This is especially true at conflict intensity's highest levels, where conflict turns largely violent. The mechanisms for this are likely complex, though we hypothesize that conflict may create more appropriate breeding grounds for sandflies, cause wide-scale displacement (which we account for), and damage or destroy critical infrastructure. This includes healthcare and WASH-related infrastructure, which are important for preventing and appropriately treating leishmaniasis cases, and vector control infrastructure. We also found curvilinear associations between mean annual temperature and CL/ML, in addition to NDVI and CL/ML, which we hypothesize are related to optimal environments for sandfly vector populations (133,134). As ectotherms, sandflies are sensitive to meteorological conditions, and the temperatures for which there was a positive association with CL/ML incidence (illustrated in **Figure 10**) align with the literature on optimal temperatures for sandfly survival and propagation (133,134). Similarly, sandflies often prefer humid environments, and thus may thrive in environments with less variation in humidity levels as reflected in the model output (134).

In addition, conflict frequently increases poverty, which is strongly associated with CL (135). The conflicts in both Yemen and Syria are good examples of this: following the onsets of their respective conflicts, 90% of the Syrian population has become impoverished, as has 80% of the Yemeni population (25,136). Both conflict and poverty—independently and jointly—can exacerbate inadequate access to healthcare, WASH infrastructure, and sufficient housing, in addition to increasing forced displacement, coinfection with other infectious diseases (especially HIV), and malnutrition (135). Vector control public health measures such as indoor residual spraying, breeding site reduction, and waste collection are often interrupted during conflict, which can create hospitable environments for sandflies while increasing individuals' exposure to these environments. This is especially true in displaced communities. While displacement was not statistically significant in our model, it did act as an important mediator in the relationship between conflict and CL/ML incidence. Displacement increases with conflict intensity (**Figure S3.5**), and thus conflict is likely indirectly affecting leishmaniasis incidence through displacement.

Conflicts globally are becoming more violent. Between 2006–2011, 23.2% of conflicts were a seven or above on BTI's conflict intensity index, indicating when conflict turns largely violent. This rose to 28.9% between 2019–2024, reflecting a 24.2% increase ($p < 0.05$). This shift can also be seen in the percentage of conflicts that are at an intensity of three or below, indicating fairly low conflict levels: 28.4% of conflicts between 2006–2011 were at a conflict intensity of three or below, and this decreased to 19.2% and 12.8% in 2012–2018 and 2019–2024 respectively, showing that fewer conflicts remain small and non-violent. In 2024, 16 nations were involved in conflicts above an intensity level of seven; CL is endemic in each of these nations (curiously, CL is not considered endemic in Ukraine, despite a history of reported cases) (131). Enhanced preparedness for leishmaniasis—and other infectious diseases—is therefore increasingly necessary as more conflicts rise to, and remain in, the highest severity category. This is also important to consider as climate change pushes more nations into the temperature range that enhances CL and ML risk (133).

Though CL is rarely fatal, it is a highly stigmatized disease (137–139). As such, the necessity for prevention extends beyond the immediate clinical effects of the disease. Stigma from CL is associated with significant adverse mental health outcomes and decreased economic well-being (137,138). Vicious cycles of poverty compound the marginalization of these communities from conflict. Women often face worse stigma from CL lesions and scarring than men, even frequently being considered unfit for marriage due to scarring (138). This ostracization is of particular economic relevance, as women in several CL-endemic nations often have fewer economic opportunities than men and rely on marriage for social, economic, and familial stability.

Strengths and limitations

Our study demonstrates an association between conflict intensity and reported CL/ML cases between 2005–2022; this builds on the minimal prior research that explores this association. However, there are several limitations. We relied on CL/ML reporting to WHO which, given challenges to diagnosis, healthcare access, and assessment in many of these settings, could reflect under- or over-reporting of cases. We were also unable to differentiate between cases of CL and ML in the WHO data. We used the BTI scale for conflict intensity which has some subjectivity and gives a nation-level score that does not reflect intra-nation variability. In the model, almost none of the environmental variables were statistically significant, but this may be due to their spatial and temporal scales; looking at the nation level may mask important environmental changes and events that occur at smaller spatial scales and impact local disease trends. This is also true of within-nation associations between the environment and conflict (i.e., in some nations, conflict parties may interact with the environment in ways that notably change them, such as through deforestation or troop movement). We encourage research that can investigate these relationships at smaller spatial scales.

We may also lack a sufficient time period over which to observe relevant environmental trends relating to climate change. However, the nation-level analysis offers an ecological view of the relationship between conflict, environmental events, and leishmaniasis that can serve as the basis of future research that operates at a smaller spatial scale. Though forced displacement did strongly modify our results when included in the model, we did not detect a significant effect despite it being frequently cited as a primary risk factor for CL and ML (109,120). As with other variables, our nation-level unit of analysis and annual time frame may have been too large to capture the impact of displacement at smaller geographic or temporal scales.

Conclusion

Conflict is significantly associated with increased incidence of cutaneous and mucocutaneous leishmaniasis globally, even when controlling for relevant economic, demographic, and environmental variables. Conflict is often marked by widespread violence and infrastructure destruction, which create hospitable environments for sandfly vectors and exacerbate individuals' vulnerability through decreased access to healthcare and WASH infrastructure, in addition to increasing malnutrition, poverty, and displacement. As conflicts globally are becoming more violent and protracted (140–142), these findings have implications for future preparedness efforts. Our work reinforces the importance of adequate preparedness and response mechanisms for the prompt recognition of unexpected CL/ML increases. This is particularly so as the time between a sandfly bite and clinically overt infection may be prolonged. As such, by the time a clinical increase in cases is seen, the opportunity for effective prevention through vector control and public health measures may have been missed. Understanding the relationship between conflict and CL/ML trends can support public health preparation, particularly when climate change and other factors are considered.

CHAPTER FIVE: Quantifying cutaneous leishmaniasis surveillance gaps amidst climate and conflict instability in northern Syria (2016–2023)

Introduction

Vector-borne diseases are generally responsive to changes in the physical environments in which they spread. Cutaneous leishmaniasis (CL), a vector-borne disease caused by parasitic protozoa and spread via sandflies, has well-documented associations with armed conflict and numerous environmental factors, including temperature, land cover changes, and precipitation. Armed conflicts are marked by displacement, infrastructure damage and destruction, poor living conditions, overcrowding, high poverty and malnutrition levels, poor healthcare access, and interrupted public health measures (including vector control operations). These conditions are ones in which leishmaniasis can (re)emerge and spread rapidly, and multiple studies have found an increase in leishmaniasis risk associated with conflict intensity (20,109). Likewise, global temperature changes have widened the hospitable geography for sandflies, contributing to a wider global distribution of disease cases (114). Sandflies are also responsive to changes in vegetation levels (which are likewise responsive to changes in precipitation and humidity), as they often breed in lush areas (115,117). Environmental factors also influence parasite development in the sandfly gut, as well as individuals' exposure risk to the vector (116). As with all ecological systems, however, the interactions between these environmental factors, and even between environmental and conflict-related factors, are complex and frequently nonlinear.

In 2024, Syria reported 50,121 autochthonous cases of leishmaniasis to the World Health Organization, second only to Afghanistan (123). Of the nearly 90,000 CL cases reported in Syria in 2019, 94% were located in northern Syria (143). Prior to the fall of the Assad regime in December 2024, this part of the country (comprising Deir-ez-Zor, Al-Hasakah, Ar-Raqqa, and parts of Aleppo and Idlib governorates) was outside of government control and subject to intense violence and internal displacement for over a decade. In northwest Syria, 82% (approximately 4.24 million people) of the population in November 2024 required humanitarian assistance, and roughly 3.54 million people were internally displaced. Northeast Syria hosted nearly 700,000 internally displaced people (IDPs), including 50,000 in Al Hol camp (144). This context is one in which the underreporting and underdiagnosis of disease is widespread due to various factors; these include the comparatively indolent nature of CL in the region compared to other infectious diseases as well as poor access to healthcare, particularly for CL diagnosis and treatment. Of the estimated 600,000 to 1 million annual new cases of CL globally, only 200,000 (roughly 20–33%) of cases are reported to the World Health Organization (WHO) (111). Similar underreporting is likely in northern Syria, especially given frequent attacks on healthcare and water, sanitation, and hygiene (WASH) infrastructure, severe underfunding of health initiatives, limited healthcare capacity, and challenges accessing care.

Over the course of the conflict, which escalated after peaceful uprisings against the former Syrian regime in March 2011, Syria's health system became fragmented into 'subnational' health systems (145). This fragmentation was also reflected in its disease surveillance. Until December 2024, two parallel syndromic surveillance systems ran within the country: the Early Warning, Alert, and Response System (EWARS) in government-controlled areas and the Early Warning, Alert, and Response Network (EWARN) in non-government-controlled areas. EWARN, run by the Assistance Coordination Unit since 2013, reported counts of syndrome clusters (as defined by the WHO), including for leishmaniasis, and total consultations at health facilities. Weekly reports were generated with high levels of completeness (~84%) and timeliness (~96%) (146). Despite these strengths, EWARN was still subject to the contextual challenges of operating in northern Syria: for example, some reporting areas would lose contact after attacks or changes in territorial control, and other facilities likely underreported cases following damage from violence. This would lead to gaps - both spatial and temporal - in reporting.

This retrospective modeling study has three primary aims: 1) quantify environmental and conflict-related variables associated with increased CL risk in northern Syria, 2) gap-fill spatiotemporal missingness in CL case data between 2016–2023 to measure underreporting, and 3) identify subdistricts with persistent elevated CL case numbers across northern Syria. Since the fall of the Assad regime in 2024, Syria has entered a critical transition, and the new Ministry of Health is tasked with rehabilitating the country's healthcare system to sustainably handle both routine health needs and those resulting from over a decade of protracted conflict. Leishmaniasis is a critical part of this consideration. Though rarely fatal, CL is highly stigmatized; this is especially true for women, who are often ostracized due to their lesions and facial scarring (138). Mean annual reported cases of CL in Syria have more than doubled from pre-conflict levels (29,342 mean annual cases during 2005–2010 versus 61,721 between 2012–2024) (123). MENTOR Initiative, the nongovernmental organization (NGO) responsible for much of the leishmaniasis response in northern Syria for several years, was forced to cease its operations in northeast Syria in July 2024 due to lack of funding (147). This combination of factors has contributed to an increase in CL cases in northern Syria (and particularly in northeast Syria) as of early 2025 alongside worsening control efforts (147). This study seeks to quantify underreporting of cases, identify risk factors for leishmaniasis (including those that could be addressed through intergovernmental work on climate change), and identify areas in particular need of concerted response and prevention efforts.

Methods

This is a retrospective study that uses routinely collected leishmaniasis, Earth observation, and conflict data between 2016 and 2023 at the subdistrict-week level in northern Syria. There are 106 subdistricts (administrative unit level 3) across 5 governorates in northern Syria (the highest administrative unit); the majority of subdistricts are in Aleppo (n=40) and Idlib (n=26) governorates in the northwest. Jebel Saman (Aleppo governorate), Al-Thawrah (Ar-Raqqa governorate), and Dana (Idlib governorates) had the highest mean population density over the study period at 25,650, 14,884, and 7,348 people per $10km^2$, respectively.

Data sources

We used 418 weeks of subdistrict-level CL data collected by EWARN between 2016 and 2023. EWARN reports the number of cases by sex and age group (<5 and ≥5 years old), as well as total clinical consultations for each week. We aggregated cases across sex and age groups for the main analyses, though subgroup analyses were run to assess differences across sex and age (**Tables S4.5–S4.7, Figures S4.5–S4.9**). Missingness (both spatial and temporal) was handled in the modeling process.

Data on several environmental variables relevant to the sandfly vector and disease transmission were extracted using Google Earth Engine for each subdistrict. Daily precipitation (mm/day) from the Climate Hazards Center InfraRed Precipitation with Station (CHIRPS) dataset, available at a 0.05° spatial resolution, was extracted and aggregated into weekly sums. Minimum, maximum, and mean daytime and nighttime land surface temperature (LST) were extracted from the NASA Terra Moderate Resolution Imaging Spectroradiometer (MODIS) satellite at 1km resolution and converted from Kelvin to Celsius. Missingness in the 8-day measurements (defined as the mean LST within an 8-day period) was interpolated by removing the seasonality, linearly interpolating between time points, and reinstating the seasonal component into the time series (using the *forecast* package in R). The LST time series were used to calculate mean temperature and temperature range. MODIS bands were used to calculate a normalized surface water index at an 8-day and 500m scale that ranges from -1 (extremely low surface water) to 1 (extremely high surface water) (18,144,148). Missingness was interpolated using the same technique as for temperature. Similarly, 16-day (250m) data on the normalized difference vegetation index (NDVI), a measure of greenness that also runs from -1 (low vegetation levels) to 1 (high vegetation levels), were extracted from MODIS. Lastly, mean monthly specific humidity was pulled from the Famine

Early Warning System Network Land Data Assimilation System at 11,132m spatial resolution. All environmental variables were mean centered and standardized, and, other than precipitation, were converted into weekly measures using weighted means. Weeks that fell entirely within a reporting period (i.e., fully included in one 8-day, 16-day, or monthly window) were given the value for that period, and weeks that were shared between two periods were given the periods' mean, weighted by the number of week days within each period. We also pulled land cover data (LULC) quarterly from Sentinel-2 Dynamic World, available at a 10m scale, and calculated the proportion of each subdistrict labeled as each land type.

Because we hypothesized that there would be a delay between an environmental variable's occurrence and its effect on CL transmission and subsequent presentation to a health facility, we lagged each variable by 4, 8, 12, and 16 weeks. In addition to the weekly time series for each environmental variable and their lags, we also assigned a weekly binary value for 'anomalies,' or weeks in which precipitation, temperature, surface water, or NDVI levels were above or below two standard deviations from the rolling three week (i.e., the current week and one week on either side) mean for that week of year over the study period. These binary counts were transformed into rolling 8-week sums and categorized based on quantiles (0 anomalous days in prior 8 weeks, 1 day, or 2+ days).

Counts of individual conflict events were pulled from the Uppsala Conflict Data Program (UCDP), which uses open-source data to report georeferenced conflict events. We only included events with location precision levels of 2 (event occurred a maximum of 25km from a known point) and 1 (exact event location known) and with date precision of 3 (week of event known), 2 (date of event occurred within 2–6-day range), or 1 (exact date known). These point data were then spatially joined to their subdistrict, aggregated weekly, mean centered, and standardized. Lastly, we used annual constrained population estimates from WorldPop and divided each subdistrict's annual population by its area to calculate population density per $10km^2$.

Statistical model: Estimating consultation counts

We fit a Bayesian hierarchical model using integrated nested Laplace approximation (INLA) to gap-fill missing case counts and identify subdistrict-level hotspots. However, CL case counts are strongly informed by the total number of consultations in the same week, and weeks with missing CL case counts also had missing consultation counts (indicating that missingness did not mean zero cases but rather represented total non-reporting). To address this, we first used a negative binomial INLA model to estimate the number of consultations for missing weeks, informed by year and week of year, which was modeled using a cyclic second-order random walk (RW2). Spatial variation across subdistricts was modeled using a Besag-York-Mollie type 2 (BYM2) conditional autoregressive specification defined by a subdistrict-level neighborhood matrix. The latent field also accounted for spatiotemporal dependence by grouping the area-level random effects by month and modeling them with a first-order autoregressive (AR1) temporal structure. Penalized complexity priors were used for the spatial and temporal hyperparameters. The spatial priors took a conservative, robust approach as outlined by Simpson et al. (2017) that assumed a relatively stable risk surface but allowed for spatial patterns should the data support them, biasing toward a simpler model (priors and posteriors are compared in **Figure S4.1)** (149,150). We assumed strong temporal correlation via priors. Next, we sampled from the posterior distribution of the model 50 times and extracted the estimated consultation means and credible intervals for each subdistrict-week. These values were then imputed into the primary dataset and used to inform variable selection.

Variable selection

To guide our variable selection for the case-estimation model, we used a combination of scientific hypotheses and model diagnostics. The baseline model contained year, week of year (with a cyclic RW2 spline), consultations (log-transformed), population density (log-transformed), and spatial and temporal random effects. Next, we individually tested each environmental variable, both in a linear and non-linear specification, in the base model and compared model fit using the Watanabe-Akaike Information Criteria (WAIC) and Deviance Information Criterion (DIC) (**Table S4.1–S4.2**). An RW2 specification was used for non-linear specifications. We then ran similar models with multiple lag periods for individual environmental factors. The variables that resulted in the greatest improvements in model fit were then combined into a multivariable candidate model. From there, we systematically removed each variable from the model; if the removal led to a better model fit, they were excluded (**Table S4.3**). Each time a variable was excluded, the removal process was rerun. Finally, the non-linear output of each non-categorical variable was assessed and those that were linear were specified as such to increase model interpretability.

Case model

Following variable selection, we used the posterior samples drawn from the consultation model to inform Bayesian multiple imputation in the final case model. Each draw was exponentiated to produce imputed consultation counts, which were then inserted into the corresponding missing subdistrict-week. The main model for case counts, run with a negative binomial distribution, was refitted separately for each imputed dataset (n=50), which accounted for uncertainty in the imputed values. The final model included variables for year, week of year (with cyclic RW2 spline), precipitation$_{t-4}$, precipitation$_{t-8}$, mean temperature$_{t-8}$, temperature range$_{t-16}$, humidity$_{t-16}$, attacks, high precipitation anomalies, low temperature anomalies, high surface water anomalies, and consultations. Both precipitation variables were modeled as an RW2. The spatiotemporal latent field was defined as it was for the consultations model.

To produce overall coefficients and 95% credible intervals, coefficient and interval values were extracted across all 50 models and averaged. Estimated case numbers and credible intervals at the subdistrict-week level were extracted by taking the median values across all 50 iterations to provide conservative and stable estimates. We also calculated the probability that the number of cases in each subdistrict-week would exceed the overall median number of estimated cases across the study period (7.16) by extracting the fitted marginal distributions from all 50 models and computing the probability that each exceeds this threshold. Coefficient stability across each imputation can be found in **Figure S4.2**, and between-imputation variability was consistently lower than within-imputation variability.

Results

Over the study period, EWARN recorded 550,947 total CL cases and 83,131,020 consultations across northern Syria (**Figure 11**). Cases were almost equally split between males and females (males: 279,981, 50.8%), and most were in patients ≥5 years old (363,127, 65.9%) (**Table S4.4**). The subdistricts that reported the highest number of cases were Dana (n=42,978, 7.8%, Idlib governorate), Ras al Ain (n=37,957, 6.9%, Al-Hasakah), and Kisreh (n=31,883, 5.8%, Deir-ez-Zor). However, the four subdistricts with the highest number of cases per 1,000 consultations were all in Al-Hasakah governorate: Ras Al Ain (101.5 cases per 1,000 consultations), Be'r Al-Hulo Al-Wardeyyeh (70.6), Tal Hmis (50.9), and Qahtaniyyeh (35.0). Across all subdistricts, the median number of weeks with missing data was 27.5 out of 418 total weeks (IQR: 3.25–230.75). There were 7 subdistricts that did not report any data over the entire study period.

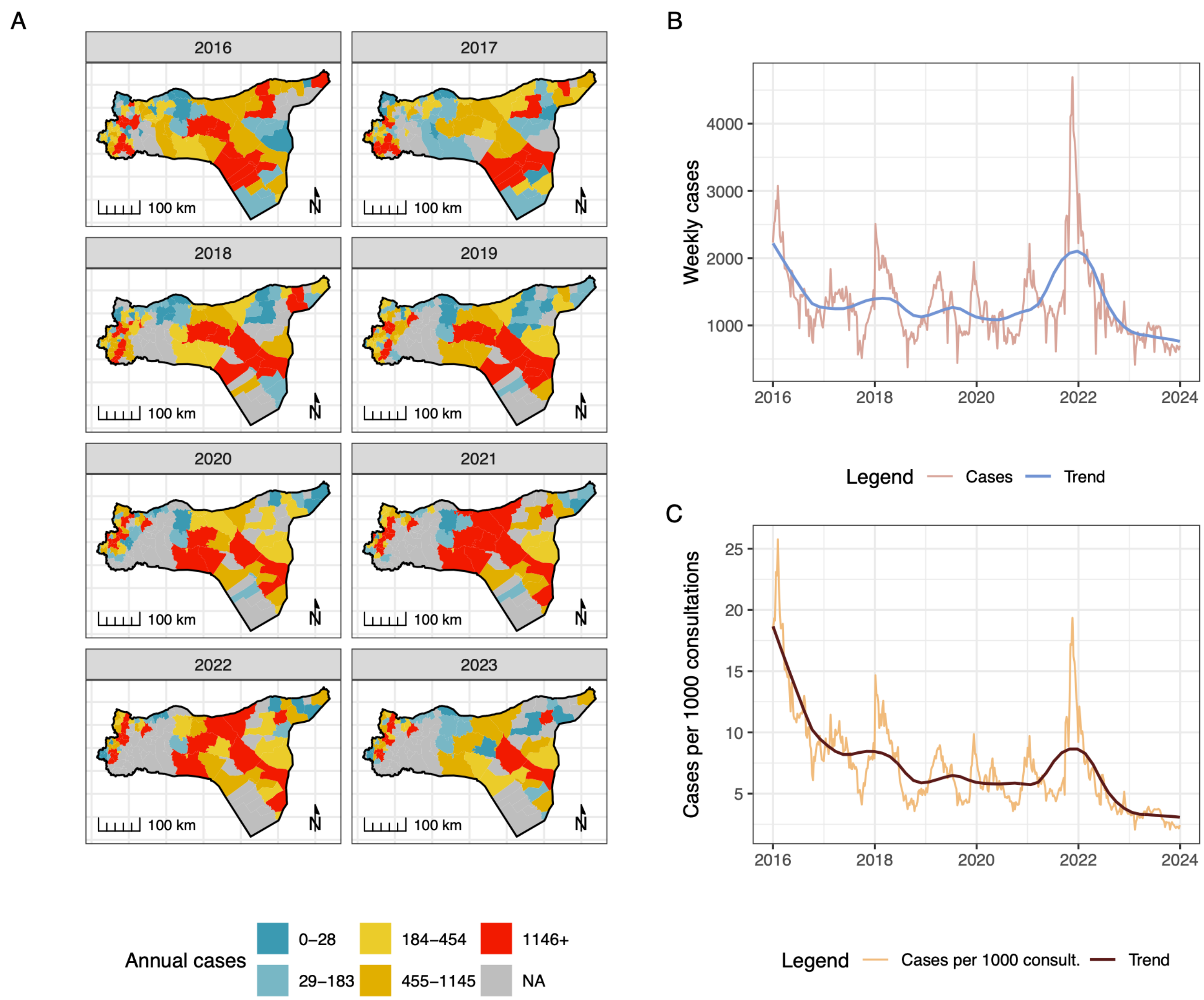

Figure 11: Total reported cutaneous leishmaniasis cases over the study period
The maps (A) display the total reported CL cases annually by subdistrict, with grey indicating reporting gaps (i.e., missingness) rather than zero cases. The graphs on the right show the time series of cases (B) and cases per 1,000 consultations (C), as well as their trendlines.

All environmental variables exhibited notable seasonality over the study period, though there were no overall trends in the variables following decomposition (**Figure 12**). In 2018, 698 subdistrict-weeks experienced anomalously high precipitation (29.9% of total over the study period), with the majority occurring in Idlib (275/698, 39.4%) and Aleppo governorates (204/698; 29.2%). Across the entire study period, Aleppo experienced the most weeks of anomalously high precipitation (913/2336; 39.1%), high surface water levels (498/1427; 34.9%), and low mean temperatures (396/1004; 39.4%), followed by Idlib in each (26.8%, 21.7%, and 23.7% respectively).

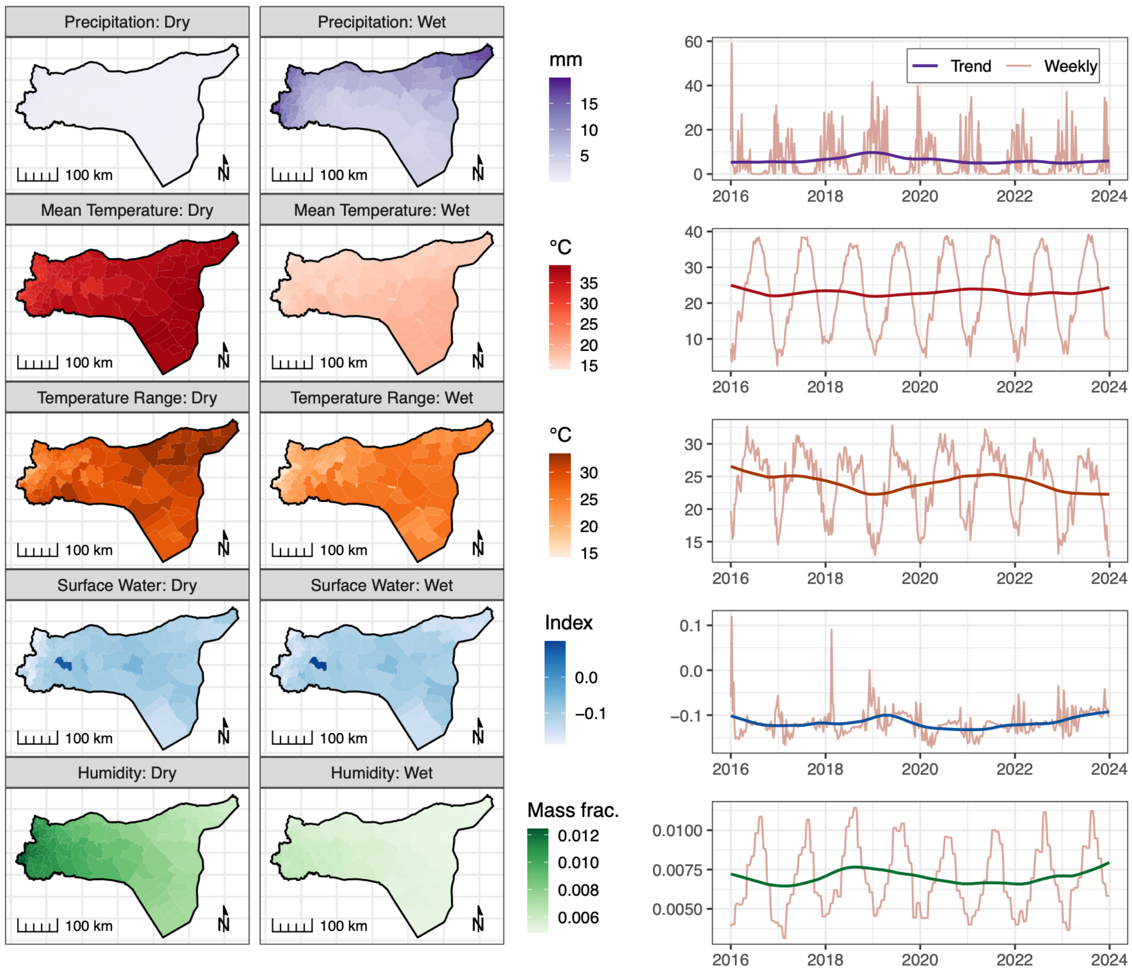

Figure 12: Environmental factors over the study period
Each map shows the average value of the environmental variable by subdistrict over the study period, separated into the dry (June–September) and wet (October–May) seasons. Each time series graph to the right of the maps shows the variable's weekly value and its decomposed trend.

Model results

Several environmental variables were significantly associated with increased risk of CL over the study period, with mean temperature$_{t\text{-}8}$ associated with 7% increased risk (95% CrI: 2%–12%) and both humidity$_{t\text{-}16}$ and temperature range$_{t\text{-}16}$ associated with 3% increased risk (1%–7%

and 1%–5%, respectively) (**Table 6**). Subdistrict-weeks with anomalously high levels of precipitation in the prior 8 weeks experienced decreased CL risk, with 2 or more days associated with 6% less risk (0.4%–10.5%) compared to zero days of precipitation extremes. Conflict events were not significantly associated with CL (**Table 6**). These incident rate ratios (IRRs) were similar across subgroups (**Table S4.5**).

Table 6: Incidence rate ratios and 95% CrIs from the final model

Covariate	IRR	95% CrI
Demographic variables		
Population density (log-transformed)	0.87	0.686–1.098
Consultations	2.66	2.563–2.754
Year		
2016	1 (ref)	
2017	0.84	0.713–0.985
2018	0.70	0.552–0.893
2019	0.56	0.414–0.753
2020	0.44	0.312–0.628
2021	0.37	0.246–0.547
2022	0.30	0.189–0.462
2023	0.18	0.109–0.298
Environmental variables		
$\text{Humidity}_{t\text{-}16}$	1.03	1.005–1.065
$\text{Temperature mean}_{t\text{-}8}$	1.07	1.017–1.123
$\text{Temperature range}_{t\text{-}16}$	1.03	1.012–1.048
Anomalously high precipitation (days in prior 8 wks.)		
0	1 (ref)	
1	0.96	0.936–0.989
2+	0.94	0.895–0.996
Anomalously high surface water (days in prior 8 wks.)		
0	1 (ref)	
1	0.96	0.924–0.995
2+	1.02	0.951–1.095
Anomalously low mean temperature (days in prior 8 wks.)		
0	1 (ref)	
1	0.98	0.944–1.012
2+	0.94	0.878–1.016
Attacks (in prior 3 months)	1.00	0.958–1.038

Outputs were calculated by averaging the outputs from the 50 model iterations. Non-linear outputs are shown in **Figure 13.**

There was also notable seasonality in CL risk (**Figure 13**). Weeks 0–25, corresponding to early January through mid-June, had significantly increased risk of CL; peak risk was seen in roughly weeks 10 (early March) through 15 (early April). This inverted for the remainder of the year, with the lowest risk around weeks 38 (mid-September) to 42 (mid-October).

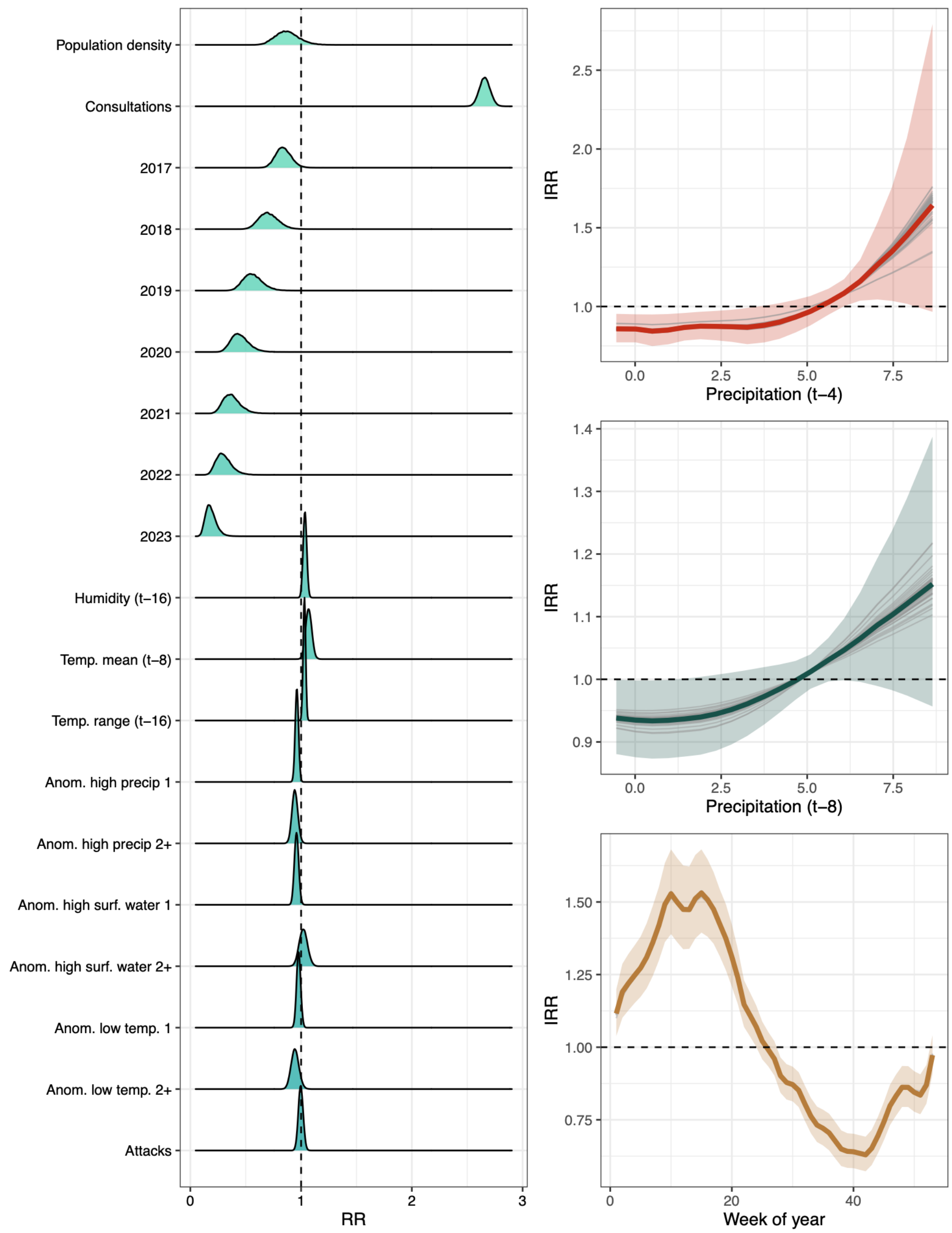

Figure 13: Ridgeline plot and non-linear outputs

On the right, the thin grey lines show the posterior mean of the precipitation curve for each model iteration, while the thick colored line is the pooled estimate and the lighter band corresponds to the pooled 95% CrI. Values are considered significant when the estimate and the 95% CrI are all above or below the horizontal dashed line.

Mapping case estimates and hotspot identification

Between 2016 and 2023 in northern Syria, there were an estimated 871,541 (95% CrI: 385,412–2,799,024) cases of CL, indicating that 36.8% of cases went unreported. **Figure 14** shows the total number of predicted cases (reported and imputed) over the study period compared to the number of reported cases. Underreporting rates were similar across all subgroups, ranging from 31.6% in patients ≥5 years old to 37.5% in children <5 years old (**Figure S4.9**).

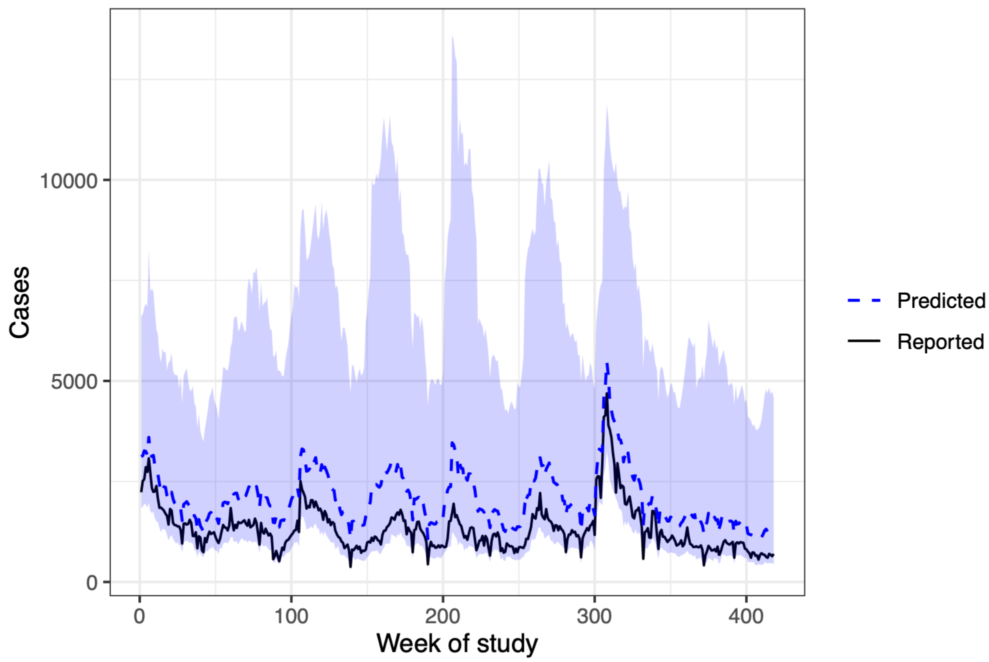

Figure 14: Reported and posterior predictive distribution of CL cases by week
The shading represents the 95% CrI of the estimated data.

In subdistricts that did report cases, the underreporting rate was highest in Jalaa (reported=71 cases, estimated=11,215), Arima (R=10, E=1,328), Tall Refaat (R=36, E=4,353). These subdistricts had 318 (76.1%), 394 (94.3%), and 411 (98.3%) weeks of missing data, respectively. Muhasan subdistrict had the highest number of estimated cases (n=63,781; 7.3%), followed by Dana (n=43,263; 5.0%), and Ras Al Ain (n=37,951; 4.4%) (**Table 7**). Estimated cases by subgroup can be found in **Tables S4.6–S4.7.** Maps of weekly case estimates by year and their credible intervals can be found in **Figure S4.3** and maps for imputed consultations in **Figure S4.4**.

Table 7: Total reported and estimated cases for subdistricts with the highest and lowest estimated case counts

Rank	Subdistrict	Governorate	Total reported cases	Total reported consult.	Total estimated cases (95% CrI)	Weeks of no reporting
1	Muhasan	Deir-ez-Zor	3,581	111,458	63,781 (2,932–394,832)	331 (79.2%)
2	Dana	Idlib	42,978	11,318,589	43,263 (30,612–59,429)	0 (0.0%)
3	Ras Al Ain	Al-Hasakah	37,957	373,868	37,951 (26,979–51,956)	0 (0.0%)
4	Kisreh	Deir-ez-Zor	31,883	2,165,952	31,566 (22,347–43,359)	3 (0.7%)
5	Ma'arrat An Nu'man	Idlib	30,652	1,476,193	31,374 (21,891–45,607)	134 (32.1%)
6	Tamanaah	Idlib	NA	NA	31,264 (47–204,327)	418 (100.0%)
7	Atareb	Idlib	24,206	3,202,800	24,452 (17,170–33,806)	0 (0.0%)
8	Ar-Raqqa	Ar-Raqqa	22,569	2,557,344	22,588 (15,868–31,226)	0 (0.0%)
9	Al Bab	Aleppo	20,266	1,809,626	20,468 (14,336–28,377)	10 (2.4%)
10	Suluk	Ar-Raqqa	19,772	773,423	19,714 (13,862–27,251)	5 (1.2%)
97	Menbij	Aleppo	497	907,772	680 (351–1,295)	19 (4.5%)
98	Amuda	Al-Hasakah	628	296,549	635 (398–997)	6 (1.4%)
99	Teftnaz	Idlib	559	663,880	572 (321–966)	9 (2.2%)
100	Sarin	Aleppo	511	245,452	527 (294–905)	22 (5.3%)
101	Ghandorah	Aleppo	344	308,110	412 (185–835)	29 (6.9%)
102	Hole	Al-Hasakah	97	62,424	343 (57–1,680)	119 (28.5%)
103	Lower Shyookh	Aleppo	6	43,382	330 (2–2,167)	221 (52.9%)
104	Abu Qalqal	Aleppo	80	122,337	127 (43–316)	20 (4.8%)
105	Ain al Arab	Aleppo	38	532,367	50 (14–142)	4 (1.0%)
106	Jawadiyah	Al-Hasakah	1	131,104	45 (1–285)	48 (11.5%)

Rank is ordered by the total number of estimated cases over the study period. NA indicates that there were no cases and no consultations reported over the study period and is not the same as having 0 cases (or consultations) for a location and time period.

When just considering estimates (and not their credible intervals), Muhasan, Atareb, and Dana subdistricts all ranked in the highest percentile (34+) of median weekly cases across all 8 years of the study period, with Ar-Raqqa, Nabul, and Tamanaah consistent across 6 years (**Figure 15A**). Dana and Atareb remained as hotspots when considering subdistricts' estimates and their credible intervals (i.e., subdistricts were considered hotspots if their estimate was in the highest quantile *and* their lower credible interval was in the highest or second-highest quantile) (**Figure 15B**). However, this definitionally excludes subdistricts that underwent significant imputation, given the related large credible intervals. Subgroup-level hotspots are compared to total hotspots in **Figure S4.10.**

There are similarities between the identified hotspots and subdistricts with elevated exceedance probabilities (**Figure 15C**). Across the entire study period, the mean probability that weekly CL cases in Dana would exceed the median number of weekly cases over the study period (7.16) was 99.9%. This was followed by Atareb (99.0%), Sur (94.7%), Ar-Raqqa (92.9%), and Maaret Tamsrin (90.5%). It is worth noting that Dana and Atareb are neighboring subdistricts in Aleppo governorate and Sur, Ar-Raqqa, and Muhasan subdistricts all directly abut the Euphrates or Khabur Rivers.

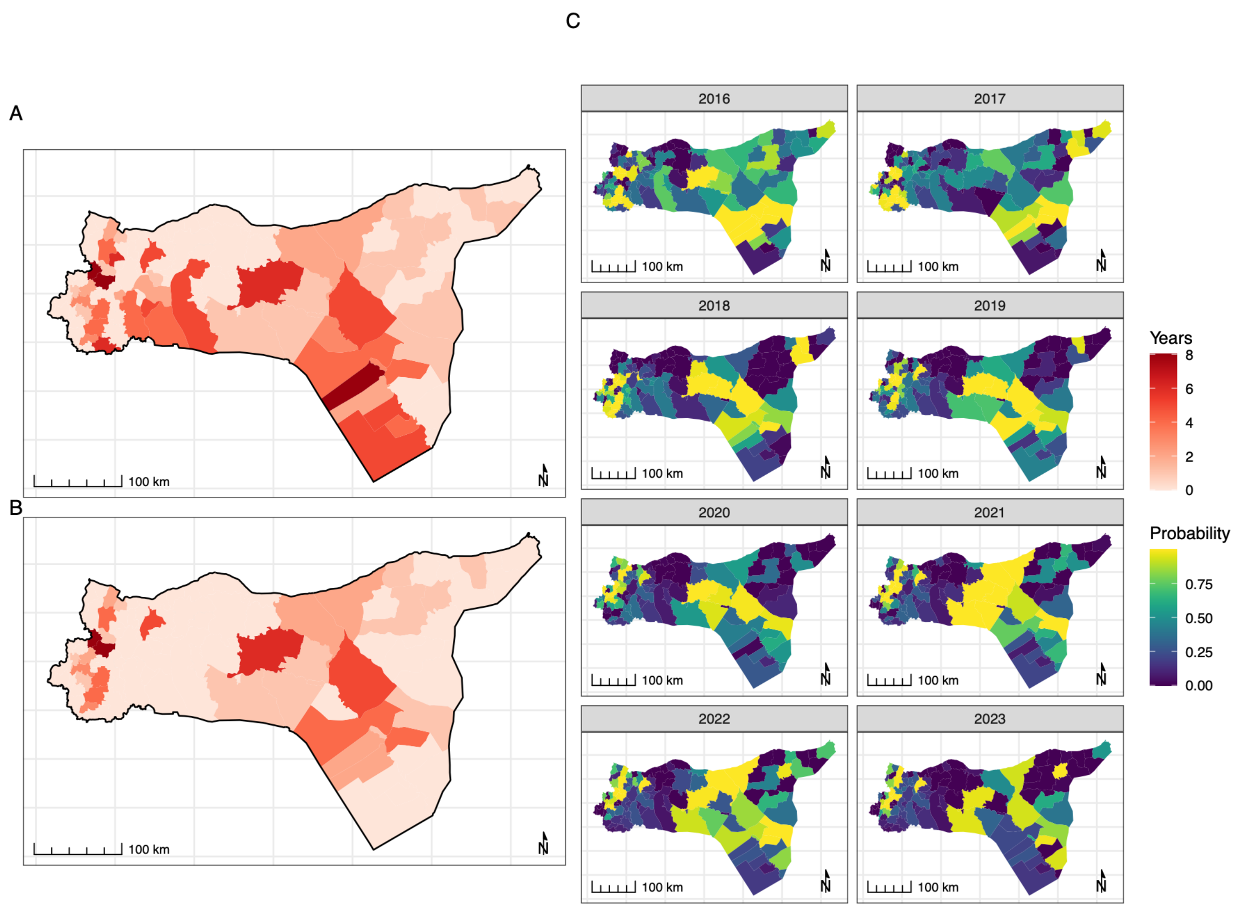

Figure 15: Hotspots and exceedance probabilities

Map A displays the number of years that each subdistrict's estimated number of CL cases was in the highest quantile. Map B displays the number of years each subdistrict's estimated number of CL cases was in the highest quantile and its lower credible interval was in either the highest or second highest quantile. The maps in (C) display the mean probability of the subdistrict's weekly number of cases exceeding the overall median number of estimated cases (7.16).

Discussion

Our retrospective modeling study has several notable results. We identified multiple environmental variables that are associated with increased CL risk across northern Syria, which can be used to inform climate change-related adaptation and mitigation efforts. Secondly, our models estimated 871,541 total cases of CL between 2016–2023, reflecting over 320,000 additional cases than the total reported. Lastly, we identified several subdistricts with persistent elevated case numbers and exceedance probabilities, many of which may have been otherwise missed due to reporting gaps. Though our estimates exhibit high levels of uncertainty because of the degree of missingness in the data, they do offer a sense of scale with potential underreporting in northern Syria, which will be useful in planning preparedness and response efforts.

The environmental associations with leishmaniasis found in this work are consistent with the existing literature. Humidity, lagged by 16 weeks, emerged as a key driver, as did mean temperature$_{t-8}$ and temperature range$_{t-16}$. Precipitation$_{t-4}$ also showed some small pockets of statistical significance. Phlebotomine sandflies thrive in humid environments, and humidity is also thought to work in conjunction with precipitation levels to create vegetated environments conducive to sandfly breeding (117). The 16-week lag period for humidity likely reflects the time lag required for vegetation growth, sandfly development, infection, and an individual's subsequent utilization of care. Sandflies are also thermophilic, preferring (and indeed requiring) high temperatures for survival and development (133). This may also partially explain the protective effects of anomalously low temperatures, though these were not statistically significant. As with humidity, the lag period may reflect the delay in temperature's effect on sandflies' development and subsequent vector activity.

Interestingly, conflict events were not significantly associated with CL risk despite its established relationship (20,109). We hypothesize that this may result from the baseline state of infrastructure and vector control measures in northern Syria at the beginning of our study period. By 2016, violent conflict over five years in northern Syria had already caused widespread damage and destruction of infrastructure and reduced vector control measures. Continued conflict events over the study period may not have caused significant deviations from this baseline, which was already highly conducive to CL spread. Another potential reason is that the recorded conflict events and leishmaniasis transmission may be occurring in different geographical areas within subdistricts, meaning that transmission may have been largely unaffected by events. The relationship between attacks and CL cases may also operate at a spatial scale unexplored in this work, which is a pertinent area for future research. This may be especially true if the relationship between armed conflict and CL is modified by displacement, which we were unable to systematically capture in our model. The findings may also stem from challenges inherent to accessing healthcare during violent conflict: though CL cases may increase following conflict events, individuals may not be able to access healthcare (or may be fearful to do so) during and after increases in attacks (151–153). This could also compound existing transportation challenges, with many patients unable to afford to travel to the communities where treatment centers were located. These factors could bias our results towards the null, even in our estimations given that they are based on the reported data.

CL is known to be underreported globally. The WHO estimates that nearly 66–80% of new cases are unreported, which is an even higher estimate than the roughly 36.8% suggested by this research (111). In northern Syria, which faced over a decade of protracted violence and large-scale displacement, such underreporting, as well as likely underdiagnosis, is unsurprising (147). The fragmentation of the healthcare system, destruction of health and WASH infrastructure, cessation of vector control measures, and widespread poverty throughout the Syrian conflict created a context in which the gains Syria made in leishmaniasis control prior to the conflict were largely erased (154). The heavy stigmatization of CL may also contribute to its underreporting, with women and girls particularly affected (138,139,155). Disease reporting throughout the Syrian conflict was also heavily politicized, which likewise may have affected reporting timeliness and completeness (146). Funding for leishmaniasis control – and the health system broadly – is also at a crisis point in Syria. As of late 2025, only 20% of the funds necessary for the UN and partners to maintain healthcare in Syria had been received (156); the funding gap for UNHCR's response was over 1 billion USD at the end of 2025 (157). Syria faces myriad health priorities in this transitionary period (including, importantly, mental health and antimicrobial resistance), the scale of which is still being calculated following the brutality of conflict. However, CL is not only recognized by local NGOs as the most critical skin disease in northern Syria, but it also fuels vicious cycles of poverty and marginalization of communities that have already endured so much (20,147).

We identified several subdistricts, many of which are in Aleppo and Idlib governorates, that may be in particular need of increased vector control and leishmaniasis response efforts and that would otherwise be missed due to gaps in reporting. Nearly 1.5 million individuals have returned to Syria since December 2024, the majority of whom have settled in Damascus, Aleppo, and Idlib governorates (158). This return necessitates increased resources for health care and epidemiological surveillance, including for leishmaniasis. MENTOR Initiative has been able to maintain their leishmaniasis activities in northwest Syria (which includes Idlib and Aleppo governorates), though northeast Syria now faces an acute gap in control activities following their withdrawal from the region. This includes several of the hotspots identified in this work. Prioritization of support to these areas should occur alongside capacity building efforts that can strengthen the regional infrastructure and its ability to support leishmaniasis control and response efforts with sustainable funding mechanisms (147). This can only occur through political will and funding that prioritizes elevating Syrians' expertise and supporting the development of systems responsive to Syria's needs.

This study is the first to our knowledge that applies advanced geospatial estimation techniques to gap-fill missing data, estimate underreporting, identify subdistrict-level hotspots, and measure associations with environmental variables. However, there are limitations. We used an imputed count of consultations to inform our main model and estimated these values using only spatial and temporal effects. This may have missed other factors that influence consultations, and therefore leishmaniasis case numbers, though any other additions would have required making numerous assumptions. We also only considered the individual effects of environmental variables in the final model, which does not capture any potential interplay between them that may be pertinent to the outcome. We were also unable to include a measurement of displacement in the model due to data availability over the time series, despite its association with leishmaniasis in the literature. Should granular data on displacement be made available, this would be a fruitful continuation of this work. Lastly, there may be other factors related to leishmaniasis transmission that we were likewise unable to capture in this work, such as living conditions or exposure risk.

As Syria rebuilds its health system, adept prioritization of response efforts will be critical. Intergovernmental collaboration on climate change adaptation strategies that integrate anticipatory action for climate sensitive diseases will also be necessary to mitigate potential disease increases, including of leishmaniasis. Our work reinforces both the need for increased CL prevention and response efforts, as well as the critical link between CL and environmental factors. However, we recognize the stark gap in support for Syria to pursue this work and urge the international community to allocate resources that enable improved health and wellbeing among a population that suffered over a decade of violent conflict.

CHAPTER SIX: Summary and Conclusions

Throughout this dissertation, I have argued that conflict and displacement actively influence disease risk rather than passively create risky environments. The (re)emergence of infectious diseases, largescale outbreaks, and related deaths are not inevitable collateral damage from war efforts; rather, I posit that they are actively considered results – and perhaps the intention – of violent action. Over four chapters, I aimed to answer the following questions: 1) Can we quantify the impact of conflict events on disease risk during an outbreak? 2) Are there alternative ways that we can measure conflict and related infrastructural changes that do not rely on ground reporting? 3) Does conflict still affect vector-borne diseases, which have their own unique environmental risk factors? And 4) Can we use this collective information to fill surveillance gaps in conflict-affected settings?

This work found that conflict events significantly increased the risk of cholera in Yemen and cutaneous and mucocutaneous leishmaniasis at a near-global scale. In Yemen, the highest level of air raids was associated with over double the risk of cholera during the 2016–2019 outbreak compared to areas with no air raids. Similarly, countries experiencing intense conflict faced more than two times the risk of leishmaniasis compared to countries with the lowest conflict levels. These results indicate that violent conflict actions significantly modify disease risk, even when considering other epidemiologically relevant variables, such as environmental or demographic factors. They also illustrate that the burden of disease within these contexts, and arguably within many conflict settings, is largely the result of human action rather than natural occurrences.

When considering the mechanisms through which armed conflict leads to increased disease risk, I hypothesized that damage and destruction of critical infrastructure caused by conflict events leads to environments that are conducive to heightened disease spread. This includes contamination of water sources, reduction of healthcare services and access, limited transportation capabilities, cessation of public health programming, and inadequate living conditions (49). Conflict also causes widescale displacement, which has well-established associations with increased disease risk (159). Despite protections under IHL for civilian infrastructure, the scale of infrastructural damage seen in recent conflicts implies a blatant disregard for these guardrails (160,161).

The impacts of conflict on infrastructure are difficult to systematically capture, especially using traditional mechanisms that report on individual conflict events. To address this, I proposed and validated the use of satellite-based NTL to measure conflict intensity and infrastructure recovery in Yemen and Ukraine. This has several practical applications. Firstly, NTL provides robust spatial and temporal coverage that allows for comparisons to pre-conflict baselines and monitoring in areas experiencing intense conflict. It also provides a tool for measuring conflict and its impacts on infrastructure that does not rely on the affected population. Importantly, it can measure infrastructure recovery, which is not possible in event-based tools, and does so with a relatively low barrier to entry compared to other Earth observation products. This work is important not only for epidemiological investigations, as shown in its application to the Chapter Two cholera model, but also for practical use in conflict settings and related response.

Chapters Two through Four highlight the detrimental costs of infrastructure damage and the protective effects of its recovery along the epidemiological pathway. As a conflict strategy, targeting infrastructure is particularly effective at harming a population through direct and indirect means (11). However, infrastructural changes are not stagnant, especially in protracted conflict settings, and this has tangible impacts on public health broadly. I found that recovery, measured via NTL, significantly reduced the risk of cholera in Yemen over the 2016–2019 outbreak. However, there is rarely sufficient investment in infrastructure recovery during conflict. Funding for the Yemen Humanitarian Fund in 2026 faces a $2 billion gap with 22.3 million people (53% of the population) in need of humanitarian assistance (162). Syria's 2026 response fund currently only meets 15% of the total need (163). Yemen has seen some meaningful urban restoration since 2017 through the World Bank's Yemen Integrated Urban Services Emergency Project

(YIUSEP), which committed over $300 million to restoring urban services in the country (164,165). By the end of 2025, YIUSEP had restored 240km of roads and over 300,000m of water and sanitation networks across several cities, among other improvements. Though restoring access to these basic services has undoubtably reduced disease risk for some, there is still an overwhelming need for concerted humanitarian response efforts, including those that target infrastructure, as Yemen is once again facing a surge in cholera cases (166,167).

In Chapter Five, I found that armed conflict was not significantly associated with increased risk of cutaneous leishmaniasis, despite its significant association found in Chapter Four and elsewhere (109). I hypothesize that this too reflects the state of infrastructure, as well as the effects of broader health system fragmentation. Northern Syria endured several years of intense conflict before the study period that resulted in the damage and destruction of critical health and WASH infrastructure (in addition to the cessation of widescale vector control measures), leaving the capacity of these systems to respond to leishmaniasis severely limited by 2016. Conflict had already created an environment in which leishmaniasis could thrive and had already reduced the region's infrastructure to a breaking point. It is therefore not the case that conflict did not contribute to leishmaniasis' spread, but rather that conflict had already taken its toll. Following the fall of the Assad regime in December 2024, efforts to rebuild the country's healthcare system and critical infrastructure have been prioritized (the reconstruction of which is conservatively estimated to cost $216 billion), though funding shortages and the debilitating economic effects of sanctions have challenged these efforts (168,169). Again, we see the devastating effects of dismantling the systems that support life, wellbeing, and dignity.

Chapters Two, Four, and Five also explore the intersection of environmental factors, armed conflict, and infectious disease. Many of the countries currently experiencing armed conflict are also those most vulnerable to the effects of climate change; this is true of both Yemen and Syria. Cholera, leishmaniasis, and numerous other infectious diseases are sensitive to changes in the physical environment, and climate change is likely to alter where, when, and how much disease appears. For example, *V. cholerae*, the causative agent for cholera, is naturally occurring in riverine, coastal, and estuarine ecosystems and forms symbiotic relationships with plankton (170). Factors such as water temperature and salinity play important roles in the growth of both *V. cholerae* and plankton, among other effects, and both these are changing under current climate conditions. Climate change also shifts humans' exposure to cholera. For example, reduced precipitation and groundwater may increase reliance on unsafe drinking water sources, and flooding can increase individuals' exposure to potentially contaminated water sources.

There are similar concerns with climate change and leishmaniasis, especially when considering the relationship between the sandfly vector and the environment. As discussed in Chapters Four and Five, rising temperatures widen sandflies' hospitable environment, changing vegetation levels alter their breeding patterns, and environmental factors are thought to influence the development of the *Leishmania* parasite in their guts (114,116,117). Environmental changes also may increase individuals' exposure to the vector through shifts in land cover and breeding areas (115,117). Armed conflict also fundamentally changes the physical environment, which likewise intersects and compounds the effects of climate change (171). For example, the United Nations Environment Program's preliminary environmental impact assessment of the ongoing Israeli assault in Gaza found extensive contamination of land, water, and air from weaponry, unexploded ordnance, solid waste and sewage, asbestos, and other hazardous substances (172). By May 2024 (7 months after the escalation of violence), the UN estimated that Israeli attacks had generated over 39 million tons of debris, under which human remains were likely trapped; the impact that this will have on the environment, including through groundwater and aquifer contamination, air pollution, destruction of agricultural land, and toxic leaching into soil, cannot be overstated (172). As conflicts become more violent and protracted, and as climate change continues to alter physical environments, disease dynamics will likely also shift. Without concerted effort put towards disease-sensitive climate change adaptation and mitigation efforts, these shifts may contribute to an even higher burden of morbidity and mortality.

When hospitals are bombed, people get sick. When access to clean water is politicized, people get sick. When electricity is cut and fuel is blockaded, people get sick. This dissertation provides support to the growing understanding that armed conflict is a primary driver of morbidity and mortality from infectious diseases, the growth of which often stems from military action that renders critical infrastructure damage or destroyed. It also calls attention to the burden faced by civilians, who are meant to be protected under international humanitarian law. This work, alongside ongoing real-time reports from conflict settings, indicates that these violations occur with impunity and deadly consequences. Reports of healthcare attacks, malnourished children, polio reemergence, and total blackouts that once rallied global outcry – take, for example, the response to the United States' 2015 attack on the MSF Kunduz Hospital in Afghanistan – now are quickly displaced by the next such occurrence (160). A central aim of this dissertation, in addition to contributing to the scientific understanding of disease dynamics in these settings, is to argue that this scale of morbidity and mortality is not inevitable. With adequate political willpower, funding, and a moral backbone, thousands of lives could be saved.

REFERENCES

1. Wise PH. The epidemiologic challenge to the conduct of Just War: Confronting indirect civilian casualties of war. Daedalus. 2017 Jan 1;146(1):139–54. doi:10.1162/DAED_a_00428

2. UNHCR. Global Trends [Internet]. UN Refugee Agency; 2025 [cited 2026 Mar 10]. Available from: https://www.unhcr.org/us/global-trends

3. ICRC. Humanitarian Outlook 2026: A World Succumbing to War [Internet]. International Committee of the Red Cross; 2025 Nov [cited 2026 Mar 10]. Available from: https://www.icrc.org/en/article/humanitarian-outlook-2026

4. UNICEF. 'Not the new normal' – 2024 "one of the worst years in UNICEF's history" for children in conflict [Internet]. UNICEF; 2024 [cited 2026 Mar 10]. Available from: https://www.unicef.org/press-releases/not-new-normal-2024-one-worst-years-unicefs-history-children-conflict

5. Mishra V. UN News [Internet]. United Nations; 2026 [cited 2026 Mar 10]. Sudan: 'Hallmarks of genocide' found in El Fasher, UN investigators detail mass killings and ethnic targeting. Available from: https://news.un.org/en/story/2026/02/1166997

6. Al Jazeera Staff. Israeli attack across Gaza kill 14 Palestinians despite 'ceasefire.' Al Jazeera [Internet]. 2026 Jan 8 [cited 2026 Mar 10]. Available from: https://www.aljazeera.com/news/2026/1/8/israeli-attack-on-gaza-tent-kills-at-least-three-palestinians

7. ICRC. International Humanitarian Law Databases [Internet]. [cited 2026 Mar 16]. Rule 7: The principle of distinction between civilian objects and military objectives. Available from: https://ihl-databases.icrc.org/en/customary-ihl/v1/rule7

8. ICRC. International Humanitarian Law Databases [Internet]. [cited 2026 Mar 16]. Rule 11: Indiscriminate attacks. Available from: https://ihl-databases.icrc.org/en/customary-ihl/v1/rule11

9. ICRC. International Humanitarian Law Databases [Internet]. [cited 2026 Mar 16]. Rule 28: Medical Units. Available from: https://ihl-databases.icrc.org/en/customary-ihl/v1/rule28

10. Stahl-Timmins W, Mahase E, Hutcheson M, Looi MK. How attacking healthcare has become a strategy of war. BMJ. 2025 Oct 23;391:r2153. doi:10.1136/bmj.r2153 PubMed PMID: 41130626.

11. Tarnas MC, Hamze M, Tajaldin B, Sullivan R, Parker DM, Abbara A. Exploring relationships between conflict intensity, forced displacement, and healthcare attacks: a retrospective analysis from Syria, 2016–2022. Conflict and Health. 2024 Nov 21;18(1):70. doi:10.1186/s13031-024-00630-4

12. Fouad FM, Sparrow A, Tarakji A, Alameddine M, El-Jardali F, Coutts AP, et al. Health workers and the weaponisation of health care in Syria: a preliminary inquiry for The Lancet–American University of Beirut Commission on Syria. The Lancet. 2017 Dec 2;390(10111):2516–26. doi:10.1016/S0140-6736(17)30741-9

13. Gleick PH. Water and terrorism. Water Policy. 2006 Dec 1;8(6):481–503. doi:10.2166/wp.2006.035

14. Sers R. The weaponisation of water. The Lancet. 2025 Sep 6;406(10507):992–4. doi:10.1016/S0140-6736(25)01087-6 PubMed PMID: 40414238.

15. Perlman B, Collins SM, Hoek J. Public health implications of satellite-detected widespread damage to WASH infrastructure in the Gaza Strip. PLOS Global Public Health. 2025 Feb 10;5(2):e0004221. doi:10.1371/journal.pgph.0004221

16. Jafarnia N. “Death is More Merciful Than This Life”: Houthi and Yemeni government violations of the right to water in Taizz [Internet]. Human Rights Watch; 2023 Dec [cited 2026 Mar 10]. Available from: https://www.hrw.org/report/2023/12/11/death-more-merciful-life/houthi-and-yemeni-government-violations-right-water

17. WHO. Accessing essential health services in fragile, conflict-affected and vulnerable settings [Internet]. World Health Organization; [cited 2026 Mar 10]. Available from: https://www.who.int/activities/accessing-essential-health-services-in-fragile-conflict-affected-and-vulnerable-settings

18. Tarnas MC, Al-Dheeb N, Zaman MH, Parker DM. Association between air raids and reported incidence of cholera in Yemen, 2016–19: an ecological modelling study. The Lancet Global Health. 2023 Dec 1;11(12):e1955–63. doi:10.1016/S2214-109X(23)00272-3 PubMed PMID: 37973343.

19. Tarnas MC, Vasylyeva TI, Minin VM, Parker DM. Nighttime lights as a proxy for conflict intensity and infrastructure recovery in Yemen and Ukraine. Res Sq. 2026 Feb 6;rs.3.rs-8725596. doi:10.21203/rs.3.rs-8725596/v1 PubMed PMID: 41674820; PubMed Central PMCID: PMC12889831.

20. Tarnas MC, Abbara A, Desai AN, Parker DM. Ecological study measuring the association between conflict, environmental factors, and annual global cutaneous and mucocutaneous leishmaniasis incidence (2005–2022). PLOS Neglected Tropical Diseases. 2024 Sep 26;18(9):e0012549. doi:10.1371/journal.pntd.0012549

21. UN News. Yemen [Internet]. 2022 [cited 2022 Nov 3]. Available from: https://news.un.org/en/focus/yemen

22. World Bank. World Bank [Internet]. [cited 2022 Nov 3]. The World Bank in Yemen. Available from: https://www.worldbank.org/en/country/yemen/overview

23. Qirbi N, Ismail SA. Health system functionality in a low-income country in the midst of conflict: the case of Yemen. Health Policy Plan. 2017 Jul 1;32(6):911–22. doi:10.1093/heapol/czx031 PubMed PMID: 28402469.

24. Hettle N. The Ohio State University Middle East Studies Center [Internet]. 2016 [cited 2023 Jan 17]. Water Wars in Yemen. Available from: https://mesc.osu.edu/news/water-wars-yemen

25. Lebbos TJ, Duran D. Health Sector in Yemen - Policy Note [Internet]. 2021. Available from: https://thedocs.worldbank.org/en/doc/8aca65c4db5338cd3a408c0d4a147123-0280012021/original/Yemen-Health-Policy-Note-Sep2021.pdf

26. Dureab F, Al-Sakkaf M, Ismail O, Kuunibe N, Krisam J, Müller O, et al. Diphtheria outbreak in Yemen: the impact of conflict on a fragile health system. Conflict and Health. 2019 May 22;13(1):19. doi:10.1186/s13031-019-0204-2

27. Alghazali KA, Teoh BT, Loong SK, Sam SS, Che-Mat-Seri NAA, Samsudin NI, et al. Dengue outbreak during ongoing civil war, Taiz, Yemen. Emerg Infect Dis. 2019 Jul;25(7):1397–400. doi:10.3201/eid2507.180046 PubMed PMID: 30924766; PubMed Central PMCID: PMC6590741.

28. Robinson K. Council on Foreign Relations [Internet]. 2023 [cited 2024 Feb 9]. Yemen's Tragedy: War, Stalemate, and Suffering. Available from: https://www.cfr.org/backgrounder/yemen-crisis

29. UN. Yemen facing 'outright catastrophe' over rising hunger, warn UN humanitarians [Internet]. 2022 [cited 2023 Jun 19]. Available from: https://news.un.org/en/story/2022/03/1113852

30. Hove-Musekwa SD, Nyabadza F, Chiyaka C, Das P, Tripathi A, Mukandavire Z. Modelling and analysis of the effects of malnutrition in the spread of cholera. Mathematical and Computer Modelling. 2011 May 1;53(9):1583–95. doi:10.1016/j.mcm.2010.11.060

31. Simpson G. Deadly consequences: Obstruction of aid in Yemen during COVID-19 [Internet]. Human Rights Watch; 2020 Sep [cited 2022 Nov 3]. Available from: https://www.hrw.org/report/2020/09/14/deadly-consequences/obstruction-aid-yemen-during-covid-19

32. Clemens JD, Nair GB, Ahmed T, Qadri F, Holmgren J. Cholera. The Lancet. 2017 Sep 23;390(10101):1539–49. doi:10.1016/S0140-6736(17)30559-7 PubMed PMID: 28302312.

33. ICRC. The Water Situation in Yemen [Internet]. International Committee of the Red Cross; 2022 Jun [cited 2022 Nov 3]. Available from: https://reliefweb.int/report/yemen/water-situation-yemen

34. von Seidlein L, Sack D, Azman AS, Ivers LC, Lopez AL, Deen JL. Cholera outbreak in Yemen. The Lancet Gastroenterology & Hepatology. 2017 Nov 1;2(11):777. doi:10.1016/S2468-1253(17)30287-X

35. ReliefWeb. Yemen: Floods [Internet]. 2022 [cited 2024 Feb 9]. Available from: https://reliefweb.int/disaster/fl-2022-000265-yem

36. Dureab FA, Shibib K, Al-Yousufi R, Jahn A. Yemen: Cholera outbreak and the ongoing armed conflict. The Journal of Infection in Developing Countries. 2018 May 31;12(05):397–403. doi:10.3855/jidc.10129

37. Blackburn CC, Lenze Jr Paul E, Casey RP. Conflict and cholera: Yemen's man-made public health crisis and the global implications of weaponizing health. Health Security. 2020 Apr 1;18(2):125–31. doi:10.1089/hs.2019.0113

38. Spiegel P, Ratnayake R, Hellman N, Ververs M, Ngwa M, Wise PH, et al. Responding to epidemics in large-scale humanitarian crises: a case study of the cholera response in Yemen, 2016–2018. BMJ Global Health. 2019 Jul 1;4(4):e001709. doi:10.1136/bmjgh-2019-001709 PubMed PMID: 31406596.

39. Federspiel F, Ali M. The cholera outbreak in Yemen: lessons learned and way forward. BMC Public Health. 2018 Dec 4;18(1):1338. doi:10.1186/s12889-018-6227-6

40. Al-Mekhlafi HM. Yemen in a time of cholera: Current situation and challenges. Am J Trop Med Hyg. 2018 Jun;98(6):1558–62. doi:10.4269/ajtmh.17-0811 PubMed PMID: 29557331; PubMed Central PMCID: PMC6086153.

41. Camacho A, Bouhenia M, Alyusfi R, Alkohlani A, Naji MAM, Radiguès X de, et al. Cholera epidemic in Yemen, 2016–18: an analysis of surveillance data. The Lancet Global Health. 2018 Jun 1;6(6):e680–90. doi:10.1016/S2214-109X(18)30230-4 PubMed PMID: 29731398.

42. Dureab F, Shibib K, Yé Y, Jahn A, Müller O. Cholera epidemic in Yemen. The Lancet Global Health. 2018 Dec 1;6(12):e1283. doi:10.1016/S2214-109X(18)30393-0 PubMed PMID: 30316747.

43. El Yaakoubi A. Saudis take control of Yemen’s Aden to end stand-off between allies. Reuters [Internet]. 2019 Oct 14 [cited 2022 Nov 11]. Available from: https://www.reuters.com/article/us-yemen-security-idUSKBN1WT19R/

44. UNMHA. UNMHA Press Release on reported airstrikes in Hudaydah city, Al Hail district and As Salif port [Internet]. 2022 [cited 2022 Nov 11]. Available from: https://reliefweb.int/report/yemen/unmha-press-release-reported-airstrikes-hudaydah-city-al-hail-district-and-salif-port

45. Simpson RB, Babool S, Tarnas MC, Kaminski PM, Hartwick MA, Naumova EN. Signatures of cholera outbreak during the Yemeni Civil War, 2016–2019. Int J Environ Res Public Health. 2021 Dec 30;19(1):378. doi:10.3390/ijerph19010378 PubMed PMID: 35010649; PubMed Central PMCID: PMC8744546.

46. Dureab F, Ahmed K, Beiersmann C, Standley CJ, Alwaleedi A, Jahn A. Assessment of electronic disease early warning system for improved disease surveillance and outbreak response in Yemen. BMC Public Health. 2020 Sep 18;20(1):1422. doi:10.1186/s12889-020-09460-4

47. Berghof Foundation, Political Development Forum Yemen. Local Governance in Yemen: Resource Hub [Internet]. 2021 [cited 2022 Dec 14]. Governorates of Yemen. Available from: https://yemenlg.org/governorates/

48. Yemen Data Project [Internet]. [cited 2022 Nov 11]. Data - Yemen Data Project. Available from: https://yemendataproject.org/data.html

49. Sowers J, Weinthal E. Humanitarian challenges and the targeting of civilian infrastructure in the Yemen war. International Affairs. 2021 Jan 1;97(1):157–77. doi:10.1093/ia/iiaa166

50. Sowers JL, Weinthal E, Zawahri N. Targeting environmental infrastructures, international law, and civilians in the new Middle Eastern wars. Security Dialogue. 2017 Oct 1;48(5):410–30. doi:10.1177/0967010617716615

51. Tandon S, Vishwanath T. The evolution of poor food access over the course of the conflict in Yemen. World Development. 2020 Jun 1;130:104922. doi:10.1016/j.worlddev.2020.104922

52. Ogbu TJ, Rodriguez-Llanes JM, Moitinho de Almeida M, Speybroeck N, Guha-Sapir D. Human insecurity and child deaths in conflict: evidence for improved response in Yemen. Int J Epidemiol. 2022 Jun 1;51(3):847–57. doi:10.1093/ije/dyac038

53. World Bank Group. World Bank Climate Change Knowledge Portal for Developing Practitioners and Policy Makers [Internet]. [cited 2023 Jun 22]. World Bank Climate Change Knowledge Portal. Available from: https://climateknowledgeportal.worldbank.org/

54. Climate Hazards Center. CHIRPS: Rainfall Estimates from Rain Gauge and Satellite Observations [Internet]. UC Santa Barbara; [cited 2022 Nov 11]. Available from: https://chc.ucsb.edu/data/chirps

55. Camacho A. Weekly rainfall precipitation data by governorate in Yemen between 2016 and 2020 [Internet]. figshare; 2023 [cited 2023 Oct 11]. Available from: https://figshare.com/articles/dataset/Weekly_rainfall_precipitation_data_by_governorate_in_Yemen_between_2016_and_2020/24290047/1 doi:10.6084/m9.figshare.24290047.v1

56. NASA. Moderate Resolution Imaging Spectroradiometer [Internet]. [cited 2022 Aug 15]. MODIS Data. Available from: https://modis.gsfc.nasa.gov/data/

57. WFP. World Food Programme [Internet]. 2019 [cited 2022 Oct 17]. Yemen - Monthly Market Watch, 2019. Available from: https://www.wfp.org/publications/yemen-monthly-market-watch-2019

58. Loo PS, Aguiar A, Kopainsky B. Simulation-based assessment of cholera epidemic response: A case study of Al-Hudaydah, Yemen. Systems. 2022 Dec 20;11(1). doi:10.3390/systems11010003

59. Carfora MF, Torcicollo I. Identification of epidemiological models: the case study of Yemen cholera outbreak. Applicable Analysis. 2022 Jul 3;101(10):3744–54. doi:10.1080/00036811.2020.1738402

60. Alsoswa A. Carnegie Endowment for International Peace [Internet]. 2023 [cited 2024 Feb 9]. The Economic Recovery of Yemen. Available from: https://carnegieendowment.org/sada/89186

61. ACTED, Action Contre la Faim, Action for Humanity, ADRA, CARE, Catholic Relief Services, et al. Yemen Pledging Falls Far Short of What is Needed to Help Yemeni People Survive [Internet]. 2023 [cited 2024 Aug 30]. Available from: https://reliefweb.int/report/yemen/yemen-pledging-falls-far-short-what-needed-help-yemeni-people-survive

62. Save the Children. Yemen: Fuel crisis pushes sickest children to the brink [Internet]. 2022 [cited 2022 Nov 11]. Available from: https://reliefweb.int/report/yemen/yemen-fuel-crisis-pushes-sickest-children-brink

63. Oxfam. Unprecedented spike in food prices puts Yemenis at risk of extreme hunger [Internet]. Oxfam; 2022 Jul [cited 2022 Nov 11]. Available from: https://reliefweb.int/report/yemen/unprecedented-spike-food-prices-puts-yemenis-risk-extreme-hunger

64. Emergency Operations Center. Yemen: cholera outbreak, 2017/2021—interactive dashboard [Internet]. [cited 2023 Jul 7]. Available from: https://app.powerbi.com/view?r=eyJrIjoiNTY3YmU0NTItMmFjYy00OTUxLWI2NzEtOTU5N2Q0MDBjMjE5IiwidCI6ImI3ZTNlYmJjLTE2ZTctNGVmMi05NmE5LTVkODc4ZDg3MDM5ZCIsImMiOjl9

65. Camacho A, Funk S. Weekly cholera cases by governorate and district in Yemen between 2016 and 2020 [Internet]. figshare; 2023 [cited 2023 Oct 11]. Available from: https://figshare.com/articles/dataset/Weekly_cholera_cases_and_rainfall_by_governorate_and_district_in_Yemen_between_2016_and_2020/24231019/2 doi:10.6084/m9.figshare.24231019.v2

66. ACLED. ACLED [Internet]. [cited 2025 Jan 7]. Armed Conflict Location and Event Data. Available from: https://acleddata.com/data/

67. UCDP - Uppsala Conflict Data Program [Internet]. [cited 2025 Mar 21]. Available from: https://ucdp.uu.se/

68. Kirschner SA, Finaret AB. Conflict and health: Building on the role of infrastructure. World Development. 2021 Oct 1;146:105570. doi:10.1016/j.worlddev.2021.105570

69. Xu P, Wang Q, Jin J, Jin P. An increase in nighttime light detected for protected areas in mainland China based on VIIRS DNB data. Ecological Indicators. 2019 Dec 1;107:105615. doi:10.1016/j.ecolind.2019.105615

70. Jiang W, He G, Long T, Wang C, Ni Y, Ma R. Assessing light pollution in China based on nighttime light imagery. Remote Sensing. 2017 Feb;9(2):2. doi:10.3390/rs9020135

71. Hu Z, Hu H, Huang Y. Association between nighttime artificial light pollution and sea turtle nest density along Florida coast: A geospatial study using VIIRS remote sensing data. Environmental Pollution. 2018 Aug 1;239:30–42. doi:10.1016/j.envpol.2018.04.021

72. Ma T, Yin Z, Zhou A. Delineating spatial patterns in human settlements using VIIRS nighttime light data: A watershed-based partition approach. Remote Sensing. 2018 Mar;10(3):3. doi:10.3390/rs10030465

73. Shi K, Huang C, Yu B, Yin B, Huang Y, Wu J. Evaluation of NPP-VIIRS night-time light composite data for extracting built-up urban areas. Remote Sensing Letters. 2014 Apr 3;5(4):358–66. doi:10.1080/2150704X.2014.905728

74. Bruederle A, Hodler R. Nighttime lights as a proxy for human development at the local level. PLOS ONE. 2018 Sep 5;13(9):e0202231. doi:10.1371/journal.pone.0202231

75. Li X, Xu H, Chen X, Li C. Potential of NPP-VIIRS nighttime light imagery for modeling the regional economy of China. Remote Sensing. 2013 Jun;5(6):6. doi:10.3390/rs5063057

76. Niedomysl T, Hall O, Archila Bustos MF, Ernstson U. Using satellite data on nighttime lights intensity to estimate contemporary human migration distances. Annals of the American Association of Geographers. 2017 May 4;107(3):591–605. doi:10.1080/24694452.2016.1270191

77. Jiang W, He G, Long T, Liu H. Ongoing conflict makes Yemen dark: From the perspective of nighttime light. Remote Sensing. 2017 Aug;9(8):8. doi:10.3390/rs9080798

78. Cao H, Li X, Belabbes S, Dell'oro L, Dou C. Estimates of power supply during the 2023 Gaza humanitarian crisis using night-time light images. Geo-spatial Information Science. 0(0):1–19. doi:10.1080/10095020.2024.2439387

79. Negash E, Birhane E, Gebrekirstos A, Gebremedhin MA, Annys S, Rannestad MM, et al. Remote sensing reveals how armed conflict regressed woody vegetation cover and ecosystem restoration efforts in Tigray (Ethiopia). Science of Remote Sensing. 2023 Dec 1;8:100108. doi:10.1016/j.srs.2023.100108

80. Zhukov YM. Near-real time analysis of war and economic activity during Russia's invasion of Ukraine. Journal of Comparative Economics. 2023 Dec 1;51(4):1232–43. doi:10.1016/j.jce.2023.06.003

81. Bennett MM, Faxon HO. Uneven frontiers: Exposing the geopolitics of Myanmar's borderlands with critical remote sensing. Remote Sensing. 2021 Jan;13(6):6. doi:10.3390/rs13061158

82. Li X, Li D. Can night-time light images play a role in evaluating the Syrian Crisis? International Journal of Remote Sensing. 2014 Sep 17;35(18):6648–61. doi:10.1080/01431161.2014.971469

83. UN OCHA. United Nations Office for the Coordination of Humanitarian Affairs - occupied Palestinian territory [Internet]. 2023 [cited 2024 Aug 1]. UNOSAT Nighttime Lights Analysis Gaza Strip. Available from: http://www.ochaopt.org/content/unosat-nighttime-lights-analysis-gaza-strip-21-october-2023

84. Center for Preventive Action. Council on Foreign Relations Global Conflict Tracker [Internet]. 2024 [cited 2025 Mar 6]. Conflict in Yemen and the Red Sea. Available from: https://www.cfr.org/global-conflict-tracker/conflict/war-yemen

85. UN. UN News [Internet]. [cited 2022 Nov 3]. Yemen. Available from: https://news.un.org/en/focus/yemen

86. UNHCR. The UN Refugee Agency [Internet]. [cited 2025 Jan 27]. Yemen Refugee Crisis: Aid, Statistics and News. Available from: https://www.unrefugees.org/emergencies/yemen/

87. Center for Preventive Action. Council on Foreign Relations Global Conflict Tracker [Internet]. 2025 [cited 2025 Mar 6]. War in Ukraine. Available from: https://www.cfr.org/global-conflict-tracker/conflict/conflict-ukraine

88. Ukraine Refugee Crisis: Aid, Statistics and News | USA for UNHCR [Internet]. [cited 2024 Aug 6]. Available from: https://www.unrefugees.org/emergencies/ukraine/

89. Scher C, Van Den Hoek J. Nationwide conflict damage mapping with interferometric synthetic aperture radar: A study of the 2022 Russia–Ukraine conflict. Science of Remote Sensing. 2025 Jun 1;11:100217. doi:10.1016/j.srs.2025.100217

90. Marty R, Vicente GS. blackmarbler: Black Marble Data and Statistics [Internet]. 2025 [cited 2025 Mar 24]. Available from: https://cran.r-project.org/web/packages/blackmarbler/index.html

91. NASA. Level-1 and Atmosphere Archive & Distribution System Distributed Active Archive Center [Internet]. VNP46A3 - VIIRS/NPP Lunar BRDF-Adjusted Nighttime Lights Monthly L3 Global 15 arc second Linear Lat Lon Grid. Available from: https://ladsweb.modaps.eosdis.nasa.gov/missions-and-measurements/products/VNP46A3/

92. Román M, Wang Z, Shrestha R, Yao T, Kalb V. Black Marble User Guide Version 1.2 [Internet]. NASA; 2021. Available from: https://viirsland.gsfc.nasa.gov/PDF/BlackMarbleUserGuide_v1.2_20210421.pdf

93. Hyndman R, Athanasopoulos G, Bergmeir C, Caceres G, Chhay L, Kuroptev K, et al. forecast: Forecasting Functions for Time Series and Linear Models [Internet]. 2024 [cited 2025 Mar 24]. Available from: https://cran.r-project.org/web/packages/forecast/index.html

94. WorldPop. WorldPop [Internet]. [cited 2025 Jan 7]. Open Spatial Demographic Data and Research. Available from: https://www.worldpop.org/

95. Brown CF, Brumby SP, Guzder-Williams B, Birch T, Hyde SB, Mazzariello J, et al. Dynamic World, Near real-time global 10 m land use land cover mapping. Sci Data. 2022 Jun 9;9(1):251. doi:10.1038/s41597-022-01307-4

96. World Food Program. Humanitarian Data Exchange [Internet]. [cited 2025 Jan 7]. Yemen - Food Prices. Available from: https://data.humdata.org/dataset/wfp-food-prices-for-yemen

97. Verbesselt J, Hyndman R, Zeileis A, Culvenor D. Phenological change detection while accounting for abrupt and gradual trends in satellite image time series. Remote Sensing of Environment. 2010 Dec 15;114(12):2970–80. doi:10.1016/j.rse.2010.08.003

98. Wood S. mgcv: Mixed GAM Computation Vehicle with Automatic Smoothness Estimation [Internet]. 2023 [cited 2025 Jan 7]. Available from: https://cran.r-project.org/web/packages/mgcv/index.html

99. Mitoulis SA, Argyroudis S, Panteli M, Fuggini C, Valkaniotis S, Hynes W, et al. Conflict-resilience framework for critical infrastructure peacebuilding. Sustainable Cities and Society. 2023 Apr 1;91:104405. doi:10.1016/j.scs.2023.104405

100. Hay A, Karney B, Martyn N. Reconstructing infrastructure for resilient essential services during and following protracted conflict: A conceptual framework. International Review of the Red Cross [Internet]. 2019 Nov 1 [cited 2024 Aug 28];(912). Available from: http://international-review.icrc.org/articles/reconstructing-infrastructure-resilient-essential-services-ir912

101. Aebi S, Hauri A, Kamberaj J. Critical Infrastructure Resilience in Ukraine: Energy, Transportation, and Communication [Internet]. Center for Security Studies, ETH Zürich; 2024 Mar. Available from: https://ethz.ch/content/dam/ethz/special-interest/gess/cis/center-for-securities-studies/pdfs/RR-Report-2024-Critical-Infrastructure-Resilience.pdf

102. World Bank Group. World Bank Group Financing Support Mobilization to Ukraine [Internet]. 2024 [cited 2024 Aug 28]. Available from: https://www.worldbank.org/en/country/ukraine/brief/world-bank-emergency-financing-package-for-ukraine

103. Bara C, Sticher V. The rural limits of conflict monitoring using nighttime lights. Humanit Soc Sci Commun. 2025 Jun 23;12(1):1. doi:10.1057/s41599-025-05074-6

104. National Power Company Ukrenergo. Energy Map [Internet]. 2026 [cited 2026 Apr 21]. Information on electricity consumption limitation measures. Available from: https://energy-map.info/en/datasets/0f8f9882-1fb2-47c6-81dc-31fbad914f16

105. DiXi Group. Electricity outages lasted almost 2 thousand hours in 2024 [Internet]. 2025 [cited 2026 Apr 21]. Available from: https://dixigroup.org/en/electricity-outages-lasted-2-thousand-hours-for-ukrainian-households-in-2024/

106. Openshaw S. The Modifiable Areal Unit Problem [Internet]. Vol. 38. Norwich: Geo Books; 1983. (Concepts and Techniques in Modern Geography). Available from: https://www.uio.no/studier/emner/sv/iss/SGO9010/openshaw1983.pdf

107. Asi Y, Mills D, Greenough PG, Kunichoff D, Khan S, Hoek JVD, et al. 'Nowhere and no one is safe': spatial analysis of damage to critical civilian infrastructure in the Gaza Strip during the first phase of the Israeli military campaign, 7 October to 22 November 2023. Conflict and Health. 2024 Apr 2;18(1):24. doi:10.1186/s13031-024-00580-x

108. Mueller H, Groeger A, Hersh J, Matranga A, Serrat J. Monitoring war destruction from space using machine learning. Proceedings of the National Academy of Sciences. 2021 Jun 8;118(23):e2025400118. doi:10.1073/pnas.2025400118

109. Berry I, Berrang-Ford L. Leishmaniasis, conflict, and political terror: A spatio-temporal analysis. Social Science & Medicine. 2016 Oct 1;167:140–9. doi:10.1016/j.socscimed.2016.04.038

110. Cecílio P, Cordeiro-da-Silva A, Oliveira F. Sand flies: Basic information on the vectors of leishmaniasis and their interactions with Leishmania parasites. Commun Biol. 2022 Apr 4;5(1):305. doi:10.1038/s42003-022-03240-z PubMed PMID: 35379881; PubMed Central PMCID: PMC8979968.

111. WHO. Leishmaniasis [Internet]. 2023 [cited 2023 Jan 25]. Available from: https://www.who.int/news-room/fact-sheets/detail/leishmaniasis

112. Alvar J, Vélez ID, Bern C, Herrero M, Desjeux P, Cano J, et al. Leishmaniasis worldwide and global estimates of its incidence. PLOS ONE. 2012 May 31;7(5):e35671. doi:10.1371/journal.pone.0035671

113. Álvarez-Hernández DA, Rivero-Zambrano L, Martínez-Juárez LA, García-Rodríguez-Arana R. Overcoming the global burden of neglected tropical diseases. Therapeutic Advances in Infection. 2020 Jan 1;7:2049936120966449. doi:10.1177/2049936120966449

114. Steverding D. The history of leishmaniasis. Parasites Vectors. 2017 Feb 15;10(1):82. doi:10.1186/s13071-017-2028-5

115. Oryan A, Akbari M. Worldwide risk factors in leishmaniasis. Asian Pacific Journal of Tropical Medicine. 2016 Oct 1;9(10):925–32. doi:10.1016/j.apjtm.2016.06.021

116. Ready PD. Leishmaniasis emergence and climate change. Rev Sci Tech. 2008 Aug;27(2):399–412. PubMed PMID: 18819668.

117. Valero NNH, Uriarte M. Environmental and socioeconomic risk factors associated with visceral and cutaneous leishmaniasis: a systematic review. Parasitol Res. 2020 Feb 1;119(2):365–84. doi:10.1007/s00436-019-06575-5

118. Tarnas MC, Desai AN, Lassmann B, Abbara A. Increase in vector-borne disease reporting affecting humans and animals in Syria and neighboring countries after the onset of conflict: A ProMED analysis 2003–2018. International Journal of Infectious Diseases. 2021 Jan 1;102:103–9. doi:10.1016/j.ijid.2020.09.1453 PubMed PMID: 33002614.

119. Beyrer C, Villar JC, Suwanvanichkij V, Singh S, Baral SD, Mills EJ. Neglected diseases, civil conflicts, and the right to health. The Lancet. 2007 Aug 18;370(9587):619–27. doi:10.1016/S0140-6736(07)61301-4 PubMed PMID: 17707757.

120. Desai AN, Ramatowski JW, Marano N, Madoff LC, Lassmann B. Infectious disease outbreaks among forcibly displaced persons: an analysis of ProMED reports 1996–2016. Confl Health. 2020 Jul 22;14(1):49. doi:10.1186/s13031-020-00295-9

121. Abdullah AYM, Dewan A, Shogib MRI, Rahman MM, Hossain MF. Environmental factors associated with the distribution of visceral leishmaniasis in endemic areas of Bangladesh: modeling the ecological niche. Trop Med Health. 2017 May 12;45(1):13. doi:10.1186/s41182-017-0054-9

122. Ramezankhani R, Sajjadi N, Nezakati esmaeilzadeh R, Jozi SA, Shirzadi MR. Climate and environmental factors affecting the incidence of cutaneous leishmaniasis in Isfahan, Iran. Environ Sci Pollut Res. 2018 Apr 1;25(12):11516–26. doi:10.1007/s11356-018-1340-8

123. WHO. World Health Organization Global Health Observatory [Internet]. [cited 2026 Mar 13]. Number of cases of cutaneous leishmaniasis. Available from: https://www.who.int/data/gho/data/indicators/indicator-details/GHO/number-of-cases-of-cutaneous-leishmaniasis-reported

124. World Bank. World Bank Open Data [Internet]. [cited 2023 Sep 13]. Population (total). Available from: https://data.worldbank.org

125. BTI. Bertelsmann Transformation Index [Internet]. [cited 2024 May 24]. Political Transformation. Available from: https://bti-project.org/en/index/governance

126. BTI. BTI 2022 Codebook for Country Assessments [Internet]. Bertelsmann Stiftung; 2022. Available from: https://bti-project.org/fileadmin/api/content/en/downloads/codebooks/BTI2022_Codebook.pdf

127. World Bank. World Bank Open Data [Internet]. [cited 2023 Jun 27]. GDP (current US$). Available from: https://data.worldbank.org

128. IDMC. Internal Displacement Monitoring Centre [Internet]. [cited 2023 Jun 27]. Global Internal Displacement Database. Available from: https://www.internal-displacement.org/database/displacement-data/

129. NASA. Global Land Data Assimilation System [Internet]. [cited 2023 Jun 27]. GLDAS. Available from: https://ldas.gsfc.nasa.gov/gldas

130. NASA. Google for Developers [Internet]. [cited 2024 May 16]. MOD13A3.061 Vegetation Indices Monthly L3 Global 1 km SIN Grid. Available from: https://developers.google.com/earth-engine/datasets/catalog/MODIS_061_MOD13A3

131. WHO. Status of endemicity of cutaneous leishmaniasis [Internet]. [cited 2023 Feb 8]. Available from: https://www.who.int/data/gho/data/indicators/indicator-details/GHO/status-of-endemicity-of-cutaneous-leishmaniasis

132. Ruiz-Postigo JA, Jain S, Madjou S, Maia-Elkhoury AN, Valadas S, Warusavithana S, et al. Global leishmaniasis surveillance: 2021, assessing the impact of the COVID-19 pandemic. Weekly Epidemiological Record. 2022;97(45):575–90.

133. Koch LK, Kochmann J, Klimpel S, Cunze S. Modeling the climatic suitability of leishmaniasis vector species in Europe. Sci Rep. 2017 Oct 17;7(1):1. doi:10.1038/s41598-017-13822-1

134. Lawyer P, Killick-Kendrick M, Rowland T, Rowton E, Volf P. Laboratory colonization and mass rearing of phlebotomine sand flies (Diptera, Psychodidae). Parasite. 2017;24:42. doi:10.1051/parasite/2017041

135. Alvar J, Yactayo S, Bern C. Leishmaniasis and poverty. Trends in Parasitology. 2006 Dec 1;22(12):552–7. doi:10.1016/j.pt.2006.09.004 PubMed PMID: 17023215.

136. Euro-Med Monitor. Euro-Med Human Rights Monitor [Internet]. 2022 [cited 2023 May 5]. Syria: Unprecedented rise in poverty rate, significant shortfall in humanitarian aid funding. Available from: https://reliefweb.int/report/syrian-arab-republic/syria-unprecedented-rise-poverty-rate-significant-shortfall-humanitarian-aid-funding-enar

137. Hotez PJ. Stigma: The stealth weapon of the NTD. PLOS Neglected Tropical Diseases. 2008 Apr 30;2(4):e230. doi:10.1371/journal.pntd.0000230

138. Kassi M, Kassi M, Afghan AK, Rehman R, Kasi PM. Marring leishmaniasis: The stigmatization and the impact of cutaneous leishmaniasis in Pakistan and Afghanistan. PLOS Neglected Tropical Diseases. 2008 Oct 29;2(10):e259. doi:10.1371/journal.pntd.0000259

139. Yanik M, Gurel MS, Simsek Z, Kati M. The psychological impact of cutaneous leishmaniasis. Clin Exp Dermatol. 2004 Sep 1;29(5):464–7. doi:10.1111/j.1365-2230.2004.01605.x

140. von Einsiedel S, Bosetti L, Cockayne J, Salih C, Wan W. Civil war trends and the changing nature of armed conflict [Internet]. United Nations University Centre for Policy Research; 2017 Mar. Report no.: 10. Available from: https://collections.unu.edu/eserv/UNU:6156/Civil_war_trends_UPDATED.pdf

141. Policinski E, Kuzmanovic J. Protracted Conflicts: The enduring legacy of endless war. International Review of the Red Cross. 2019 Dec;101(912):965–76. doi:10.1017/S1816383120000399

142. United Nations, World Bank. Pathways for Peace: Inclusive Approaches to Preventing Violent Conflict [Internet]. Washington, DC: World Bank; 2018 [cited 2023 Sep 12]. Available from: https://openknowledge.worldbank.org/entities/publication/4c36fca6-c7e0-5927-b171-468b0b236b59

143. WHO EMRO. Leishmaniasis [Internet]. Regional Office for the Eastern Mediterranean: World Health Organization; [cited 2026 Mar 31]. Available from: https://www.emro.who.int/syria/priority-areas/leishmaniasis.html

144. Tarnas MC, Almhawish N, Ratnayake R, Elferruh Y, Aladhan I, Alhaffar MBA, et al. Climate change, armed conflict, forced displacement, and epidemic-prone diseases: an exploratory study in northern Syria. BMC Public Health. 2025 Aug 4;25(1):2642. doi:10.1186/s12889-025-23918-3

145. Abbara A, Marzouk M, Mkhallalati H. Health System Fragmentation and the Syrian Conflict. In: Bseiso J, Hofman M, Whittall J, editors. Everybody's War: The Politics of Aid in the Syria Crisis [Internet]. New York: Oxford University Press; 2021 [cited 2026 Mar 31]. Available from: https://doi.org/10.1093/oso/9780197514641.003.0003 doi:10.1093/oso/9780197514641.003.0003

146. Alhaffar MBA, Abbara A, Almhawish N, Tarnas MC, AlFaruh Y, Eriksson A. The early warning and response systems in Syria: A functionality and alert threshold assessment. IJID Regions. 2025 Mar 1;14:100563. doi:10.1016/j.ijregi.2024.100563

147. Abbara A, González-Sanz M, AlKharrat A, Khalife M, Elferruh Y, Almhawish N, et al. Leishmaniasis in Syria – A call for action of the European Society for Clinical Microbiology and Infectious Diseases (ESCMID) Study Groups for Infections in Travellers and Migrants (ESGITM) and for Clinical Parasitology (ESGCP). Travel Medicine and Infectious Disease. 2025 Jul 1;66:102849. doi:10.1016/j.tmaid.2025.102849

148. Boschetti M, Nutini F, Manfron G, Brivio PA, Nelson A. Comparative analysis of normalised difference spectral indices derived from MODIS for detecting surface water in flooded rice cropping systems. PLOS ONE. 2014 Feb 20;9(2):e88741. doi:10.1371/journal.pone.0088741

149. Moraga P. Geospatial Health Data: Modeling and Visualization with R-INLA and Shiny [Internet]. Chapman and Hall/CRC Texts in Statistical Science; 2019 [cited 2026 Apr 7]. Available from: https://www.paulamoraga.com/book-geospatial/sec-arealdatatheory.html

150. Simpson D, Rue H, Riebler A, Martins TG, Sørbye SH. Penalising model component complexity: A principled, practical approach to constructing priors. Statistical Science. 2017 Feb;32(1):1–28. doi:10.1214/16-STS576

151. Gurses G, Ozaslan M, Zeyrek FY, Kılıç IH, Doni NY, Karagöz ID, et al. Molecular identification of Leishmania spp. isolates causes cutaneous leishmaniasis (CL) in Sanliurfa Province, Turkey, where CL is highly endemic. Folia Microbiol. 2018 May 1;63(3):353–9. doi:10.1007/s12223-017-0556-1

152. Carew J, Simpson R, Pillay TD, Desai A, Toalster R, Parkes P, et al. Vector-borne diseases and the Syrian conflict: A systematic review of literature from Syria and neighbouring, refugee-hosting countries. PLOS Neglected Tropical Diseases. 2025 Nov 26;19(11):e0013721. doi:10.1371/journal.pntd.0013721

153. Muhjazi G, Gabrielli AF, Ruiz-Postigo JA, Atta H, Osman M, Bashour H, et al. Cutaneous leishmaniasis in Syria: A review of available data during the war years: 2011–2018. PLOS Neglected Tropical Diseases. 2019 Dec 12;13(12):e0007827. doi:10.1371/journal.pntd.0007827

154. Youssef A, Harfouch R, Zein SE, Alshehabi Z, Shaaban R, Kanj SS. Visceral and cutaneous leishmaniases in a city in Syria and the effects of the Syrian conflict. The American Journal of Tropical Medicine and Hygiene. 2019 Jul 3;101(1):108–12. doi:10.4269/ajtmh.18-0778

155. Reithinger R, Aadil K, Kolaczinski J, Mohsen M, Hami S. Social impact of leishmaniasis, Afghanistan. Emerging Infectious Diseases. 2005 Apr;11(4). doi:10.3201/eid1104.040945

156. UN News. Syria's future under threat from acute funding shortages [Internet]. 2025 [cited 2026 Mar 31]. Available from: https://news.un.org/en/story/2025/11/1166267

157. UNHCR. Syria situation response as of 30 September 2025 [Internet]. The UN Refugee Agency; 2025. Available from: https://www.acnur.org/co/sites/default/files/2025-10/syria-situation-response-funding-30-09-2025.pdf

158. UNHCR. Regional Flash Update #66 Syria Situation (27 February 2026) [Internet]. The UN Refugee Agency; 2026 [cited 2026 Mar 31]. Available from: https://reliefweb.int/report/syrian-arab-republic/regional-flash-update-66-syria-situation-27-february-2026

159. Tarnas MC, Ching C, Lamb JB, Parker DM, Zaman MH. Analyzing health of forcibly displaced communities through an integrated ecological lens. The American Journal of Tropical Medicine and Hygiene. 2023 Mar 1;108(3):465–9. doi:10.4269/ajtmh.22-0624

160. Rubenstein L, Haar RJ, Amon JJ. Attacks on healthcare in war are being steadily normalized—we need to end impunity. BMJ. 2025 Sep 19;390:r1964. doi:10.1136/bmj.r1964 PubMed PMID: 40973435.

161. Spiegel PB, Karadag O, Blanchet K, Undie CC, Mateus A, Horton R. The CHH–Lancet Commission on Health, Conflict, and Forced Displacement: reimagining the humanitarian system. The Lancet. 2024 Mar 30;403(10433):1215–7. doi:10.1016/S0140-6736(24)00426-4 PubMed PMID: 38493793.

162. OCHA. Yemen [Internet]. United Nations Office for the Coordination of Humanitarian Affairs; 2026 [cited 2026 Apr 7]. Available from: https://www.unocha.org/yemen

163. OCHA. Syrian Arab Republic [Internet]. United Nations Office for the Coordination of Humanitarian Affairs; 2026 [cited 2026 Apr 7]. Available from: https://www.unocha.org/syrian-arab-republic

164. World Bank. Yemen: Rebuilding Urban Life Amid Conflict [Internet]. World Bank Group; 2026 [cited 2026 Apr 7]. Available from: https://www.worldbank.org/en/news/feature/2026/03/13/yemen-rebuilding-urban-life-amid-conflict

165. UNOPS. UNOPS to further improve critical urban services across Yemen [Internet]. United Nations Office for Project Services; 2025 [cited 2026 Apr 7]. Available from: https://www.unops.org/news-and-stories/news/unops-to-further-improve-critical-urban-services-across-yemen

166. Yang J, Perlman B. Yemen health crisis spikes after aid cuts and U.S., Israeli airstrikes. The Washington Post [Internet]. 2025 Sep 5 [cited 2026 Apr 8]. Available from: https://www.washingtonpost.com/world/2025/09/05/yemen-airstrikes-humanitarian-cholera-crisis/

167. Mishra V. UN News [Internet]. United Nations; 2024 [cited 2026 Apr 8]. Yemen bears world's highest cholera burden, deepening humanitarian crisis. Available from: https://news.un.org/en/story/2024/12/1158491

168. Ibrahim AA. What Lifting U.S. Sanctions Means for Syria's Transition [Internet]. Harvard University: Belfer Center for Science and International Affairs; 2025 [cited 2026 Apr 8]. Available from: https://www.belfercenter.org/research-analysis/what-lifting-us-sanctions-means-syrias-transition

169. World Bank. The Syrian conflict: Physical damage and reconstruction assessment report [Internet]. Washington DC: World Bank Group; 2025 Aug [cited 2026 Apr 8]. Available from: https://www.worldbank.org/en/news/press-release/2025/10/21/syria-s-post-conflict-reconstruction-costs-estimated-at-216-billion

170. Constantin de Magny G, Colwell RR. Cholera and climate: A demonstrated relationship. Trans Am Clin Climatol Assoc. 2009;120:119–28. PubMed PMID: 19768169; PubMed Central PMCID: PMC2744514.

171. Garry S, Checchi F. Armed conflict and public health: into the 21st century. J Public Health (Oxf). 2020 Aug 18;42(3):e287–98. doi:10.1093/pubmed/fdz095

172. United Nations Environment Program. Environmental impact of the conflict in Gaza: Preliminary assessment of environmental impacts [Internet]. Nairobi; 2024. Available from: https://wedocs.unep.org/rest/api/core/bitstreams/241fbead-4f28-4c11-8451-894d62218de3/content

173. Wang Z, Shrestha RM, Román MO, Kalb VL. NASA's Black Marble multiangle nighttime lights temporal composites. IEEE Geoscience and Remote Sensing Letters. 2022;19:1–5. doi:10.1109/LGRS.2022.3176616

174. Iddawela Y. Not all nightlight datasets are the same: Introducing NASA’s Black Marble dataset [Internet]. 2023 [cited 2025 Mar 6]. Available from: https://www.spatialedge.co/p/not-all-nightlight-datasets-are-the

175. IOM. Annual DTM Report on Displacement 2023 [Internet]. International Organization for Migration Displacement Tracking Matrix; 2024 Apr. Available from: https://dtm.iom.int/reports/yemen-annual-dtm-report-displacement-2023

APPENDIX ONE: Chapter Two

Model equations and results

Model A

cases = f_1*(popDensLog)* + f_2*(week)* + f_3*(lat, lon)* + β_1*(severity$_{interm}$)* + β_2*(severity$_{medium}$)* + β_3*(severity$_{high}$)* + β_4*(severity$_{severe}$)*

where f_{1-3} are smooth functions estimated by the model using restricted maximum likelihood.

Model B

cases = f_1*(popDensLog)* + f_2*(week)* + f_3*(lat, lon)* + β_1*(severity$_{interm}$)* + β_2*(severity$_{medium}$)* + β_3*(severity$_{high}$)* + β_4*(severity$_{severe}$)* + β_5*(precip)* + β_6*(surf_wat)* + β_7*(temp)* + β_8*(NDVI)*

where f_{1-3} are smooth functions estimated by the model using restricted maximum likelihood.

Model C (Final Model)

cases = f_1*(popDensLog)* + f_2*(week)* + f_3*(lat, lon)* + β_1*(severity$_{interm}$)* + β_2*(severity$_{medium}$)* + β_3*(severity$_{high}$)* + β_4*(severity$_{severe}$)* + β_5*(precip)* + β_6*(surf_wat)* + β_7*(temp)* + β_8*(NDVI)* + f_4*(PC1)*

where f_{1-4} are smooth smooth functions estimated by the model using restricted maximum likelihood. PC1 is the economic principal component and lat, lon is an interaction term between the latitudes and longitudes derived from each centroid.

The results for the linear variables of each model are shown in the manuscript (**Table 2**) and in the forest plot below (**Figure S1.1**), and the spline outputs are shown in **Figures S1.2**–**S1.3**. The latitude and longitude interaction for the final model is shown in **Figure S1.4** (the remainder of the splines are located in the main text).

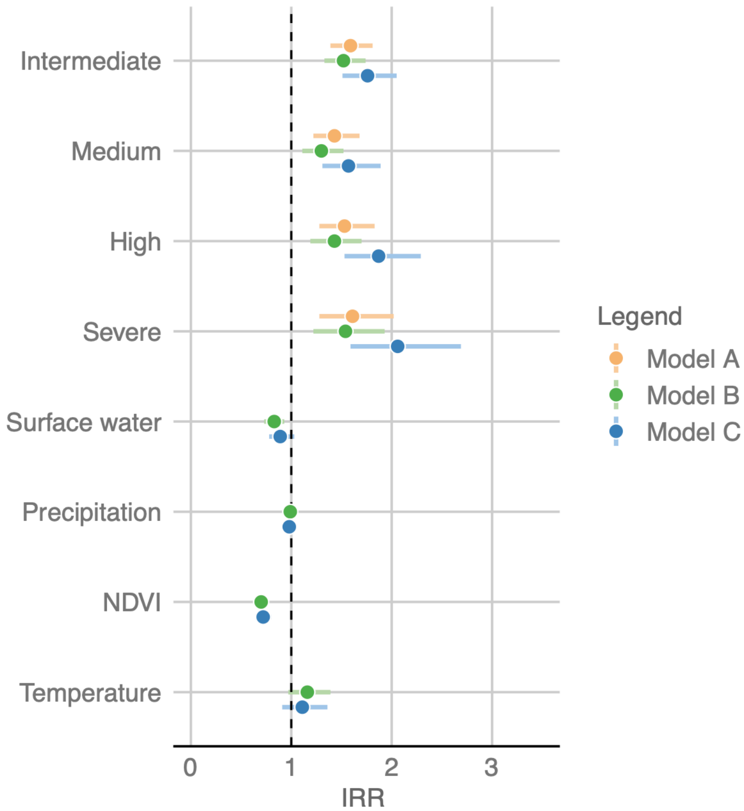

Figure S1.1: A forest plot showing the results of the linear variables in Models A-C, where A is the base model and C is the final model

The AIC (Akaike Information Criterion) for Model A was 36,826.77, Model B had an AIC of 36,787.85, and the final model (Model C) had an AIC of 30,240.97.

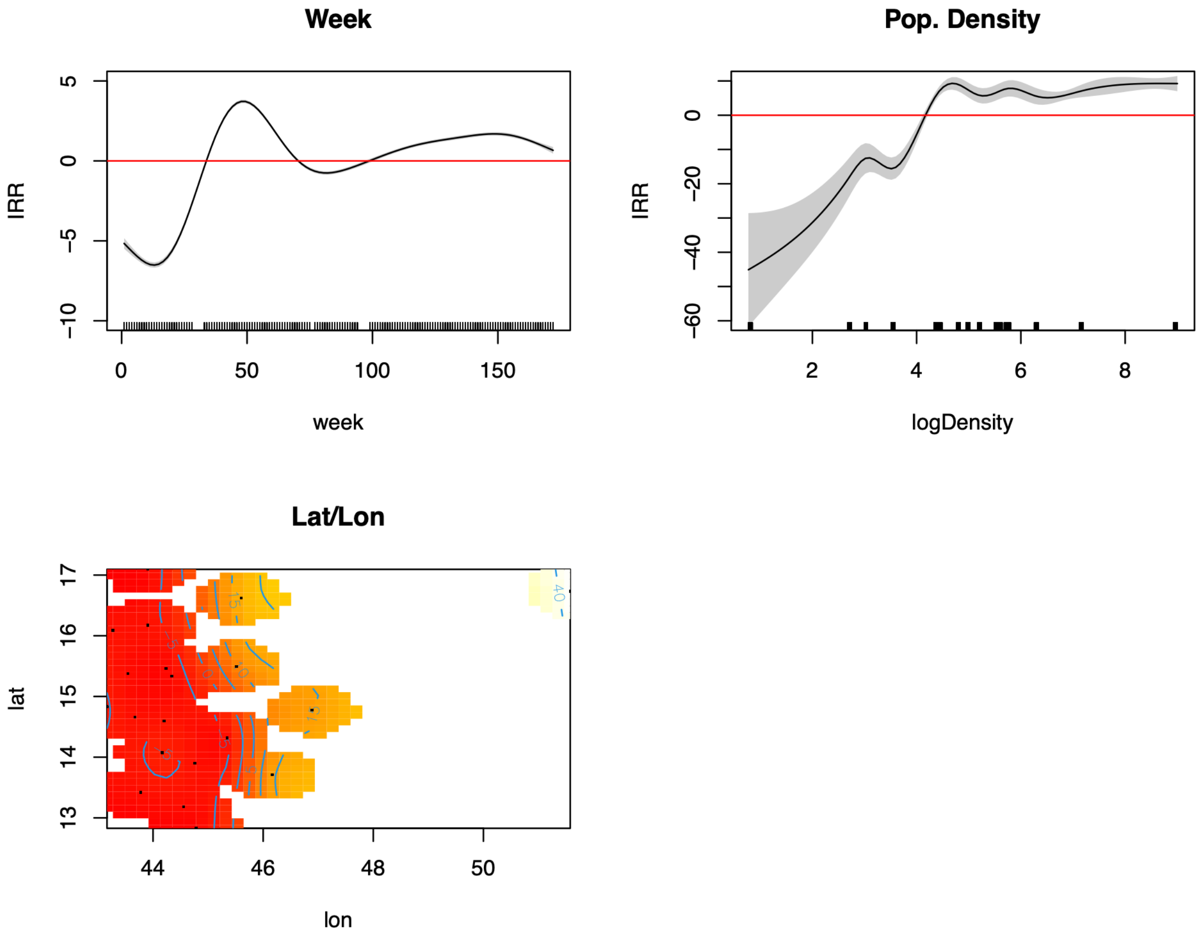

Figure S1.2: Spline outputs from **Model A** for week, population density, and the interaction between the latitude and longitude of the geometric centroids

The red lines can be used to measure significance, whereby the output is significant at values when the solid line and grey areas are all either above or below the line. The grey areas indicate the 95% confidence intervals. In the latitude/longitude interaction, reds indicate geographical areas with less risk of cholera and yellows indicate areas with higher risk, after controlling for other variables in the model. The large gap in the figure is due to missing data from Hadramawt governorate.

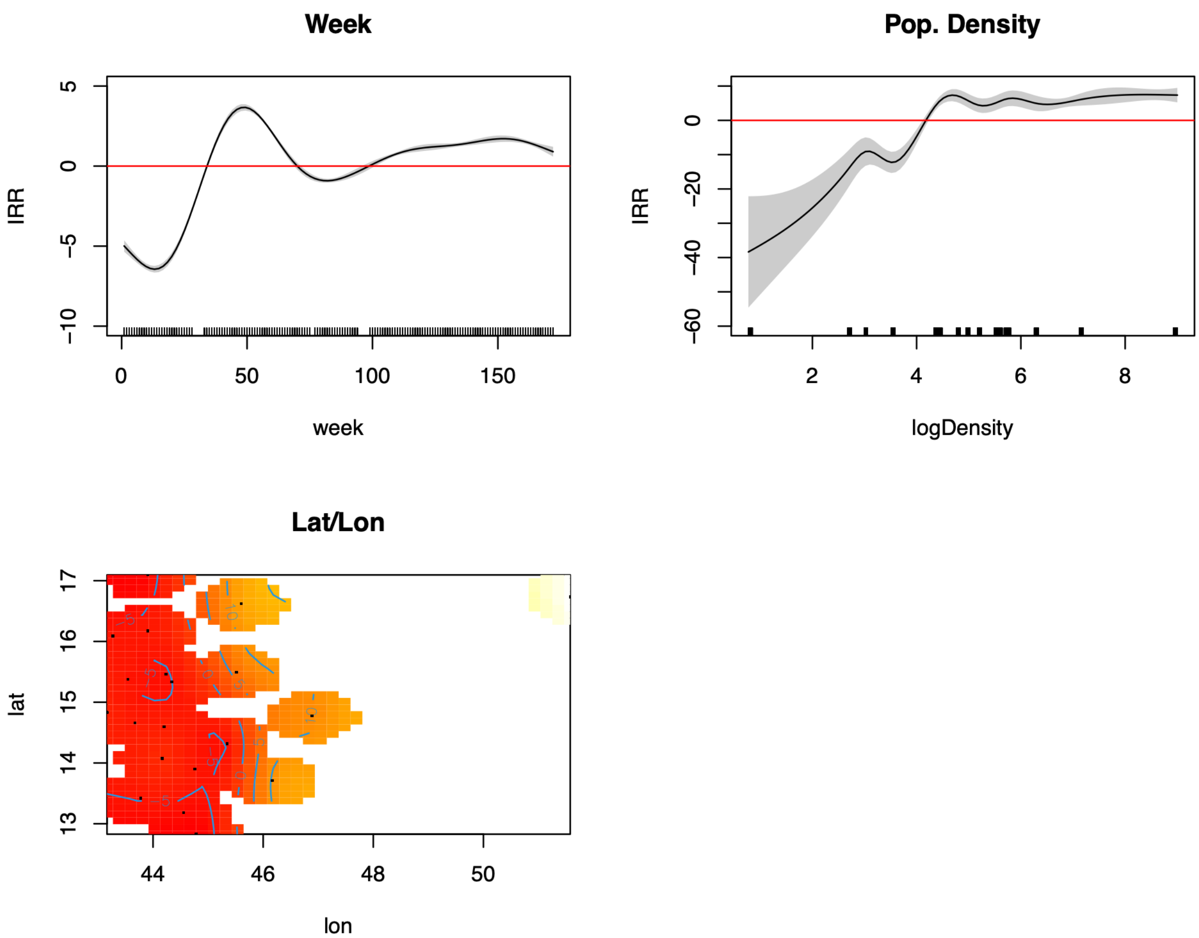

Figure S1.3: Spline outputs from **Model B** for week, population density, and the interaction between the latitude and longitude of the geometric centroids

The red lines can be used to measure significance, whereby the output is significant at values when the solid line and grey areas are all either above or below the line. The grey areas indicate the 95% confidence intervals. In the latitude/longitude interaction, reds indicate geographical areas with less risk of cholera and yellows indicate areas with higher risk, after controlling for other variables in the model. The large gap in the figure is due to missing data from Hadramawt governorate.

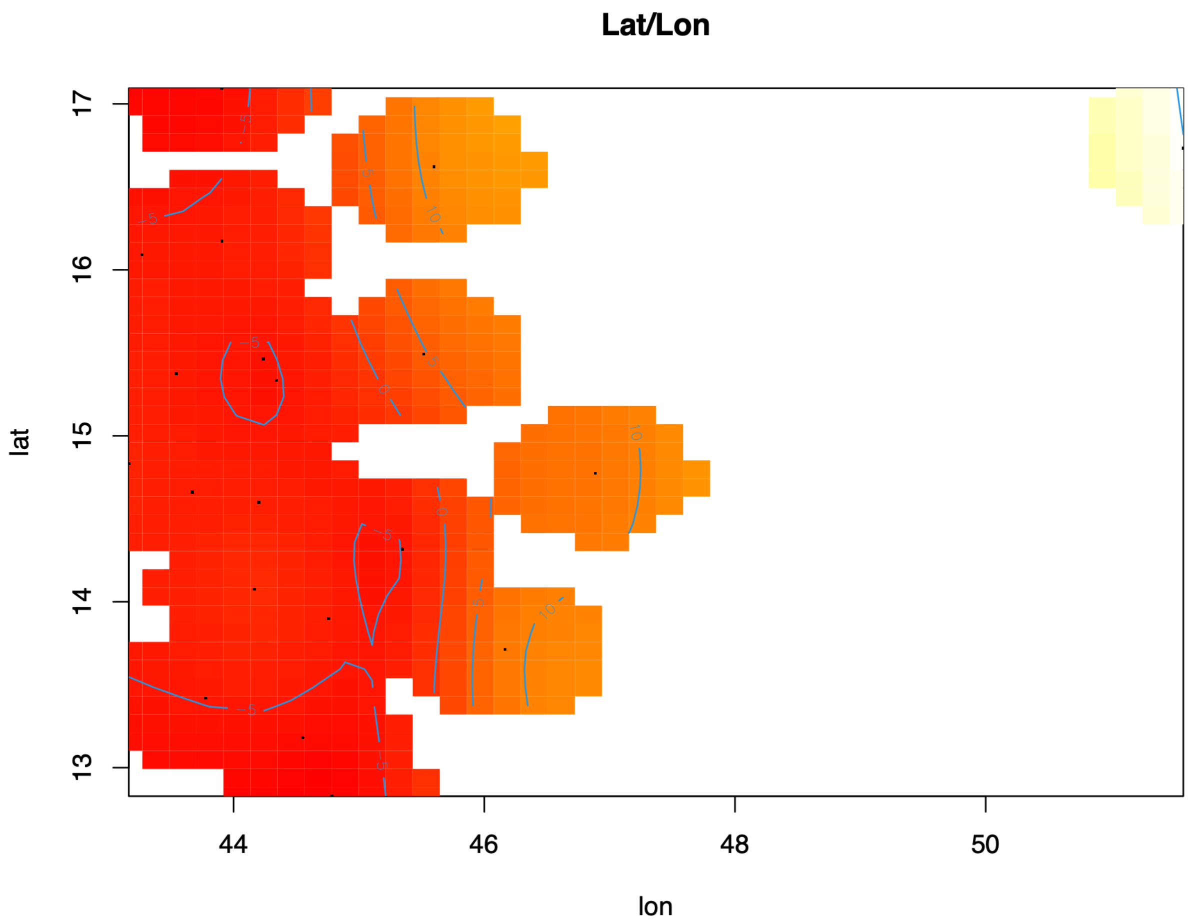

Figure S1.4: The interaction between the latitude and longitudes of each governorate's geometric centroid for **Model C**, the final model

The reds indicate geographical areas with less risk of cholera and yellows indicate areas with higher risk, after controlling for other variables in the model. The large gap in the figure is due to missing data from Hadramawt governorate.

Additional variables

In addition to the variables discussed in the Methods, we pulled several other variables that were ultimately not included in the model due to overfitting and concurvity. This included the governorate-level monthly minimum and maximum observed temperature from the World Bank Group's Climate Change Knowledge Portal. These observations were used to calculate a temperature range for each governorate. Data extracted on governorate-level elevation (mean and range values) were also not included in the final model. The digital elevation model (DEM) for each governorate was extracted from NASA's Shuttle Radar Topography Mission DEM; from the DEM, we calculated the mean elevation and elevation range of each governorate. This remained a constant throughout the period of study. To account for spatial effects and differences in baseline cholera risk, we also initially included a random intercept for each governorate in our model. Ultimately, these variables all had high concurvity with the latitude/longitude interaction and were excluded from the final model. The original non-reduced model was as follows:

$$cases = \beta_0 + f_1(population) + f_2(week) + f_3(lat, lon) + \beta_1(severity_{interm}) + \beta_2(severity_{medium}) + \beta_3(severity_{high}) + \beta_4(severity_{severe}) + \beta_5(precip) + \beta_6(surf\_wat) + \beta_7(temp_{mean}) + \beta_8(NDVI) + \beta_9(DEM_{mean}) + \beta_{10}(DEM_{variance}) + \beta_{11}(temp_{range}) + f_4(PC1)$$

where $\beta_0$is the random governorate-level interecpt, f_{1-4} are smooth functions estimated by the model using restricted maximum likelihood. PC1 is the economic principal component and lat, lon is an interaction term between the latitudes and longitudes derived from each centroid.

After reducing the model, we initially set each variable (except severity, which was set as a categorical variable) as a spline so as to not assume linearity. Variables that appeared relatively linear as a spline were then set as linear in order to increase interpretability. The final model includes population density, week, an interaction between geometric centroid latitude and longitude, and the economic principal component as splines. We ran the final model both with and without a binary variable for Ramadan; the inclusion of this variable made no difference to the model.

Precipitation data sensitivity analysis

We ran our model using daily modelled precipitation data from the Climate Hazards Group Infrared Precipitation with Stations (CHIRPS) dataset and found no meaningful difference from our final model (**Table S1.1**).

Table S1.1: Results for sensitivity analysis using precipitation data from the CHIRPS dataset

	CHIRPS Data		**Original Model**	
	IRR (95% CI)	p value	IRR (95% CI)	p value
Air raid severity				
Low	1 (ref)		1 (ref)	
Intermediate	1.75 (1.50–2.04)	<0.0001	1.76 (1.51–2.05)	<0.0001
Medium	1.57 (1.30–1.89)	<0.0001	1.57 (1.31–1.89)	<0.0001
High	1.86 (1.52–2.28)	<0.0001	1.87 (1.53–2.29)	<0.0001
Severe	2.06 (1.58–2.68)	<0.0001	2.06 (1.59–2.69)	<0.0001
Environmental variables				
Surface water	0.89 (0.78–1.02)	0.106	0.89 (0.78–1.03)	0.11
Precipitation	1.00 (0.96–1.05)	0.812	0.98 (0.91–1.06)	0.69
NDVI	0.71 (0.64–0.79)	<0.0001	0.72 (0.64–0.80)	<0.0001
Temp (mean)	1.11 (0.91–1.35)	0.299	1.11 (0.91–1.36)	0.29
AIC	30,240.79		30,240.97	

Case data sensitivity analysis

We conducted a sensitivity analysis using cholera case data from the Emergency Operations Center (EOC), an alternative source of case data run by the Yemen Health Authorities. A repository with these case data for the study period can be found at Reference 65. The results are presented in **Table S1.2**. We cannot state whether the highest level is statistically different from the lowest, but the mid-levels are significant in each presented model. We interpret this as a non-linear effect. We believe that in places where air strikes are most severe people may flee (including healthcare workers), and this can lead to reductions in infections, diagnoses, and case reports. We discuss this further in our Discussion section and elsewhere in the Supplemental Materials.

Table S1.2: Results for sensitivity analysis using cholera case data from the EOC dataset

	EOC Data		Original Model	
	IRR (95% CI)	p value	IRR (95% CI)	p value
Air raid severity				
Low	1 (ref)		1 (ref)	
Intermediate	1.62 (1.33–1.96)	<0.0001	1.76 (1.51–2.05)	<0.0001
Medium	1.59 (1.26–2.01)	<0.0001	1.57 (1.31–1.89)	<0.0001
High	1.49 (1.16–1.90)	0.002	1.87 (1.53–2.29)	<0.0001
Severe	1.22 (0.88–1.69)	0.23	2.06 (1.59–2.69)	<0.0001
Environmental variables				
Surface water	0.92 (0.78–1.09)	0.34	0.89 (0.78–1.03)	0.11
Precipitation	0.86 (0.78–0.95)	0.005	0.98 (0.91–1.06)	0.69
NDVI	0.79 (0.69–0.91)	0.0009	0.72 (0.64–0.80)	<0.0001
Temp (mean)	1.48 (1.16–1.87)	0.001	1.11 (0.91–1.36)	0.29
AIC	35,392.16		30,240.97	

Model specification

We experimented with several different aggregations of air raids and time lags before settling on the final 3-month measure with no lag. These included monthly, 2-month, 6-month, and annual aggregations lagged at 0–4 weeks. The results for each are included in **Tables S1.3–S1.7**. Because there was no scientific or hypothesis-driven rationale for choosing a particular aggregation or lag, we chose the model with the lowest AIC value, indicating the best model fit. This was the 3-month aggregation with no lag. Interestingly, the effect size for high and severe air raids beings to decrease at 6-month and annual aggregations. We hypothesize that this is due to either a) long periods of high or severe conflict may result in large-scale displacement, therefore reducing the incidence and reporting of cholera in a governorate, and/or b) long periods of high or severe conflict may result in the destruction of health care centers or other surveillance facilities that would report cholera case numbers, leading to an underreporting in cases.

Table S1.3: Results for annual air raid aggregation and various lags

	No Lag		1 Week		2 Weeks	
	IRR (95% CI)	p value	IRR (95% CI)	p value	IRR (95% CI)	p value
Air raid severity						
Low	1 (ref)		1 (ref)		1 (ref)	
Intermediate	2.62 (2.13–3.22)	<0.0001	2.59 (2.10–3.19)	<0.0001	2.59 (2.10–3.19)	<0.0001
Medium	2.17 (1.73–2.72)	<0.0001	2.07 (1.65–2.60)	<0.0001	2.04 (1.62–2.56)	<0.0001
High	1.44 (1.10–1.89)	0.009	1.40 (1.07–1.85)	0.02	1.33 (1.01–1.76)	0.04
Severe	1.58 (1.14–2.20)	0.006	1.50 (1.08–2.09)	0.02	1.46 (1.05–2.05)	0.03
Environmental factors						
Surface water	0.90 (0.79–1.03)	0.14	0.90 (0.79–1.03)	0.13	0.90 (0.78–1.03)	0.12
Precipitation	1.02 (0.94–1.10)	0.70	1.02 (0.94–1.10)	0.67	1.02 (0.94–1.10)	0.69
NDVI	0.64 (0.57–0.71)	<0.0001	0.64 (0.57–0.71)	<0.0001	0.64 (0.57–0.71)	<0.0001
Temp (mean)	1.10 (0.90–1.34)	0.34	1.10 (0.90–1.34)	0.35	1.10 (0.90–1.34)	0.35
AIC	30,290.22		30,290.42		30,286.97	

	3 Weeks		4 Weeks	
	IRR (95% CI)	p value	IRR (95% CI)	p value
Air raid severity				
Low	1 (ref)		1 (ref)	
Intermediate	2.61 (2.12–3.21)	<0.0001	2.63 (2.14–3.24)	<0.0001
Medium	2.10 (1.67–2.64)	<0.0001	2.00 (1.59–2.52)	<0.0001
High	1.35 (1.02–1.78)	0.03	1.33 (1.00–1.75)	0.047
Severe	1.47 (1.06–2.05)	0.02	1.42 (1.02–1.98)	0.04
Environmental variables				
Surface water	0.90 (0.79–1.03)	0.12	0.90 (0.78–1.03)	0.11
Precipitation	1.01 (0.94–1.10)	0.71	1.02 (0.94–1.10)	0.71
NDVI	0.64 (0.58–0.71)	<0.0001	0.64 (0.58–0.71)	<0.0001
Temp (mean)	1.10 (0.90–1.34)	0.35	1.10 (0.90–1.34)	0.35
AIC	30,283.54		30,279.79	

Table S1.4: Results for 6-month air raid aggregation and various lags

	No Lag		1 Week	
	IRR (95% CI)	p value	IRR (95% CI)	p value
Air raid severity				
Low	1 (ref)		1 (ref)	
Intermediate	1.43 (1.20–1.70)	<0.0001	1.40 (1.18–1.68)	0.0002
Medium	1.27 (1.04–1.56)	0.02	1.31 (1.07–1.60)	0.01
High	1.51 (1.20–1.90)	0.0005	1.47 (1.17–1.85)	0.001
Severe	1.53 (1.14–2.04)	0.004	1.47 (1.10–1.97)	0.01
Environmental variables				
Surface water	0.89 (0.77–1.02)	0.08	0.88 (0.77–1.01)	0.07
Precipitation	1.00 (0.93–1.09)	0.91	1.00 (0.93–1.09)	0.91
NDVI	0.71 (0.64–0.80)	<0.0001	0.71 (0.63–0.80)	<0.0001
Temp (mean)	1.16 (0.95–1.41)	0.15	1.15 (0.94–1.40)	0.17
AIC	30,282.35		30,286.29	

Table S1.5: Results for 3-month air raid aggregation and various lags

	No Lag		1 Week		2 Weeks	
	IRR (95% CI)	p value	IRR (95% CI)	p value	IRR (95% CI)	p value
Air raid severity						
Low	1 (ref)		1 (ref)		1 (ref)	
Intermediate	1.76 (1.51–2.05)	<0.0001	1.73 (1.48–2.02)	<0.0001	1.70 (1.45–1.98)	<0.0001
Medium	1.57 (1.31–1.89)	<0.0001	1.56 (1.29–1.87)	<0.0001	1.57 (1.30–1.89)	<0.0001
High	1.87 (1.53–2.29)	<0.0001	1.82 (1.48–2.23)	<0.0001	1.69 (1.38–2.08)	<0.0001
Severe	2.06 (1.59–2.69)	<0.0001	1.97 (1.51–2.57)	<0.0001	1.81 (1.39–2.36)	<0.0001
Environmental factors						
Surface water	0.89 (0.78–1.03)	0.11	0.89 (0.78–1.02)	0.10	0.88 (0.77–1.01)	0.08
Precipitation	0.98 (0.91–1.06)	0.69	0.98 (0.91–1.06)	0.65	0.98 (0.91–1.06)	0.63
NDVI	0.72 (0.64–0.80)	<0.0001	0.72 (0.64–0.80)	<0.0001	0.71 (0.64–0.80)	<0.0001
Temp (mean)	1.11 (0.91–1.36)	0.29	1.13 (0.92–1.37)	0.24	1.11 (0.91–1.36)	0.28
AIC	30,240.97		30,247.25		30,257.12	

	3 Weeks		4 Weeks	
	IRR (95% CI)	p value	IRR (95% CI)	p value
Air raid severity				
Low	1 (ref)		1 (ref)	
Intermediate	1.67 (1.43–1.95)	<0.0001	1.63 (1.40–1.91)	<0.0001
Medium	1.54 (1.28–1.86)	<0.0001	1.53 (1.27–1.84)	<0.0001
High	1.69 (1.37–2.08)	<0.0001	1.67 (1.36–2.06)	<0.0001
Severe	1.70 (1.30–2.22)	0.0001	1.67 (1.28–2.18)	0.0002
Environmental variables				
Surface water	0.88 (0.77–1.01)	0.08	0.89 (0.78–1.02)	0.09
Precipitation	0.98 (0.91–1.06)	0.68	0.99 (0.92–1.07)	0.79
NDVI	0.71 (0.63–0.79)	<0.0001	0.70 (0.63–0.79)	<0.0001
Temp (mean)	1.11 (0.91–1.35)	0.32	1.10 (0.90–1.34)	0.36
AIC	30,257.40		30,259.64	

Table S1.6: Results for 2-month air raid aggregation and various lags

	No Lag		1 Week	
	IRR (95% CI)	p value	IRR (95% CI)	p value
Air raid severity				
Low	1 (ref)		1 (ref)	
Intermediate	1.20 (1.03–1.40)	0.02	1.34 (1.15–1.56)	0.0001
Medium	1.22 (1.04–1.44)	0.01	1.32 (1.12–1.55)	0.0009
High	1.46 (1.22–1.76)	<0.0001	1.62 (1.35–1.94)	<0.0001
Severe	1.51 (1.18–1.92)	0.001	1.56 (1.22–1.99)	0.0004
Environmental variables				
Surface water	0.89 (0.77–1.02)	0.09	0.89 (0.78–1.02)	0.10
Precipitation	1.02 (0.94–1.10)	0.61	1.01 (0.93–1.09)	0.87
NDVI	0.72 (0.64–0.80)	<0.0001	0.72 (0.64–0.81)	<0.0001
Temp (mean)	1.13 (0.93–1.38)	0.22	1.13 (0.93–1.38)	0.21
AIC	30,274.61		30,261.25	

Table S1.7: Results for 1-month air raid aggregation and various lags

	No Lag		1 Week	
	IRR (95% CI)	p value	IRR (95% CI)	p value
Air raid severity				
Low	1 (ref)		1 (ref)	
Intermediate	1.00 (0.84–1.19)	1.00	1.02 (0.86–1.21)	0.82
Medium	1.06 (0.92–1.22)	0.41	1.12 (0.97–1.28)	0.12
High	1.14 (0.97–1.34)	0.12	1.17 (0.99–1.38)	0.07
Severe	1.21 (0.97–1.52)	0.09	1.19 (0.95–1.49)	0.13
Environmental variables				
Surface water	0.89 (0.77–1.02)	0.08	0.89 (0.77–1.02)	0.09
Precipitation	1.03 (0.95–1.11)	0.52	1.02 (0.95–1.11)	0.56
NDVI	0.71 (0.63–0.79)	<0.0001	0.71 (0.64–0.80)	<0.0001
Temp (mean)	1.14 (0.94–1.39)	0.19	1.13 (0.93–1.38)	0.22
AIC	30,293.00		30,291.56	

Model stratified by time

In order to assess changes in covariate effects over time, we divided the time series into three equal parts to create a time-stratified model (**Table S1.8**). We find that the association with air raids is significant across the final two-thirds of the time series. We hypothesize that we do not see the significant association in the first third because of power loss and because these smaller time units do not allow for the effect of air raids to accumulate, which would most heavily affect the first time period (we discuss this cumulative effect in our Discussion section). It is also to be expected that the exact associations would vary over time, though as this is an ecological study over the total outbreak period, we aim to assess the associations over the course of the outbreak.

Table S1.8: Results for time-stratified model

	Weeks 1–57		Weeks 58–114		Weeks 115–172	
	IRR (95% CI)	p value	IRR (95% CI)	p value	IRR (95% CI)	p value
Air raid severity						
Low	1 (ref)		1 (ref)		1 (ref)	
Intermediate	1.20 (0.95–1.53)	0.13	1.78 (1.40–2.27)	<0.0001	1.53 (1.32–1.78)	<0.0001
Medium	1.08 (0.74–1.56)	0.69	1.55 (1.08–2.24)	0.02	1.42 (1.19–1.70)	<0.0001
High	0.86 (0.54–1.35)	0.51	1.89 (1.25–2.88)	0.003	2.23 (1.78–2.80)	<0.0001
Severe	0.57 (0.32–1.02)	0.06	3.48 (2.07–5.87)	<0.0001	2.11 (1.51–2.94)	<0.0001
Environmental factors						
Surface water	0.84 (0.64–1.09)	0.19	0.80 (0.64–0.99)	0.04	1.10 (0.96–1.26)	0.19
Precipitation	0.98 (0.82–1.16)	0.78	1.19 (1.19–1.59)	<0.0001	0.96 (0.87–1.05)	0.33
NDVI	0.65 (0.52–0.80)	<0.0001	0.57 (0.47–0.69)	<0.0001	1.07 (0.95–1.20)	0.25
Temp (mean)	1.52 (1.04–2.22)	0.03	1.02 (0.75–1.40)	0.89	1.26 (0.98–1.63)	0.08

Links to data sources

Case and population: https://www.mdpi.com/1660-4601/19/1/378 (data can be downloaded in the Supplemental Material)

Area: https://yemenlg.org/governorates/ (acc. December 14, 2022)

Air raids: https://yemendataproject.org/ (acc. June 28, 2022)

Precipitation and temperature: https://climateknowledgeportal.worldbank.org/ (acc. August 12, 2022)

Surface water and NDVI: https://modis.gsfc.nasa.gov/data/ (acc. August 15, 2022) and downloaded via NASA's Application for Extracting and Exploring Analysis Ready Samples: https://appeears.earthdatacloud.nasa.gov/

Economic variables:

2019: https://www.wfp.org/publications/yemen-monthly-market-watch-2019 (acc. 17 Oct. 2022)

2018: https://www.wfp.org/publications/yemen-monthly-market-watch-2018 (acc. 17 Oct. 2022)

2017: https://www.wfp.org/publications/yemen-monthly-market-watch-2017 (acc. 17 Oct. 2022)

2016: https://www.wfp.org/publications/yemen-monthly-market-watch-2016 (acc. 17 Oct. 2022)

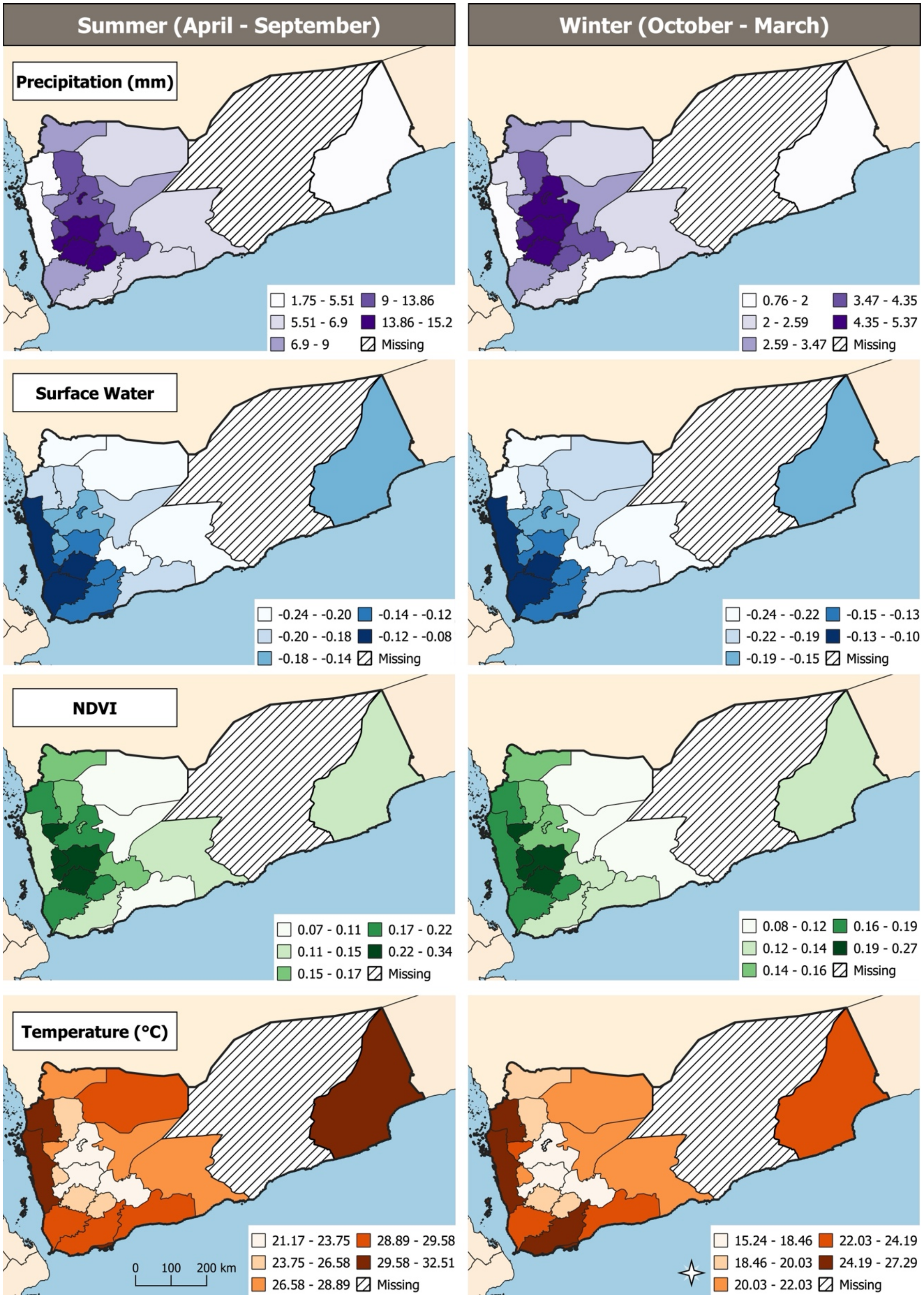

Figure S1.5: Choropleth maps of mean precipitation (mm), surface water, NDVI, and temperature (°C) in the winter and summer seasons over the study period

Missingness test

To assess the potential impact of missing cholera case on our results, we ran two sensitivity analyses for periods of time without any missing data: weeks 38–75 and 99–172 (**Table S1.9**). The results were in line with our full model results, indicating that cholera case missingness likely did not significantly impact the model.

Table S1.9: Results for 1-month air raid aggregation and various lags

	Weeks 38–75		Weeks 99–172	
	IRR (95% CI)	p value	IRR (95% CI)	p value
Air raid severity				
Low	1 (ref)		1 (ref)	
Intermediate	1.07 (0.82–1.40)	0.63	1.45 (1.27–1.65)	<0.0001
Medium	1.78 (1.20–2.65)	0.004	1.41 (1.20–1.65)	<0.0001
High	2.19 (1.38–3.50)	0.001	1.86 (1.54–2.25)	<0.0001
Severe	1.38 (0.78–2.45)	0.26	1.63 (1.23–2.18)	0.0008
Environmental variables				
Surface water	1.00 (0.73–1.35)	0.98	1.01 (0.91–1.13)	0.82
Precipitation	1.04 (0.88–1.22)	0.65	1.01 (0.94–1.09)	0.82
NDVI	0.49 (0.40–0.61)	<0.0001	1.03 (0.93–1.13)	0.57
Temp (mean)	1.19 (0.88–1.61)	0.27	1.14 (0.93–1.40)	0.22

Figure S1.6: Map of Yemen with governorates labeled

APPENDIX TWO: Chapter Three

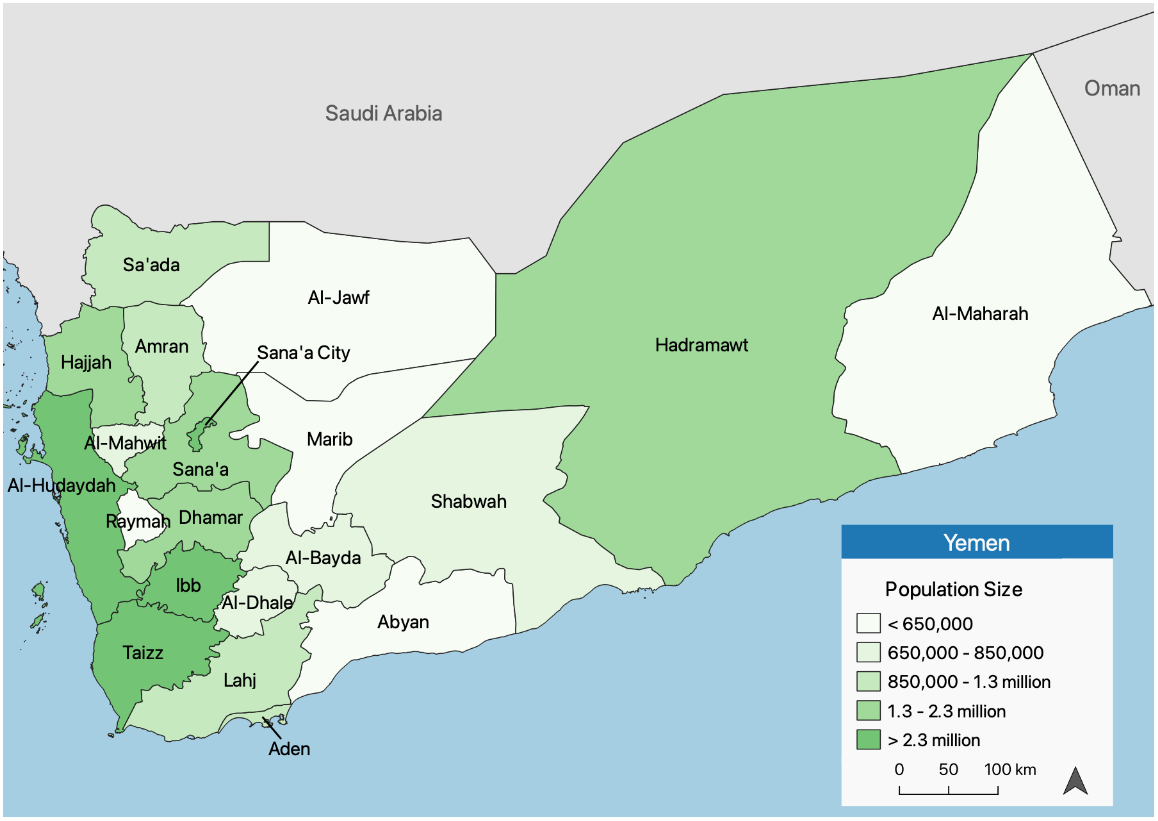

Figure S2.1: Map of Yemen with mean estimated population size over the study period
Map made in QGIS v3.34

Figure S2.2: Map of Ukraine with mean estimated population size over the study period
Map made in QGIS v3.34

Comparison of view angles

Black Marble provides monthly NTL data generated from three view zenith angle (VZA) categories: near-nadir, off-nadir, and all-angles. Near-nadir composites utilize high-quality observations at VZA ≤ 20° (directly above), and off-angle composites utilize observations at VZA ≥ 40° (at an angle). All-angles composites are derived from all angular observations (i.e., a combination of near-nadir and off-nadir data) (173,174). Prior work indicates that each angle detects different luminosity levels (which may in part reflect different sources of light emission) and have varying stability (173,174). For this study, we chose to use the all-angles dataset as it is a middle ground in both radiance and stability compared to other view angles. This is especially relevant as we were not attempting to detect radiance from specific light sources and had a large overall spatial scale. All Black Marble data were extracted using *blackmarbleR* in R v.4.4.2 (90).

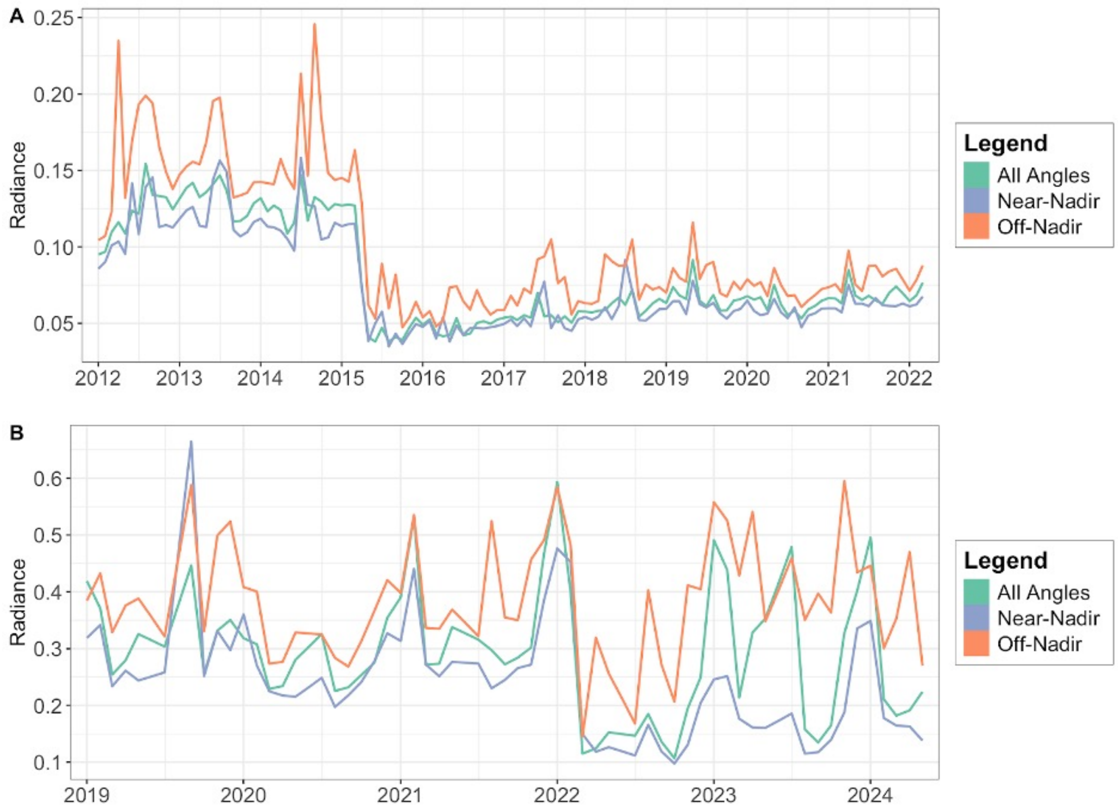

Figure S2.3: Plot of available view zenith angles for NASA Black Marble in Yemen (A) and Ukraine (B)

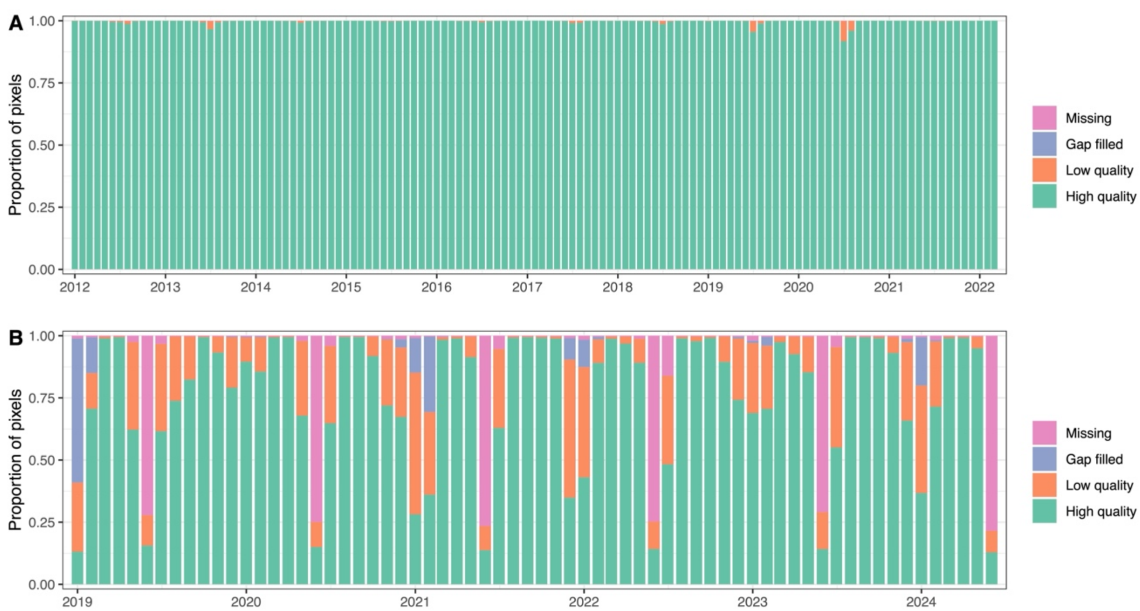

Figure S2.4: Data quality and completeness of monthly NTL data for Yemen (A) and Ukraine (B)

Black Marble defines high-quality pixels as those informed by more than 3 observations, and low-quality pixels as those with 3 or fewer observations. Gap-filled pixels are based on historical data. In Ukraine, the large variability in quality and missingness likely stems from seasonality (i.e., fewer snow-free observations in winter months to inform the composite) and Black Marble's stray light correction protocols in northern latitudes. Given this reported missingness in the summer months, we interpolated those NTL values for analysis.

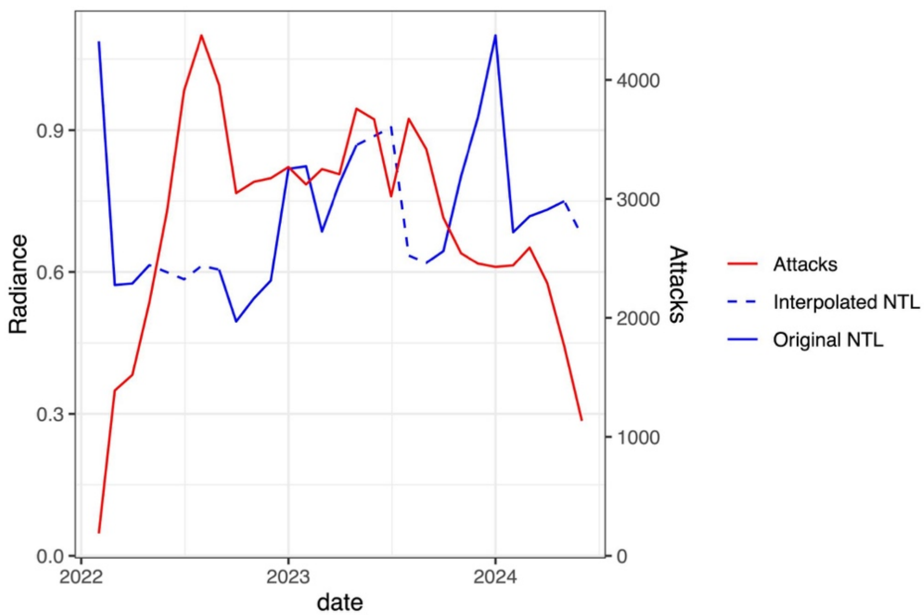

Figure S2.5: Comparison of original mean NTL time series, interpolated data, and total number of aerial attacks in Ukraine

Table S2.1: Outputs of sensitivity analysis without NTL interpolation

	Mean NTL		NTL Ratio	
	β (95% CI)	% change in outcome (95% CI)	β (95% CI)	% change in outcome (95% CI)
Ukraine				
Aerial attacks				
None	Comparison		Comparison	
1 – 2	0.693 (0.581, 0.827)	-30.69% (-41.93%, -17.27%)	0.758 (0.646, 0.890)	-24.20% (-35.41%, -11.04%)
3 – 6	0.73 (0.598, 0.907)	-26.34% (-40.17%, -9.30%)	0.798 (0.661, 0.963)	-20.18% (-33.87%, -3.66%)
7–117	0.541 (0.414, 0.708)	-45.86% (-58.61%, -29.18%)	0.628 (0.495, 0.797)	-37.18% (-50.48%, -20.32%)
118 +	0.290 (0.203, 0.414)	-71.01% (-79.68%, -58.65%)	0.401 (0.294, 0.547)	-59.92% (-70.61%, -45.34%)

NTL values in June–August of each year were left as missing (NA). These outputs do not meaningfully differ from those with interpolation.

Secondary population analysis

As a secondary analysis, we ran GAMs to measure the association between mean NTL and population size (as the response variable) in each administrative unit; these also included light recovery. This was primarily done to assess whether, in the absence of reliable population data, NTL could provide estimates of relative population size. The following GAMs were run using the *mgcv* package in R:

Yemen

$pop = f_1(month) + f_2(perc\_built) + f_3(NTL_{mean}) + f_4(recovery) + \beta_1(attacks_{low}) + \beta_2(attacks_{medium}) + \beta_3(attacks_{high}) + \beta_4(attacks_{severe}) + f_5(lat,lon)$

Where percentage built (*perc_built*), mean NTL (NTL_{mean}), and light recovery (*recovery*) were log-transformed and f_{1-5} are smooth functions estimated by the model using restricted maximum likelihood. Study month (*month*) was modeled using a cyclic cubic regression spline, centroid latitude and longitude (*lat,lon*) using two-dimensional splines on a sphere, and all others with thin plate regression splines. Aerial attack categories were defined as none (0 attacks), low (1–4), medium (5–12), high (13–35), and severe (36+). None was used as the reference category. Light recovery was originally tried as an interaction term with time since light nadir, but the interaction term was not meaningful and therefore not included.

Ukraine

$$pop = f_1(month) + f_2(NTL_{mean}) + f_3(recovery) + \beta_1(attacks_{low}) + \beta_2(attacks_{medium}) + \beta_3(attacks_{high}) + \beta_4(attacks_{severe}) + f_4(lat,lon)$$

Where mean NTL (NTL_{mean}) and light recovery (*recovery*) were log-transformed and f_{1-4} are smooth functions estimated by the model using restricted maximum likelihood. Study month (*month*) was modeled using a cyclic cubic regression spline, centroid latitude and longitude (*lat,lon*) using two-dimensional splines on a sphere, and all others with thin plate regression splines. Aerial attack categories were defined as none (0 attacks), low (1–2), medium (3–6), high (7–117), and severe (118+). None was used as the reference category. Light recovery was originally tried as an interaction term with time since light nadir, but the interaction term was not meaningful and therefore not included.

We found that NTL was positively associated with governorate and oblast population size. Conversely, recovery had a near-linear negative association with population size in both countries (**Figure S2.6**).

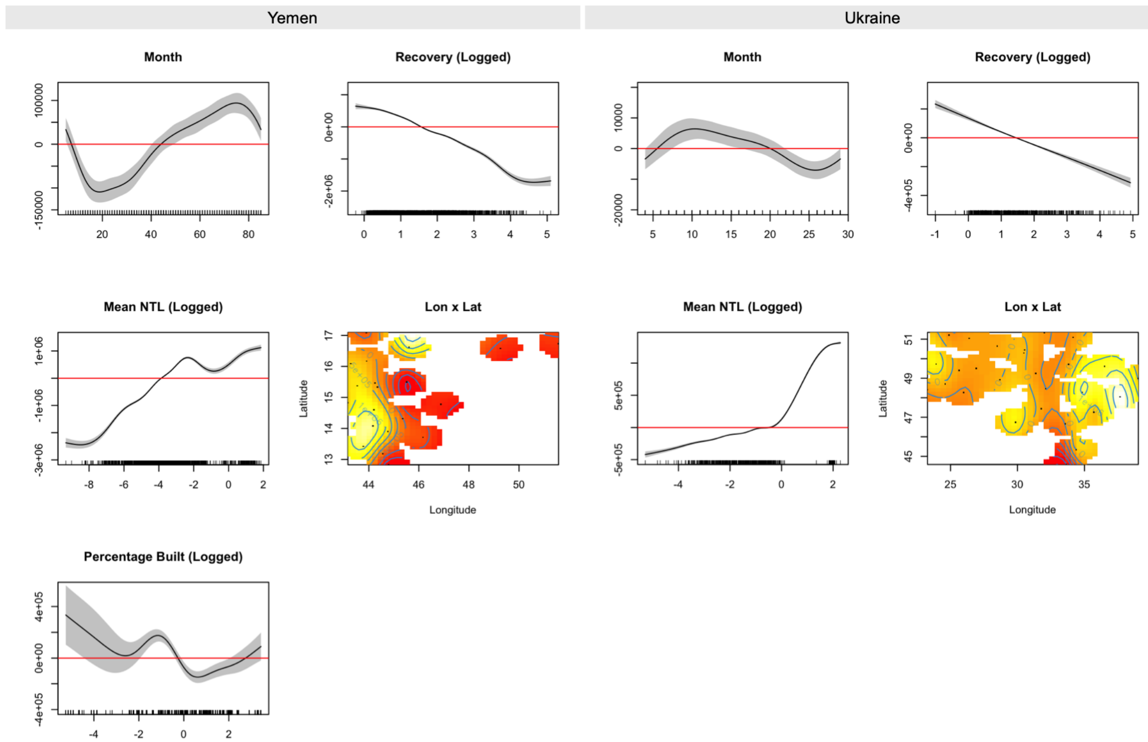

Figure S2.6: Spline outputs for the NTL and population size GAMs for Yemen and Ukraine
The output is considered significant when the black line and gray shaded areas (95% CIs) are entirely above or below the red horizontal line. In interaction plots, yellows indicate higher population size and reds indicate lower population size.

In both countries, administrative units with more attacks had higher population levels, indicating that highly populated areas were more likely to be attacked (**Table S2.2**). Together with the spline outputs, this reflects that areas with higher population were unable to recover as strongly likely because they experienced more attacks.

Table S2.2: Linear outputs for the NTL and population size GAMs for Yemen and Ukraine

	Yemen	**Ukraine**
	β (95% CI)	β (95% CI)
Aerial attacks		
Low	27,933.00 (-722.20–56,688.20)	4,743.00 (-635.20–10,121.20)
Medium	60,374.00 (26,983.40–93,764.60)	1,248.00 (-5,555.20–8,051.20)
High	70,243.00 (31,666.30–108,819.70)	27,263.00 (16,140.00–38,386.00)
Severe	-9,722.00 (-52,485.30–33,041.30)	28,294.00 (12,604.20–43,983.80)

Sensitivity analysis of population size estimates

To address any concerns over potential endogeneity in our models, we ran sensitivity analyses using population estimates from Gridded Population of the World (GPW) in place of WorldPop estimates. WorldPop population estimates are informed by NTL data, though the exact scope and scale of NTL data use in the population estimates used in our analyses is unclear. GPW provides non-modeled population estimates that are based on historical census data and do not use NTL data; estimates are available every five years between 2000 and 2015. We ran the sensitivity analyses using the unadjusted and UN-adjusted estimates. To create annual measurements, we used two techniques: 1) applying the growth rate between 2015 and 2020 to all years between 2015 and 2022, and 2) applying the mean growth rate of the entire 2000–2015 period to all years between 2015 and 2022. This resulted in four population estimates for sensitivity analyses. Results for Yemen's NTL and aerial attacks model can be found in **Tables S2.3**–**S2.4**, and outputs for the secondary population estimate and NTL models are in **Table S2.5** and **Figures S2.7**–**S2.8**. There are no meaningful differences from the models that use WorldPop data, indicating that endogeneity is not a concern in our models. We have therefore opted to use WorldPop data in the main text because it is available annually and thus requires less interpolation.

Table S2.3: Outputs of sensitivity analysis showing the association between attacks and mean NTL

	Gridded Population of the World (unadj.)		Gridded Population of the World (adj.)	
	Interp. 1 (2015–20 growth rate)	Interp. 2 (Av. growth rate)	Interp. 1 (2015–20 growth rate)	Interp. 2 (Av. growth rate)
	β (95% CI)	β (95% CI)	β (95% CI)	β (95% CI)
Air raids				
Individual	0.997 (0.995, 0.999)	0.997 (0.995, 0.999)	0.997 (0.995, 0.999)	0.997 (0.995, 0.999)
Scaled	0.919 (0.874, 0.967)	0.919 (0.874, 0.967)	0.916 (0.872, 0.964)	0.918 (0.873, 0.965)
Diesel (10% change)	0.975 (0.963, 0.987)	0.975 (0.963, 0.987)	0.976 (0.964, 0.989)	0.975 (0.963, 0.987)
% change in outcome				
Air raids				
Individual	-0.31% (-0.49%, -0.12%)	-0.31% (-0.49%, -0.12%)	-0.32% (-0.51%, -0.14%)	-0.32% (-0.50%, -0.13%)
Scaled	-8.05% (-12.56%, -3.31%)	-8.05% (-12.56%, -3.31%)	-8.35% (-12.84%, -3.63%)	-8.22% (-12.71%, -3.49%)
Diesel (10% change)	-2.51% (-2.52%, -2.49%)	-2.51% (-2.52%, -2.49%)	-2.38% (-2.39%, -2.36%)	-2.49% (-2.51%, -2.47%)

These results can be compared to those in **Table 3**, which use WorldPop population estimates.

Table S2.4: Outputs of sensitivity analysis showing the association between attacks and NTL ratio

	Gridded Population of the World (unadj.)		Gridded Population of the World (adj.)	
	Interp. 1 (2015–20 growth rate)	Interp. 2 (Av. growth rate)	Interp. 1 (2015–20 growth rate)	Interp. 2 (Av. growth rate)
	β (95% CI)	β (95% CI)	β (95% CI)	β (95% CI)
Air raids				
Individual	0.996 (0.993, 0.998)	0.996 (0.993, 0.998)	0.995 (0.993, 0.998)	0.995 (0.993, 0.998)
Scaled	0.885 (0.829, 0.945)	0.885 (0.829, 0.945)	0.883 (0.827, 0.943)	0.884 (0.828, 0.944)
Diesel (10% change)	0.976 (0.960, 0.993)	0.976 (0.960, 0.993)	0.976 (0.960, 0.992)	0.976 (0.960, 0.993)
% change in outcome				
Air raids				
Individual	-0.45% (-0.69%, -0.21%)	-0.45% (-0.69%, -0.21%)	-0.46% (-0.70%, -0.22%)	-0.45% (-0.69%, -0.21%)
Scaled	-11.49% (-17.10%, -5.49%)	-11.49% (-17.10%, -5.49%)	-11.72% (-17.32%, -5.73%)	-11.59% (-17.20%, -5.60%)
Diesel (10% change)	-2.37% (-2.39%, -2.34%)	-2.37% (-2.39%, -2.34%)	-2.40% (-2.42%, -2.38%)	-2.37% (-2.40%, -2.35%)

These results can be compared to those in **Table 3**, which use WorldPop population estimates.

Table S2.5. Outputs of sensitivity analysis for the secondary NTL and population size models

	Gridded Population of the World (unadj.)		Gridded Population of the World (adj.)	
	Interp. 1 (2015–20 growth rate)	Interp. 2 (Av. growth rate)	Interp. 1 (2015–20 growth rate)	Interp. 2 (Av. growth rate)
Yemen				
Air raids				
Low	20,978.00	20,978.00	21,451.00	21,348.00
	(-8,429.84, 50,385.84)	(-8,429.84, 50,385.84)	(-7,641.28, 50,543.28)	(-8,295.04, 50,991.04)
Medium	55,972.00	55,971.00	58,309.00	57,234.00
	(21,752.36, 90,191.64)	(21,751.36, 90,190.64)	(24,444.12, 92,173.88)	(22,738.00, 91,730.00)
High	61,923.00	61,924.00	66,378.00	63,839.00
	(22,350.60, 101,495.40)	(22,351.60, 101,496.40)	(27,234.84, 105,521.20)	(23,951.04, 103,727.00)
Severe	-27,136.00	-27,135.00	-18,652.00	-25,093.00
	(-71,057.64, 16,785.64)	(-71,056.64, 16,786.64)	(-62,089.52, 24,785.52)	(-69,361.56, 19,175.56)
Ukraine				
Air raids				
Low	4,015.00	4,009.00	3,998.00	3,986.00
	(-451.84, 8,481.84)	(-520.56, 8,538.56)	(-464.92, 8,460.92)	(-535.72, 8,507.72)
Medium	1,096.00	1,136.00	1,129.00	1,151.00
	(-4,554.68, 6,746.68)	(-4,593.08, 6,865.08)	(-4,517.76, 6,775.76)	(-4,568.28, 6,870.28)
High	22,250.00	22,298.00	22,270.00	22,261.00
	(13,008.60, 31,491.40)	(12,929.20, 31,666.80)	(13,036.44, 31,503.56)	(12,907.88, 31,614.12)
Severe	23,930.00	23,895.00	23,977.00	23,908.00
	(10,894.04, 36,965.96)	(10,676.76, 37,113.24)	(10,950.84, 37,003.16)	(10,713.28, 37,102.72)

These results can be compared to those in **Table S2.2**, and spline outputs are shown in **Figures S2.7**–**S2.8**.

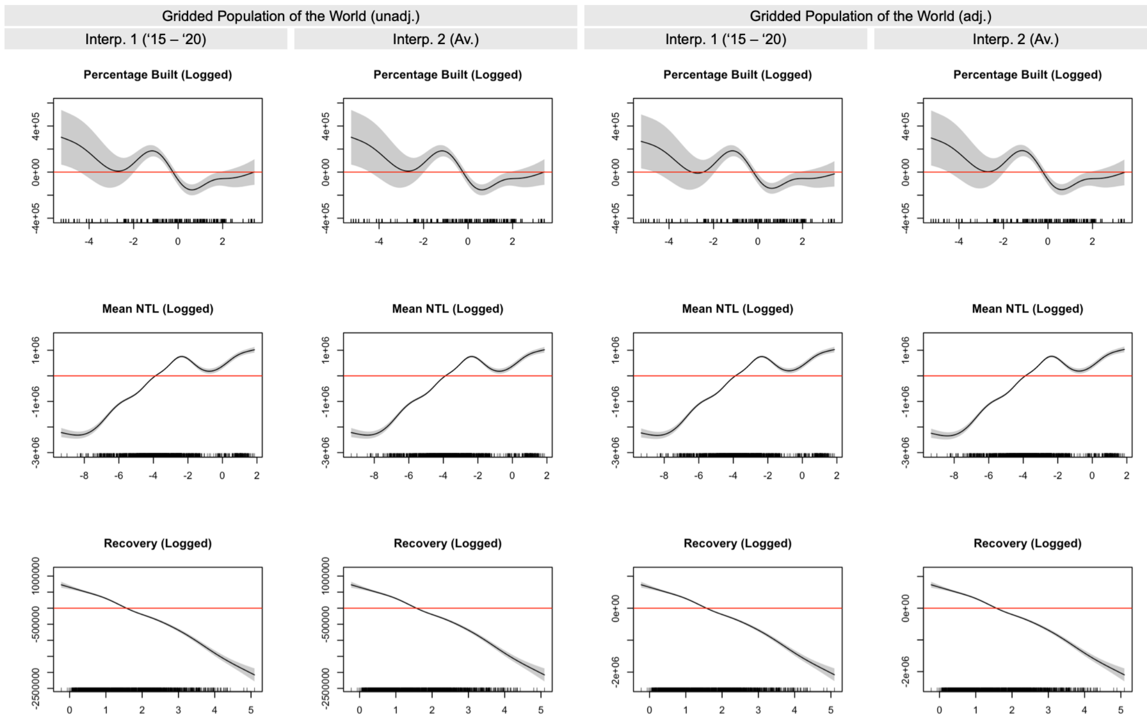

Figure S2.7: Select spline outputs for the NTL and population size sensitivity analysis for Yemen

The model also controls for month and location, though these are not shown for brevity; they are not meaningfully different from those shown in **Figure S2.6**. The output is considered significant when the black line and gray shaded areas (95% CIs) are entirely above or below the red horizontal line. The parametric outputs for these models are shown in **Table S2.5** and can be compared to the outputs from the model using WorldPop population estimates in **Figure S2.6** and **Table S2.2.**

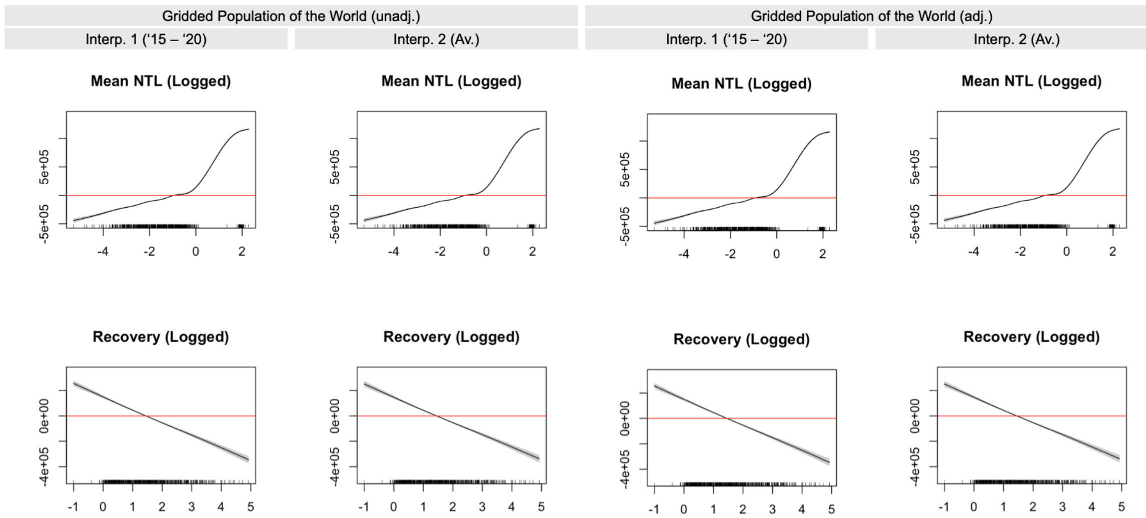

Figure S2.8: Select spline outputs for the NTL and population size sensitivity analysis for Ukraine

The model also controls for month and location, though these are not shown for brevity; they are not meaningfully different from those shown in **Figure S2.6**. The output is considered significant when the black line and gray shaded areas (95% CIs) are entirely above or below the red horizontal line. The parametric outputs for these models are shown in **Table S2.5** and can be compared to the outputs from the model using WorldPop population estimates in **Figure S2.6** and **Table S2.2**.

BFAST simulations

We used the Breaks for Additive Season and Trend (BFAST) change detection approach to identify negative breakpoints in the mean NTL time series for each administrative unit to assess whether the onset of attacks was evident in units' NTL signals. BFAST decomposes time series into seasonal, trend, and noise components while estimating the number, timing, magnitude, and direction of significant changes within them. To validate our use of BFAST, we simulated monthly NTL time series that were informed by the real data (see Methods for more detail). Parameters used in the simulations are in **Table S2.6,** and examples of the simulated time series are in **Figure S2.9.** Simulations were first run over all trend values while holding noise values for each period constant (**Figures S2.10–S2.11**). We then ran a second set of simulations that held the trend values for each period constant and ran over all noise values (**Figure S2.12–S2.13**). Importantly, the pre, peri, and post values for both trend and noise are quite similar in all the simulations, meaning there was often minimal signal in the data to detect change.

Table S2.6: Parameters used in BFAST simulations

	Yemen-Informed Simulations	Ukraine-Informed Simulations
Trend		
Pre-break	0.07, 0.11, 0.15, 0.19, 0.23, 0.27	0.15, 0.20, 0.25, 0.30, 0.40, 0.45, 0.50, 0.60
Peri-break	0.005, 0.01, 0.02, 0.03, 0.04	0.10, 0.12, 0.15, 0.17, 0.20, 0.25, 0.30
Post-break	0.01, 0.03, 0.05, 0.07, 0.09	0.15, 0.20, 0.25, 0.30, 0.40, 0.45
Noise		
Pre-break	0.01, 0.02, 0.03, 0.04, 0.05	0.04, 0.05, 0.06, 0.07, 0.08
Peri-break	0.005, 0.008, 0.011, 0.014	0.04, 0.05, 0.06, 0.07, 0.08, 0.09
Post-break	0.005, 0.01, 0.015, 0.02	0.06, 0.07, 0.08, 0.09, 0.10, 0.11
Pulse	[0, 0, 0.002, 0.004, -0.004, 0.003, 0, -0.004]	[0.017, -0.032, 0.008, 0.047, 0.025, -0.026, -0.003, -0.012]
Seasonality	[-0,001, -0.0002, 0.0011, 0.0003, -0.0025, 0, 0.0038, 0.0006, -0.0025, -0.002, 0.0021, 0.002]	[0.1414, 0.0653, -0.0439, -0.056, -0.0042, 0.0168, -0.0121, -0.0282, -0.0602, -0.0693, -0.0256, 0.0994]
Breakpoints	18, 19, 20, 21…105	9, 10, 11, 12…57

Parameters were informed by decomposing each administrative unit's real NTL time series; the trend and noise parameters encompass the median and quartile values across all administrative units in each country. The pulse and seasonality parameters are the median values across all administrative units. Note that in the simulations, individual values were selected for the trend, noise, and breakpoint, and the pulse and seasonality values were included as a block. Ten simulations were generated for each set of parameters at every breakpoint, resulting in 164,640 simulations informed by the Ukraine data and 132,000 by the Yemen data.

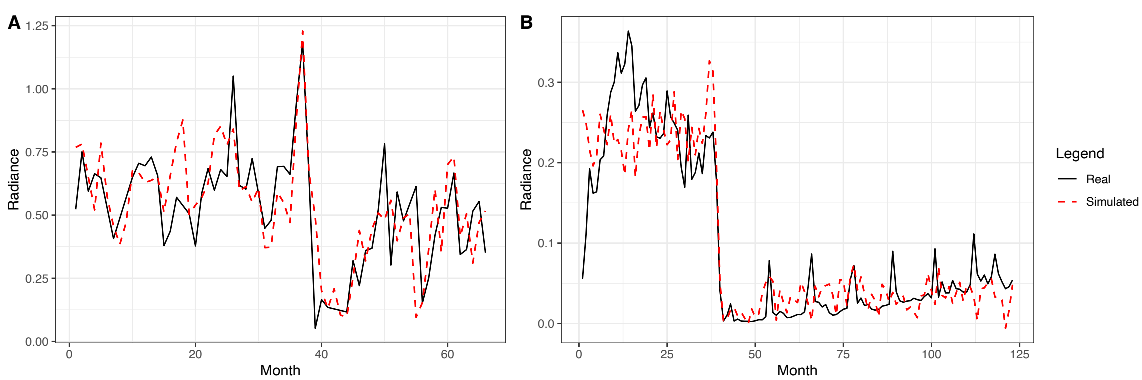

Figure S2.9: Examples of simulated time series compared to real data from Ukraine (A) and Yemen (B)

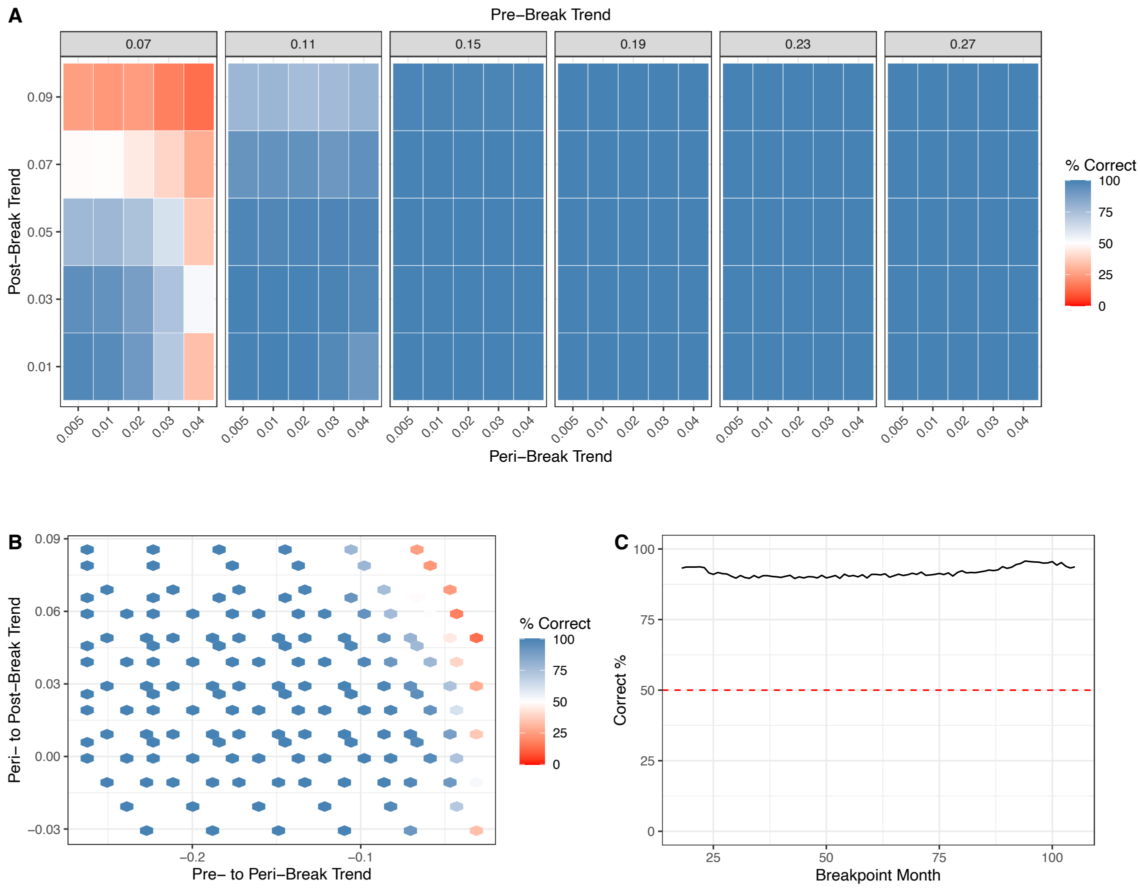

Figure S2.10: Yemen-informed simulations with changing trend values

A) Heat plot showing percentage of simulations (n=132,000) in which BFAST correctly detected the breakpoint by pre-break NTL trend values (i.e., each box is labeled by pre-break trend level). Across all grids, x-axes show peri-break trend values and y-axes show post-break trend values. Noise values for each period were held at the median parameter values (0.027, 0.008, and 0.011 respectively). B) Plot showing percentage of correct BFAST detections by difference in trend between periods. Values on the x-axis are the difference in trend values from the pre-break to the peri-break periods, whereby negative values indicate a decrease in the trend from the pre- to the peri-break period. Values on the y-axis are the difference in trend values between the peri-break and post-break periods, with positive values indicating an increase in the trend from the peri- to the post-break period. C) Percentage of correct BFAST detections by month of breakpoint over all simulations. The red horizonal dashed line shows a correct detection rate of 50%.

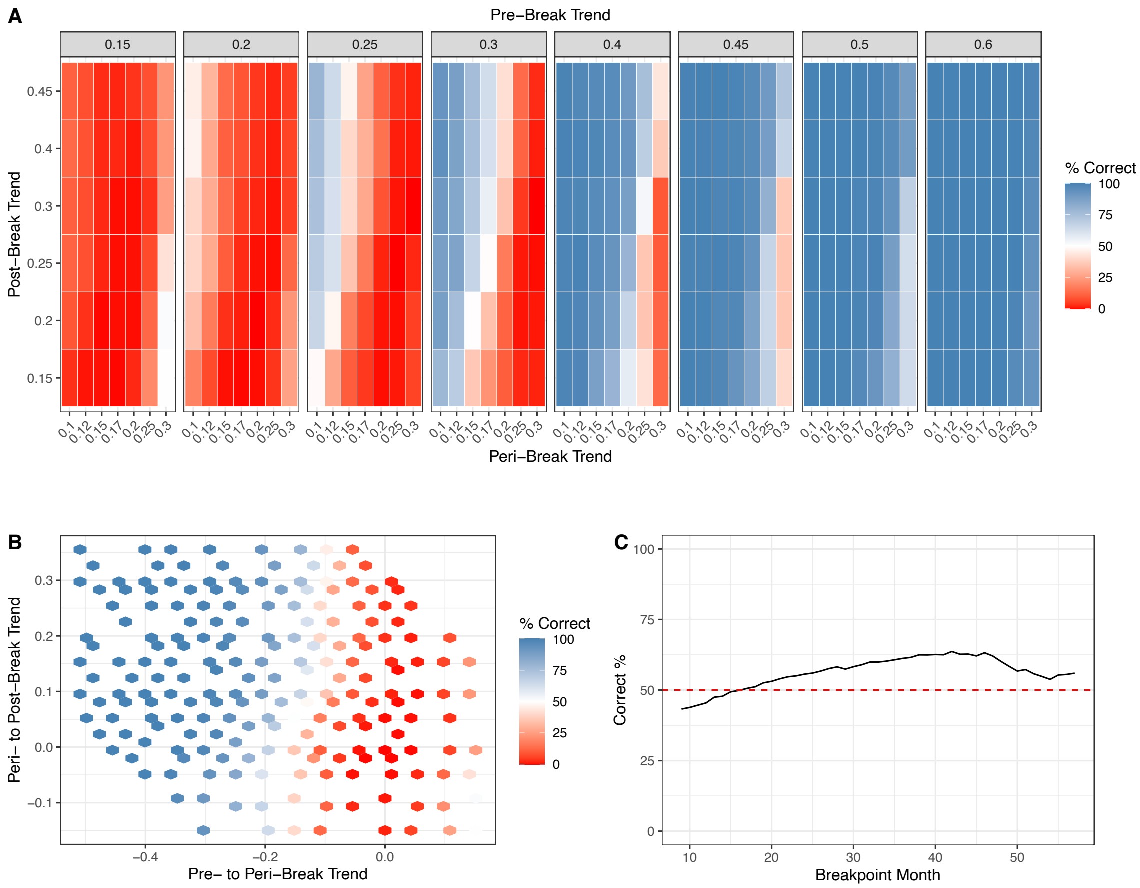

Figure S2.11: Ukraine-informed simulations with changing trend values
A) Heat plot showing percentage of simulations (n=164,640) in which BFAST correctly detected the breakpoint by pre-break NTL trend values (i.e., each box is labeled by pre-break trend level). Across all grids, x-axes show peri-break trend values and y-axes show post-break trend values. Noise values for each period were held at the median parameter values (0.060, 0.069, and 0.090 respectively). B) Plot showing percentage of correct BFAST detections by difference in trend between periods. Values on the x-axis are the difference in trend values between the pre-break and peri-break periods, whereby negative values indicate a decrease in the trend from the pre- to the peri-break period. Values on the y-axis are the difference in trend values between the peri-break and post-break periods, with positive values indicating an increase in the trend from the peri- to the post-break period. C) Percentage of correct BFAST detections by month of breakpoint over all simulations. The red horizonal dashed line shows a correct detection rate of 50%. We hypothesize that the non-linear shape indicates that BFAST performs better when breakpoints are surrounded by available data rather than in proximity to unavailable data (i.e., the end points); this may be especially relevant in these simulations given the shorter time series length compared to the Yemen-informed simulations (66 versus 123 months).

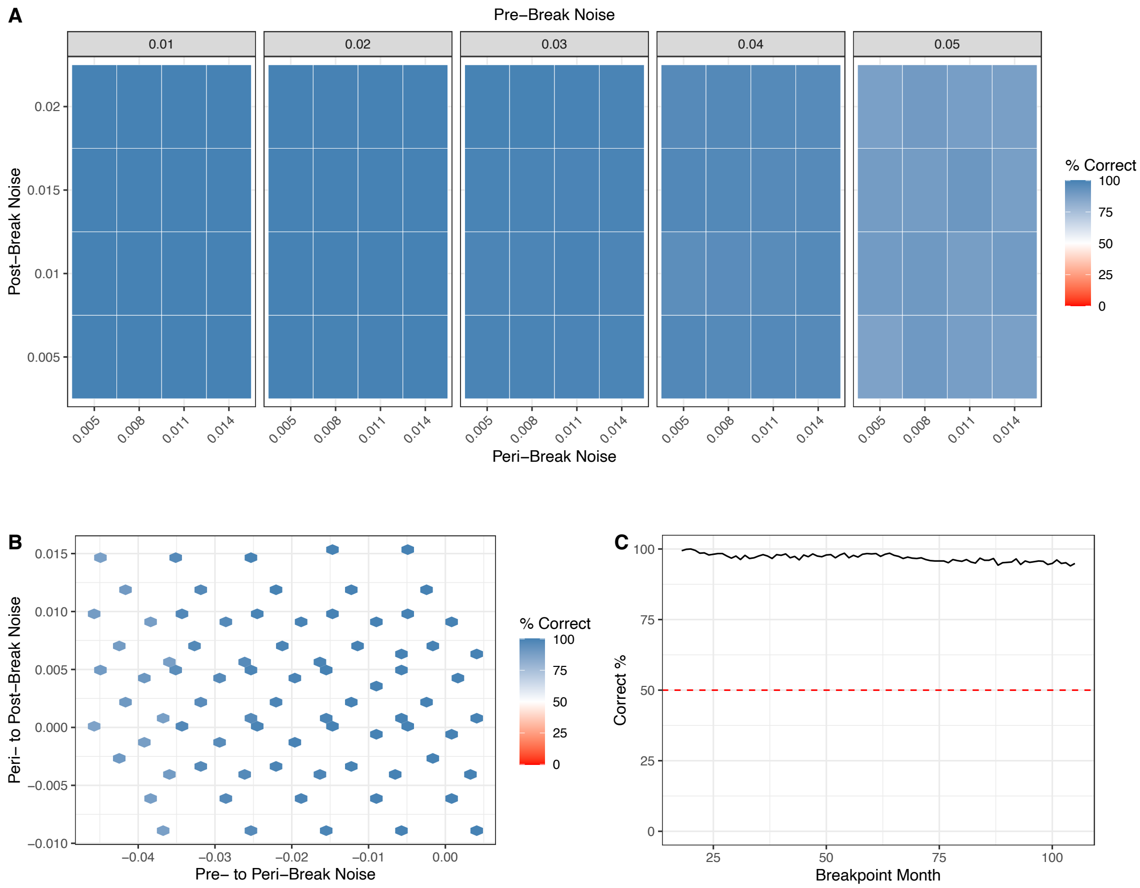

Figure S2.12: Yemen-informed simulations with changing noise values

A) Heat plot showing percentage of simulations (n=70,400) in which BFAST correctly detected the breakpoint by pre-break noise values (i.e., each box is labeled by pre-break noise level). Across all grids, the x-axes show peri-break noise values and y-axes show post-break noise values. Trend values for each period were held at the median parameter values (0.110, 0.019, and 0.031 respectively). B) Plot showing percentage of correct BFAST detections by difference in noise between periods. Values on the x-axis are the difference in noise values between the pre-break and peri-break periods, whereby negative values indicate a decrease in noise from the pre- to the peri-break period. Values on the y-axis are the difference in noise values between the peri-break and post-break periods, with positive values indicating an increase in noise from the peri- to the post-break period. C) Percentage of correct BFAST detections by month of breakpoint over all simulations. The red horizonal dashed line shows a correct detection rate of 50%.

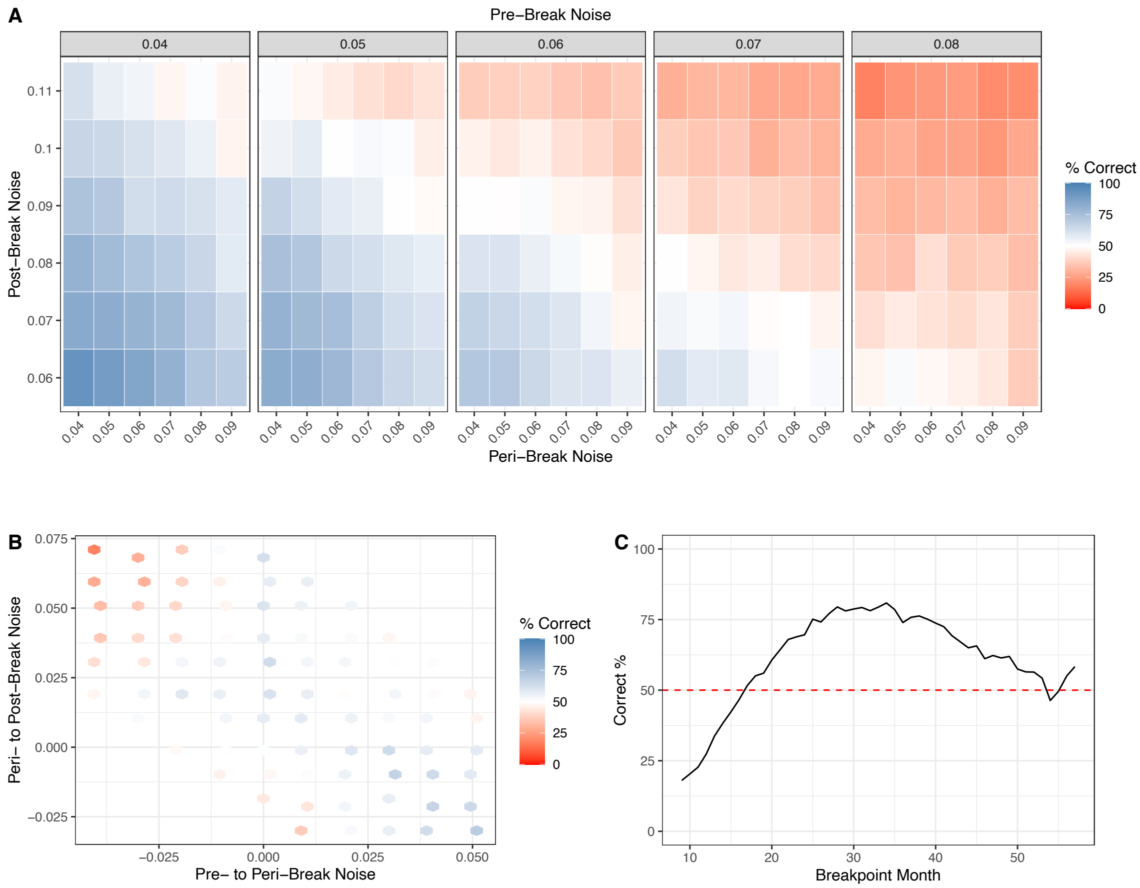

Figure S2.13: Ukraine-informed simulations with changing noise values

A) Heat plot showing percentage of simulations (n=88,200) in which BFAST correctly detected the breakpoint by pre-break noise values (i.e., each box is labeled by pre-break noise level). Across all grids, the x-axes show peri-break noise values and y-axes show post-break noise values. Trend values for each period were held at the median parameter values (0.282, 0.165, and 0.241 respectively). B) Plot showing percentage of correct BFAST detections by difference in noise between periods. Values on the x-axis are the difference in noise values between the pre-break and peri-break periods, whereby negative values indicate a decrease in noise from the pre- to the peri-break period. Values on the y-axis are the difference in noise values between the peri-break and post-break periods, with positive values indicating an increase in noise from the peri- to the post-break period. C) Percentage of correct BFAST detections by month of breakpoint over all simulations. The red horizonal dashed line shows a correct detection rate of 50%. We hypothesize that the non-linear shape indicates that BFAST performs better when breakpoints are surrounded by available data rather than in proximity to unavailable data (i.e., the end points); this may be especially relevant in these simulations given the shorter time series length compared to the Yemen-informed simulations (66 versus 123 months).

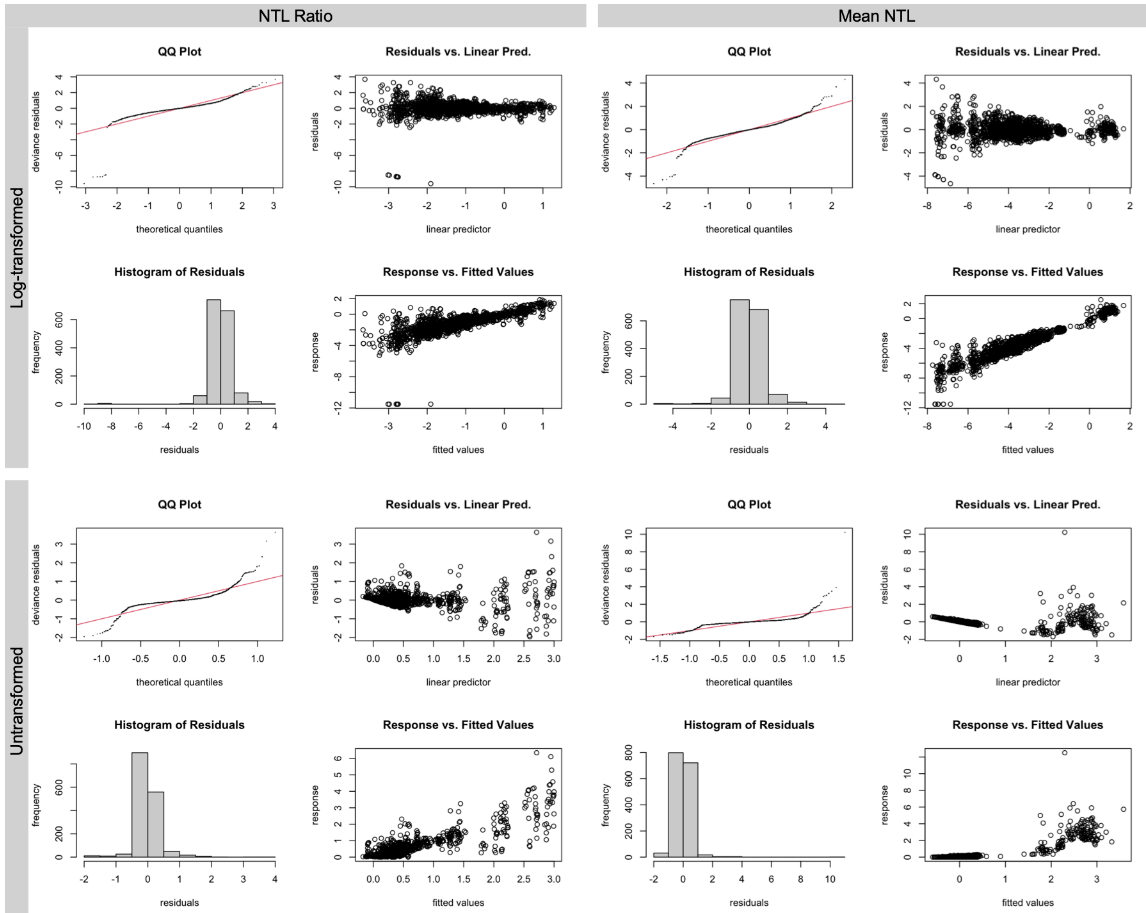

Figure S2.14: Residual plots for the GAM used to measure the relationship between NTL and aerial attacks in Yemen

In the GAMs modeling the relationship between NTL and aerial attacks, mean NTL and NTL ratio (as the response variable) were both log-transformed to handle skewness and based on model residuals. The top row shows the residuals when NTL (both mean and ratio) as the response is log-transformed, and the bottom row shows the residuals when NTL is not transformed. The residuals for the models with NTL log-transformed indicate a better fit.

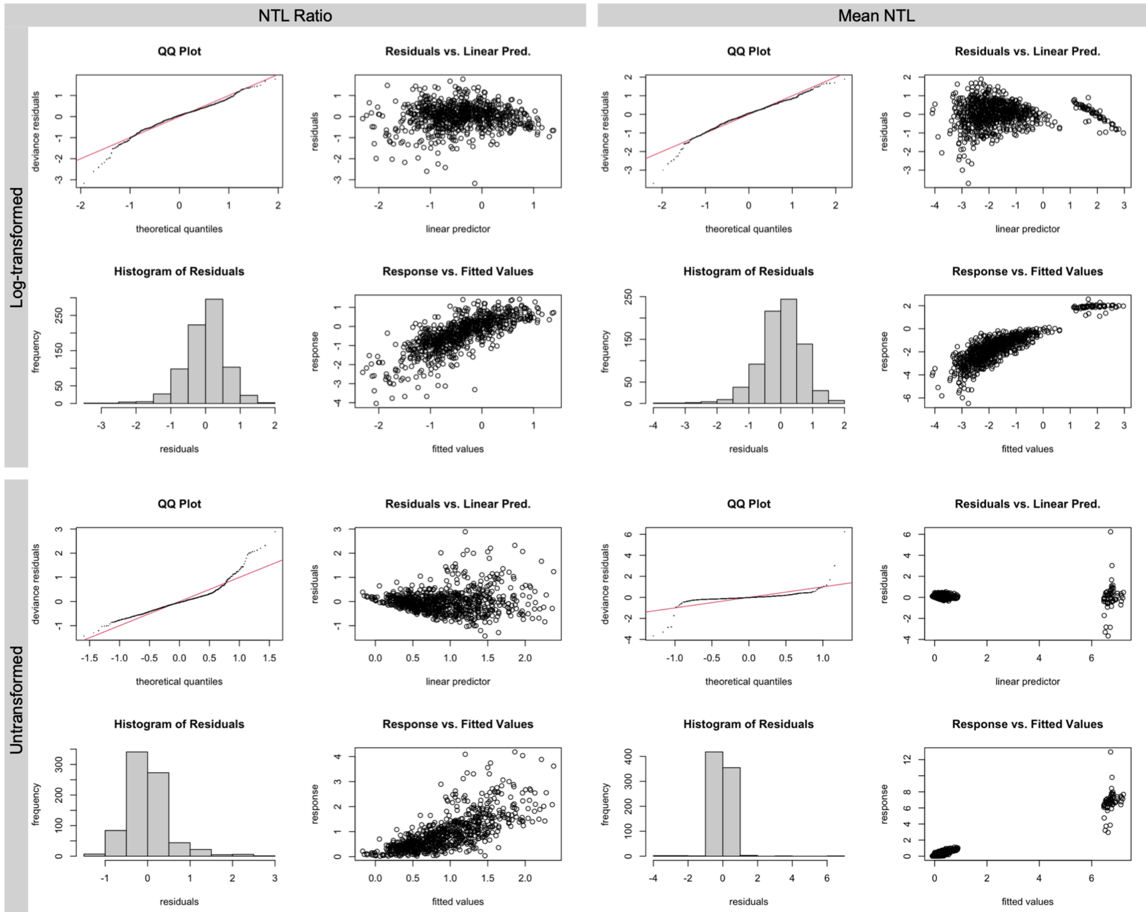

Figure S2.15: Residual plots for the GAM used to measure the relationship between NTL and aerial attacks in Ukraine

In the GAMs modeling the relationship between NTL and aerial attacks, mean NTL and NTL ratio (as the response variable) were both log-transformed to handle skewness and based on model residuals. The top row shows the residuals when NTL (both mean and ratio) as the response is log-transformed, and the bottom row shows the residuals when NTL is not transformed. The residuals for the models with NTL log-transformed indicate a better fit.

Equations: Nighttime lights and aerial attacks

We ran the following generalized additive models (GAMs) with a Gaussian distribution to analyze the relationship between nighttime lights and aerial attacks. GAMs were run in the *mgcv* package in R v.4.4.2 (98). Linear outputs for each model can be found in **Table 3** and spline outputs in **Figure S2.19**.

<u>Yemen</u>

$log(NTL_{mean}) = \beta_1(attacks) + f_1(month) + f_2(pop) + f_3(perc\_built) + \beta_2(diesel) + f_4(lat,lon)$

$log(NTL_{ratio}) = \beta_1(attacks) + f_1(month) + f_2(pop) + f_3(perc\_built) + \beta_2(diesel) + f_4(lat,lon)$

Where population (*pop*), percentage built (*perc_built*), and diesel (*diesel*) were log-transformed and f_{1-4} are smooth functions estimated by the model using restricted maximum likelihood. Study month (*month*) was modeled using a cyclic cubic regression spline, *pop* and *perc_built* with thin plate regression splines, and centroid latitude and longitude (*lat,lon)* using two-dimensional splines on a sphere. Each model was run with the raw number of aerial attacks (*attacks*) and with the number of attacks mean-centered and standardized (mean: 14, SD: 27).

<u>Ukraine</u>

$log(NTL_{mean}) = \beta_1(attacks_{low}) + \beta_2(attacks_{medium}) + \beta_3(attacks_{high}) + \beta_4(attacks_{severe}) + f_1(month) + f_2(perc\_built) + f_3(lat,lon)$

$log(NTL_{ratio}) = \beta_1(attacks_{low}) + \beta_2(attacks_{medium}) + \beta_3(attacks_{high}) + \beta_4(attacks_{severe}) + f_1(month) + f_2(perc\_built) + f_3(lat,lon)$

Where f_{1-3} are smooth functions estimated by the model using restricted maximum likelihood. *Month* was modeled using a cyclic cubic regression spline, *perc_built* with a thin plate regression spline, and *lat,lon* using two-dimensional splines on a sphere.

Aerial attack categories were defined as none (0 attacks), low (1–2), medium (3–6), high (7–117), and severe (118+). None was used as the reference category.

Equation: Cholera model

We applied nighttime lights-defined conflict categories to an existing model assessing the relationship between conflict and cholera in Yemen between 2016 and 2019. Details on the original work can be found here (18). GAMs were run in the *mgcv* package in R v.4.4.2 with a negative binomial distribution (98). Linear outputs are in **Table 4**, plots of the light recovery interactions (f_5) are in **Figure 6**, and other spline outputs are in **Figure S2.20**.

Without recovery

$$cases = f_1(pop\_density) + f_2(week) + f_3(lat,lon) + \beta_1(conflict_{interm.}) + \beta_2(conflict_{medium}) + \beta_3(conflict_{high}) + \beta_4(conflict_{severe}) + \beta_5(precip) + \beta_6(surf\_wat) + \beta_7(temp) + \beta_8(NDVI) + f_4(economy)$$

With recovery

$$cases = f_1(pop\_density) + f_2(week) + f_3(lat,lon) + \beta_1(conflict_{interm.}) + \beta_2(conflict_{medium}) + \beta_3(conflict_{high}) + \beta_4(conflict_{severe}) + \beta_5(precip) + \beta_6(surf\_wat) + \beta_7(temp) + \beta_8(NDVI) + f_4(economy) + f_5(recovery, months\_since\_min) \quad (6)$$

Conflict categories were defined using air raids in the original model and with mean NTL in the NTL-based model. Air raid-defined categories were defined as low (zero air raids in prior 3 months), intermediate (1–4), medium (5–18), high (19–75), and severe (≥76). Mean NTL-based categories were defined as low (0.087–5.904 $nW \cdot cm^{-2} \cdot sr^{-1}$), intermediate (0.031–0.086), medium (0.016–0.030), high (0.007–0.015), and severe (0–

0.006). f_{1-5} are smooth functions estimated by the model using restricted maximum likelihood. Study week (*week*) was modeled using a cyclic cubic regression spline, centroid latitude and longitude (*lat,lon)* using two-dimensional splines on a sphere, and all others with thin plate regression splines.

Table S2.7: Model outputs for original cholera model and models without Raymah governorate

	Original Model *No. gov. = 20*	**Original Model** *No. gov. = 19* *(ex. Raymah)*	**Mean NTL Model (with recovery)** *No. gov. = 19*
	IRR (95% CI)	IRR (95% CI)	IRR (95% CI)
Conflict severity			
Low	Comparison	Comparison	Comparison
Intermediate	1.76 (1.51, 2.05)	1.90 (1.61, 2.25)	1.34 (1.06, 1.69)
Medium	1.57 (1.31, 1.89)	1.54 (1.26, 1.87)	1.89 (1.42, 2.52)
High	1.87 (1.53, 2.29)	2.09 (1.69, 2.59)	1.94 (1.38, 2.73)
Severe	2.06 (1.59, 2.69)	1.96 (1.49, 2.57)	1.71 (1.10, 2.64)
Surface water	0.89 (0.78, 1.03)	0.94 (0.81, 1.08)	0.90 (0.79, 1.02)
Precipitation	0.98 (0.91, 1.06)	1.03 (0.95, 1.11)	1.10 (1.02, 1.19)
Vegetation index	0.72 (0.64, 0.80)	0.75 (0.65, 0.85)	0.74 (0.66, 0.84)
Temperature	1.11 (0.91, 1.36)	1.01 (0.83, 1.23)	1.10 (0.92, 1.32)

To assess whether the exclusion of Raymah from the NTL-based model biased the results, we ran the original model (using air raids to define conflict categories) without Raymah. These results were consistent with the full original model and the NTL-based model with light recovery, indicating minimal bias.

Cholera model with NTL ratio

We ran the cholera model, without recovery, using conflict categories defined by NTL ratios of low (0.54–0.99), intermediate (0.32–0.53), medium (0.17–0.31), high (0.10–0.16), and severe (0–0.09). We also created a separate category (“above”) for NTL levels that were above pre-event means. We did not use this specification in a model with the recovery interaction term, as the NTL ratio already captures recovery over time relative to pre-event NTL levels. We included the model that combined mean NTL-defined conflict categories and the recovery interaction in the main text as it highlights the role of recovery in the epidemiological process more explicitly. However, the results from this model likewise indicate that areas with NTL levels closest to pre-event levels had the lowest cholera risk and that this risk increased as the ratio approached zero (**Table S2.8**).

We hypothesize that population displacement is captured in the “above” conflict category, which was associated with increased cholera risk (IRR: 1.51; 95% CI: 1.21–1.87) (**Table S2.8**). Most of the included governorate-weeks were from Marib, Al-Jawf, and Al-Maharah; as of 2023, Marib hosts roughly 60% of Yemen’s IDPs, or around 1.6 million people (175). Though Al-Jawf and Al-Maharah host far fewer IDPs (26,000 and 18,000, respectively), their pre-conflict light levels were considerably lower than that of other governorates (175). The influx of IDPs to these governorates may have had a greater effect on their NTL levels as the IDP developments accounted for a larger proportion of the overall light. We can use high-resolution satellite imagery to identify development in areas with observed NTL growth (**Figure S2.17**). Other governorates which hosted more IDPs started with higher light levels, and thus the impact of displacement may not have affected their overall means as strongly, though increases in specific areas may be detectable at smaller spatial scales.

Table S2.8: Outputs for the original cholera model and the model using NTL ratio to define conflict categories

	Original Model *No. gov. = 20*		**NTL Ratio Model** *No. gov. = 20*	
Covariate	**IRR (95% CI)**	**p-value**	**IRR (95% CI)**	**p-value**
Conflict severity				
Low	Comparison		Comparison	
Intermediate	1.76 (1.51–2.05)	<0.0001	1.29 (1.11–1.49)	0.0008
Medium	1.57 (1.31–1.89)	<0.0001	1.38 (1.18–1.62)	<0.0001
High	1.87 (1.53–2.29)	<0.0001	1.57 (1.30–1.90)	<0.0001
Severe	2.06 (1.59–2.69)	<0.0001	1.47 (1.18–1.83)	0.0005
Above			1.51 (1.21–1.87)	0.0002
Surface water	0.89 (0.78–1.03)	0.11	0.90 (0.78–1.03)	0.13
Precipitation	0.98 (0.91–1.06)	0.69	1.08 (0.99–1.17)	0.07
Vegetation index	0.72 (0.64–0.80)	<0.0001	0.70 (0.62–0.79)	<0.0001
Temperature	1.11 (0.91–1.36)	0.29	1.03 (0.85–1.25)	0.75
AIC	30,240.97		30,337.26	

Spline outputs for the NTL-based model are in **Figure S2.16.**

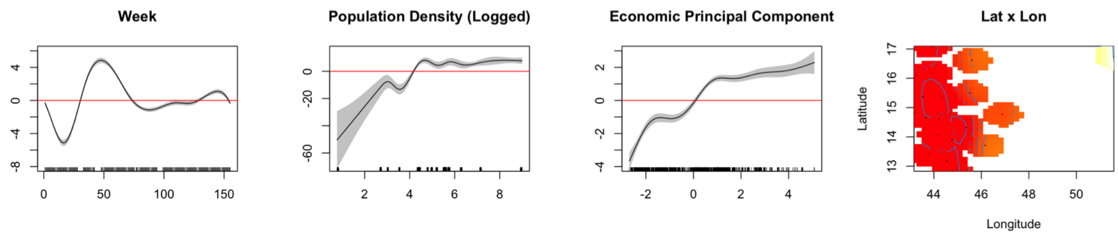

Figure S2.16: Spline outputs of the cholera model using NTL ratios to define conflict categories

“Above” category

There were some governorates that had higher NTL values after the onset of large-scale military operations than before, which was captured in the “above” category in the NTL ratio. We hypothesize that this was capturing displacement, especially in areas that hosted a markedly high number of displaced individuals (e.g., Marib), or that had very low light levels before the onset of large-scale military operations, meaning that displaced settlements would have a proportionately larger effect on NTL levels. In **Figure S2.17**, we investigated two areas that saw higher NTL levels post-event: Al-Hazim in Al-Jawf governorate, and Marib City in Marib governorate. In Al-Hazim, increases in light levels reflect widespread development of the area, which previously had both low development and light levels. In Marib City, the creation of Jufainah camp, seen in the satellite image in **Figure S2.17**, likely contributed to the growth in NTL in the post-event period.

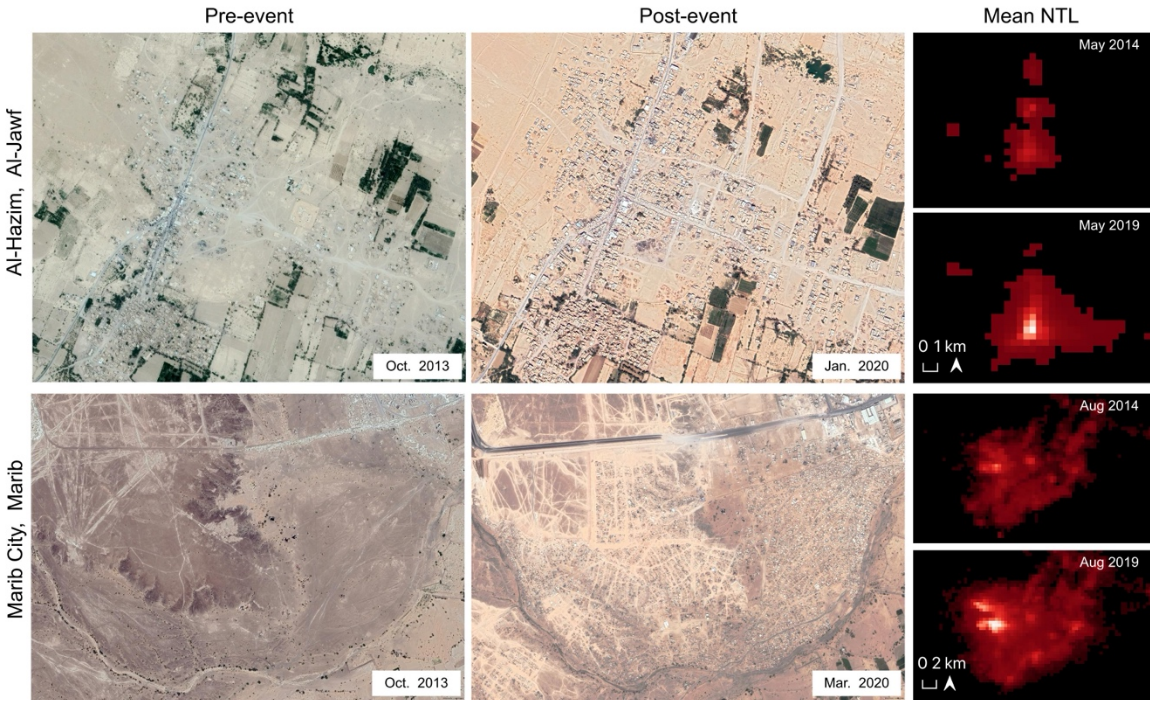

Figure S2.17: Examples of displacement-related infrastructural development
The high-resolution satellite images were extracted from Google Earth.

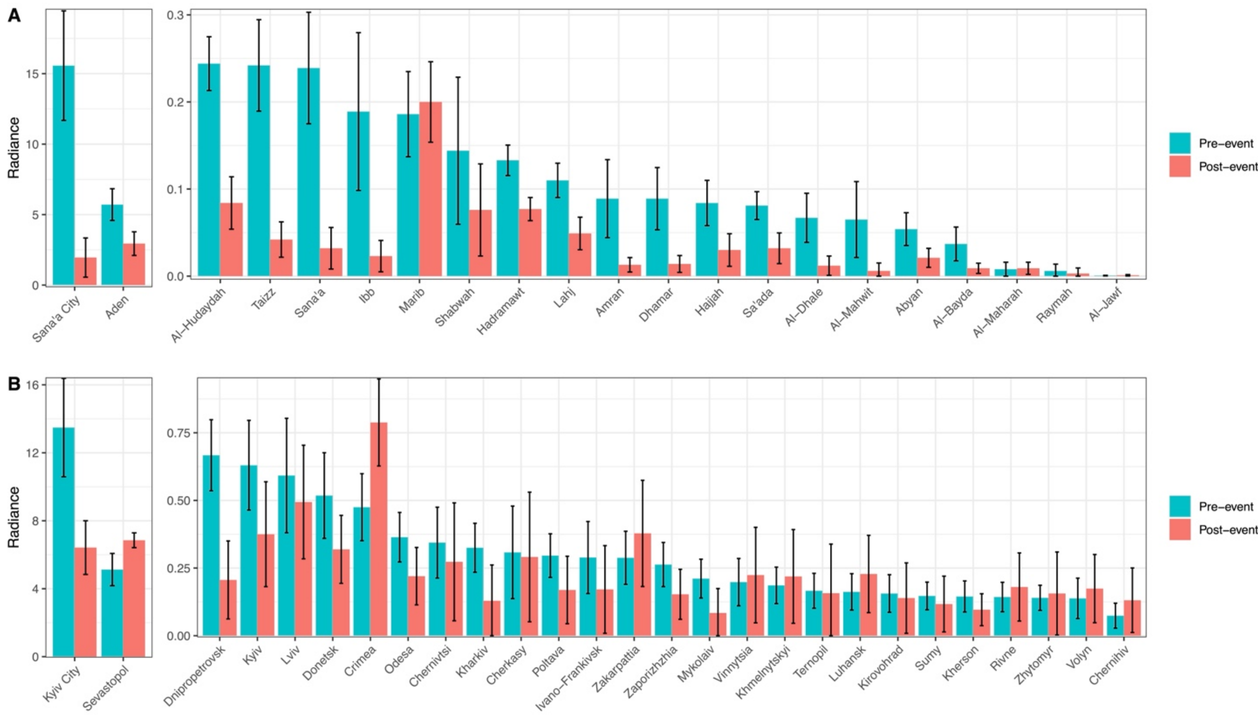

Figure S2.18: Pre- and post-event NTL means and standard deviations in Yemen (A) and Ukraine (B)

Table S2.9: BFAST-identified negative breakpoints with 95% confidence intervals in Yemen

	Month of First Aerial Attack	**Breakpoint (95% CI)**	**h-value**
Total Yemen	39 (Mar 2015)	39 (38–40)	0.15
Brightest quartile			
Sana'a City	39	39 (38–40)	0.15
Aden	39	39 (38–40)	0.15
Al-Hudaydah	39	39 (38–40)	0.15
Taizz	39	39 (38–40)	0.15
Sana'a	39	39 (38–40)	0.15
Second quartile			
Ibb	39	39 (38–40)	0.10
Marib	39	40 (38–41)	0.15
Shabwah	39	39 (38–40)	0.15
Hadramawt	43 (Jul 2015)	40 (38–41)	0.15
Lahj	39	39 (38–40)	0.15
Third quartile			
Amran	39	39 (38–40)	0.15
Dhamar	39	39 (37–40)	0.15
Hajjah	39	40 (38–41)	0.15
Sa'ada	39	40 (39–41)	0.15
Al-Dhale	39	39 (36–40)	0.15
Dimmest quartile			
Al-Mahwit	42 (Jun 2015)	40 (39–42)	0.10
Abyan	39	39 (38–40)	0.15
Al-Bayda	39	39 (38–40)	0.15
Al-Maharah	90 (Jun 2019)	None detected	–
Raymah	41 (May 2015)	None detected	–
Al-Jawf	39	39 (34–40)	0.10

The h-value refers to the minimal segment size between potential breaks. Quartiles refer to pre-event NTL levels.

Table S2.10: BFAST-identified negative breakpoints with 95% confidence intervals in Ukraine

	Month of First Aerial Attack	**Breakpoint (95% CI)**	**h-value**
Ukraine	38 (Feb 2022)	38 (37–39)	0.15
Brightest Quartile			
Kyiv City	38	38 (37–39)	0.25
Sevastopol	43 (Jul 2022)	None detected	–
Dnipropetrovsk	38	38 (37–39)	0.10
Kyiv	38	38 (37–39)	0.15
Lviv	38	38 (37–39)	0.15
Donetsk	38	38 (37–40)	0.15
Second Quartile			
Crimea	44 (Aug 2022)	None detected	–
Odesa	38	None detected	–
Chernivtsi	46 (Oct 2022)	45 (44–46)	0.15
Kharkiv	38	38 (36–39)	0.20
Cherkasy	39 (Mar 2022)	37 (33–38)	0.15
Poltava	38	37 (36–41)	0.15
Ivano-Frankivsk	38	38 (36–39)	0.15
Third Quartile			
Zakarpattia	41 (May 2022)	47 (45–48)	0.10
Zaporizhzhia	38	38 (37–39)	0.15
Mykolaiv	38	None detected	–
Vinnytsia	38	None detected	–
Khmelnytskyi	39 (Mar 2022)	40 (38–41)	0.15
Ternopil	40 (Apr 2022)	40 (37–41)	0.15
Luhansk	38	None detected	–
Dimmest Quartile			
Kirovohrad	39	None detected	–
Sumy	38	38 (36–39)	0.05
Kherson	38	None detected	–
Rivne	39	None detected	–
Zhytomyr	38	38 (37–39)	0.05
Volyn	38	None detected	–
Chernihiv	38	44 (43–45)	0.10

The h-value refers to the minimal segment size between potential breaks. Quartiles refer to pre-event NTL levels.

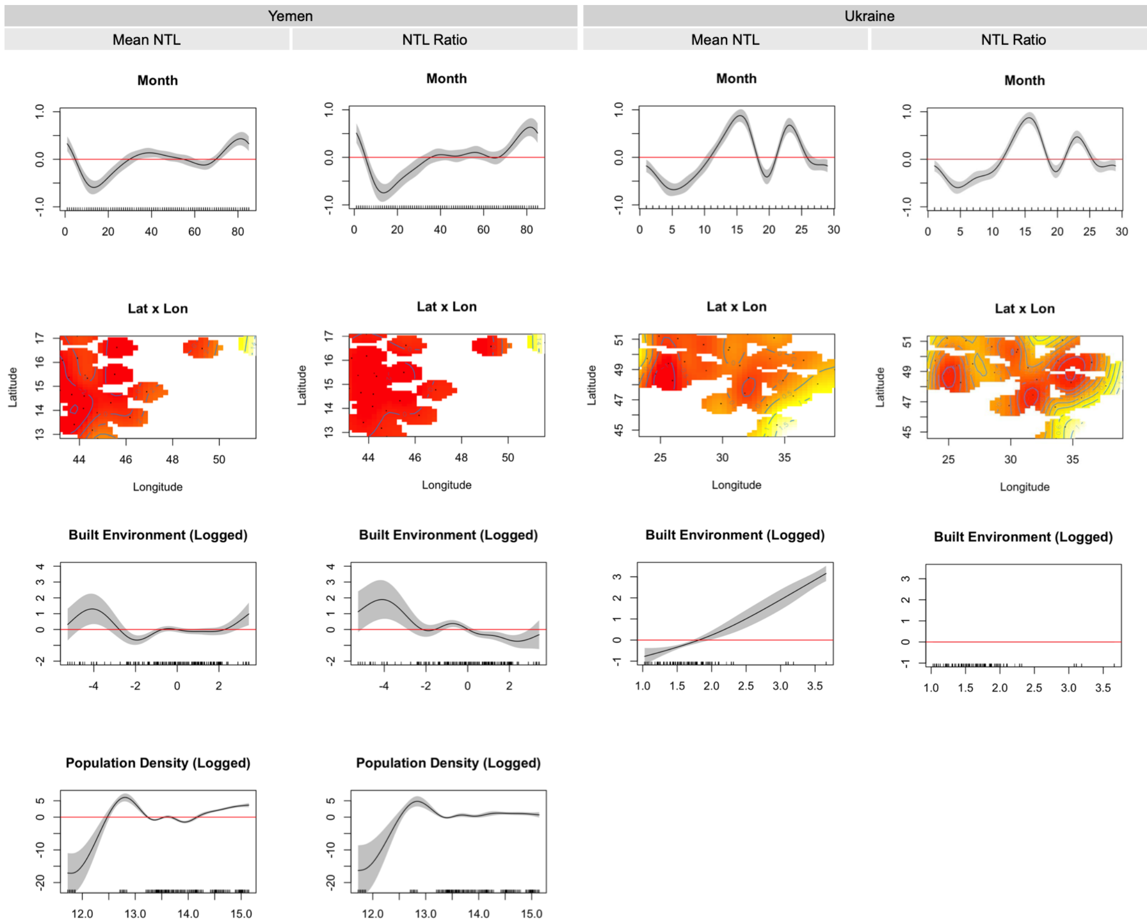

Figure S2.19: Splines for the non-parametric variables included in the NTL and aerial attacks models

The output is considered significant when the black line and gray shaded areas (95% CIs) are entirely above or below the red horizontal line. In interaction plots, yellows indicate higher population size and reds indicate lower population size. The linear components for these models are in **Table 3.**

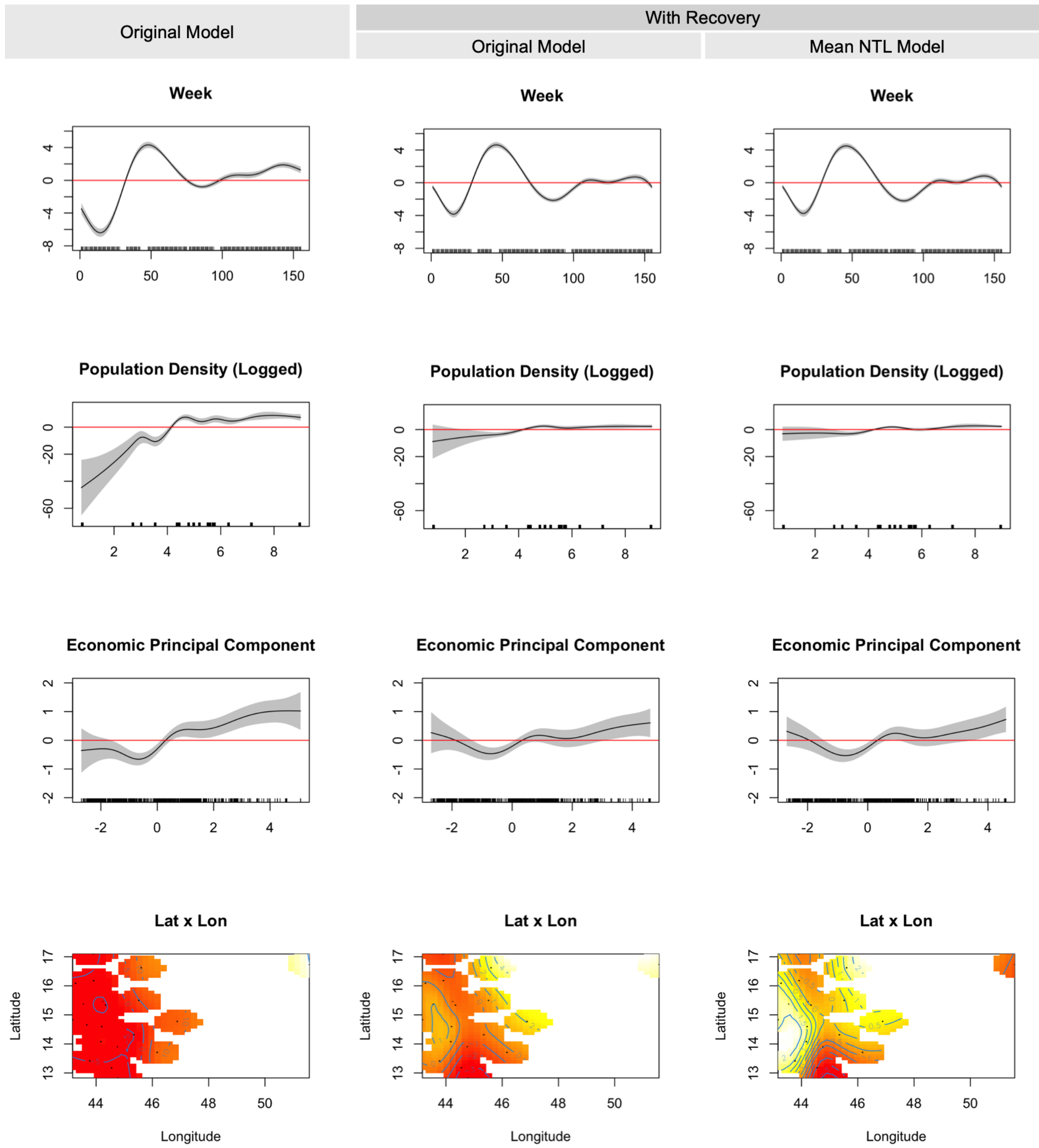

Figure S2.20: Spline outputs for the cholera models
"Original" refers to the model from Tarnas et al. (18), which used air raids to define the conflict categories. Models with recovery included an interaction term between light recovery and months since light nadir. The output is considered significant when the black line and gray shaded areas (95% CIs) are entirely above or below the red horizontal line. In interaction plots, yellows indicate higher population size and reds indicate lower population size. The linear outputs are shown in **Table 4** and the interaction plots for light recovery (in the "With Recovery" models) are shown in **Figure 6**.

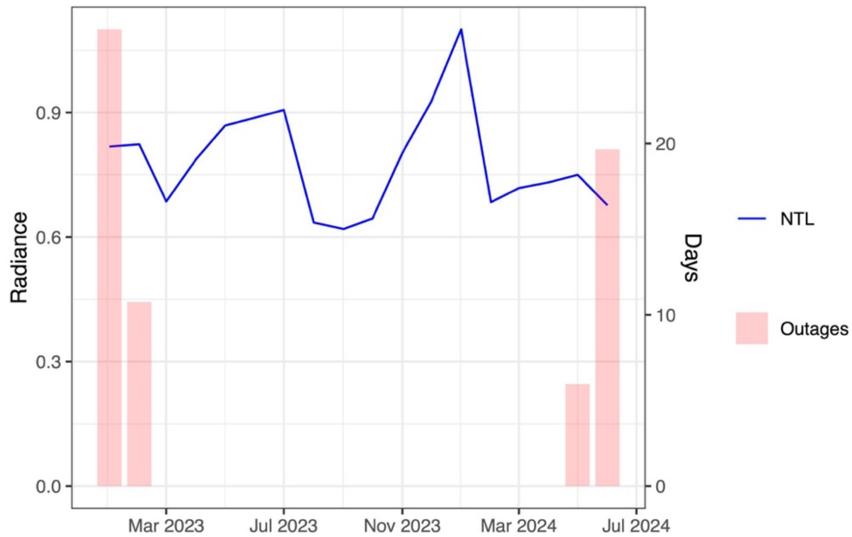

Figure S2.21: Mean NTL and days of stabilization blackouts in Ukraine
Blackouts are reported hourly and the total hours were aggregated by month and divided by 24 to determine the total number of days per month. Over this period, blackouts affected most or all regions in the country. Data were not available for 2022. The mean NTL time series is for all of Ukraine.

APPENDIX THREE: Chapter Four

Table S3.1: Description of variables included in the final model

Variable	Description	Source	Spatial Scale	Time
case	Counts of reported cutaneous and mucocutaneous leishmaniasis cases (combined imported and autochthonous)	Cases: WHO Global Health Observatory (123)	Nation level	Annual
year	Year, from 2005 to 2022			Annual
gdpScale	Annual gross domestic product, in US dollars ($). Mean centered and standardized	World Bank (127)	Nation level	Annual
conIntens	Conflict intensity rating ranging from 1 to 10	Bertelsmann Transformation Index (125)	Nation level	Biennially; converted into annual measures by averaging scores in years between reports
Environmental *(all environ. variables are mean centered and standardized)*				
precip	Total observed rainfall in mm	Climate Change Knowledge Portal (World Bank Group) (53)[7/21/26 7:42:00 AM]	Nation level	Annual
meanTemp	Mean ambient temperature in °C	Climate Change Knowledge Portal (World Bank Group) (53)	Nation level	Annual
rangeTemp	Range of ambient temperature in °C, calculated using minimum and maximum ambient temperature	Climate Change Knowledge Portal (World Bank Group) (53)	Nation level	Annual
meanHum	Mean specific humidity in g/kg	NASA's Global Land Data Assimilation System Land Surface Model (129)	1° x 1°, mean taken at nation level	Monthly; converted to annual by averaging
rangeHum	Range of specific humidity in g/kg, calculated using minimum and maximum humidity	NASA's Global Land Data Assimilation System Land Surface Model (129)	1° x 1°, range taken at nation level	Monthly; converted to annual by averaging
NDVI	Normalized difference vegetation index, range from -1 to 1	Terra MODIS satellite (130)	1km, mean taken at nation level	Monthly; converted to annual by averaging
Demographic *(both are log-transformed)*				
displaceProp	Proportion of the total population internally displaced at the end of each year. This includes	Displacement: International Displacement Monitoring Center (128)	Nation level	Annual

	conflict- and disaster-related displacement	Population: World Bank (124)		
pop	Annual population estimate	World Bank (124)	Nation level	Annual

Model specification: Conflict intensity interpolation

BTI reports conflict intensity scores every two years (on the even years), beginning in 2006. We tested four different ways of interpolating these data between years in order to test for the sensitivity of our model results to interpolation. These methods included: 1) averaging conflict intensity scores between years, 2) applying the score from the prior year to the following odd year, 3) applying the score from the following year to the prior odd year, and 4) only using years for which conflict intensity scores were reported (i.e., the even years, with no interpolation at all). In each of these specifications, conflict intensity was lagged one year. Results for each specification are below (**Table S3.2**). Note that each of these models also included splines for mean temperature, temperature range, and NDVI though these are not shown for brevity. The model outputs for conflict intensity did not markedly change between tested specifications, and thus we utilized the first method in the final model.

Table S3.2: Outputs for each model specification

	Averaged Scores		**Forward Score App.**		**Backward Score App.**		**No Interpolation**	
	IRR (95% CI)	p value	IRR (95% CI)	p value	IRR (95% CI)	p value	IRR (95% CI)	p value
Conflict	1.09 (1.01–1.16)	0.02	1.08 (1.01–1.15)	0.02	1.07 (1.00–1.14)	0.05	1.12 (1.01–1.24)	0.03
GDP	0.86 (0.70–1.06)	0.16	0.86 (0.70–1.06)	0.16	0.86 (0.70–1.06)	0.16	0.80 (0.60–1.05)	0.11
Year	1.00 (0.98–1.01)	0.69	1.00 (0.98–1.01)	0.70	1.00 (0.98–1.02)	0.76	1.00 (0.97–1.03)	0.96
Displace.	0.96 (0.93–1.00)	0.07	0.97 (0.93–1.01)	0.09	0.96 (0.93–1.01)	0.08	0.95 (0.88– .02)	0.17
Precip.	1.12 (0.78–1.62)	0.53	1.13 (0.78–1.63)	0.52	1.13 (0.78–1.63)	0.52	1.16 (0.63–2.14)	0.64
Humidity (mean)	1.39 (0.67–2.90)	0.38	1.41 (0.68–2.93)	0.36	1.39 (0.67–2.90)	0.38	1.22 (0.42–3.52)	0.72
Humidity (range)	0.74 (0.63–0.86)	0.0001	0.74 (0.63–0.86)	0.0001	0.73 (0.63–0.86)	0.0001	0.69 (0.53–0.89)	0.004

Model specification: Conflict lag

We experimented with two different lag specifications for the conflict variable in the model: no lag and lagged one year. We anticipated that lagging the conflict variable would be appropriate, since vectors would need time to reproduce in newly acquired niches and other hospitable environments following conflict-related destruction. However, we were interested in comparing the two model versions. As seen in **Table S3.3**, the model with lagged conflict does result in a slightly better model fit. This also affirms that there is a delay between conflict and the associated increase in leishmaniasis incidence.

Table S3.3: Outputs for each model specification

	No Lag		**Conflict Lagged 1 year**	
	IRR (95% CI)	p value	IRR (95% CI)	p value
Conflict intensity	1.06 (0.99–1.14)	0.11	1.09 (1.01–1.16)	0.02
GDP	0.86 (0.70–1.06)	0.16	0.86 (0.70–1.06)	0.16
Year	1.00 (0.98–1.02)	0.84	1.00 (0.98–1.01)	0.69
Displace.	0.97 (0.93–1.01)	0.10	0.96 (0.93–1.00)	0.07
Precip.	1.14 (0.79–1.64)	0.50	1.12 (0.78–1.62)	0.53
Humidity (mean)	1.39 (0.67–2.91)	0.38	1.39 (0.67–2.90)	0.38
Humidity (range)	0.73 (0.62–0.85)	<0.0001	0.74 (0.63–0.86)	0.0001
AIC	7,750.89		7,746.96	

The AIC (Akaike Information Criterion) indicates model fit, where a lower number signifies better fit.

Model equations

<u>Model A</u>

cases = β_{0i} + β_1*(year)* + β_2*(gdp_scale)* + β_3*(conflict_intensity)* + *log(pop)*

<u>Model B</u>

cases = β_{0i} + β_1*(year)* + β_2*(gdp_scale)* + β_3*(conflict_intensity)* + β_4*(displaceProp)* + *log(pop)*

Model C (final model)

cases = β_{0i} + β_1*(year)* + β_2*(gdp_scale)* + β_3*(conflict_intensity)* +β_4*(dsplace_prop)* + β_5*(precip_scale)* + β_6*(hum_scale$_{mean}$)* + β_7*(hum_scale$_{range}$)* + f_1*(temp_scale$_{mean}$)* + f_2*(temp_scale$_{range}$)* + f_3*(ndvi_scale)* + *log(pop)*

Where β_{0i} is the random nation-level (i) intercept, with a Gaussian distribution ($\beta_{0i} \sim N(\mu,\sigma^2)$); β_3 is lagged at t-1; f_{1-3} are smooth functions estimated by the model using restricted maximum likelihood; and *log(pop)* is the offset term.

Model from 2005–2019

COVID-19 likely affected the reporting of leishmaniasis cases between 2020 and 2022 (132). We ran our analysis with a restricted date range (2005–2019) to assess the relationships outside the influence of COVID-19 on case reporting.

Table S3.4: Outputs for the date-restricted model

	No Lag	
	IRR (95% CI)	p value
Conflict intensity	1.11 (1.02 – 1.20)	0.01
GDP	0.75 (0.58 – 0.97)	0.03
Year	1.03 (1.00 – 1.06)	0.09
Displace.	0.95 (0.91 – 0.998)	0.04
Precip.	1.30 (0.87 – 1.94)	0.20
Humidity (mean)	1.40 (0.58 – 3.39)	0.45
Humidity (range)	0.81 (0.66 – 1.01)	0.06

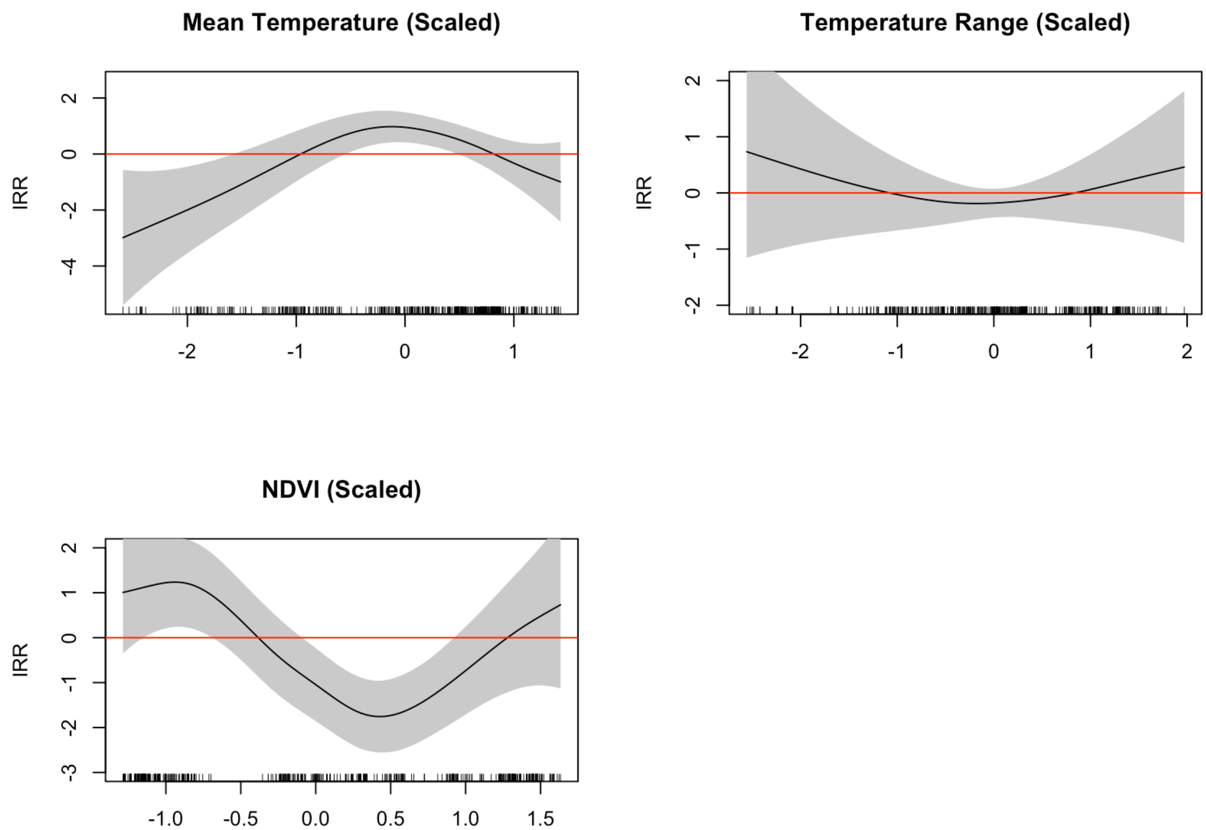

Figure S3.1: Spline outputs from the date-restricted model for mean and range temperature The red lines can be used to measure significance, whereby the output is significant at values when the solid line and grey areas are all either above or below the line. The grey areas indicate the 95% confidence intervals.

Model without imported cases (2013–2022)

The WHO jointly imported and autochthonous CL and ML cases between 2005 and 2012 before separating them in 2013. We tested our model using just autochthonous cases between 2013 and 2022. Notably, when compared to the full model, GDP is negatively associated with CL/ML cases and humidity range is no longer significant.

Table S3.5: Outputs for the model without imported leishmaniasis cases

	No Lag	
	IRR (95% CI)	p value
Conflict intensity	1.09 (1.01 – 1.19)	0.03
GDP	0.45 (0.25 – 0.82)	0.008
Year	0.99 (0.97 – 1.02)	0.66
Displace.	0.98 (0.93 – 1.02)	0.32
Precip.	1.05 (0.70 – 1.56)	0.82
Humidity (mean)	1.00 (0.48 – 2.10)	0.9997
Humidity (range)	0.84 (0.66 – 1.07)	0.16

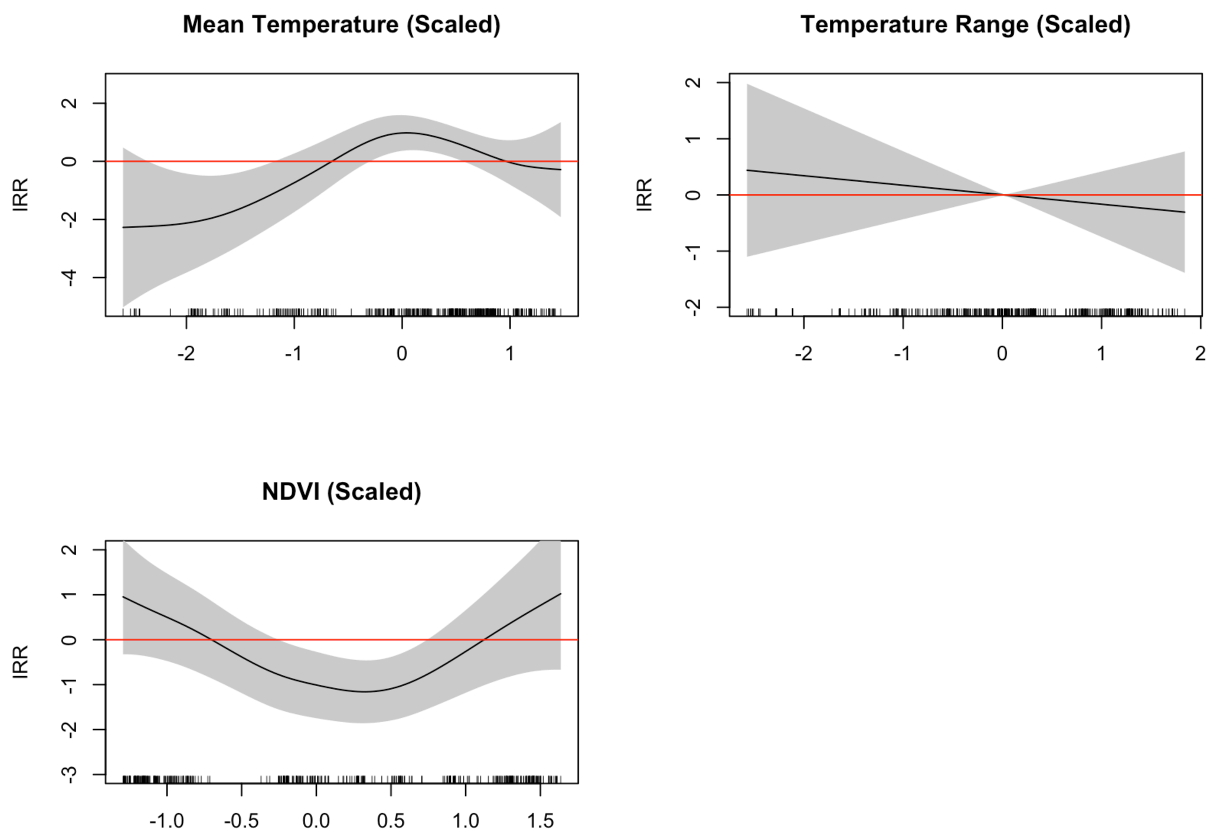

Figure S3.2: Spline outputs from the model without imported leishmaniasis cases
The red lines can be used to measure significance, whereby the output is significant at values when the solid line and grey areas are all either above or below the line. The grey areas indicate the 95% confidence intervals.

Interaction terms

During model specification, we tested two interaction terms: one between conflict intensity and year, and another between displacement and conflict intensity. Though we did not include either term in the final model based on model fit and interpretability, they both show interaction effects between the variables and the outcome (cases of leishmaniasis). The conflict and year interaction (**Figure S3.3**) suggests that the relationship between conflict intensity and cases of leishmaniasis changed over the study period: in the beginning of the study period, conflict levels had to be higher to have a significant effect on cases, but in more recent years a lower level of conflict could have a significant effect. The conflict and population displacement interaction (**Figure S3.4**) indicates that when displacement is above a certain level and conflict is high, it has a positive association with leishmaniasis incidence. The highest levels of displacement (toward the top of the y-axis), however, do not show the strongest associations. Additionally, when conflict intensity is low, displacement has a negative association with leishmaniasis, even when displacement levels are high. This relationship is clearly complex, and factors such as reporting challenges and healthcare availability may play a role.

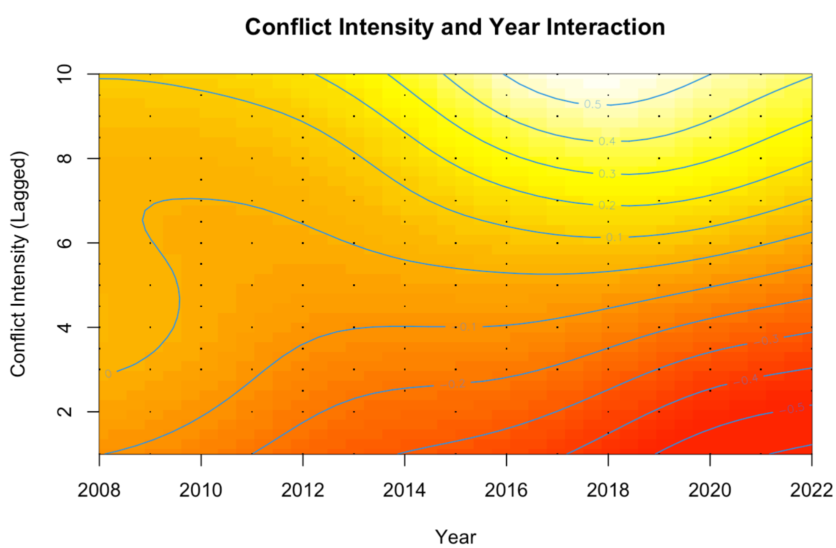

Figure S3.3: Interaction spline between lagged conflict intensity and year
Yellows indicate higher risk and reds indicate lower risk

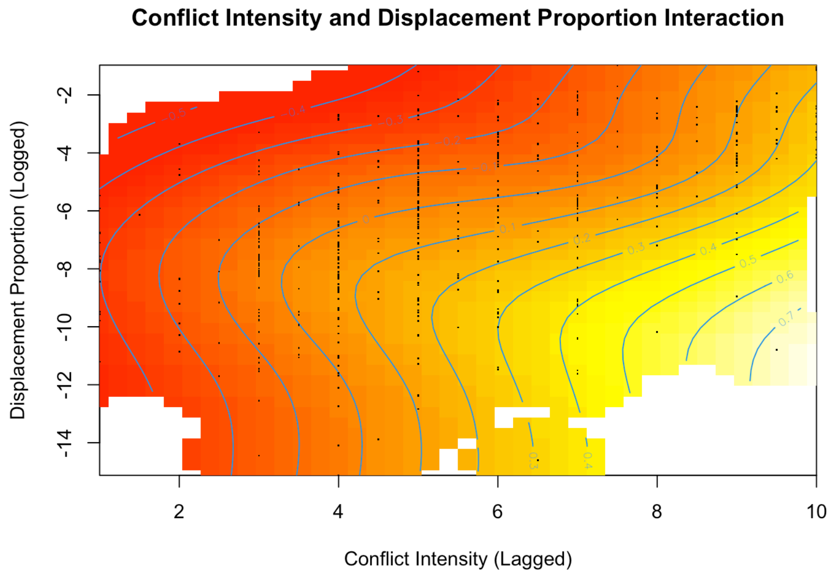

Figure S3.4: Interaction spline between lagged conflict intensity and displacement proportion Yellows indicate higher risk and reds indicate lower risk

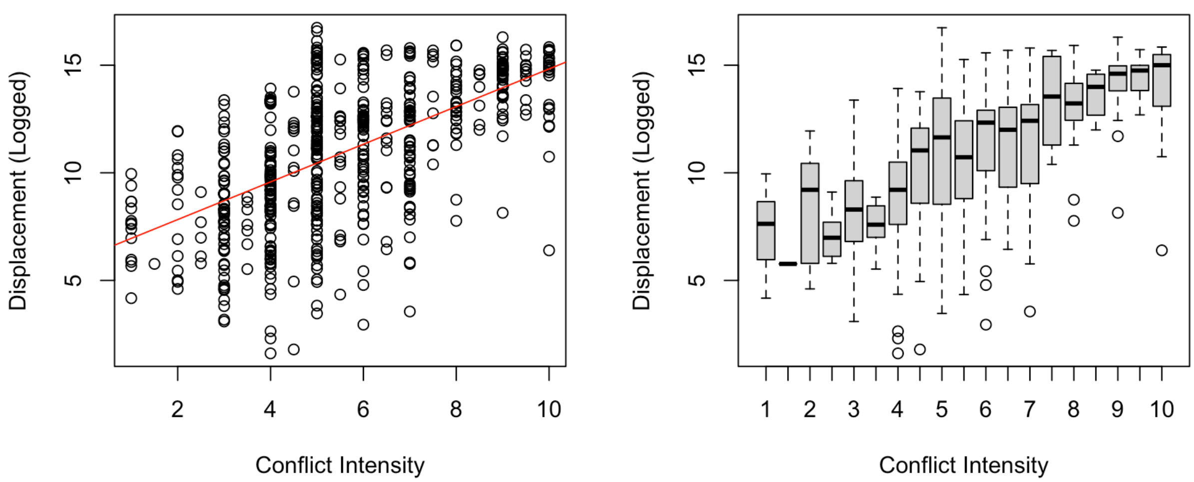

Figure S3.5: Scatterplot with fitted regression line and boxplot
Both figures show the relationship between conflict intensity and logged total displacement without any lag (i.e., the displacement and conflict intensity occur in the same year). The regression line has a slope of 0.8752.

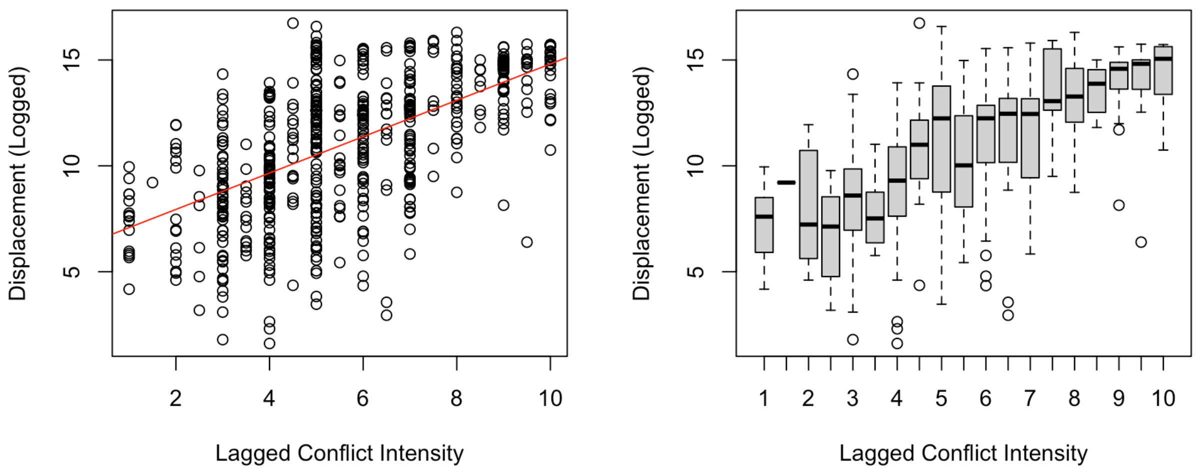

Figure S3.6: Scatterplot with fitted regression line and boxplot
Both figures show the relationship between conflict intensity and logged total displacement with conflict intensity lagged one year (i.e., the displacement occurred one year following the conflict intensity). The regression line has a slope of 0.8592.

APPENDIX FOUR: Chapter Five

Table S4.1: Change in DIC from base model for environmental variables

	PR	Hum	Temp_M	Temp_R	NDVI	SW	Built	Bare	S_S	Crops
Linear							0.56	0.85	0.02	0.47
Lag 4	-3.48	1.06	-2.06	-0.10	1.06	1.37				
Lag 8	-0.53	2.08	-0.75	2.83	0.85	2.15				
Lag 12	1.92	-0.43	-0.96	0.45	2.53	2.13				
Lag 16	1.31	-1.91	1.96	-12.07	1.63	5.92				
Nonlinear							3.75	36.34	5.64	6.68
Lag 4	-19.08	2.32	4.98	5.49	7.87	3.33				
Lag 8	1.61	7.22	0.05	7.09	4.85	8.56				
Lag 12	8.31	7.61	7.82	7.64	5.84	9.06				
Lag 16	8.5	5.80	6.95	-8.26	6.30	7.69				
Multiple										
Lags 4-8	-29.19		-6.52							

The base model included year, week of year (with a cyclic RW2 spline), consultations (log-transformed), population density (log-transformed), and spatial and temporal random effects. Pr = precipitation; Hum = humidity; Temp_M = mean temperature; Temp_R = temperature range; NDVI = normalized difference vegetation index; SW = surface water; S_S = scrub and shrub.

Table S4.2: Change in DIC from base model for environmental anomalies

	Pr_H	Temp_H	Temp_L	SW_H	SW_L	Hum_H	Hum_L
Linear	-8.51	0.47	-3.10	-2.80	0.66	2.39	3.71

The base model included year, week of year (with a cyclic RW2 spline), consultations (log-transformed), population density (log-transformed), and spatial and temporal random effects. Pr_H = anomalously high precipitation; Temp_H = anomalously high mean temperature; Temp_L = anomalously low mean temperature; SW_H = anomalously high surface water; SW_L = anomalously low surface water; Hum_H = anomalously high humidity; Hum_L = anomalously low humidity.

Table S4.3: Changes in DIC from removing variables from the full model

	Full model	Full model - Temp_M$_{t-4}$
	Δ	Δ
Removal		
Pr$_{t-4}$	18.34	
Precip$_{t-8}$	2.43	
Hum$_{t-16}$	1.92	
Temp_M$_{t-4}$	-6.94	
Temp_M$_{t-8}$	7.24	
Temp_R$_{t-16}$	7.69	
PR_H	4.02	
Temp_L	-1.91	3.01
SW_H	2.97	

Temp_M$_{t-4}$ was first removed from the full model because it improved DIC by the greatest amount. Removing Temp_L from the reduced model no longer improved model fit and was therefore retained in the final model.

Table S4.4: Annual reported case distribution by sex and age

	Female	Male	P value	<5	≥5	p value
2016	41,762 (49.6%)	42,401 (50.4%)	0.03	26,173 (31.1%)	57,990 (68.9%)	<0.0001
2017	30,897 (48.3%)	33,105 (51.7%)	<0.0001	20,922 (32.7%)	43,080 (67.3%)	<0.0001
2018	33,738 (48.7%)	35,501 (51.3%)	<0.0001	25,170 (36.4%)	44,069 (63.6%)	<0.0001
2019	32,044 (48.8%)	33,616 (51.2%)	<0.0001	24,764 (37.7%)	40,896 (62.3%)	<0.0001
2020	27,243 (49.1%)	28,217 (50.9%)	<0.0001	19,726 (35.6%)	35,734 (64.4%)	<0.0001
2021	48,883 (49.8%)	49,241 (50.2%)	0.25	30,072 (30.6%)	68,052 (69.4%)	<0.0001
2022	36,490 (49.9%)	36,569 (50.1%)	0.77	25,764 (35.3%)	47,295 (64.7%)	<0.0001
2023	19,909 (48.3%)	21,331 (51.7%)	<0.0001	15,229 (36.9%)	26,011 (63.1%)	<0.0001

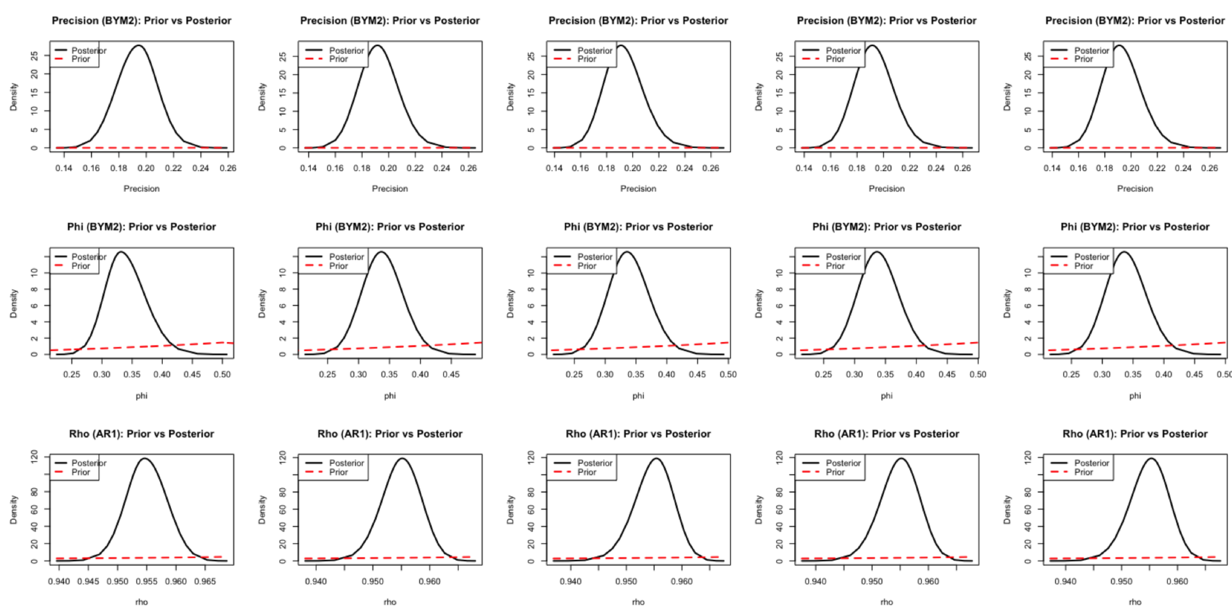

Figure S4.1: Prior versus posterior plots for 5 (out of the total 50) randomly selected models

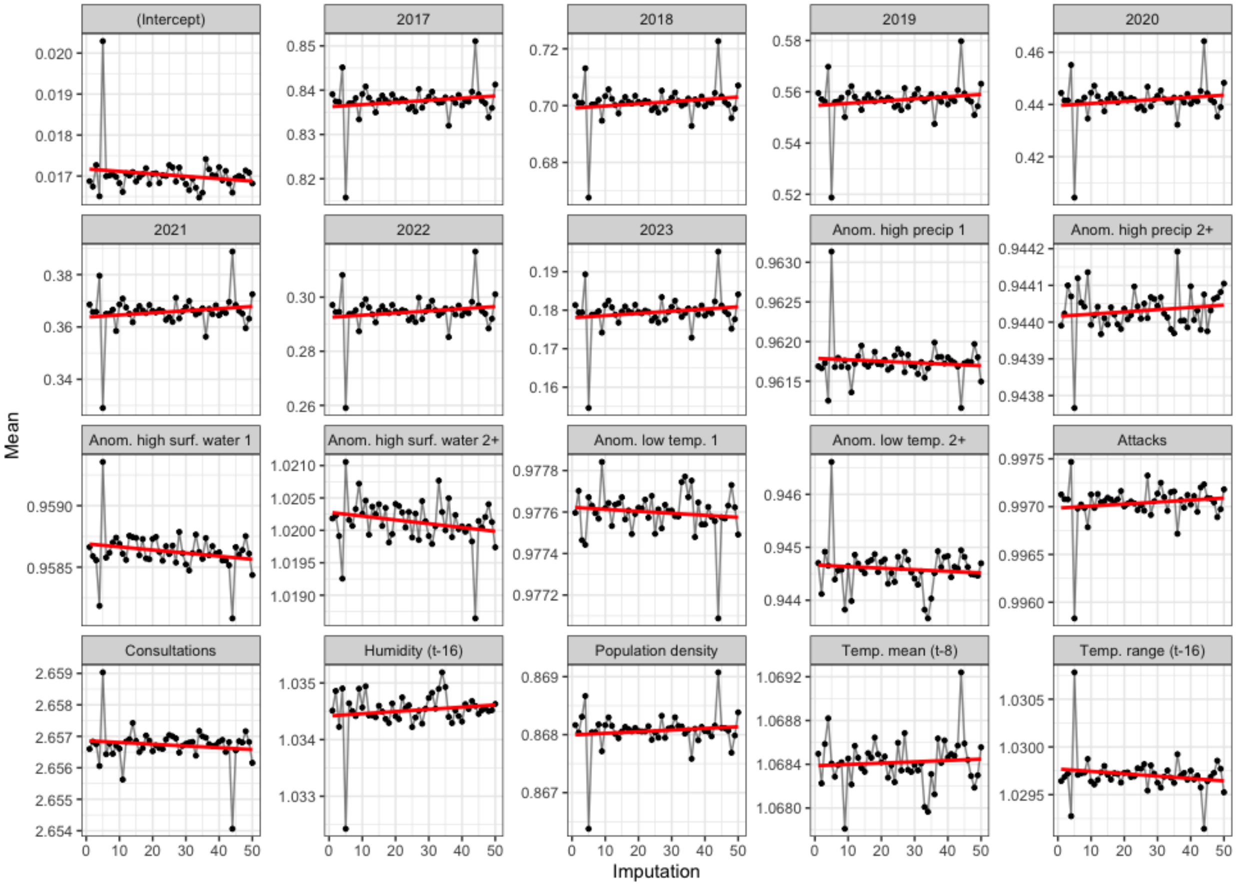

Figure S4.2: Model coefficient stability across imputations

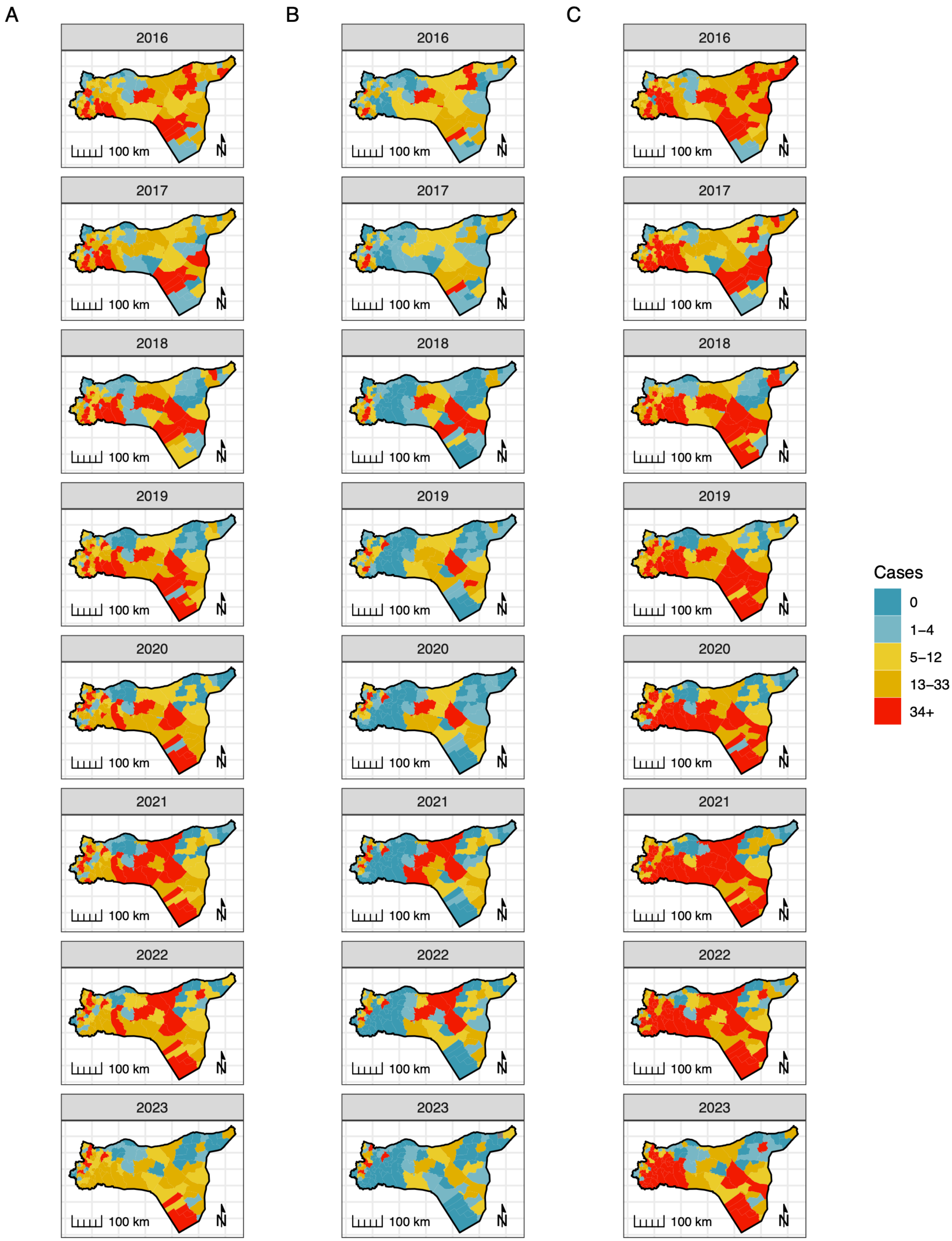

Figure S4.3: Estimated cases (A), lower credible interval (B), and upper credible interval (C) Each map displays the median weekly counts for each year by quantile.

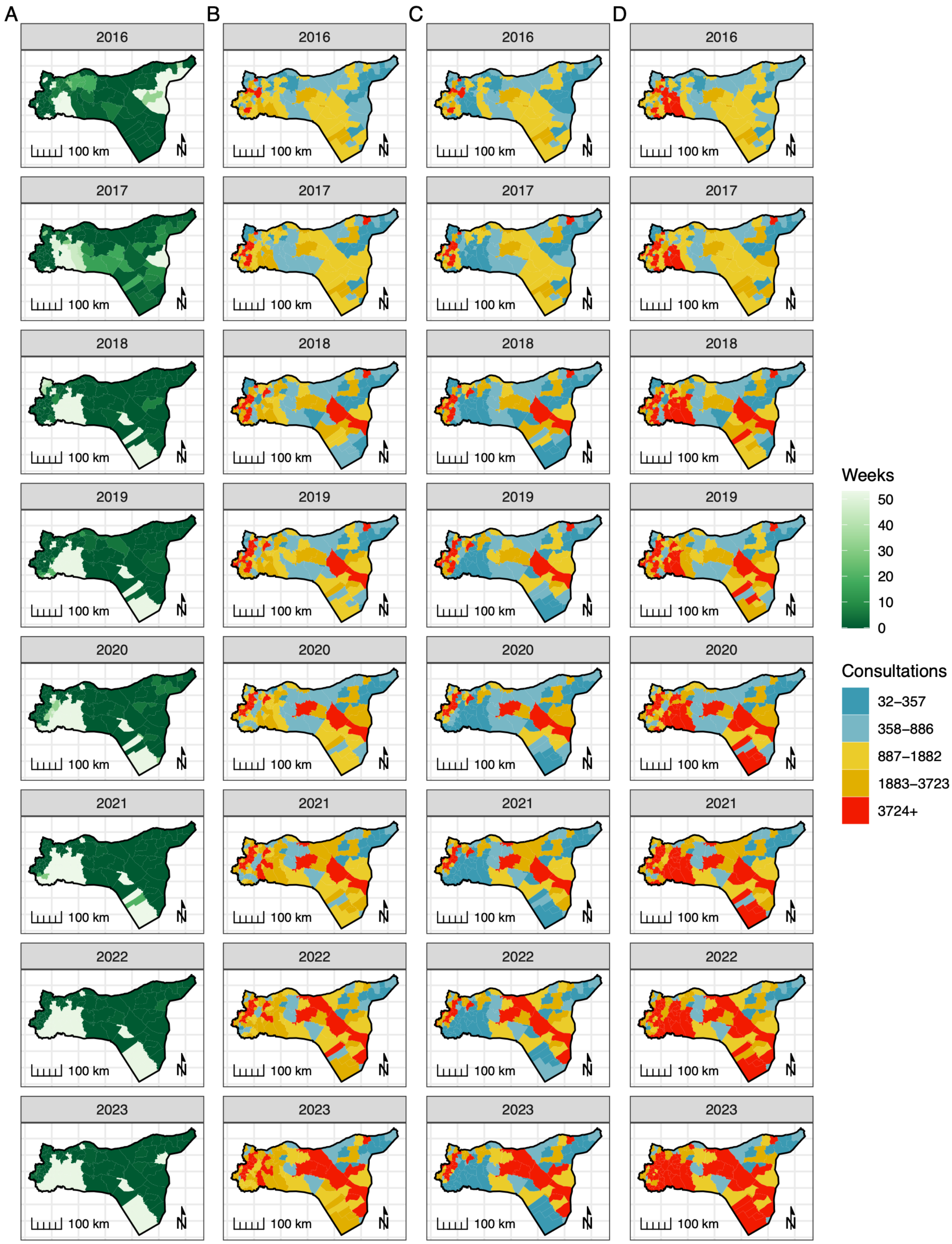

Figure S4.4: Number of missing weeks (A), mean estimated consultations (B), lower credible interval (C), and upper credible interval (D)
Each map displays the mean weekly counts for each year by quantile.

Table S4.5: Incidence rate ratios and 95% CrI from subgroup analyses

Covariate	All cases	Female	Males	<5 years old	≥5 years old
Demographic variables					
Population density	0.87 (0.686–1.098)	0.88 (0.698–1.099)	0.87 (0.697–1.088)	0.85 (0.671–1.068)	0.91 (0.719–1.139)
Consultations	2.66 (2.563–2.754)	2.59 (2.488–2.689)	2.66 (2.560–2.763)	2.69 (2.565–2.812)	2.60 (2.502–2.698)
Year					
2016	1 (ref)				
2017	0.84 (0.713–0.985)	0.85 (0.723–0.995)	0.82 (0.701–0.960)	0.92 (0.760–1.112)	0.84 (0.715–0.982)
2018	0.70 (0.552–0.893)	0.74 (0.588–0.943)	0.66 (0.521–0.830)	0.73 (0.555–0.966)	0.71 (0.564–0.903)
2019	0.56 (0.414–0.753)	0.59 (0.443–0.794)	0.55 (0.413–0.735)	0.65 (0.467–0.912)	0.57 (0.428–0.768)
2020	0.44 (0.312–0.628)	0.48 (0.344–0.680)	0.45 (0.319–0.625)	0.55 (0.375–0.809)	0.44 (0.312–0.619)
2021	0.37 (0.246–0.547)	0.42 (0.282–0.612)	0.38 (0.260–0.559)	0.45 (0.290–0.686)	0.39 (0.261–0.570)
2022	0.30 (0.189–0.462)	0.33 (0.211–0.501)	0.31 (0.202–0.476)	0.34 (0.208–0.541)	0.32 (0.203–0.488)
2023	0.18 (0.109–0.298)	0.19 (0.116–0.306)	0.20 (0.125–0.327)	0.23 (0.133–0.386)	0.18 (0.112–0.300)
Environmental variables					
Humidity$_{t-16}$	1.03 (1.005–1.065)	1.04 (1.009–1.071)	1.03 (0.998–1.057)	1.03 (1.000–1.069)	1.04 (1.007–1.069)
Temperature mean$_{t-8}$	1.07 (1.017–1.123)	1.07 (1.013–1.124)	1.06 (1.006–1.113)	1.07 (1.003–1.131)	1.07 (1.012–1.123)
Temperature range$_{t-16}$	1.03 (1.012–1.048)	1.04 (1.017–1.056)	1.02 (1.000–1.037)	1.02 (1.003–1.046)	1.03 (1.013–1.052)
Anomalously high precipitation					
0	1 (ref)				
1	0.96 (0.936–0.989)	0.95 (0.928–0.983)	0.97 (0.941–0.995)	0.98 (0.944–1.008)	0.95 (0.926–0.981)
2+	0.94 (0.895–0.996)	0.93 (0.875–0.979)	0.96 (0.911–1.016)	0.98 (0.920–1.047)	0.93 (0.881–0.985)
Anomalously high surface water					
0	1 (ref)				
1	0.96 (0.924–0.995)	0.96 (0.926–1.001)	0.96 (0.929–1.001)	0.99 (0.943–1.030)	0.95 (0.915–0.989)
2+	1.02 (0.951–1.095)	1.02 (0.949–1.100)	1.01 (0.938–1.082)	1.03 (0.951–1.125)	1.00 (0.933–1.081)
Anomalously low mean temp.					
0	1 (ref)				
1	0.98 (0.944–1.012)	0.97 (0.939–1.010)	0.98 (0.942–1.011)	0.97 (0.930–1.012)	0.97 (0.939–1.009)
2+	0.94 (0.878–1.016)	0.97 (0.898–1.042)	0.94 (0.878–1.014)	0.97 (0.892–1.055)	0.93 (0.858–0.998)
Attacks (in prior 3 months)	1.00 (0.958–1.038)	0.98 (0.945–1.025)	1.00 (0.965–1.045)	0.99 (0.943–1.034)	1.01 (0.966–1.048)

Outputs were calculated by averaging the outputs from the 50 model iterations. Non-linear outputs are shown in **Figures S4.5–S4.8**.

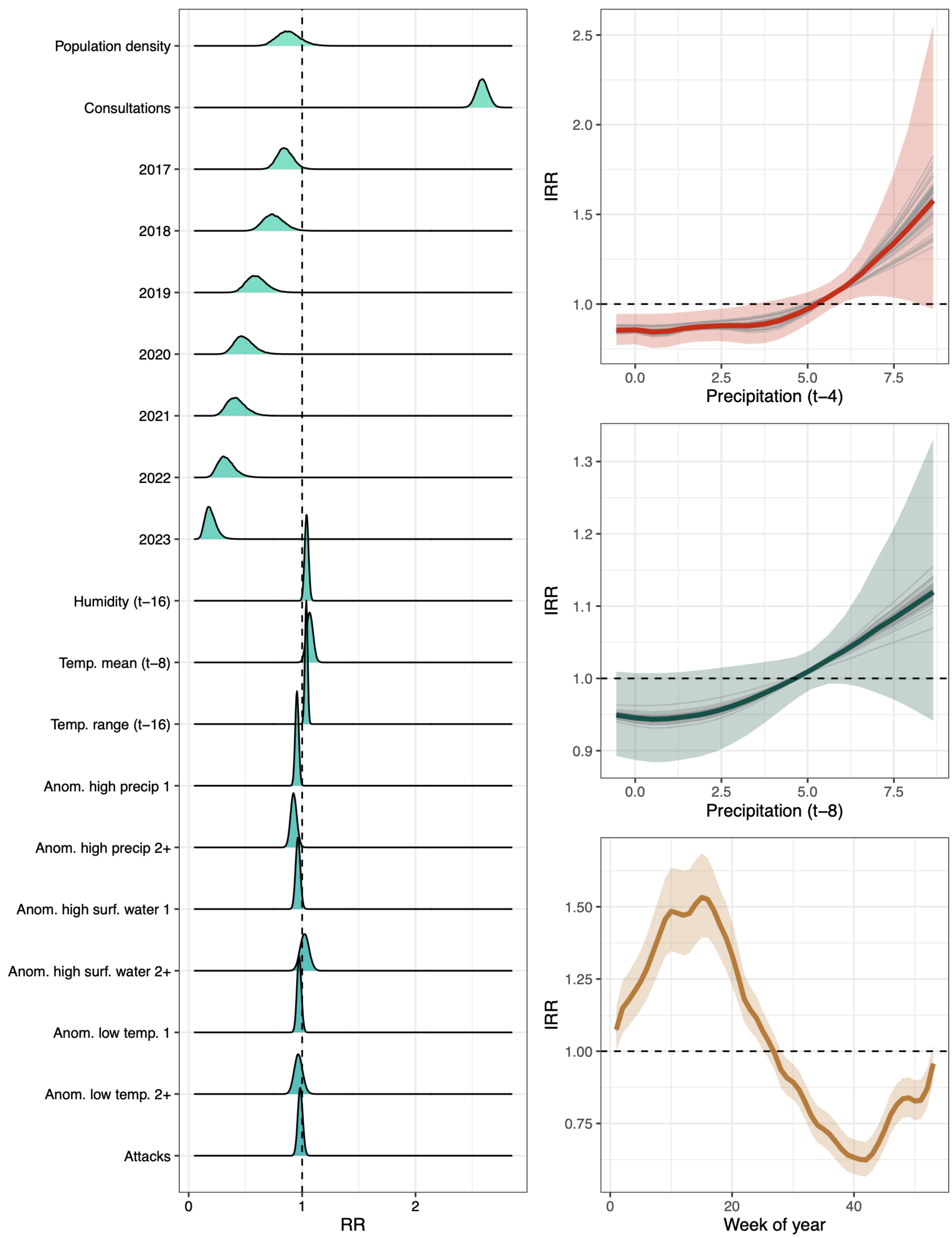

Figure S4.5: Ridgeline plot and non-linear outputs for cases in females

On the right, the thin grey lines show the posterior mean of the precipitation curve for each model iteration, while the thick colored line is the pooled estimate and the lighter band corresponds to the pooled 95% CrI. Values are considered significant when the estimate and the 95% CrI are all above or below the horizontal dashed line.

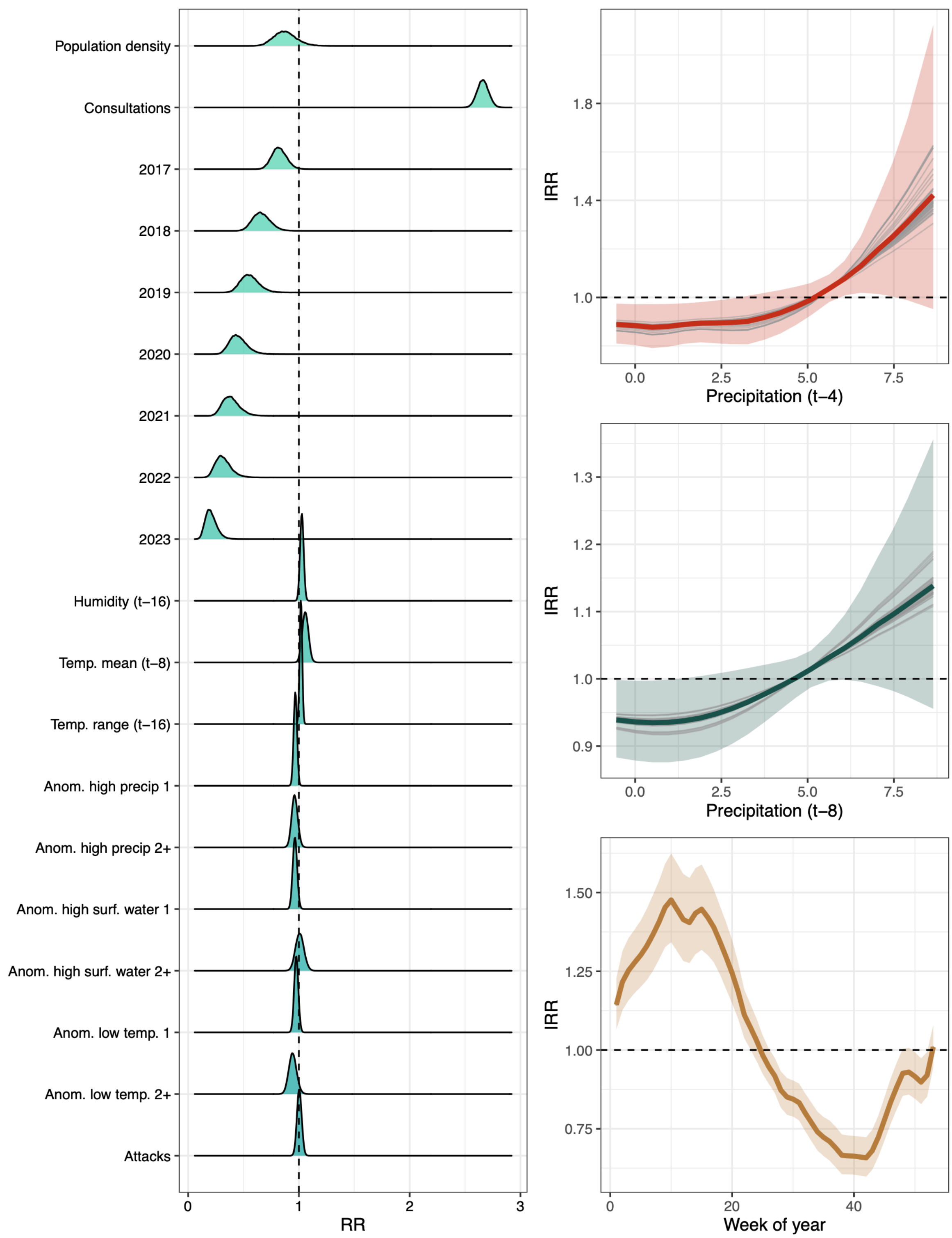

Figure S4.6: Ridgeline plot and non-linear outputs for cases in males

On the right, the thin grey lines show the posterior mean of the precipitation curve for each model iteration, while the thick colored line is the pooled estimate and the lighter band corresponds to the pooled 95% CrI. Values are considered significant when the estimate and the 95% CrI are all above or below the horizontal dashed line.

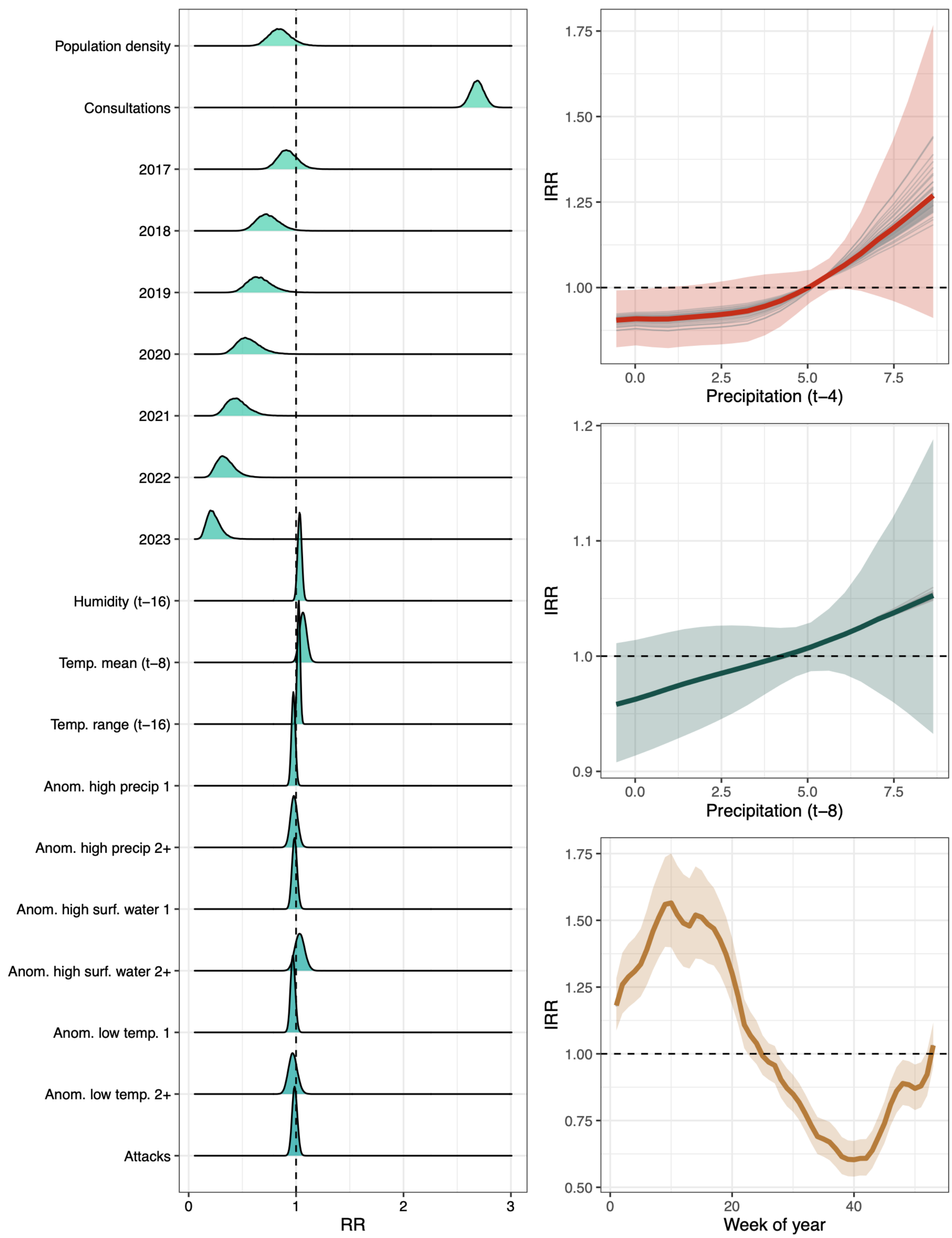

Figure S4.7: Ridgeline plot and non-linear outputs for cases in children <5 years old

On the right, the thin grey lines show the posterior mean of the precipitation curve for each model iteration, while the thick colored line is the pooled estimate and the lighter band corresponds to the pooled 95% CrI. Values are considered significant when the estimate and the 95% CrI are all above or below the horizontal dashed line.

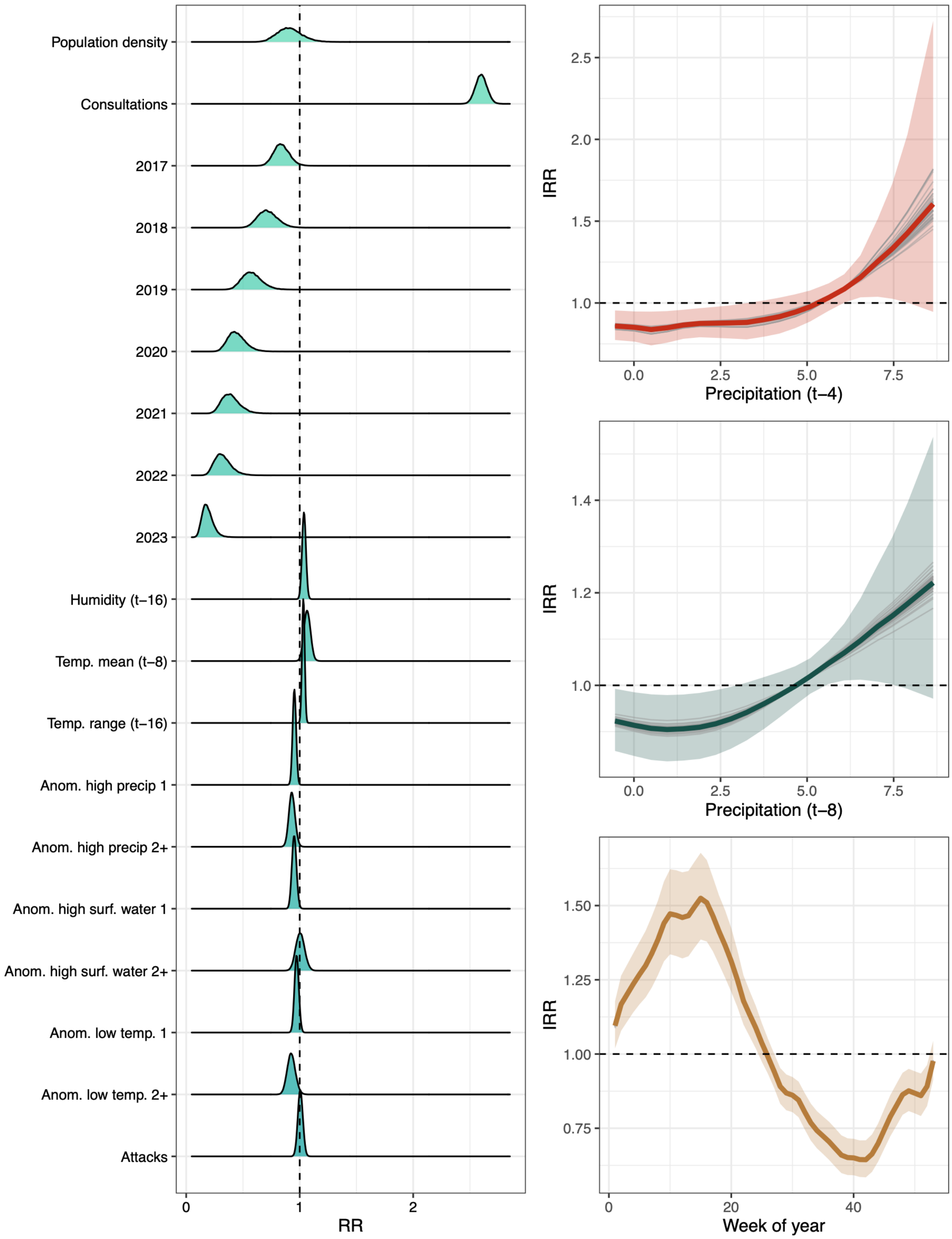

Figure S4.8: Ridgeline plot and non-linear outputs for cases in patients ≥5 years old

On the right, the thin grey lines show the posterior mean of the precipitation curve for each model iteration, while the thick colored line is the pooled estimate and the lighter band corresponds to the pooled 95% CrI. Values are considered significant when the estimate and the 95% CrI are all above or below the horizontal dashed line.

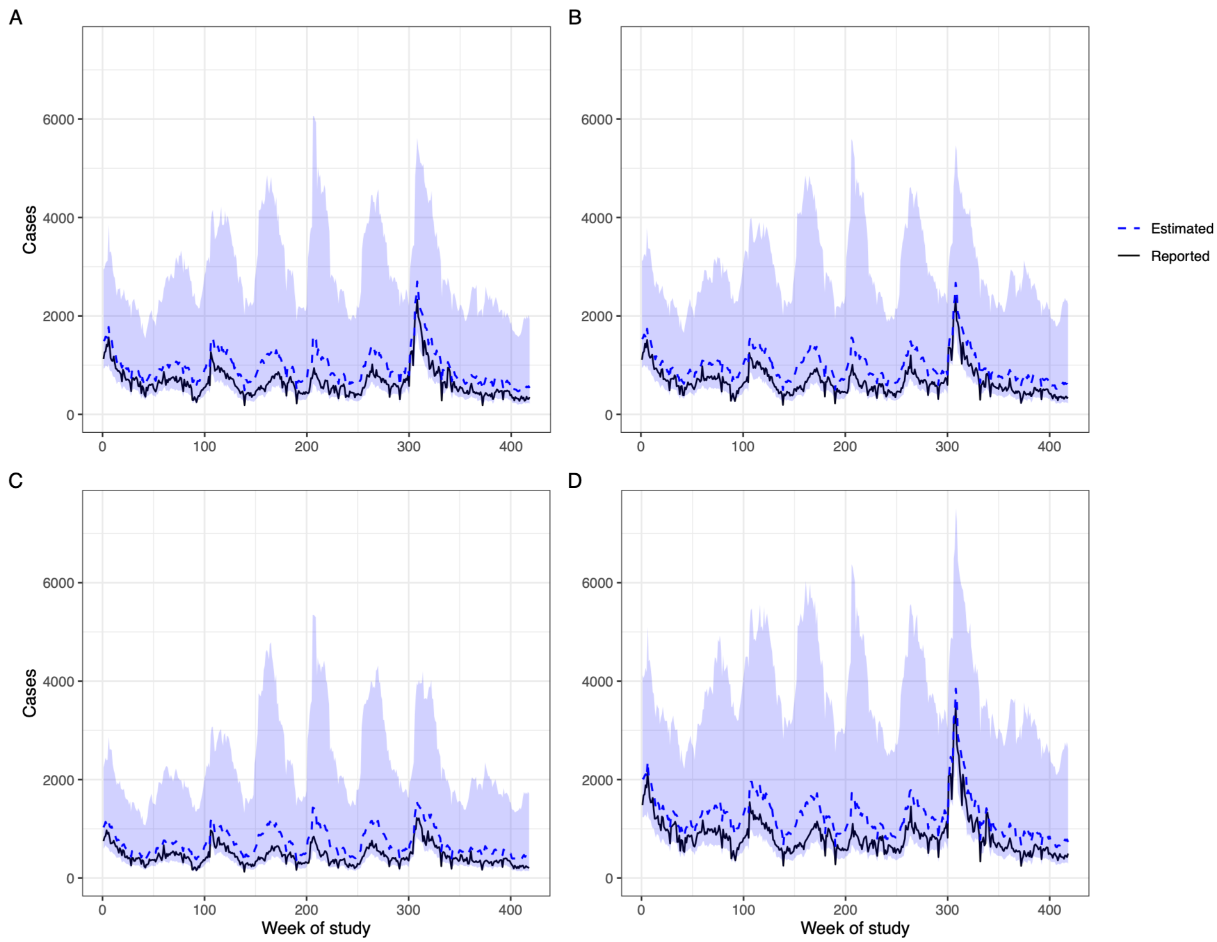

Figure S4.9: Reported and estimated CL cases by week for females (A), males (B), <5 years old (C), and ≥5 years old (D)
The shading represents the 95% CrI of the estimated data.

Table S4.6: Total estimated cases in female and male patients in subdistricts with the highest number of total estimated cases over the study period

Subdistrict	Rank	Total cases Estimated cases	Rank	Female Estimated cases	Rank	Male Estimated cases
Muhasan	1	63,780.6 (2,931.5–394,831.6)	1	25,963.1 (1,382.6–162,652.0)	1	25,380.7 (1,658.8–156,551.4)
Dana	2	43,262.9 (30,611.8–59,428.9)	2	20,843.7 (15,203.3–27,907.6)	2	22,340.1 (16,445.4–29,676.5)
Ras Al Ain	3	37,951.2 (26,978.9–51,955.8)	3	20,323.5 (14,971.0–27,018.2)	3	17,596.6 (13,026.8–23,299.2)
Kisreh	4	31,566.3 (22,347.0–43,358.6)	5	15,677.2 (11,435.1–21,009.6)	4	15,931.8 (11,707.9–21,214.5)
Ma’arrat An Nu’man	5	31,373.8 (21,890.7–45,606.8)	4	15,833.1 (11,508.0–21,884.9)	5	15,412.3 (11,181.8–21,846.1)
Tamanaah	6	31,263.7 (47.3–204,327.3)	6	12,477.8 (29.1–84,538.8)	7	12,266.4 (32.5–83,233.7)
Atareb	7	24,451.5 (17,170.1–33,806.1)	7	11,750.0 (8,422.3–15,968.8)	6	12,661.0 (9,168.8–17,058.7)
Ar-Raqqa	8	22,588.4 (15,867.6–31,225.6)	8	11,570.6 (8,317.5–15,693.6)	8	11,011.9 (7,957.7–14,870.1)
Al Bab	9	20,467.8 (14,335.6–28,376.6)	9	10,214.8 (7,311.4–13,917.1)	9	10,246.2 (7,378.2–13,888.0)
Suluk	10	19,714.0 (13,862.2–27,250.6)	10	9,796.0 (7,060.1–13,284.3)	10	9,927.6 (7,215.4–13,366.9)
Total (est.)		871,541.4 (385,412.0–2,799,024.0)		402,797.8 (191,635.0–1,226,538.0)		412,793.8 (199,834.3–1,237,622.0)
Total (reported)		550,947.0		270,966.0		279,981.0

Rank is ordered by the total number of estimated cases over the study period.

Table S4.7: Total estimated cases in patients <5 and ≥5 years old in subdistricts with the highest number of total estimated cases over the study period

Subdistrict	Rank	Total cases Estimated cases	Rank	<5 years old Estimated cases	Rank	≥5 years old Estimated cases
Muhasan	1	63,780.6 (2,931.5–394,831.6)	1	27,148.2 (1,121.5–171,545.3)	3	26,830.7 (1,753.9–165,216.4)
Dana	2	43,262.9 (30,611.8–59,428.9)	3	13,228.3 (9,387.6–18,136.6)	2	30,003.4 (21,388.5–40,957.4)
Ras Al Ain	3	37,951.2 (26,978.9–51,955.8)	17	6,018.3 (4,214.3–8,380.4)	1	31,819.3 (22,871.8–43,164.2)
Kisreh	4	31,566.3 (22,347.0–43,358.6)	2	14,659.2 (10,513.7–19,931.9)	6	16,953.6 (12,031.8–23,249.3)
Ma’arrat An Nu’man	5	31,373.8 (21,890.7–45,606.8)	4	9,947.3 (7,026.3–14,212.1)	4	21,367.3 (15,036.3–30,822.8)
Tamanaah	6	31,263.7 (47.3–204,327.3)	6	8,191.9 (10.1–54,088.6)	5	18,431.4 (38.5–124,467.8)
Atareb	7	24,451.5 (17,170.1–33,806.1)	8	7,884.0 (5,464.3–11,025.8)	7	16,561.2 (11,669.7–22,832.0)
Ar-Raqqa	8	22,588.4 (15,867.6–31,225.6)	7	8,046.8 (5,612.4–11,204.1)	8	14,552.4 (10,247.9–20,079.9)
Al Bab	9	20,467.8 (14,335.6–28,376.6)	11	7,116.0 (4,957.2–9,932.1)	9	13,360.2 (9,367.0–18,512.5)
Suluk	10	19,714.0 (13,862.2–27,250.6)	5	9,094.7 (6,431.7–12,536.5)	11	10,630.5 (7,478.4–14,707.4)
Total (est.)		871,541.4 (385,412.0–2,799,024.0)		300,534.1 (128,841.5–989,339.5)		530,660.7 (253,002.1–1,592,476.0)
Total (reported)		550,947.0		187,820.0		363,127.0

Rank is ordered by the total number of estimated cases over the study period.

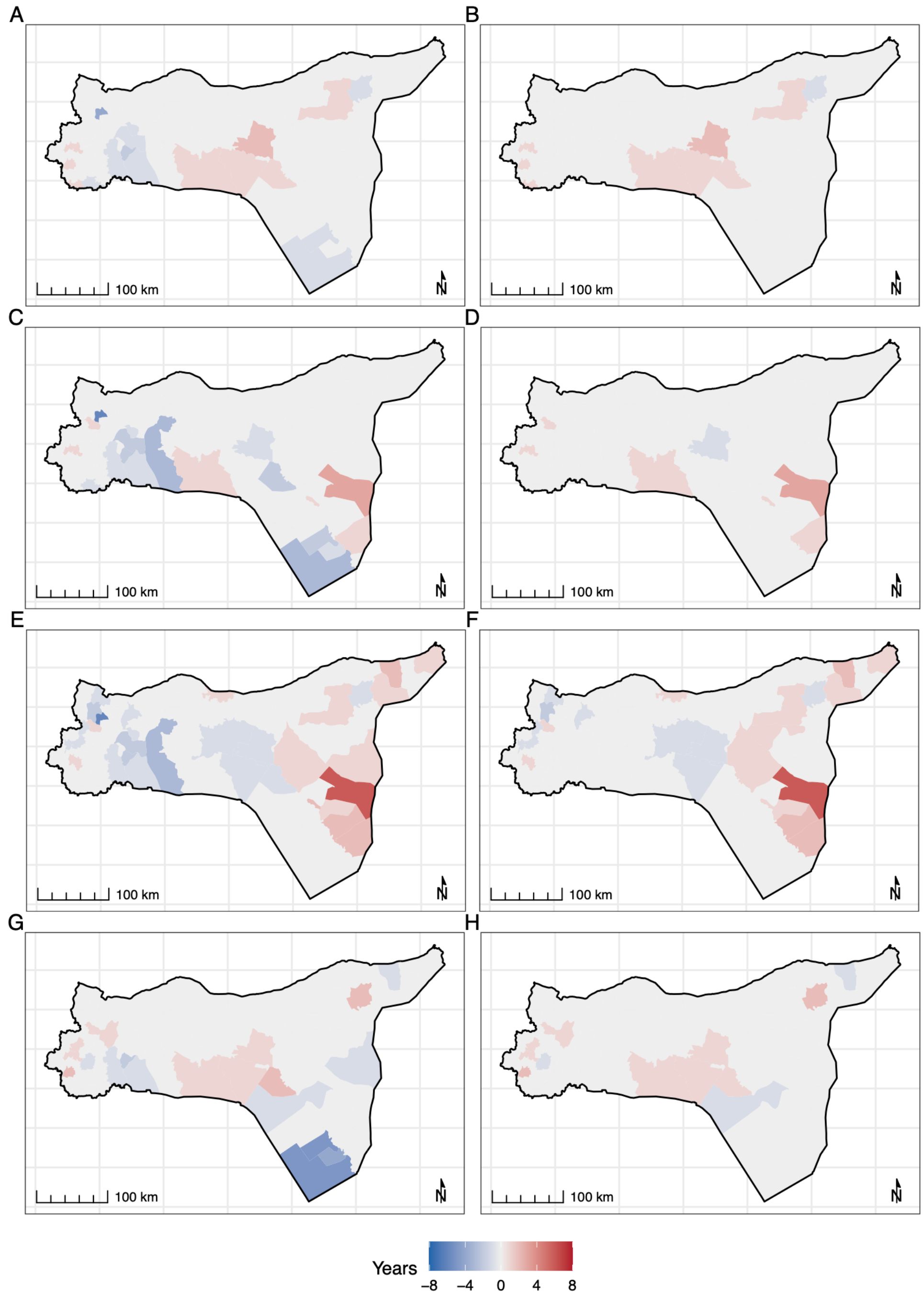

Figure S4.10: Difference in hotspot status between total cases and cases in females (A-B), males (C-D), patients <5 years old (E-F), and patients ≥5 years old (G-H)

The left column displays the number of years that each subdistrict's estimated number of CL cases was in the highest quantile. The right column displays the number of years each subdistrict's estimated number of cases was in the highest quantile and its lower credible interval was in either the highest or second highest quantile. Negative values (blues) indicate that the subdistrict had fewer years as a subgroup-level hotspot than a total case-level hotspot, and positive values (reds) indicate that the subdistricts had more years as a subgroup-level hotspot. For example, the dark red subdistrict in Maps E and F indicates that Sur was considered a hotspot for cases in children <5 years old for 6 more years than it was for total cases.